Mechanical Function of the Left Atrium

A Dissertation

Presented to

the faculty of the School of Engineering and Applied Science

University of Virginia

---

in partial fulfillment

of the requirements for the degree

Doctor of Philosophy

by

Christian B. Moyer

December

2013

APPROVAL SHEET

The dissertation

is submitted in partial fulfillment of the requirements

for the degree of

Doctor of Philosophy

AUTHOR

The dissertation has been read and approved by the examining committee:

Jeffrey W. Holmes

Advisor

Craig H. Meyer

Silvia S. Blemker

John D. Ferguson

Jeffrey J. Saucerman

Accepted for the School of Engineering and Applied Science:

Dean, School of Engineering and Applied Science

December

2013

Abstract

Atrial fibrillation is a growing epidemic in the developed world and current methods of evaluating AF patients and therapies are limited. In this thesis, we developed a novel set of tools to measure and simulate global and regional atrial function, both in healthy and diseased hearts. We used these tools to discover regional heterogeneity in healthy atrial function: some parts of the atrium move more than others, some are mostly passive while others are more active. We applied the same wall motion analysis to AF patients and found changes in global and regional mechanics: the heart enlarges, relies more on active contraction to move blood, and deteriorates in regions that were originally high-functioning and passive. Since AF develops alongside a series of other cardiac disease, we used pressure-volume loops to quantify changes in global mechanics. P-V loops revealed how ventricular dysfunction (congestive heart failure, left ventricular hypertrophy) and atrial dysfunction (type and duration of AF, any prior ablations) alter P-V loop shape and disrupt normal function.

To better understand why function changes due to AF, we built a novel finite element model of the left atrium and varied five factors that normally change due to AF: size, shape, pressure, fibrosis, and conduction. We found that pressure and size have the largest effect on function while shape and conduction have a smaller effect. We were able to recreate over 80% of the observed changes in atrial function between healthy adults and AF patients by simulating three of the five factors: size, pressure, and fibrosis. We discovered that atrial factors could not recreate the increased reliance on active contraction that was a hallmark of the wall motion analysis. We used a coupled circuit model of ventricular function to test

the influence of changes in LV properties and discovered that impaired LV relaxation during early diastole recreated the increased reliance on active contraction.

We adapted this finite element model to simulate common ablation procedures and found that more aggressive procedures (wide area circumferential ablation) impaired atrial function more than the conservative procedures (pulmonary vein isolation). We also discovered that changes in global function depended on both the amount and location of ablation scar, and found that regional function and stress increased the most in areas where scar was applied. We used P-V loop analysis to measure acute changes in post-ablation function and used the wall motion analysis to measure long-term changes in global and regional function. We found that atrial function is acutely depressed, but recovers within one-month post-ablation. At six-months, the atrium shrinks in size and becomes more passive. These changes outweighed the effects of simulated scarring, and represented a return to healthier function following recovery of sinus rhythm.

To my mom,
who gave me an analytical mind and unmatched perseverance.

Acknowledgments

I would like to acknowledge my advisor, Jeff Holmes, for five years of superb mentorship. Everything I achieved in this thesis was a direct result of his guidance. His dedication to teaching and developing his graduate students was unparalleled and his enthusiastic approach to scientific discovery was infectious. Wherever I go in life, I am confident I will carry with me the many lessons he imparted. Thank you Jeff.

I would also like to acknowledge my committee for their constant support of my research. I would like to thank Silvia Blemker for her keen insights into finite element models and the many discussions I shared with her lab. I would like to thank Jeff Saucerman for sharing his ideas about computational modeling and our discussions about the clinical applications of this work. I would like to thank Craig Meyer for many discussions about MRI sequences, imaging protocols, and two awesome graduate courses that he taught – these courses helped cement MRI as a cornerstone of my research. I would like to thank John Ferguson for exposing me to the clinical eletrophysiology lab and allowing me to observe and engage with his many colleagues in the UVa hospital. The experience was extremely rewarding and helped me to guide my thesis towards clinical translation. Thank you Silvia, Jeff, Craig, and John.

I would like to acknowledge the many other physicians, fellows, residents, interns, technicians, and staff members that assisted me in my research. I would especially like to thank Craig Goodman for many laughs during long imaging studies, Tad Adams for clinical support in the hospital, and David Lopez, Chris Clark, and Patrick Norton for their engaging and supportive collaborations. Thank you all.

I would also like to acknowledge the former and present members of the Cardiac Biomechanics Group. You guided me, cheered me on, challenged me, and laughed with me through the many days and nights of presentations, simulations, and experiments. You heightened my successes and softened my struggles through your unwavering friendship. Thank you all.

I would especially like to acknowledge Katy Parker, Andrew Roulliard, and Beth Ames, who shared with me countless laughs and stories in our little office in the corner of MR-5. Thank you Katy, Andrew, and Beth.

Finally, I would like to acknowledge my family: my father Steve, my mom Joan, my brothers Tyson and Stephen, and my finance Linsey (and our dog Watson). Everything I have achieved, both in this thesis and in life, was because of your care and support. Without all of you, none of this is possible. I try to remind myself of this every day.

Contents

List of Tables

List of Figures

List of Nomenclature

Mathematical Symbols

Symbol	Description
P	Pressure
V	Volume
G	Conductance
G_p	Parallel conductance
E	Elastance
t	Time (continuous)
T	Time (discrete)
R	Resistance
Q	Flow
k_c	Chamber stiffness
k_t	Tissue stiffness
SW	Stroke work
$\hat{y}$	Fitted value
ξ	Position in element space
x	Position in Cartesian space
L_i	Lagrangian interpolation function of node i
H_i^j	Hermite interpolation function of node i and derivative j
S_e	Scaling factor of element e

Δ_{ei}	Connectivity matrix
Y_n	Nodal parameter matrix
$\mathbf{u}$	Surface mesh
$F(\mathbf{u})$	Error function
$\mathbf{u}^*$	Optimized surface mesh
$\mathbf{H}$	Basis function matrix
$\mathbf{S}$	Scaling factor matrix
$\mathbf{B}$	Global interpolation matrix
∇	Gradient
$\mathbb{H}$	Hessian
G	Sobolev smoothing penalty function
$\mathbf{C}$	Constraint matrix
$\mathcal{L}$	Lagrangian
λ	Lagrangian multiplier
$\mathbf{X}$	Undeformed (material) coordinates
$\mathbf{x}$	Deformed coordinates
$\mathbf{F}$	Deformation gradient tensor
J	Jacobian
$\mathbf{C}$	Right Cauchy-Green deformation gradient tensor
$\mathbf{E}$	Green-Lagrange strain tensor
$\boldsymbol{\sigma}$	Cauchy stress tensor
$\mathbf{S}$	Second Piola-Kirchhoff stress
$\mathcal{C}$	Material elasticity tensor
W	Strain energy
$\mathbf{\Pi}$	Total potential energy
κ	Surface curvature
$\mathbf{K}$	Global stiffness matrix

λ	Stretch
$\mathbf{A}$	Undeformed fiber vectors

Acronyms

AED	Atrial end-diastole
AF	Atrial fibrillation
AIC	Akaike information criterion
AV	Aortic valve
BIC	Bayesian information criterion
BL	Baseline
BMI	Body-mass index
BSA	Body surface area
BOS	Booster-pump (LA flow)
CAD	Coronary artery disease
CHF	Congestive heart failure
CMR	Cardiac magnetic resonance
CON	Conduit (LA flow)
CT	Computed tomography
CY	Cryoablation
DE	Delayed enhancement
DENSE	Displacement encoding with stimulated echo
DM	Diabetes mellitus
EF	Emptying fraction (LA)
EF	Ejection fraction (LV)
EPE	End of passive emptying
FEA	Finite element analysis

FEM	Finite element model
HS	Healthy subjects
HTN	Hypertension
IAS	Intra-atrial septum
IRB	Institutional review board
LA	Left atri (-um,-al)
LGE	Late gadolinium enhancement
LIPV	Left inferior pulmonary vein
LSPV	Left superior pulmonary vein
LV	Left ventric (-le,-ular)
LVH	Left ventricular hypertrophy
MR	Mitral (valve) regurgitation
MRI	Magnetic resonance imaging
MS	Mitral (valve) stenosis
MV	Mitral valve
MVO	Mitral valve opening
MVC	Mitral valve closing
OSA	Obstructive sleep apnea
PV	Pulmonary vein
PVI	Pulmonary vein isolation
P-V	Pressure-volume
RES	Reservoir (LA flow)
RF	Radiofrequency
RIPV	Right inferior pulmonary vein
RSPV	Right superior pulmonary vein
SEF	Strain energy function
SPF	Start of passive filling

SSFP	Steady-state free precession
ST	Speckle tracking
SV	Stroke volume
US	Ultrasound
WACA	Wide area circumferential ablation
WMA	Wall motion analysis
WPW	Wolff-Parkinson-White

Chapter 1

Introduction

The human heart is a wondrous pump. It weighs less than a pound and moves over a gallon of blood every minute. That blood moves through four one-way valves and four separate chambers in a coordinated sequence called a *beat*. The heart starts beating four weeks after conception and continues with an unwavering cadence, once per second, for the rest of its life. A beat starts in upper right chamber of the heart, in a small cluster of pacemaking cells called the sinoatrial node. From there, an electrical signal travels through the heart muscle, activating each of the four chambers in a precise sequence of coordinated contraction. The upper chambers contract first, followed by the lower chambers and all in under a second. Although smaller in size and strength, these upper chambers (the atria) play a vital role in moving that gallon of blood each minute. Their importance grows with age, so much so that by the eightieth year our hearts rely on those small chambers to pump over half of the total volume. The function of the atrium, the diseases that impair it, and the therapies that affect it, are all crucial aspects of cardiovascular research.

1.1 The heart and the soul

The heart's role in life has fascinated physicians and laymen alike since the antiquities, where it was believed to house not blood and muscle but soulful passions and desires. The Egyptians

and Mesopotamians held a cardiocentric belief – that conscious thought arose from and resided in the heart (Crivellato and Ribatti, 2007). Plato and the Greeks believed that conscious thought arose in the mind while the mortal soul resided in the heart, describing the organ as "the knot of veins and the fountain of blood". Aristotle (c. 320 BC) postulated that the heart heated the rest of the body using three chambers (the right, middle, and left cavity), which we now know referred to the right ventricle, left ventricle, and left atrium, respectively. In Egypt (c. 300 BC) Herophilus, the founder of the medical school in Alexandria, realized that the right and left atria were part of the heart and not a simple extension of veins (Van Praagh and Van Praagh, 1983). Around the same time, the Hippocratic Corpus (text derived from the work of Hippocrates) noted that the orifices (valves) of the heart could be viewed by removing the heart's "ears" (Cheng, 2001). The text noted the unique motion of the ears, inflating and collapsing separate from the ventricle. Years later Rufus of Ephesus (c. 0 BC) identified tissue resting on top of the ventricles as the heart's "ears" or "auricles" in Latin, noting that they pulsated with the rest of the heart.

1.1.1 The ears of the heart

The auricles of the heart were identified prior to 0 BC, but their function was highly contested. Some believed they housed air and heat from the lungs and warmed the blood in the ventricle. Others believed that the heart was a self-contained life that could actually hear through it's ears! The atrium can do many things, but it does not have auditory function. Claudius Galen (c. 130 - c. 200 AD), one of the most prominent medical researchers in history, advanced the view that the atria contained air from the lungs. He postulated that blood flowed from the right to left ventricle through small holes in the septum as air was added. This view persisted for over a thousand years. In the early sixteenth century, Leonardo da Vinci was the first to note the difference between the atrium (an "upper ventricle") and the atrial appendage ("ear"). He understood that the heart was a muscle supplied by its own arteries and veins yet he was not able to discern the exact function of the atrium. It was not until an English

physician named William Harvey unveiled his theory of circulation that the current view of atrial function was developed.

1.1.2 William Harvey

In 1628, William Harvey published his seminal work on the heart and cardiac function called *Exercitatio Anatomica de Motu Cordis, et Sanguinis in Animalibus* also known as "An Anatomical Study on the Motion of the Heart and Blood" (Harvey and Leake, 1928). In this work, Harvey discovered that the pulmonary vasclature and atrium were full of blood, not air. He tried to find the small septal pores described by Galen, but writes in frustration:

> Even less tolerable is the opinion which supposes two materials, air and blood, necessary for the formation of vital spirits. The blood is supposed to ooze through tiny pores in the septum of the heart from the right to the left ventricle, while air is drawn from the lungs by the large pulmonary vein. According to this many little openings exist in the septum of the heart suited to the passage of blood. But, damn it, no such pores exist nor can they be demonstrated!

This negative experimental result forced Harvey to reconsider atrial function. He uncovered a wealth of insights: he observed atrial fibrillation as palpitations, he found the source of pacemaking in the right atrium (it was the last part of the heart to stop beating), and discovered that auricles exist in all animals with a ventricle, but not the reverse. He noted that the atria beat separately from the ventricles, writing that the movement "seems to start in the auricles [atria] and spread to the ventricles". He defined atrial contraction as "...necessary in order to cast the blood conveniently into the ventricles. These [atria], continually contracting, throw out more fully and forcibly the blood already in motion." Finally, he discovered a large variation in atria among men, writing "I marvel that there is such variation in this in different men." His insights laid a broad foundation for understanding the atrium's role in cardiac function, its ability to pump blood into the ventricle, and the variation in atrial size among adults.

1.1.3 Jean-Baptiste de Senac

Harvey was the first to develop a modern view of healthy heart function, and Jean-Baptiste de Senac (1693-1770) built upon his work to understand diseases in the heart (McMichael, 1982). de Senac intently studied atrial and ventricular fibrillation and discovered that they usually occur immediately prior to death. In cases of atrial fibrillation, he discovered that "the causes of palpitation are not causes of the natural heart-beat". He was the first to discover that atrial fibrillation had an *ectopic* origin, meaning that the errant signal did not originate in the sino-atrial node, but rather some other part of the heart. de Senac described AF as "beats which are either more active and more frequent, such as occur in fever or in any action demanding effort, and even mental agitation. But these are not illnesses by themselves and do not leave any sequential damage." Though his insights were powerful, de Senac was not able to observe the long term effects of fibrillation, which we now know has a lasting and damaging influence on the atrium.

1.2 Left atrial anatomy and physiology

The left atrium is one of four muscular chambers in the heart. It is one of the two upper chambers, along with the right atrium, located near the base of the heart and away from its apex. The atrium is seated in the posterior region of the chest cavity directly anterior to the spinal column, aligned in the medial-lateral direction. It is connected to the pulmonary circulation by three to five pulmonary veins, which supply oxygenated blood from the lungs, and connected to the left ventricle via the mitral valve. The atrium is part of the "preload" system for the left ventricle. Along with the pulmonary vasculature, the atrium stores blood pumped from the right ventricle during ventricular systole, then empties it into the left ventricle during ventricular diastole.

The left atrium is composed of a main chamber that is 4-5 cm in diameter and 50 mL in volume (roughly the size of a flattened golf ball) and an appendage that is 15 mL in volume

and varies in shape. The appendage rests on the free wall of the left ventricle; it is highly muscular, trabeculated, and aids in atrial function. It also has an elevated amount of artrial natriuretic factor, used to regulate pressure during overload conditions (Al-Saady et al., 1999). The left atrial wall is composed of myocytes, collagen, and other extracellular matrix. It is 1-5 mm thick, with an average muscle thickness of 2 mm. The pulmonary veins attach to the left atrium on the posterior wall at points called the ostia. Two veins from the right lung and two from the left attach to the atrium in a symmetric, vertical pattern and are generally labeled as left superior, left inferior, right superior, and right inferior pulmonary veins. In some patients, the number of veins can range from 3 to 5. The pulmonary veins are oval in shape and approximately 0.5-1 cm in diameter. They contain a thick muscular "sleeve" that extends from the left atrial ostium 1-3 cm along the vein (Calkins et al., 2008). It is believed that this sleeve aids in prevented reverse flow during atrial contraction, and also might contribute to the onset of rhythm disorders such as atrial fibrillation.

1.2.1 Left atrial physiology

The atrium behaves as a passive chamber during ventricular systole, allowing blood to accumulate as pressure increases. This behavior is generally called the "reservoir" or "filling" function of the atrium, as it collects blood while the ventricle contracts. After the mitral valve opens, blood passively leaves the atrium across the mitral valve. This phase is generally called the "passive emptying" phase or "conduit function". Here, both the atrium and ventricle are relaxed and blood passively flows across the valve. Once pressure equalizes, flow decreases and the atrium and ventricle are in "diastasis" or "slow filling" phase. Diastasis does not always exist, and sometimes involves no change in volume. Finally, the atrium contracts and pumps additional blood into the ventricle. This phase is called the "active emptying" phase, "contractile function", "booster-pump function", or colloquially "the atrial kick". Changes to the atrium – whether due to demographics, natural aging, or a cardiac disorder – will influence each of these phases in different ways.

Because the pulmonary veins lack valves, blood flows in and out of the atrium at any time during the cardiac cycle. To account for this, clinicians sometimes evaluate atrial function in the context of ventricular stroke volume. Ventricular stroke volume is separated into three contributions: passive atrial emptying, active atrial emptying, and conduit flow. Conduit flow is equal to the difference between ventricular stroke volume and total atrial volume change. In a typical adult, total atrial volume change is approximately 45 mL, and ventricular stroke volume is 70 mL, for a conduit volume of 25 mL. Active emptying contributes approximately 20-30% of left ventricular stroke volume in healthy adults (20-29 years old), but increases to 45-50% in older populations (60-69 years old) (Alhogbani et al., 2010; Boyd et al., 2011). As we age, the role of the atrium changes and contraction becomes more important to filling the ventricle.

1.2.2 Imaging the left atrium to assess structure and function

Cardiac imaging has become the primary tool to assess atrial function (To et al., 2011). Trans-thoracic 2-D echocardiography is used to estimate atrial size by measuring the length of the atrium in the parasternal long-axis view. Doppler techniques are used to measure pulmonary vein and mitral valve flow, assessing passive and active emptying into the ventricle. Trans-esophageal echocardiography is typically done in AF patients to assess for clot formation in the left atrial appendage. Three-dimensional echocardiography, speckle tracking, tissue Doppler, and other advanced imaging techniques have yet to enter the standard of care, but their use to assess atrial function remains an area of active research.

Non-ultrasound techniques, included computed tomography (CT) and magnetic resonance imaging (MRI) have gained prominence in recent years as an alternative to echocardiogrphy. Both CT and MRI can provide three dimensional structure at higher resolutions than ultrasound, and more recent techniques have the ability to measure phasic function (motion) in the atrium. Currently, CT and MRI are used for a detailed anatomical renderings of the atrium prior to electrophysiology procedures. The imaging sequence uses contrast (an MR

"angiography") to visualize a bright blood pool in the atrium and pulmonary veins, which then gets converted into a 3-D volume rendering to help guide catheter placement during procedures. MRI has also gained recent acceptance as a tool to assess atrial fibrosis and ablation scarring (Oakes et al., 2009; Peters et al., 2007). Each modality can measure left atrial volume or dimensional surrogates, which adds value in patient classification (Wann et al., 2011) and treatment monitoring (Jeevanantham et al., 2010). However, measures of regional function, including tissue Doppler, speckle tracking, MR tagging, and DENSE, are limited by the thin wall and dorsal position of the atrium.

1.3 Atrial fibrillation

Atrial fibrillation (AF) is a rhythm disorder of the upper chambers in the heart. It starts as sparks of electrical activity in the pulmonary vein ostia (Haissaguerre et al., 1998), a region of disorganized muscle fibers and dense autonomic innervation (Tan et al., 2006). The effects are slowly realized, but cumulative and self-reinforcing. Overwhelmed cellular ion channels remodel, slowing conduction velocity (Nattel, 2002), (Gaspo et al., 1997). Myocytes, contracting 400 times a minute in AF, grow, remodel, and die. They are replaced and surrounded by fibrotic collagen (Allessie et al., 2002), (Burstein and Nattel, 2008). In a vicious circle, these electrical and structural changes generate and sustain more episodes of AF, leading to the more severe versions of the disease.

Clinicians typically classify AF patients based on the duration of the disease, the length of AF episodes, and the resistance to corrective therapies, though classifications are not universal. Following the AHA guidelines (Fuster et al., 2006), AF is classified as: 1) Newly discovered AF, 2) Recurrent Paroxysmal AF, 3) Recurrent Persistent AF, 4) Permanent AF. Recurrence is defined as two or more episodes of AF. If each episode terminates spontaneously, the AF is classified as paroxysmal. If episodes last longer than seven days without terminating, the AF is classified as persistent. Permanent or "long-standing" AF lasts for over a year and

electrical shock (Cardioversion) cannot recover sinus rhythm. In this thesis, we will analyze paroxysmal and persistent AF subjects, and in most cases we will focus on paroxysmal AF.

1.3.1 Management of AF

The most serious complication of AF is an increased risk of embolic stroke. During episodes of AF, the blood stagnates in the atrium and forms clots, especially in the left atrial appendage. Secondary risks include elevated ventricular heart rate and disrupted atrial contraction. Symptomatic patients are given drugs to prevent clotting (Connolly et al., 2009) and control either heart rate or heart rhythm (anti-arrhythmic drugs or AADs). There is an ongoing debate as to whether rate-control or rhythm-control drugs are the optimum strategy. A major comparison trial (AFFIRM) found no differences between the strategies (Wyse et al., 2002), and a series of follow-up studies found only small differences (Fuster et al., 2006). The choice in strategy may depend on the patient age, clinical history, and type of AF.

A meta-analysis of forty-four randomized trials (Lafuente-Lafuente C et al., 2006) identified the best available anti-arrhythmic drugs (flecainide, amiodarone, dofetilide, among others) and found that they had a significant effect in controlling sinus rhythm but no significant effect on mortality. Given the limited effectiveness of AADs and the known side effects of AADs and chronic anticoagulants, clinicians have moved towards catheter-based ablation therapy as an alternative treatment. In a small clinical trial (Wilber et al., 2010), ablation improved outcomes of paroxsymal AF compare to AAD therapies, but larger randomized trials are needed. A large-scale multi-center trial "Catheter Ablation vs Antiarrhythmic Drug Therapy for Atrial Fibrillation" (CABANA) is currently underway.

1.3.2 Ablation of AF

In single-center studies, ablation can reach 90% success at 1-year follow-up (Hocini et al., 2005; Oral et al., 2003), but drops to 60-80% when including more advanced AF cases and extending follow-up period (Pappone et al., 2003; Terasawa et al., 2009). Accurate assessment

of success rates is confounded by frequent and divergent procedure refinement (Cappato et al., 2005). Despite this, catheter ablation has become a primary method to treat AF (Wann et al., 2011) and has been proposed as a front-line therapy (Wazni et al., 2005) with more aggressive ablation patterns (Elayi et al., 2008; Schmitt et al., 2007; Terasawa et al., 2009). Ablation strategies focus on returning a patient to sinus rhythm, and rarely consider the mechanical effects of scarring the atrial wall.

1.4 Clinical significance

A forty-year old person faces a one-in-four chance of developing atrial fibrillation (AF) in his lifetime (Roger et al., 2011). If he does, it will increase his risk of stroke 4.5-fold (Wolf et al., 1991), lower his quality-of-life by 25% (Dorian et al., 2000), and nearly double his medical costs (Kim et al., 2011). Three million people live with these statistics in the United States (Naccarelli et al., 2009). AF carries a large societal cost, fueling increases in AF research in recent decades (Nieuwlaat et al., 2007), (Johnston et al., 2006). Despite advances in disease management, the number of AF cases is expected to triple by 2050 (Miyasaka et al., 2006), indicating an pressing need for new diagnostic and therapeutic tools to combat this epidemic.

When a patient arrives in clinic with AF, a doctor faces two questions: 1) how much cardiac dysfunction has AF created, and 2) what is the best treatment for that amount of dysfunction? Although we know AF progresses from a single episode to permanent symptomatic dysfunction, it is difficult to assess individual patients on this continuum. Some cases may remain asymptomatic for years, while others may progress rapidly to failure. Treatment options are also quite variable, as choices in anti-coagulation and anti-arrhythmic drugs are adjusted based on a host of demographic and clinical factors. Although ablation had proven itself a viable alternative to AADs, clinicians are faced with dozens of possible ablation strategies. Successful management of AF requires clinicians to consider an array of treatment options mapped onto a variable progression of disease. Clinicians are limited by

a lack of information – they cannot easily assess AF-related dysfunction in the atrium nor can they estimate effects of various ablation procedures. Our capabilities in managing AF are limited because we lack a complete understanding of left atrial function and its relation to AF and its therapies. Current diagnostic measures have failed to adequately answer the two posed questions and have curtailed the development of patient-specific AF management (Nattel and Opie, 2006).

1.4.1 Diagnostic potential

Diagnostic tools have not kept pace with new treatment methods. Patients are classified based on frequency and duration of AF episodes, while current imaging uses 2-D approximations of atrial size. Global measures, such as volume, assume homogeneity in the atrium. Yet, tissue damage, from AF and ablation alike, are local events with implicit heterogeneity. Any diagnostic tool that ignores this heterogeneity loses some ability to differentiate patients. More specific measures of left atrial function could refine patient classification and improve the current success rates for anti-arrhythmic drugs and RF ablation. Similarly, the aggressiveness of RF ablation is chosen solely to achieve electrical isolation. Clinicians could use specific measures of mechanical function to evaluate the trade-off between successful electrical isolation and excessive damage of left atrial tissue. This trade-off is especially important in the 25% of ablations that fail, where patients have surrendered healthy tissue without recovering sinus rhythm.

In both disease progression and ablation therapy, regional heterogeneity of mechanical function could be a valuable indicator in evaluating patient health and procedure efficacy. By measuring regional mechanics, clinicians could: 1) quantify the effects of medical and catheter-based therapies on preserving LA mechanical function, 2) select ablation patterns that minimize injury to regions that contribute most to mechanical function, 3) measure AF-related damage based on loss of mechanical function, and 4) monitor regional function and remodeling following catheter ablation.

1.4.2 Unmet need

Given the unmet needs in AF management and the limitations of current diagnostics, we developed several novel tools to measure global and regional atrial function. We used these tools to test our hypotheses of function in healthy adults, AF patients, and patients with recovered sinus rhythm following catheter ablation. Our overall hypothesis is that **left atrial function is regionally heterogeneous and changes in atrial function (due to disease and therapy) are regional phenomena that need to be evaluated in the context of regional contributions to heart function**.

We dedicated three chapters to explain the detailed development and technical aspects of three methods: pressure-volume loops (global mechanics) in Chapter 2, wall motion analysis (global and regional function) in Chapter 4, and an atrial finite element model (simulated global and regional mechanics) in Chapter 6. We used these methods to test the following hypotheses:

One

Left atrial wall motion is spatially heterogeneous (Chapter 5).

Two

Left atrial mechanical function deteriorates due to AF and related cardiac disorders (Chapter 3).

Three

Changes in wall motion in AF patients are spatially heterogeneous (Chapter 7).

Four

Changes in wall motion in AF patients are caused by changes in local wall stress and not by changes in fibrosis or electrical conduction (Chapter 7).

Five

Ablation scar temporarily depresses function independent of location, and chronically depresses function dependent on amount and location of scar (Chapter 8).

Six

Global and regional function will improve in AF patients following successful ablation despite the presence of ablation scar (Chapter 8).

In answering these hypotheses, we will advance our understanding of left atrial mechanical function and how it changes due to atrial fibrillation and ablation. The methods and tools designed in this thesis will help clinicians to better diagnose, treat, and monitor AF patients over time.

References

N. M. Al-Saady, O. A. Obel, and A. J. Camm. Left atrial appendage: structure, function, and role in thromboembolism. *Heart*, 82(5):547–554, Nov. 1999.

T. Alhogbani, O. Strohm, and F. Matthias. Evaluation of normal atrial contribution to left ventricular filling. *Journal of Cardiovascular Magnetic Resonance*, 12:1, Jan. 2010.

M. Allessie, J. Ausma, and U. Schotten. Electrical, contractile and structural remodeling during atrial fibrillation. *Cardiovasc Res*, 54(2):230–246, May 2002.

A. C. Boyd, N. B. Schiller, D. Leung, D. L. Ross, and L. Thomas. Atrial dilation and altered function are mediated by age and diastolic function but not before the eighth decade. *J Am Coll Cardiol Img*, 4(3):234–242, Mar. 2011.

B. Burstein and S. Nattel. Atrial fibrosis: Mechanisms and clinical relevance in atrial fibrillation. *J Am Coll Cardiol*, 51(8):802–809, Feb. 2008.

H. Calkins, S. Y. Ho, J. Angel Cabrera, P. Della Bella, J. Farre, J. Kautzner, and P. Tchou. Anatomy of the left atrium and pulmonary veins. In A. N. M.D and A. R. M.D, editors, *Atrial Fibrillation Ablation*, page 110. Blackwell Publishing Ltd, 2008.

R. Cappato, H. Calkins, S.-A. Chen, W. Davies, Y. Iesaka, J. Kalman, Y.-H. Kim, G. Klein, D. Packer, and A. Skanes. Worldwide survey on the methods, efficacy, and safety of catheter ablation for human atrial fibrillation. *Circulation*, 111(9):1100 –1105, Mar. 2005.

T. O. Cheng. Hippocrates and cardiology. *American Heart Journal*, 141(2):173–183, Feb. 2001.

S. J. Connolly, M. D. Ezekowitz, S. Yusuf, J. Eikelboom, J. Oldgren, A. Parekh, J. Pogue, P. A. Reilly, E. Themeles, J. Varrone, S. Wang, M. Alings, D. Xavier, J. Zhu, R. Diaz, B. S. Lewis, H. Darius, H.-C. Diener, C. D. Joyner, and L. Wallentin. Dabigatran versus

warfarin in patients with atrial fibrillation. *New England Journal of Medicine*, 361(12): 1139–1151, Sept. 2009.

E. Crivellato and D. Ribatti. Soul, mind, brain: Greek philosophy and the birth of neuroscience. *Brain Res. Bull.*, 71(4):327–336, Jan. 2007.

P. Dorian, W. Jung, D. Newman, M. Paquette, K. Wood, G. M. Ayers, J. Camm, M. Akhtar, and B. Luderitz. The impairment of health-related quality of life in patients with intermittent atrial fibrillation: implications for the assessment of investigational therapy. *J Am Coll Cardiol*, 36(4):1303–1309, Oct. 2000.

C. S. Elayi, A. Verma, L. Di Biase, C. K. Ching, D. Patel, C. Barrett, D. Martin, B. Rong, T. S. Fahmy, Y. Khaykin, R. Hongo, S. Hao, G. Pelargonio, A. Dello Russo, M. Casella, P. Santarelli, D. Potenza, R. Fanelli, R. Massaro, M. Arruda, R. A. Schweikert, and A. Natale. Ablation for longstanding permanent atrial fibrillation: Results from a randomized study comparing three different strategies. *Heart Rhythm*, 5(12):1658–1664, Dec. 2008.

V. Fuster, L. E. Ryden, D. S. Cannom, H. J. Crijns, A. B. Curtis, K. A. Ellenbogen, J. L. Halperin, J.-Y. Le Heuzey, G. N. Kay, J. E. Lowe, S. B. Olsson, E. N. Prystowsky, J. L. Tamargo, and S. Wann. ACC/AHA/ESC 2006 guidelines for the management of patients with atrial fibrillation: A report of the american college of Cardiology/American heart association task force on practice guidelines and the european society of cardiology committee for practice guidelines (writing committee to revise the 2001 guidelines for the management of patients with atrial fibrillation): Developed in collaboration with the european heart rhythm association and the heart rhythm society. *Circulation*, 114(7): e257–354, Aug. 2006.

R. Gaspo, R. F. Bosch, M. Talajic, and S. Nattel. Functional mechanisms underlying tachycardia-induced sustained atrial fibrillation in a chronic dog model. *Circulation*, 96 (11):4027–4035, Dec. 1997.

M. Haissaguerre, P. Jais, D. C. Shah, A. Takahashi, M. Hocini, G. Quiniou, S. Garrigue, A. Le Mouroux, P. Le Metayer, and J. Clementy. Spontaneous initiation of atrial fibrillation by ectopic beats originating in the pulmonary veins. *N Engl J Med*, 339(10):659–666, Sept. 1998.

W. Harvey and C. D. Leake. *Exercitatio anatomica de motu cordis et sanguinis in animalibus (English translation and annotations by C.D. Leake)*. Thomas, Springfield, IL, 1928.

M. Hocini, P. Jas, P. Sanders, Y. Takahashi, M. Rotter, T. Rostock, L.-F. Hsu, F. Sacher, S. Reuter, J. Clmenty, and M. Hassaguerre. Techniques, evaluation, and consequences of linear block at the left atrial roof in paroxysmal atrial fibrillation: a prospective randomized study. *Circulation*, 112(24):3688–3696, Dec. 2005.

V. Jeevanantham, W. Ntim, S. D. Navaneethan, S. Shah, A. C. Johnson, B. Hall, A. Shah, W. G. Hundley, J. P. Daubert, and D. Fitzgerald. Meta-analysis of the effect of radiofrequency catheter ablation on left atrial size, volumes and function in patients with atrial fibrillation. *Am. J. Cardiol*, 105(9):1317–1326, May 2010.

S. C. Johnston, J. D. Rootenberg, S. Katrak, W. S. Smith, and J. S. Elkins. Effect of a US national institutes of health programme of clinical trials on public health and costs. *Lancet*, 367(9519):1319–1327, Apr. 2006.

M. H. Kim, S. S. Johnston, B.-C. Chu, M. R. Dalal, and K. L. Schulman. Estimation of total incremental health care costs in patients with atrial fibrillation in the united states. *Circ Cardiovasc Qual Outcomes*, 4(3):313–320, May 2011.

Lafuente-Lafuente C, Mouly S, Longs-Tejero M, Mah I, and Bergmann J. Antiarrhythmic drugs for maintaining sinus rhythm after cardioversion of atrial fibrillation: A systematic review of randomized controlled trials. *Arch Intern Med*, 166(7):719–728, Apr. 2006.

J. McMichael. History of atrial fibrillation 1628-1819 harvey - de senac - lannec. *Br Heart J*, 48(3):193–197, Sept. 1982.

Y. Miyasaka, M. E. Barnes, B. J. Gersh, S. S. Cha, K. R. Bailey, W. P. Abhayaratna, J. B. Seward, and T. S. Tsang. Secular trends in incidence of atrial fibrillation in olmsted county, minnesota, 1980 to 2000, and implications on the projections for future prevalence. *Circulation*, 114(2):119–125, July 2006.

G. V. Naccarelli, H. Varker, J. Lin, and K. L. Schulman. Increasing prevalence of atrial fibrillation and flutter in the united states. *Am. J. Cardiol.*, 104(11):1534–1539, Dec. 2009.

S. Nattel. New ideas about atrial fibrillation 50 years on. *Nature*, 415(6868):219–226, Jan. 2002.

S. Nattel and L. H. Opie. Controversies in atrial fibrillation. *The Lancet*, 367(9506):262–272, Jan. 2006.

R. Nieuwlaat, L. W. Eurlings, A. Capucci, and H. J. Crijns. Atrial fibrillation in the 'real world': undecided issues. *European Heart Journal Supplements*, 9(Suppl I):I122–I128, Dec. 2007.

R. S. Oakes, T. J. Badger, E. G. Kholmovski, N. Akoum, N. S. Burgon, E. N. Fish, J. J. E. Blauer, S. N. Rao, E. V. R. DiBella, N. M. Segerson, M. Daccarett, J. Windfelder, C. J. McGann, D. Parker, R. S. MacLeod, and N. F. Marrouche. Detection and quantification of left atrial structural remodeling with delayed-enhancement magnetic resonance imaging in patients with atrial fibrillation. *Circulation*, 119(13):1758–1767, Apr. 2009.

H. Oral, C. Scharf, A. Chugh, B. Hall, P. Cheung, E. Good, S. Veerareddy, F. Pelosi, and F. Morady. Catheter ablation for paroxysmal atrial fibrillation. *Circulation*, 108(19):2355 –2360, Nov. 2003.

C. Pappone, S. Rosanio, G. Augello, G. Gallus, G. Vicedomini, P. Mazzone, S. Gulletta, F. Gugliotta, A. Pappone, V. Santinelli, V. Tortoriello, S. Sala, A. Zangrillo, G. Crescenzi, S. Benussi, and O. Alfieri. Mortality, morbidity, and quality of life after circumferential

pulmonary vein ablation for atrial fibrillation: Outcomes from a controlled nonrandomized long-term study. *Journal of the American College of Cardiology*, 42(2):185–197, July 2003.

D. C. Peters, J. V. Wylie, T. H. Hauser, K. V. Kissinger, R. M. Botnar, V. Essebag, M. E. Josephson, and W. J. Manning. Detection of pulmonary vein and left atrial scar after catheter ablation with three-dimensional navigator-gated delayed enhancement MR imaging: Initial experience1. *Radiology*, 243(3):690 –695, June 2007.

V. L. Roger, A. S. Go, D. M. Lloyd-Jones, R. J. Adams, J. D. Berry, T. M. Brown, M. R. Carnethon, S. Dai, G. de Simone, E. S. Ford, C. S. Fox, H. J. Fullerton, C. Gillespie, K. J. Greenlund, S. M. Hailpern, J. A. Heit, P. M. Ho, V. J. Howard, B. M. Kissela, S. J. Kittner, D. T. Lackland, J. H. Lichtman, L. D. Lisabeth, D. M. Makuc, G. M. Marcus, A. Marelli, D. B. Matchar, M. M. McDermott, J. B. Meigs, C. S. Moy, D. Mozaffarian, M. E. Mussolino, G. Nichol, N. P. Paynter, W. D. Rosamond, P. D. Sorlie, R. S. Stafford, T. N. Turan, M. B. Turner, N. D. Wong, and J. Wylie-Rosett. Heart disease and stroke statistics–2011 update: A report from the american heart association. *Circulation*, 123(4): e18–209, Feb. 2011.

C. Schmitt, H. Estner, B. Hecher, A. Luik, C. Kolb, M. Karch, G. Ndrepepa, B. Zrenner, G. Hessling, and I. Deisenhofer. Radiofrequency ablation of complex fractionated atrial electrograms (CFAE): preferential sites of acute termination and regularization in paroxysmal and persistent atrial fibrillation. *Journal of Cardiovascular Electrophysiology*, 18(10): 1039–1046, Oct. 2007.

A. Y. Tan, H. Li, S. Wachsmann-Hogiu, L. S. Chen, P.-S. Chen, and M. C. Fishbein. Autonomic innervation and segmental muscular disconnections at the human pulmonary vein-atrial junction: Implications for catheter ablation of atrial-pulmonary vein junction. *Journal of the American College of Cardiology*, 48(1):132–143, July 2006.

T. Terasawa, E. M. Balk, M. Chung, A. C. Garlitski, A. A. Alsheikh-Ali, J. Lau, and S. Ip. Systematic review: Comparative effectiveness of radiofrequency catheter ablation for atrial fibrillation. *Annals of Internal Medicine*, 151(3):191 –202, 2009.

A. C. Y. To, S. D. Flamm, T. H. Marwick, and A. L. Klein. Clinical utility of multimodality la imaging assessment of size, function, and structure. *JACC Cardiovasc Imaging*, 4(7): 788–798, July 2011.

R. Van Praagh and S. Van Praagh. Aristotle's "triventricular" heart and the relevant early history of the cardiovascular system. *Chest*, 84(4):462–468, Oct. 1983.

L. S. Wann, A. B. Curtis, C. T. January, K. A. Ellenbogen, J. E. Lowe, N. M. Estes, R. L. Page, M. D. Ezekowitz, D. J. Slotwiner, W. M. Jackman, W. G. Stevenson, C. M. Tracy, and A. K. Jacobs. 2011 ACCF/AHA/HRS focused update on the management of patients with atrial fibrillation (updating the 2006 guideline): A report of the american college of cardiology Foundation/American heart association task force on practice guidelines. *Circulation*, 123(1):104–123, Jan. 2011.

O. M. Wazni, N. F. Marrouche, D. O. Martin, A. Verma, M. Bhargava, W. Saliba, D. Bash, R. Schweikert, J. Brachmann, J. Gunther, K. Gutleben, E. Pisano, D. Potenza, R. Fanelli, A. Raviele, S. Themistoclakis, A. Rossillo, A. Bonso, and A. Natale. Radiofrequency ablation vs antiarrhythmic drugs as first-line treatment of symptomatic atrial fibrillation. *JAMA*, 293(21):2634 –2640, June 2005.

D. J. Wilber, C. Pappone, P. Neuzil, A. De Paola, F. Marchlinski, A. Natale, L. Macle, E. G. Daoud, H. Calkins, B. Hall, V. Reddy, G. Augello, M. R. Reynolds, C. Vinekar, C. Y. Liu, S. M. Berry, D. A. Berry, and for the ThermoCool AF Trial Investigators. Comparison of antiarrhythmic drug therapy and radiofrequency catheter ablation in patients with paroxysmal atrial fibrillation: A randomized controlled trial. *JAMA*, 303(4):333–340, Jan. 2010.

P. Wolf, R. Abbott, and W. Kannel. Atrial fibrillation as an independent risk factor for stroke: the framingham study. *Stroke*, 22(8):983–988, Aug. 1991.

D. G. Wyse, A. L. Waldo, J. P. DiMarco, M. J. Domanski, Y. Rosenberg, E. B. Schron, J. C. Kellen, H. L. Greene, M. C. Mickel, J. E. Dalquist, and S. D. Corley. A comparison of rate control and rhythm control in patients with atrial fibrillation. *N. Engl. J. Med.*, 347(23): 1825–1833, Dec. 2002.

Chapter 2

The pressure-volume relationship in the left atrium

The heart is a mechanical pump with four stages. Each stage (chamber) varies its pressure and volume in a precise sequence to move blood through the heart. The relationship between these quantities - the *pressure-volume relationship* - offers a simple but fundamental description of the sequence of events: filling, pressure generation, ejection, and relaxation. Each chamber has a unique P-V relationship, also called a P-V *loop*, that acts as a fingerprint of mechanical function. A left atrial P-V loop captures both the passive and active behavior during phasic filling and emptying. We measured pressure and volume simultaneously in the left atrium using intravenous catheters. We calibrated the volume to cardiac MRI and acquired loops at natural and paced heart rates. The loops revealed common patterns - an exponential filling curve, an exponential passive emptying curve, and a circular active ejection loop - that we quantified into measures of global mechanics. Individual loops had unique shapes and patterns (a subject-specific chamber fingerprint), and we used circuit flow modeling to understand these variations. We performed a sensitivity analysis to quantify which model parameters influenced loop shape and size. We applied these experimental measures and simulations in later chapters to quantify global mechanics in healthy and diseased atria,

before and after intervention.

2.1 Indicator diagrams

Pressure and volume are fundamental concepts of physics. They characterize the energy in a closed system (they are energy conjugates) such that changes in pressure and volume represent energy entering or leaving the system. In a mechanical system like a pump, the pressure-volume relationship quantifies how efficiently the pump stores and distributes energy. The pressure-volume relationship arose during the Industrial Revolution as a means to quantify the efficiency of steam engines. Originally called an indicator diagram, the first P-V loop appeared in the work of James Watt and his assistant John Southern in the late eighteenth century (Miller, 2011). They attached a tracing pencil to a barometer (moved with changes in pressure) and placed it against a paper board attached to the piston (moved with changes in volume). Watt kept the diagram a secret to exploit its value in steam engine design, and dissemination to the public only began thirty years later in an anonymous letter (Jun, 1822). The P-V loops of engines quantified energy transfer and laid the groundwork for the Carnot cycle and fundamental concepts in thermodynamics.

2.1.1 Cardiac pressure-volume loops

A P-V loop of the heart did not appear until 80 years later, when Otto Frank measured the pressure and volume in an isolated frog ventricle (Sagawa et al., 1990). Other groups replicated his work through the early twentieth century and expanded upon it in the 1960's using the isolated canine ventricles (Sagawa, 1978). A group of researchers at Johns Hopkins University (led by Hiroyuki Suga and Kiichi Sagawa) pioneered the use of time-varying elastance (linear relationships between pressure and volume) to characterize loop behavior in response to a changing afterload (Suga et al., 1973). The elastance at end-systole (the end-systolic pressure-volume relationship or ESPVR for short) was measured in human

subjects soon after (Grossman et al., 1977; Marsh et al., 1979), as was a full pressure-volume loop (Nivatpumin et al., 1979). Characterizations of the right ventricle and right atrium were done by the group at Johns Hopkins in a similar manner to their work on the LV (Lau et al., 1979; Maughan et al., 1979). Most P-V studies through the 1980s remained focused on the left ventricle due to its central role in cardiac function.

2.1.2 Left atrial pressure-volume loops

Through the 1980s, the left atrium lagged other chambers in P-V loop analyses. Left atrial pressures and volumes were difficult to measure due to poor imaging windows and risky trans-septal catheterizations. The first mention of a left atrial pressure-volume loop came in a study of atrial fibrillation and its effects on atrial volumes and flows, although the group did not create an actual P-V loop (White et al., 1982). Five years later, a complete left atrial P-V loop was plotted for an *ex vivo* isolated heart (Alexander et al., 1987) and an *in vivo* open-chest heart (Hoit et al., 1994). P-V loops of the left atrium were first acquired in humans in the late 1990s using 2-d ultrasound and retrograde catheterization (Matsuzaki et al., 1991; Stefanadis et al., 1998b). Interestingly, pressure-volume loops were extensively studied by anethesiologists to quantify the effects of volatile anesthetics on canine cardiac function (Gare et al., 2001).

All of these studies identified common patterns in atrial P-V diagrams, including an atrial contraction loop and a passive non-linear filling curve. Where possible, some studies varied loading (either physically or pharmacologically) to generate elastance curves, which were then implemented in models of cardiac circulation. Although cardiac P-V loops have been studied for decades, analysis of atrial P-V loops has been limited. No prior work measured atrial pressure and volume simultaneously in humans nor has any study captured multiple P-V loops in the same subject before and after intervention. We therefore developed a catheter-based technique to measure atrial pressure and volume simultaneously in humans.

We calibrated the volume to external MRI and quantified global mechanical parameters from the loop.

2.1.3 Circuit flow modeling

Experimental studies typically collected data for a single chamber (atrium or ventricle), and rarely measured multiple chamber P-V loops simultaneously. In lieu of this, some researchers used elastance curves to create models of cardiac circulation called *circuit flow modeling*. Circuit flow modeling, also known as the "electronic-hydraulic analogy", links the principles of electronics with those of hydrodynamics. The analogy was first used by William Preece in the late 1800s to describe electrical circuits as a "flow" of electrons (Abbott, 1902). Preece relied on the analogy to avoid the detailed mathematics of electromagnetism, which he despised. His stance created adversaries in Oliver Heavyside (Nahin, 2002) and Oliver Lodge, who chided the analogy as the "drain-pipe theory" (Lodge, 1893). Although it insulted electromagnetism, a circuit flow model provided valuable insights into fluid dynamics and was later adapted to cardiac applications.

Circuit flow models use the principles of electrical circuits but replace electricity (potential, charge, current, capacitance) with fluid (pressure, volume, flow, elastance). The earliest and simplest type of this model was the 3-element Windkessel model, designed by Frank in 1899 to simulate blood flow in the aorta (Sagawa et al., 1990). Suga and Sagawa adapted this modeling technique to the entire left heart alongside their experimental studies (Alexander et al., 1987). Similar circuit flow models have been used to study the entire circulatory system (Arts et al., 2005) and coupled to finite element models (Kerckhoffs et al., 2007). This thesis used a circuit flow model as part of the atrial finite element model (see Chapter 6).

Though circuit flow models have been built for the atrium, none have been used to explain the size and shape of P-V loops. We developed a novel to method to collect atrial P-V loops in clinical settings using a single catheter, then calibrated volumes to cineMR. We used a single calibration to collect P-V loops at natural and paced heart rates. We used data from

P-V loops and other clinical studies to build an atrial circuit flow model, which we harnessed to explain the observed patterns in clinical loops.

2.2 Methods to collect and analyze P-V loops

We used intravenous catheters to collect pressure and volume simultaneously in the left atrium. We collected P-V loops at natural and paced heart rates immediately prior to a clinical procedure. Loops were then segmented into phases, calibrated to cineMR, and quantified into global measures of atrial mechanics.

2.2.1 Theory of conductance

A conductance catheter estimates volume by generating an electrical field and measuring the gradient of that field through a medium. Materials with high conductance (blood) transmit the field more easily than materials with low conductance (tissue). Since the vast majority of field energy travels the preferred path through blood, changes in blood volume create changes in the potential gradient. To simplify this understanding it is assumed that a pair of catheter electrodes represents a set of parallel plates filled with a resistive material (blood), such that the blood resistivity ρ is

$$\rho = R\,\frac{A}{l} \tag{2.1}$$

where $R\,(\Omega)$ is the electrical resistance, $A\,(\mathrm{cm}^2)$ is the area of the plates, and $l\,(\mathrm{cm})$ is the length between the plates. For the conductance catheter, the spacing between the electrodes l is known and fixed. Conductance $G\,(^1/\Omega)$ is simply the inverse of resistance. We assumed a constant blood resistivity so that the change in potential was proportional to area as

$$\begin{aligned} Area &= \rho l G \\ Volume &= \frac{1}{\alpha}\rho l^2 G \end{aligned} \tag{2.2}$$

where α is a dimensionless scaling coefficient. To measure conductance, the catheter generated a field with known current I (A) and measured the change in potential ΔV (Volts), where $G = {}^{I}/_{\Delta V}$. A good review of the theory and protocols for using conductance catheters can be found in (Pacher et al., 2008) and (Porterfield et al., 2009).

2.2.2 Loop acquisition

A 5-French (1.67 mm diameter) Millar conductance catheter (Model No. SPC-550-5, Millar Instruments, Houston, TX) was used for all P-V studies (Fig. 2.1). The catheter measured volume using twelve electrodes spaced across 7 cm of its 125 cm length. Four outer electrodes generated the field (also known as a "dual-field configuration") and eight central electrodes measured potential gradients between sequential pairs. Since there were eight receiving electrodes, the catheter was able to measure seven "segments" of volume between each pair. Segment volumes were summed to calculate total volume. The eight central electrodes were spaced at 7 mm increments, capturing volume along a 4.9 cm length. Pressure was measured from a single semiconducting piezoelectric membrane, located in the center of the catheter in the third volume segment (Fig. 2.1b, green box). The catheter was connected to the Millar Ultra Pressure-Volume System (MPVS Ultra), which translates the catheter signal to an analog voltage output. Note that this voltage output is not the same as the raw potential difference between electrodes. We set the volume gain factor to its highest setting (gain=100x) to prevent signal saturation, especially in larger hearts. Note that larger gain settings lower the sensitivity and *increase* the volume ranges for a given change in signal voltage. We set the excitation current to "high" (100 μA) to ensure adequate field strength. The scaling factor α was always set to one. Analog voltage signals were digitized at 1 kHz using a PowerLab ADInstruments data acquisition system.

All studies were approved by the University of Virginia Institutional Review Board (IRB). Forty six subjects ($n = 46$) were recruited from the University of Virginia Health System for a research study with informed consent. All subjects were scheduled for an interventional

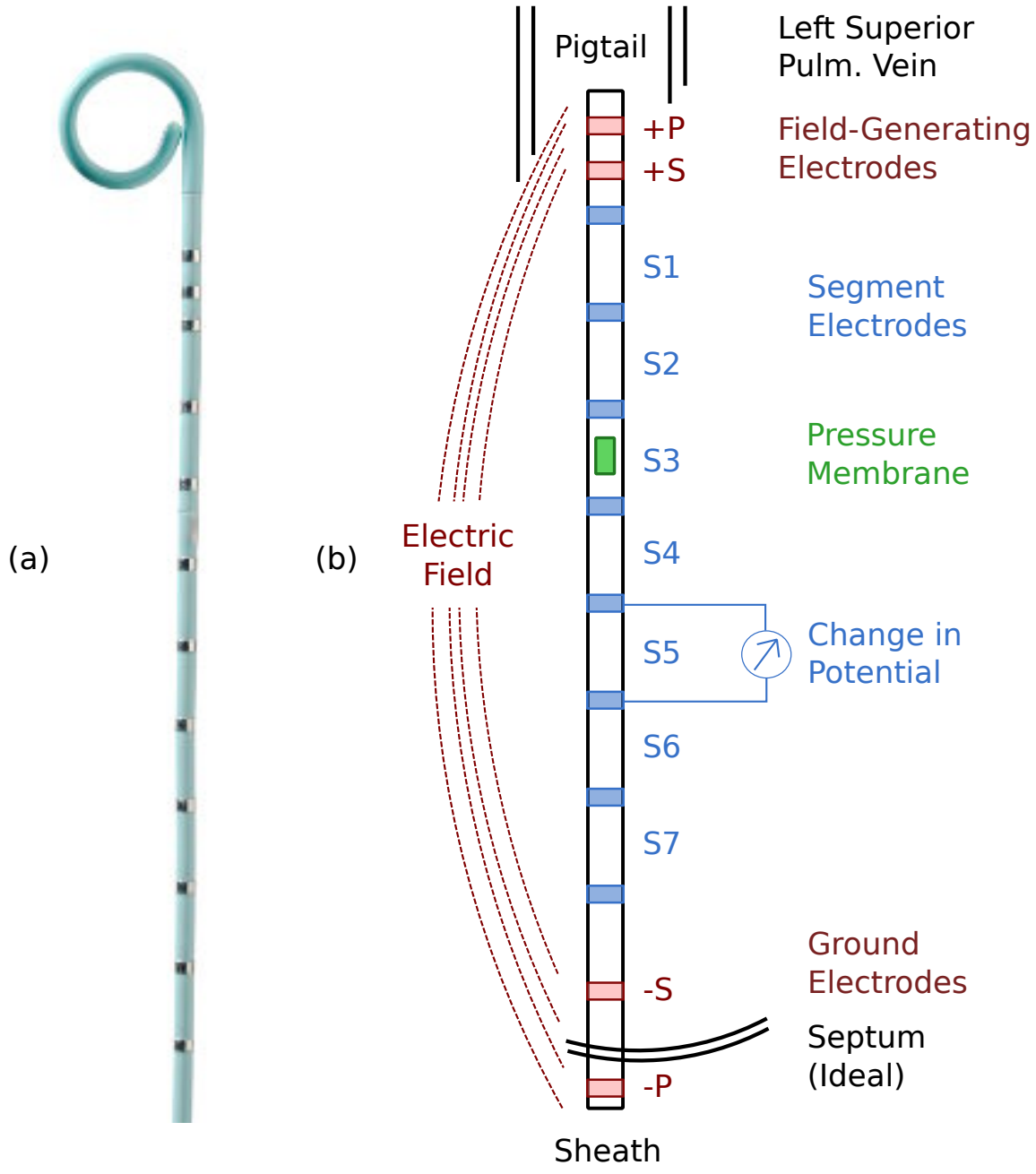

Figure 2.1: The Millar conductance catheter. (a) The catheter contains twelve metal electrodes, a single pressure transducer, and a pigtail end (top). The full length of the catheter is 125 cm (only 10 cm are shown). The pigtail is flexible and can be extended to a straight line for insertion into a sheath. (b) The catheter measures conductance by generating an electrical field and measuring the changes in that field along its length. The outer four electrodes generated the field while the central eight electrodes measured volume across seven segements. A single membrane in the third segment measured pressure.

ablation procedure prior to recruitment. The ablation procedure followed the current standard of care and was not altered by collection of P-V data. A cardiac electrophysiologist gained venous access through the femoral vein under local sedation and guided a series of pacing lead wires, catheters and sheaths into the right atrium (Fig. 2.2a). The left atrium was reached via a trans-septal puncture and followed with administration of anti-coagulation (Heparin). The P-V catheter was guided into the left atrium, where its distal end (pigtail) was lodged in the left superior pulmonary vein (Fig. 2.2b). The left superior pulmonary vein anchored the catheter, aligned its electrodes through the center of the chamber, and provided stability during data acquisition. The sheath was recessed into the right atrium to fully expose available electrodes. Real-time cardiac fluoroscopy confirmed the position of the catheter's electrodes and identified any segments in the right atrium (Fig. 2.2c). If volume segments appeared to cross the septal wall, the grounding electrodes were set to a more distal position and the extra segments were discarded. Thus, the electric field traversed through the left atrium and erroneous right atrial volumes were minimized.

We collected pressure and volume data at intrinsic and paced heart rates. The physician controlled heart rate using a pacing lead situated in the coronary sinus. The coronary sinus wraps around the annular portion of the left atrium along the inferior wall, and stimulation of the lead depolarizes the neighboring atrial wall. We typically acquired data at 600, 500, and 400 msec pacing, equivalent to 100, 120, and 150 beats per minute. In some cases, the intrinsic rate was greater than 600 msec, but never greater than 500 ms. In other cases, pacing at 400 ms induced an atrio-ventricular block (a Wenckebach periodicity) where the atrium and ventricle lost a one-to-one conduction pattern. These data sets were discarded. We acquired all data at held expiration to limit the diaphragm's influence on atrial hemodynamics. Collected data was monitored in LabChart software (Millar Instruments) and exported as a text file for offline processing in MATLAB.

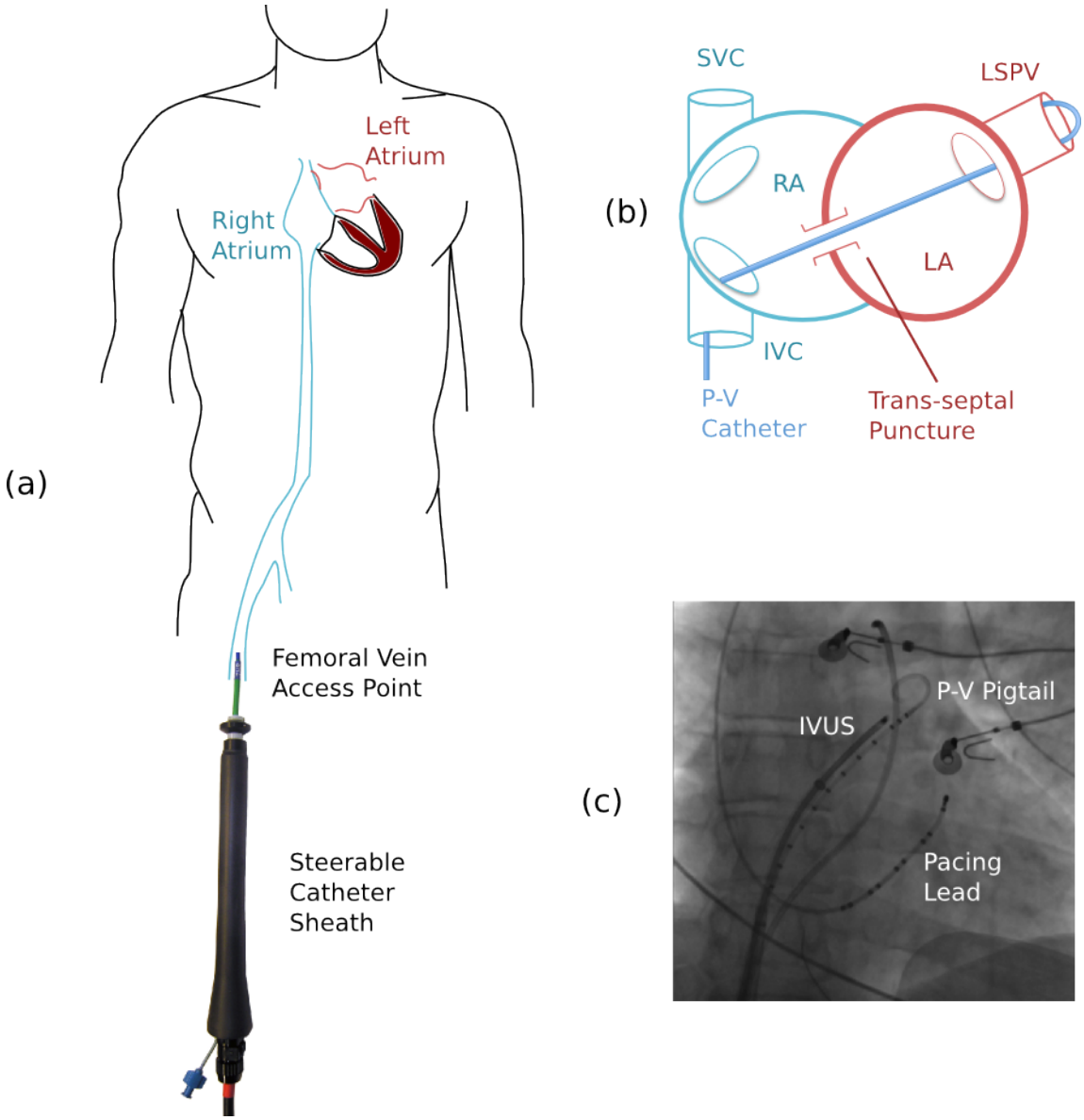

Figure 2.2: The P-V catheter was guided intraveneously into the LA and its position confirmed with X-ray. (a) The P-V catheter was steered through the femoral vein and inferior vena cava (IVC) into the right atrium (RA), then passed into the left side of the heart via a trans-septal puncture. (b) The catheter pigtail was guided into the left superior pulmonary vein (LSPV) using intravascular ultrasound (IVUS) as a guide. The LSPV held the catheter position during data acquisition. (c) A physician confirmed the P-V catheter's position using real-time fluoroscopy, including any distal segments in the right atrium. Conductance measurements were adjusted acoordingly.

2.2.3 Image acquisition

Volume measurements from intravenous catheters have known biases that distort their accuracy. To limit this effect, we calibrated catheter volume data to volumes derived from cardiac cineMR. Each subject agreed to a research CMR scan prior to the ablation procedure. All scans were performed on a 1.5-T Magnetom Avanto (Siemens Healthcare, Erlangen, Germany). A steady-state free procession (SSFP) imaging sequence with electrocardiographic gating was used in a slice-selective image acquisition during held expiration with a 6mm slice thickness. A stack of slices was acquired in the axial plane with no interslice gap. Roughly 15-20 axial images were acquired to ensure adequate coverage of the left atrium. The pixel size was 1.2x1.2 mm, where the RF bandwidth was 930 Hz/pixel. Each imaging sequence was reconstructed into 25 time phases, equally spaced across the cardiac cycle based on the R-R interval. The endocardial border of the left atrium was manually contoured in each image, then integrated to find atrial area in the slice. Contouring was done using ARGUS (Siemens Healthcare) and Segment (Medviso, Lund, Sweden). Area was scaled by slice thickness to calculate a slice volume. Slice volumes were summed for all axial images that contained a contour, controlling for any slice overlap. This process was repeated for each of the 25 time steps to produce a volume-vs-time curve. All volume calculations were done in MATLAB.

2.2.4 Loop segmentation

We imported pressure and volume data into MATLAB as digitized voltage signals. The pressure signal ranged from 0 to 1 Volts, capable of measuring pressures from 0 to 100 mmHg (a linear relationship). Segment volumes ranged from -10 to +10 Volts, capable of measuring volumes from 0 to 83 mL (a linear relationship). The calibration between voltage and segment volume was linear for each segment, but the factors (slope and intercept) varied between segments. These variations were accounted for prior to any conversions. When summed, the seven segments were capable of measuring 575 mL volume at a gain of 100x. We converted digitized voltages into their respective units using the prescribed linear calibrations, then

summed the segment volumes into a composite volume. We ignored segment volumes for electrodes positioned outside the left atrium on fluoroscopic images.

We smoothed the pressure signal using a 17-sample local weighted regression with a second-degree polynomial (the MATLAB *smooth* command, *rloess* method). This smoothing was roughly equivalent to a 60 Hz low-pass filter, given the 1 kHz sampling rate. We chose this cutoff based on the slow rates of change in physiological pressure, assuming that high frequency changes were noise. Volume signals were smoothed with the same method using a 100 sample window (equivalent to a 10 Hz low-pass filter). Volume signals tended to be noisier than pressure signals, especially the composite summation of individual segments. We observed low-frequency variation (< 1 Hz) in some patients who had trouble holding their breath. When necessary, we used a low-pass filter (cutoff frequency of 1 Hz) to filter out these respiratory effects (Fig. 2.3).

We selected a range of the filtered data with stable pressures and volumes that contained typical peaks and valleys of a normal cardiac cycle (Fig. 2.3b). This isolated window was further segmented into individual loops (single cardiac cycles). We identified the start of an atrial cycle as the minimum pressure following a minimum volume, marking the start of passive filling. We passed each of these loops through an automatic segmentation algorithm that identified key points in the cycle. We used a combination of measures to automatically detect points (extrema of pressures, volumes, and the rates of change in each; distances and slopes in the P-V plane). This automated detection was augmented with an interactive graphical user interface, which was used to correct any errant points (automated detection was less accurate with poorly-defined loops).

2.2.5 Loop definition

A typical atrial P-V loop contained four hemodynamic phases: 1) passive filling, 2) passive emptying, 3) active emptying, 4) active filling. The start and end of each phase was marked by a maximum or minimum in either pressure or volume. An isolated loop from the data in

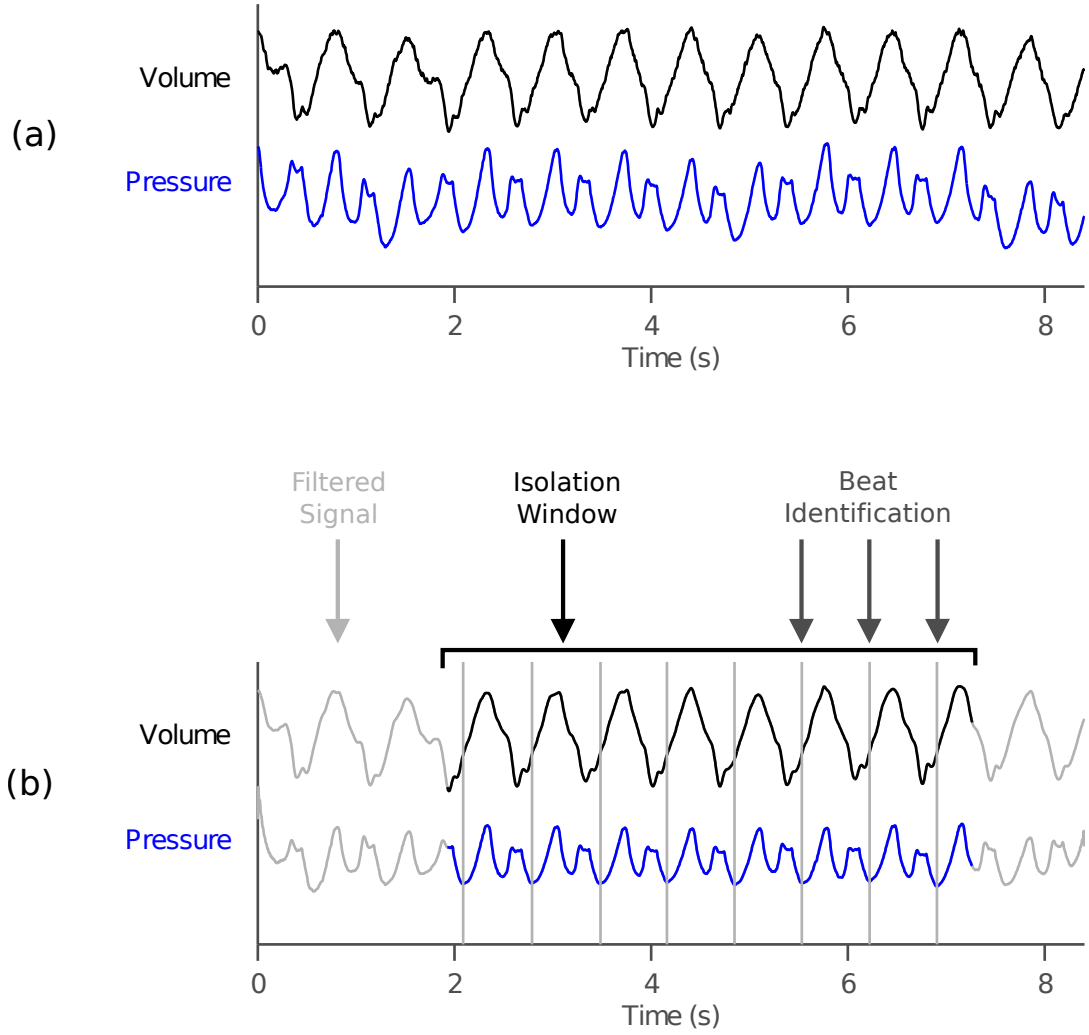

Figure 2.3: Pressure and volume data were recorded at 1 kHz and transferred to MATLAB for processing. (a) Signals were recorded at held-expiration for at least 6 seconds. Pressure and volume signals were filtered to remove high frequency noise and low frequency oscillations. (b) The filtered signals were segmented into a 6-10 beat region, then further segmented into individual cardiac cycles. The start of each cycle was defined by a minimum in pressure following a minimum in volume.

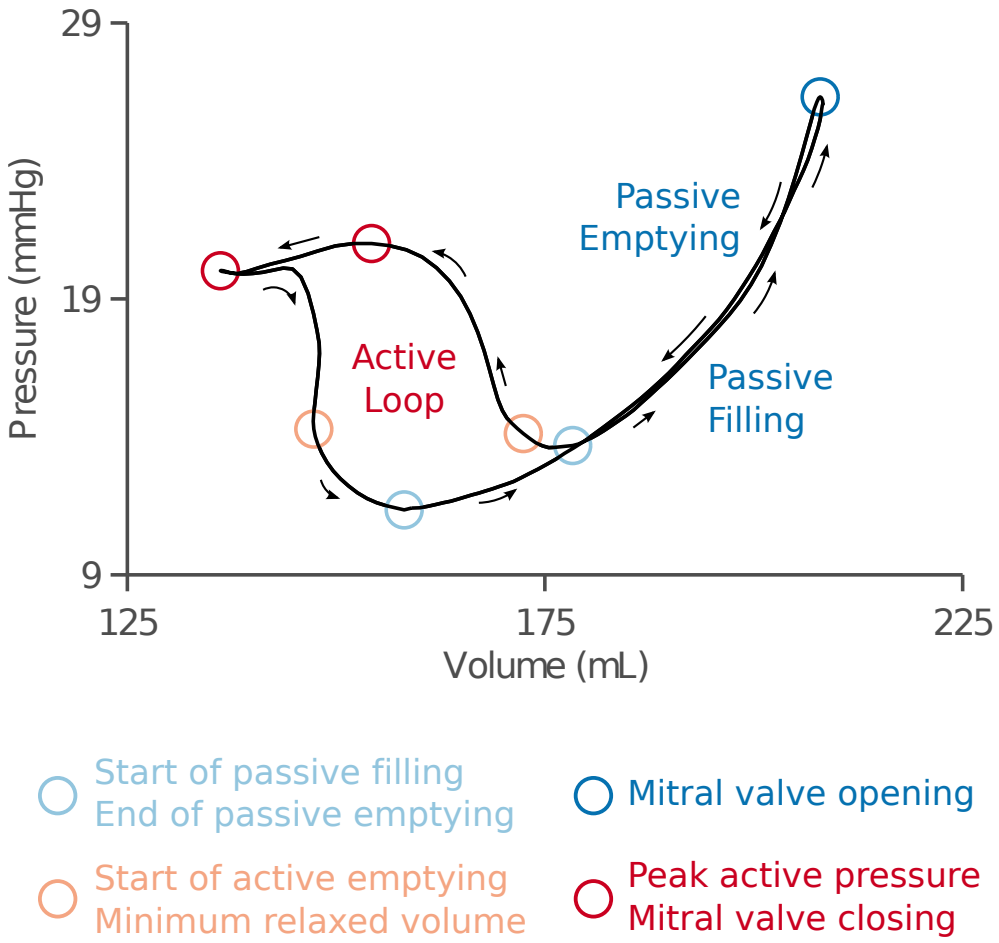

Figure 2.4: P-V loops were segmented into passive and active phases using pressure and volume extrema. We identified mitral valve opening (LV end systole) based on the peak pressure and volume during passive filling. We identified the start and end of the passive phases based on local pressure minima. We segmented the active loop into the start (initial rise in pressure with decrease in volume), peak (highest active pressure), and end (local volume minimum). We also segmented minimum volume during decreasing pressure (active recovery) prior to the start of passive filling).

Fig. 2.3b can be seen in Fig. 2.4. Using the start of atrial filling, we segmented the phases by identifying key points: 1) mitral valve opening (peak pressure and volume on passive curve), 2) end of passive emptying (minimum pressure following mitral valve opening), 3) start of contraction (maximum volume prior to active emptying), 4) mid atrial contraction (peak pressure during active emptying), 5) mitral valve closing (minimum volume during active emptying), 6) atrium relaxation (minimum volume following decrease in active pressure). These points acted as boundaries for the four hemodynamic phases. In some cases, there was a lag between the end of passive emptying and the start of contraction. During this time, the atrium and ventricle were in diastasis, both slowly filling from higher upstream pressures. We considered diastasis a fifth phase and did not include it in either passive emptying or active emptying.

We repeated this process for each beat in the isolated window, then averaged the results (Fig. 2.5). The averaged loop was created by generating isochronal points of each loop (with respect to fractional time) and averaging the pressure and volume. To confirm accurate loop segmentation, we also averaged the phase points and found their variation. This variation was displayed as an ellipse against the average loop (Fig. 2.5b), where larger ellipses represent more variation between segmented beats. The Millar P-V catheter contained an internal ECG probe which recorded instantaneous electrical potential inside the atrium. Although not integral to our analysis, the ECG plot was helpful in confirmed the start and end of atrial contraction (Fig. 2.5c).

2.2.6 Loop calibration

Conductance-based measures of volume had known biases and required external calibration. Conductance-based volumes were influenced by variations in the electric field, placement of the catheter relative to the atrial cavity, and parallel conductance from surrounding tissue. To correct these effects, we calibrated conductance volumes to atrial volumes obtained from CMR in (§2.2.3). CMR measured volume at 25 equally-spaced time points through the

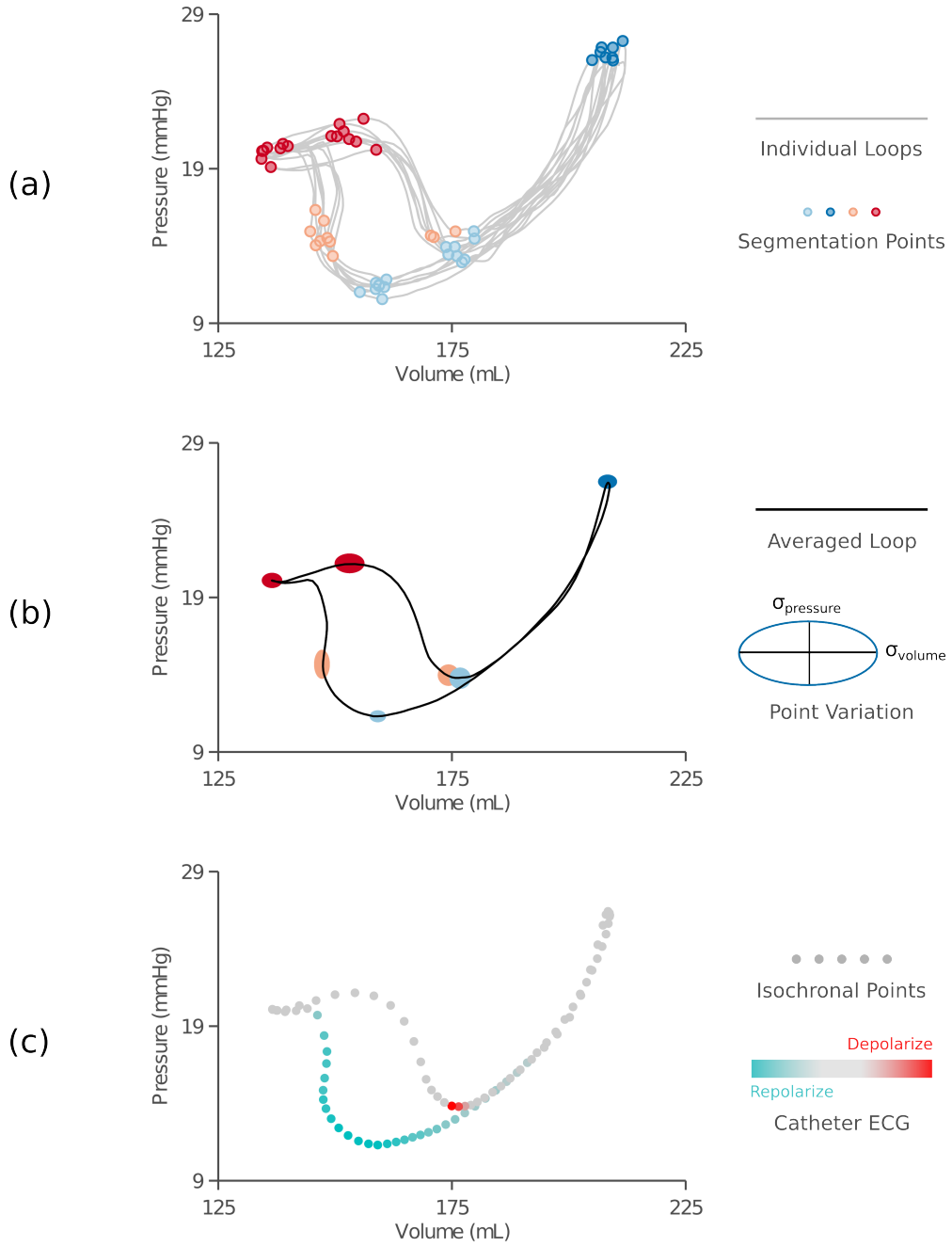

Figure 2.5: (a) Individual loops were segmented into phases using a semi-automated detection algorithm. (b) The loops and points were averaged into a single loop, representing average atrial P-V function in the subject. Phase points were also averaged and their variation was displayed as an ellipse (smaller ellipses denoted less beat-to-beat variation). (c) ECG measurements from the P-V catheter confirmed the start of atrial contraction and repolarization during relaxation.

cardiac cycle. We interpolated conductance volumes at equivalent time points and calibrated volumes using a simple linear regression. A single calibration was done for all segmented loops in one acquisition. We calculated a calibration slope and intercept, as well as the residual and quality of the fit (R^2). This calibration was performed using the intrinsic heart rate data (no pacing), then applied to all subsequent acquisitions at paced rates. Of the 46 patients recruited for this study, half ($n = 23$) had a pre-procedure MRI available for calibration. Patients were excluded from MRI if they had any abnormal heart rhythm during admission, expressed fear or claustrophobia, or were otherwise unable or unwilling to have a CMR scan. In later sections and chapters we will specify if an analysis group included all patients (calibrated and un-calibrated data) or the calibrated subset.

2.2.7 Loop quantification

We measured the passive stiffness and contractile work of each atrial P-V loop to quantify global mechanics. We excluded one outlier who was in atrial flutter during data collection. Following calibration to CMR, we separated a loop into its four hemodynamic phases using the semi-automated segmentation (Fig. 2.7). Because all passive filling curves exhibited a non-linear pressure-volume relationship, we fit them with an exponential function. We used a single coefficient k_c to represent "chamber" stiffness and subtracted the pressure and volume at the start of filling (V_o, P_o) to correct for offsets in the measurement (Fig. 2.7a). Data was compiled from each passive filling curve into a single array prior to fitting, producing a single coefficient per acquisition.

$$P = \left(e^{k_c(V-V_o)} - 1\right) + P_o \tag{2.3}$$

The chamber stiffness k_c ($^1/_{mL}$) had dimensional units such that it varied with atrial size. In other words, larger hearts appeared less stiff compared to smaller hearts, even if both were made of the same tissue. This effect was confirmed in later chapters (Chapter 6 and 7) using analytical and finite element modeling. To correct this, we normalized stiffness by an

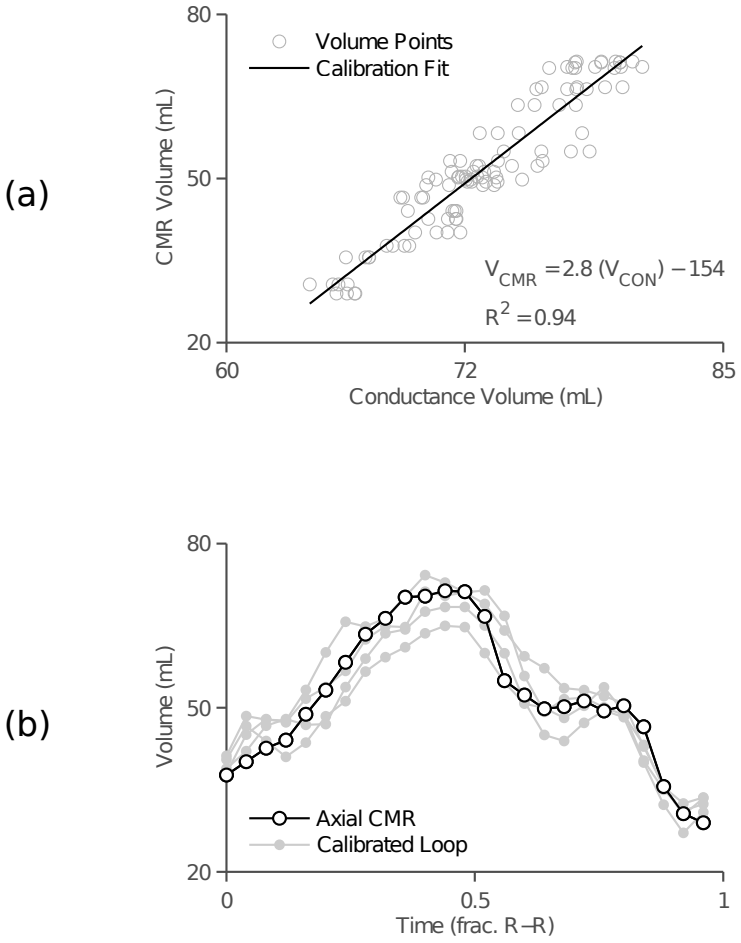

Figure 2.6: Conductance volumes were calibrated to cine CMR. (a) Each subject underwent cine CMR imaging separate from the interventional study, and atrial volumes were quantified from a stack of axial images. CMR volumes calibrated conductance volumes using a linear regression. (b) Calibration corrected offsets in conductance volumes while maintaining patterns of passive and active emptying.

absolute volume measure (the volume at mitral valve opening) to produce a "tissue" stiffness k_t.

$$P = \left(e^{k_t \frac{V - V_o}{V_{mvo}}} - 1\right) + P_o \tag{2.4}$$

We reported both chamber and tissue stiffness, and used tissue stiffness for comparisons in later chapters.

The pressure-volume relationship followed a similar non-linear path during passive emptying (Fig. 2.7b). We compared passive emptying to passive filling (if the paths were similar) by fitting a chamber and tissue stiffness to the passive emptying curve using the same equations (Eqn. 2.3 and 2.4). Passive emptying data was normalized using the same reference point (V_o, P_o) and the same normalization (V_{mvo}). Just like the filling curves, we compiled multiple beats into a single data set and fit a single coefficient. We labeled the emptying coefficients as chamber stiffness $k_{e,c}$ and tissue stiffness $k_{e,t}$. We compared passive filling and emptying properties using standard paired t-tests.

We calculated energy the atrium exerted on blood during contraction by integrating the area of the active P-V loop (stroke work). We defined the stroke work from the start of atrial contraction through active emptying and active filling to a point on the passive filling curve that matched the volume at the start of contraction. We integrated the area using the basic trapezoid rule, where

$$SW = \sum_{i}^{n} \frac{P_i + P_{i+1}}{2} \left(V_{i+1} - V_i\right) \tag{2.5}$$

Stroke work was computed for each loop in an acquisition then averaged. We also computed any negative work (energy added to the atrium from flowing blood) during passive filling and emptying (Fig. 2.7d). This area is typically called the V-loop in atrial P-V studies and tended to be much smaller than its active counterpart.

Following a baseline P-V loop at an intrinsic heart rate, we externally paced the heart using a lead in the coronary sinus. Paced rates included 600, 500, and 400 ms. We repeated the quantification steps described above. In cases where the passive emptying curve disappeared

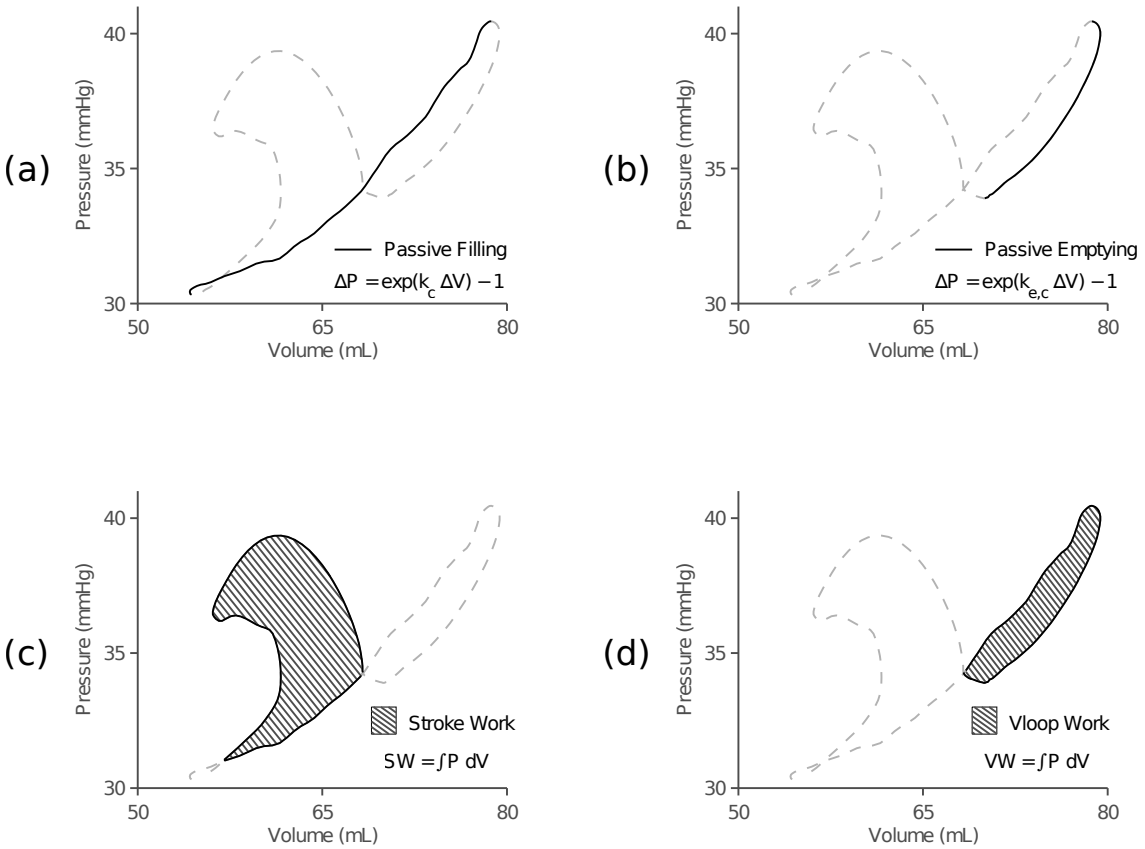

Figure 2.7: We quantified the passive and active properties of atrial mechanics. (a) Passive filling was fit to a single-parameter exponential function to measure chamber stiffness. The component was corrected for volume to measure tissue stiffness. (b) Passive emptying was measured in a similar way. (c) Energy expended during active emptying was measured from the integrated area of the active loop. (d) In a similar way, the area between passive curves was also measured.

(loop was completely active during emptying) we discarded the passive emptying stiffness coefficient and used the internal ECG to determine start of active contraction.

2.3 Results of global mechanics in atrial P-V loops

We acquired and analyzed atrial P-V loops from forty six subjects at intrinsic and paced heart rates (Fig. 2.8). All loops revealed a non-linear P-V curve during passive filling and passive emptying, followed by a circular loop with positive stroke work during active emptying (atrial contraction). Although all loops followed a general sequence of filling and emptying, each had a unique set of shapes and patterns within these phases, demonstrating how atrial mechanics varied between patients. We quantified the stiffness of the atrium during its passive phases and the stroke work expended on ejecting blood during active phases. We calibrated conductance volumes to accurate CMR volumes in $n = 23$ cases where CMR was available, and measured changes in stiffness and stroke work as a function of heart rate.

2.3.1 Loop calibration

We calibrated a subset of 23 P-V loops who had a pre-procedure CMR. Conductance volumes were fit to summed axial volumes from CMR using a first-degree polynomial (Fig. 2.9. Calibrations had an average slope of $1.7 \pm 0.9\ {}^{\mathrm{mL}}/_{\mathrm{mL}}$ and an average offset of -173 ± 95 mL. Goodness-of-fit (R^2) ranged from 0.48 to 0.98 with an average of 0.80 ± 0.13. An offset less than zero and a slope greater than one implied that conductance overestimated absolute atrial volumes and underestimated the cyclic changes in volume. We estimated the scaling term α in Eqn. 2.2 using the calibration slope and found an average $\alpha = 0.74 \pm 0.40$. Similarly, we estimated the parallel conductance from atrial tissue using the calibration offset and found $G_p = 0.13 \pm 0.07\ {}^{1}/_{\Omega}$.

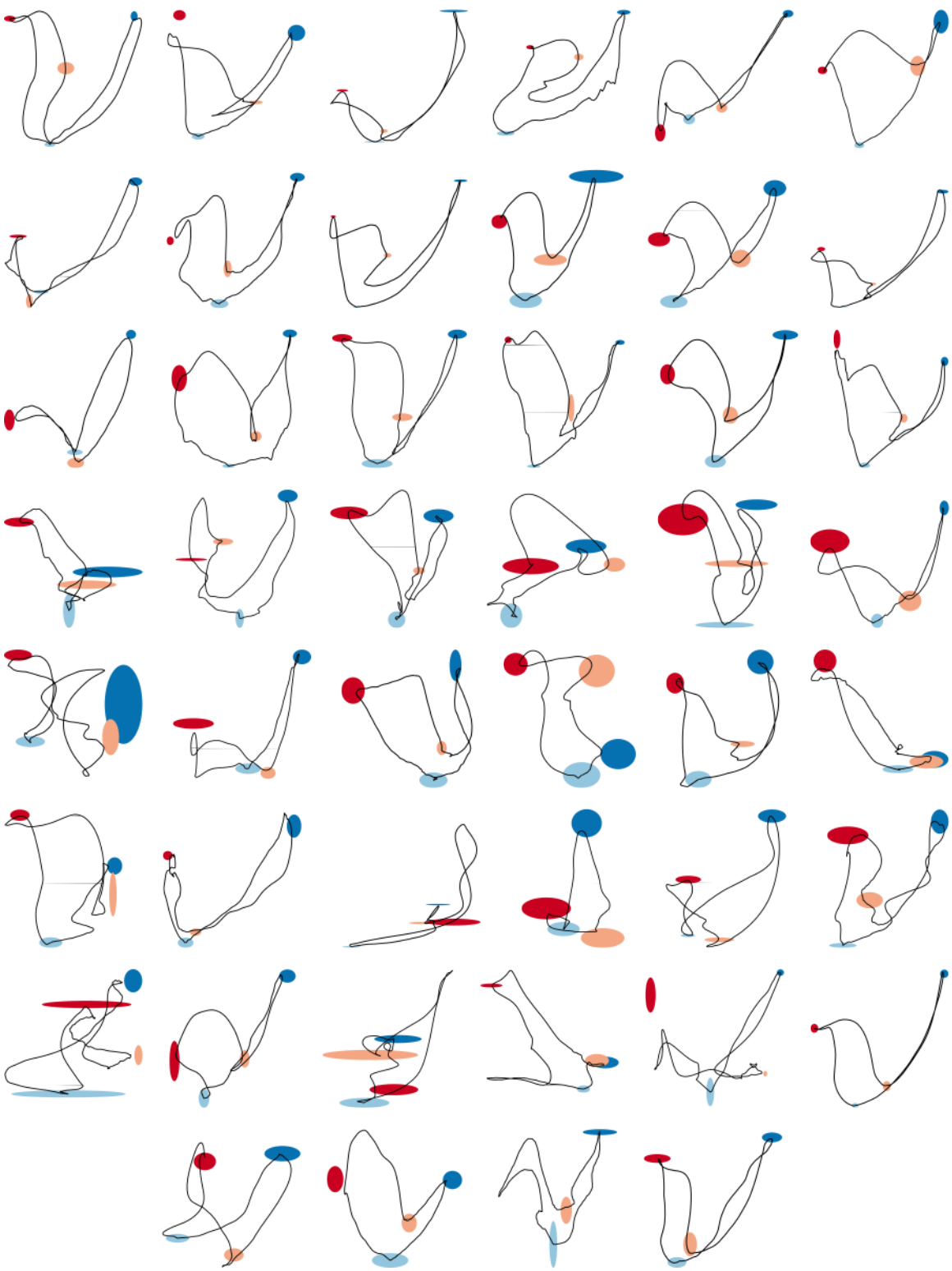

Figure 2.8: Forty six atrial P-V loops revealed a wide array of shapes and patterns. Four phase points are shown - mitral valve opening (dark blue), start of contraction (light red), mitral valve closing (dark red), and start of passive filling (light blue).

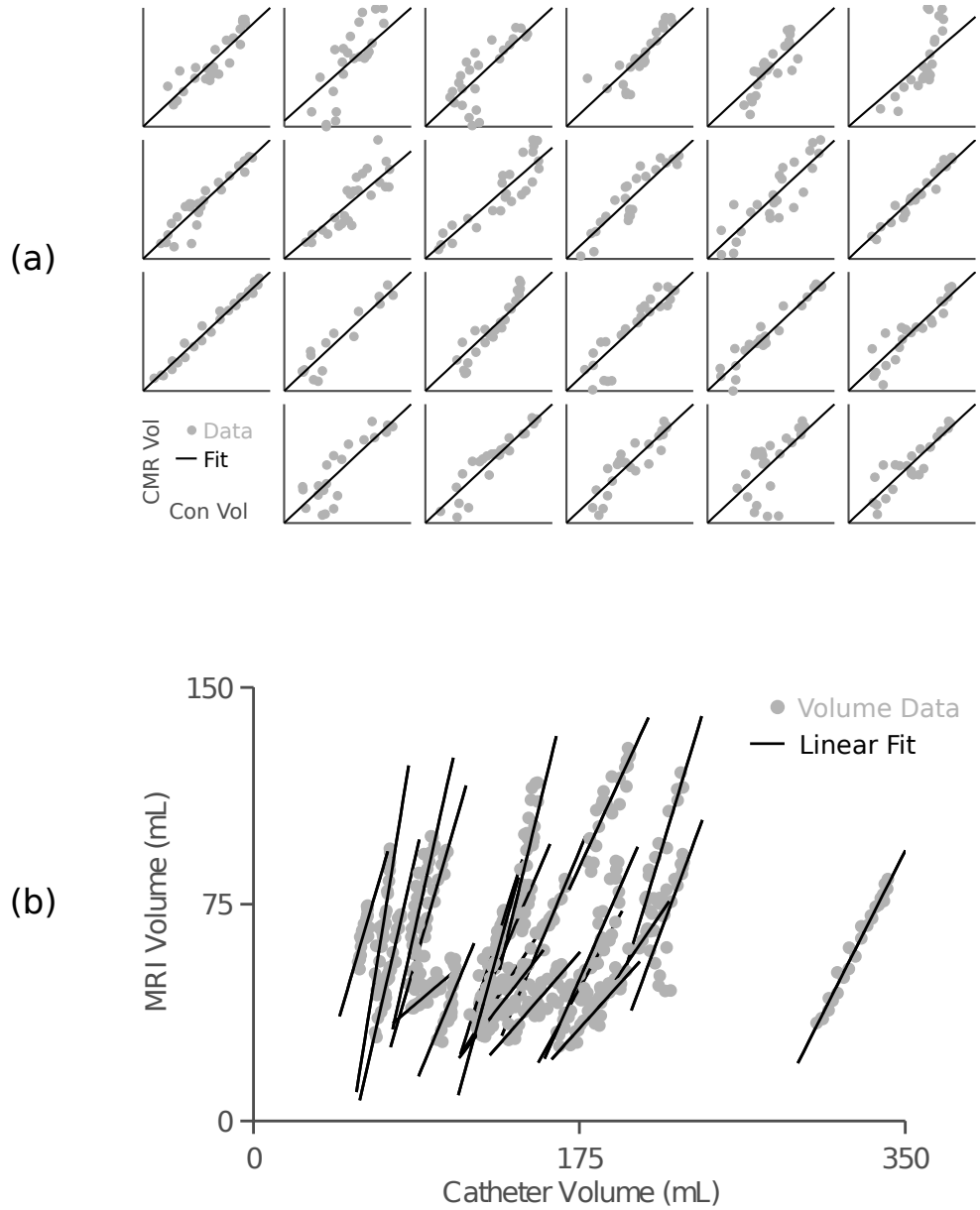

Figure 2.9: (a) CMR calibrated conductance volumes in twenty three subjects. (b) Conductance volumes tended to overestimate atrial size and underestimate phasic changes in size. Calibration slope was fairly consistent between patients while the offset (y-intercept) varied.

2.3.2 Loop quantification

We quantified the passive stiffness and stroke work of each calibrated P-V loop. Chamber stiffness k_c ranged from 0.04 to 0.21 mL^{-1} with a mean of $0.11 \pm 0.04\,\mathrm{mL}^{-1}$. Tissue stiffness k_t ranged from 4.0 to 16.3 with a mean of 7.6±2.6. We also measured chamber stiffness during passive emptying ($k_{e,c} = 0.11 \pm 0.04\,\mathrm{mL}^{-1}$) and compared it to stiffness measured during filling. The two measures of chamber stiffness differed by less than 5% of their pooled standard deviation. This result implied that passive filling and emptying occurred along a single passive curve. This comparison held for tissue stiffness as well. Stroke work ranged from -1.0 to 24.0 mJ with a mean of 8.8±5.7 mJ. V-loop work (the area between the passive filling and emptying curves) ranged from -3.2 to 7.3 with a mean of 1.5 ± 3.0. The area of the V-loop was only slightly positive ($p = 0.03$) and was typically small compared to its active counterpart (< 30% of stroke work).

2.3.3 Loop pacing

We acquired paced P-V loops at three heart rates above the intrinsic rate of each subject. Increased pacing rates tended to shift the P-V loops towards larger volumes and higher operating pressures (Fig. 2.10a). The passive emptying phase disappeared as active contraction dominated the cycle, especially at rates of 500 ms and higher. Tissue stiffness slowly but significantly increased as a function of pacing rate ($p < 0.02$, one-way repeated measures ANOVA), peaking at 400 ms (Fig. 2.10b). At this pace, the atrium most likely never fully relaxed and had a stiffer P-V relationship during filling. Atrial stroke work varied with pacing rates ($p < 0.001$), peaking at 500 ms then decreasing at 400 ms (Fig. 2.10c). As the pace increased, active contraction began to dominate emptying until the entire loop was active at 500 ms. Above this rate, the loop remained entirely active but had less time to empty, leading to a decreased stroke work. Interestingly, the power generated by the atrium (stroke work x heart rate) peaked at 500 ms around 40 mW (Fig. 2.10d).

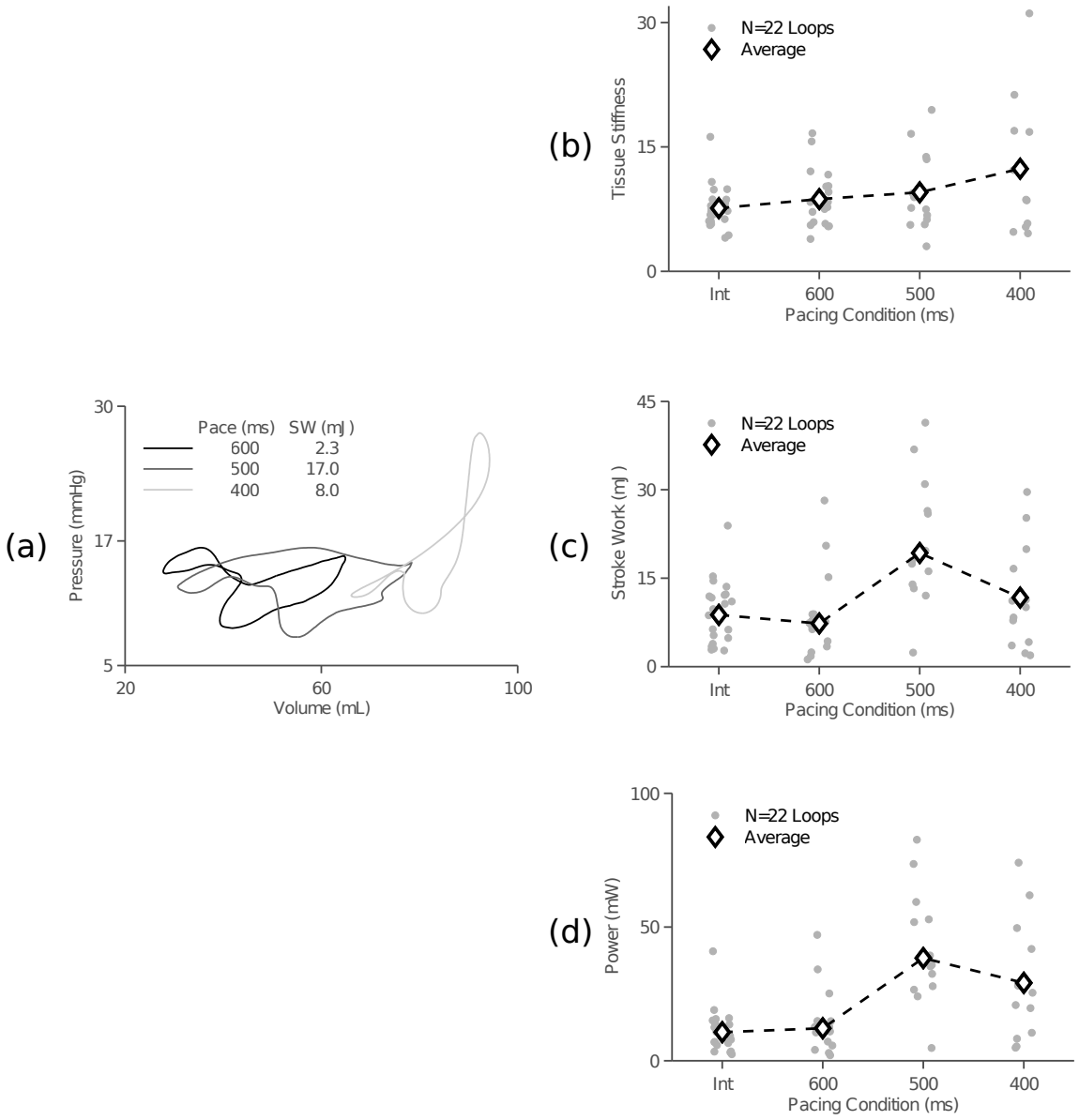

Figure 2.10: Atrial pacing revealed adaptation to elevated heart rates. (a) Three pacing rates showed a rightward shift in atrial P-V loops and an increase in peak pressure in an example subject. (b) Tissue stiffness increased slightly due to pacing, especially at rates above 500 ms. (c) Stroke work increased with pacing as the P-V loops became more active and passive emptying diminished. Stroke work peaked at 500 ms where the loops became entirely active. (d) The power generated by the atrium plateaued at 500ms and 40 mW.

2.4 Methods to simulate P-V loops with circuit flow models

Left atrial pressure-volume loops revealed a wide variety of shapes and patterns that distinguished each subject's loop as a "fingerprint" of cardiac function (Fig. 2.8). We hypothesized that variations in loop patterns arose from changes in hemodynamics, including preload and afterload as well as timing and extent of atrial and ventricular contraction. To explore these factors and understand their relative influence, we constructed an atrial circuit flow model based on work by Alexander and colleagues (Alexander et al., 1987). We then simulated changes in P-V loops through a parameter sensitivity analysis.

2.4.1 Time-varying elastance

Elastance is the relationship between pressure and volume in a chamber at a moment in time (hence its description as the *instantaneous* P-V relationship). Elastance *curves* characterize the stiffness of the atrium or ventricle through the cardiac cycle. As the atrium stiffens, elastance increases and the chamber expands less (dV) for the same change in pressure (dP). Elastance simulates atrial contraction as a big increase in stiffness. A stiffer chamber with the same volume results in higher pressures, which creates blood flow. Typically, elastance is modeled as a linear relationship between pressure and volume, where

$$P(t) = E(t)\,[V(t) - V_o(t)] \tag{2.6}$$

Here, (V, P) represent pressure and volume changing through time t and $E(t)$ represents the time-varying elastance. $V_o(t)$ is the unloaded volume (volume where $P = 0$) and can also vary through time. Both elastance terms (E and Vo) are experimentally determined by varying the load state of the atrium (typically by physically constricting blood flow or pharmacologically altering pressure). This causes the loop to shift to a new operating range

of pressure and volume. Using multiple load states, a linear regression line is fit to isochronal points in each loop to produce a slope (elastance) and intercept (unloaded volume). This process was done for the left atrium in isolated canine hearts (Alexander et al., 1987) and in open-chest canine experiments (Hoit et al., 1994). We used time-varying elastance to describe atrial and ventricular mechanics in our ciruit flow model.

2.4.2 Circuit flow model design

The circuit flow model or "hydraulic circuit" described blood movement using classical circuit components (resistors and capacitors) in the context of pressure, volume, and flow. We used a simplified version of the circuit described by Alexander and colleagues based on the canine left heart (Fig. 2.11a). We simulated a constant upstream pressure from the pulmonary vasculature P_v and resistor representing the pulmonary veins R_{pv}. Both the atrium and ventricle were modeled as a time-varying elastance functions $E_{la}(t)$ and $E_{lv}(t)$ with constant unloaded volumes $V_{la,o}$ and $V_{lv,o}$. We used a constant unloaded volume since previous studies measured small changes in V_o and a constant unloaded volume simplified the contraction model. We represented the mitral valve as a resistor that only allowed flow from the atrium into the ventricle. Similarly, we modeled the aortic valve as a resistor with one-way flow out of the ventricle. Finally, we set a constant downstream pressure P_a representing mean aortic pressure.

We defined the active portion of the time-varying curve using a piece-wise cosine function, which was scaled to a maximum elastance $E_{la,max}$ at a time of maximum contraction $T_{la,max}$. The elastance then recovered to a baseline level $E_{la,base}$ where it remained during passive phases of filling and emptying (Fig. 2.11b). We modeled left ventricular contraction using the same piece-wise function with different scaling factors and shifted in time (Fig. 2.11c). We modeled the circuit to start at the P-wave (the start of atrial contraction), followed by ventricular contraction then early ventricular diastole. The choice in parameters were based on canine heart function and expected patterns in atrial and ventricular P-V loops (Table

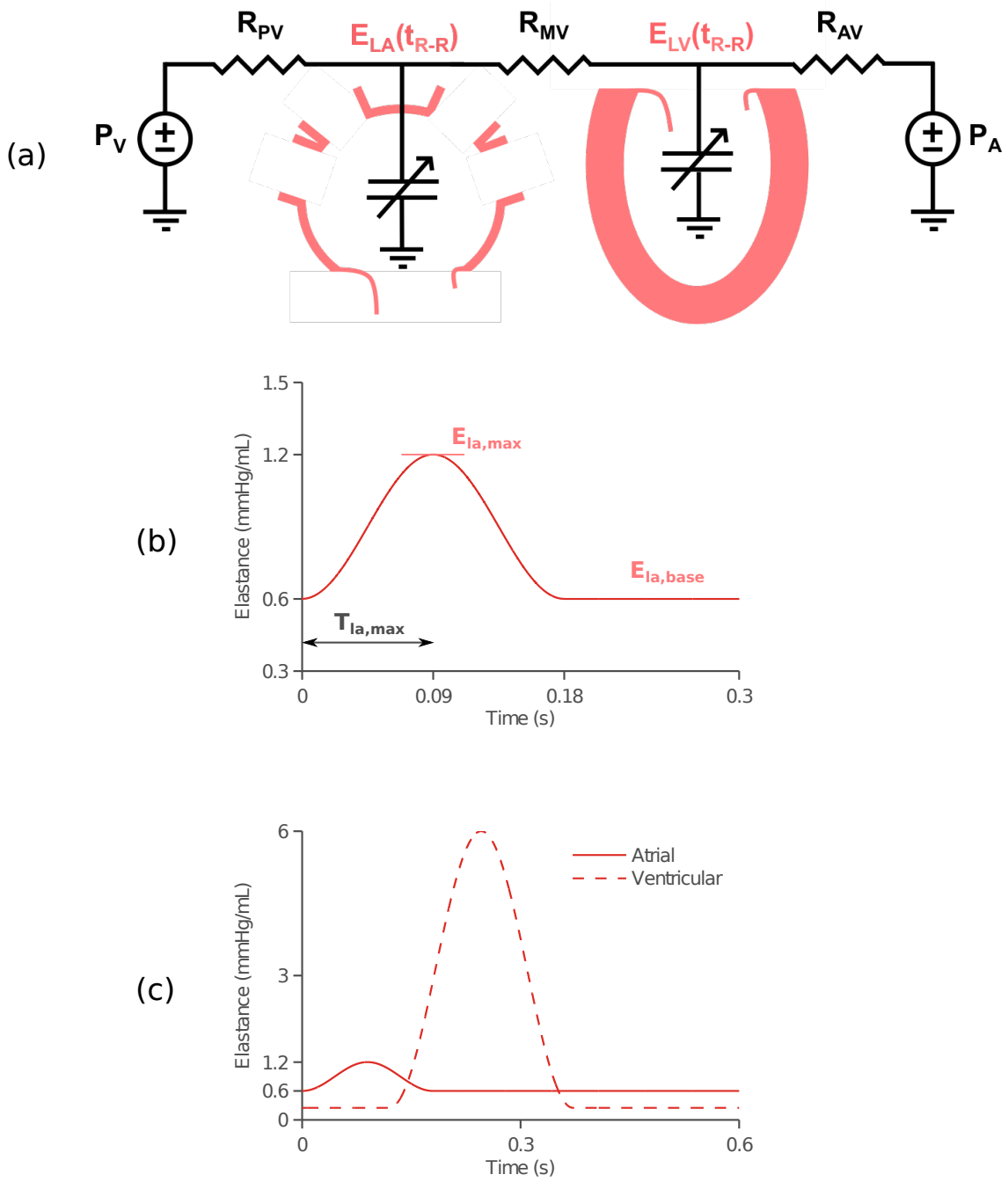

Figure 2.11: The left heart circuit flow model. (a) The circuit includes a constant pulmonary vasculature pressure (P_v) and a pulmonary vein resistance R_{pv}. Atrial and ventricular mechanics are modeled using time-varying elastance $E(t)$ with constant unloaded volumes V_o. Mitral and aortic valves are represented as single resistors R_{mv} and R_av and aortic pressure is modeled as a constant P_a. (b) Time-varying elastance curves are defined using a piece-wise cosine function. Key function parameters include the time to peak elastance T_{max}, peak elastance E_{max}, and baseline elastance E_{base} that characterize the curve. (c) Ventricular elastance was softer than the atrium when passive and stiffer during contraction. The $E_{lv}(t)$ curve was offset by 0.15 seconds relative to the start of atrial contraction.

Parameter	Symbol	Units	Baseline Value	Reference
Pulmonary pressure	P_v	mmHg	17	22
Aortic pressure	P_a	mmHg	100	100
Pulmonary resistance	R_{pv}	$^{\text{mmHg}\cdot\text{s}}/_{\text{mL}}$	0.4	2
Mitral valve resistance	R_{mv}	$^{\text{mmHg}\cdot\text{s}}/_{\text{mL}}$	0.004	0.02
Aortic valve resistance	R_{av}	$^{\text{mmHg}\cdot\text{s}}/_{\text{mL}}$	0.04	0.2
Cardiac cycle length	t_{R-R}	s	0.6	0.5
Time-Varying Elastance				
Peak LA elastance	$E_{la,max}$	$^{\text{mmHg}}/_{\text{mL}}$	1.2	1.8
Passive LA elastance	$E_{la,base}$	$^{\text{mmHg}}/_{\text{mL}}$	0.6	0.7
Time of $E_{la,max}$	$T_{la,max}$	s	0.09	0.15
Unloaded LA volume	$V_{la,o}$	mL	10	6
Peak LV elastance	$E_{lv,max}$	$^{\text{mmHg}}/_{\text{mL}}$	6	5
Passive LV elastance	$E_{lv,base}$	$^{\text{mmHg}}/_{\text{mL}}$	0.25	0.25
Time of $E_{lv,max}$	$T_{lv,max}$	s	0.25	0.18
Unloaded LV volume	$V_{lv,o}$	mL	20	10

Table 2.1: Parameters of the circuit flow model. The model was a simplified version of the work of Alexander and colleagues (Alexander et al., 1987).

2.1). Because we simplified (Alexander et al., 1987) circuit, we modified some parameters to maintain the P-V loop operating range. We used a ratio between resistors corresponding to 100:1:10 for pulmonary veins, mitral valve, and aortic valve, matching the ratios in the reference model.

2.4.3 Solving the circuit model

We solved the circuit by creating a set of equations to describe blood flow across elements, using Euler's method to discretely solve those equations, and iterating until the P-V loops converged to an equilibrium. Equations of flow were made using the hydraulic equivalent of Ohm's law, where

$$\Delta P = QR \tag{2.7}$$

We made an initial guess for pressure and volume in the chambers. We then solved for flow in and out of each chamber using Eqn. 2.7. We applied a small time step (typically less than 10μs) and calculated the net change in volume in the atrium and ventricle. We used the elastance values and Eqn. 2.6 to find the new pressure in each chamber, then incremented in time and repeated the process. Since our initial chamber values were a guess, we had to solve multiple loops in series, iterating until we reached an equilibrium (defined by the Euclidean residuals between loops N and N-1 falling below a tolerance of tol = 10^{-4}). We then computed characteristics of the atrial and ventricular P-V loops, including pressure and volume end points, stroke volumes and pressures, peak flows, and stroke work.

2.4.4 Parameter sensitivity analysis

We performed a parameter sensitivity analysis by varying each element in the circuit (pressure, resistances, and elastances) and measuring how that variation altered various loop characteristics. We varied each element at a dense set of points along a geometric scale between 0.5x and 2x of its baseline value. We tracked changes in output by normalizing them to their baseline value, such that a scaled change in an input could be match to a scaled change in an output. Finally, we fit a linear regression to this set of points to report a slope as the "sensitivity" of each input-output pair. We measured the sensitivity of timing inputs (start, peak, and end of contraction) in a separate analysis, since their ranges were limited by the length of the cardiac cycle. All simulations and sensitivity analyses were performed in MATLAB (r2010b) on a Intel MacBook Pro running OSX 10.6 or later.

2.5 Results of circuit flow modeling

Circuit models converged in less than 50 iterations, typically requiring 10 iterations to reach the specified tolerance. The equilibrium circuit modeled realistic pressures and volumes in both the atrium and ventricle (Fig. 2.12). Left atrial pressure had a characteristic dual-peak

Parameter	Symbol	Value	Units
Pressure			
LA pressure at mvo	$P_{la,mvo}$	8.1	mmHg
LA pressure at aed	$P_{la,aed}$	6.6	mmHg
LA pressure at mvc	$P_{la,mvc}$	8.1	mmHg
LV pressure at ed	$P_{lv,ed}$	8.1	mmHg
LV pressure at es	$P_{lv,es}$	100	mmHg
Volume			
LA volume at mvo	$V_{la,mvo}$	23.4	mL
LA volume at aed	$V_{la,aed}$	20.9	mL
LA volume at mvc	$V_{la,mvc}$	16.8	mL
LV volume at ed	$V_{lv,ed}$	52.4	mL
LV volume at es	$V_{lv,es}$	36.8	mL
LA active emptying	$\Delta V_{la,a}$	4.1	mL
LV stroke volume	$\Delta V_{lv,sv}$	15.6	mL
LA active emptying frac.	$EF_{la,a}$	19.8	%
LV ejection fraction	EF_{lv}	29.8	%

Table 2.2: Baseline output of the circuit flow model. Pressures and volumes were measured at mitral valve opening (mvo), start of atrial contraction (aed), and mitral valve closing (mvo). Ventricular outputs were measured at end diastole (ed, roughly the same as mvc) and end systole (es, roughly the same as mvc). We measured active empyting volume in the atrium $\Delta V_{la,a}$ and stroke volume in the ventricle, as well as ejection fraction EF_{lv}.

pattern (one peak during atrial contraction, the other at the end of passive filling), in contrast to the single-peak ventricular pressure-time curve. The single resistor model for valves and veins exaggerated peak flows (Fig. 2.12, Flow and Table 2.3) compared to the more complex source model, although average flows were similar. A summary of the baseline output is listed in Tables 2.2 and 2.3.

In addition to pressure and volumes, we measured the change in volume during atrial ejection $\Delta V_{la,a}$ and ventricular stroke volume $\Delta V_{lv,sv}$. We calculated ejection fraction by normalizing each of these stroke volumes to the pre-contraction volume $V_{la,aed}$ and $V_{lv,ed}$,

Parameter	Symbol	Value	Units
	Flow		
MV passive emptying flow	$Q_{lv,res}$	32	%
MV conduit flow	$Q_{lv,con}$	27	%
MV active emptying flow	$Q_{lv,bos}$	41	%
Peak passive MV flow	$Q_{mv,d1}$	326	$^{\mathrm{mL}}/_{\mathrm{sec}}$
Peak active MV flow	$Q_{mv,d2}$	106	$^{\mathrm{mL}}/_{\mathrm{sec}}$
Peak aortic valve flow	Q_{av}	427	$^{\mathrm{mL}}/_{\mathrm{sec}}$
	Work		
LA stroke work	SW_{la}	0.73	mJ
LV stroke work	SW_{lv}	219.5	mJ
	Shape		
LA ejection work	$SW_{la,1}$	1.3	mJ
LA recovery work	$SW_{la,2}$	-0.4	mJ
LA relaxation work	$SW_{la,3}$	-0.2	mJ
Length of passive curve	MD_{la}	5.4	arb.

Table 2.3: We calculated the proportion of blood flow across the mitral valve (MV) into the ventricle from three sources: atrial passive emptying (reservoir or res), atrial contraction (booster or bos), and conduit flow (con). We also measured peak mitral valve flow during early (d1) and late (d2) diastole. Atrial stroke work was decomposed into three components to better quantify atrial shape.

respectively. Ejection fractions were depressed compared to *in vivo* averages since model inputs were based on an isolated canine heart. We estimated flow into the ventricle during each phase of atrial emptying as a portion of total stroke volume, including passive emptying "reservoir" function ($Q_{lv,res}$), active emptying "booster pump" ($Q_{lv,bos}$), and the conduit flow from the pulmonary veins ($Q_{lv,con}$). In the baseline model, atrial contraction accounted for approximately 40% of left ventricular stroke volume. We calculated the peak flows across the mitral valve during passive emptying $Q_{mv,d1}$ and atrial contraction $Q_{mv,d2}$ and well as peak flow across the aortic valve Q_{av}. The model simulated an E:A ratio of 3.1. We computed stroke work as the area of the active loop, which was much higher in the ventricle compared

to the atrium (220 mJ vs. 0.7 mJ) as expected.

Because we were interested in the shape of subject P-V loops, we separated atrial stroke work into three components of energy: the amount accumulated from 1) onset of contraction to peak elastance, 2) peak elastance to minimum pressure, and 3) minimum pressure to V_{aed}. This is roughly equivalent to the shape of the top, bottom left, and bottom right portions of the active loop. Additionally, we calculated a "distance" metric as the maximum Euclidean distance between the start of passive filling and any other point on the loop (Table 2.3, Shape). Although crude, these metrics helped to quantify shape changes as a function of parameter variation.

2.5.1 Parameter sensitivity analysis

Parameter sensitivity analysis revealed a high loop sensitivity to atrial and ventricular elastances, especially the passive atrial elastance (average sensitivity of 0.73 among all outputs). The outputs of atrial stroke work and its components were the most sensitive to changes in atrial elastance, indicating that passive atrial stiffness may play a role in the variation of active loop shapes (Fig. 2.13). Among the pressures, model outputs were more sensitive to upstream pulmonary pressure compared to downstream aortic pressure (0.66 vs. 0.52), especially for early diastolic flow across the mitral valve (Fig. 2.14). The vein and valve resistances generally had less influence on model outputs, although pulmonary vein resistance had a higher sensitivity compared to either mitral or aortic valve resistance (0.34 vs. 0.02 and 0.04, respectively). From the global sensitivity analysis, it appeared that pulmonary factors (pressure and resistances) had a larger effect on atrial mechanics than their downstream counterparts. Unloaded volumes had the smallest influence on model outputs, which is expected given the definition of elastance and our choice to hold the factor constant through time. Interestingly, changing heart rate (modified pacing rate t_{r-r}) tended to increase atrial stroke work, matching *in vivo* trends in Fig. 2.10, but decreased atrial pressures and volumes, disagreeing with *in vivo* trends. Modifying pacing rate had roughly

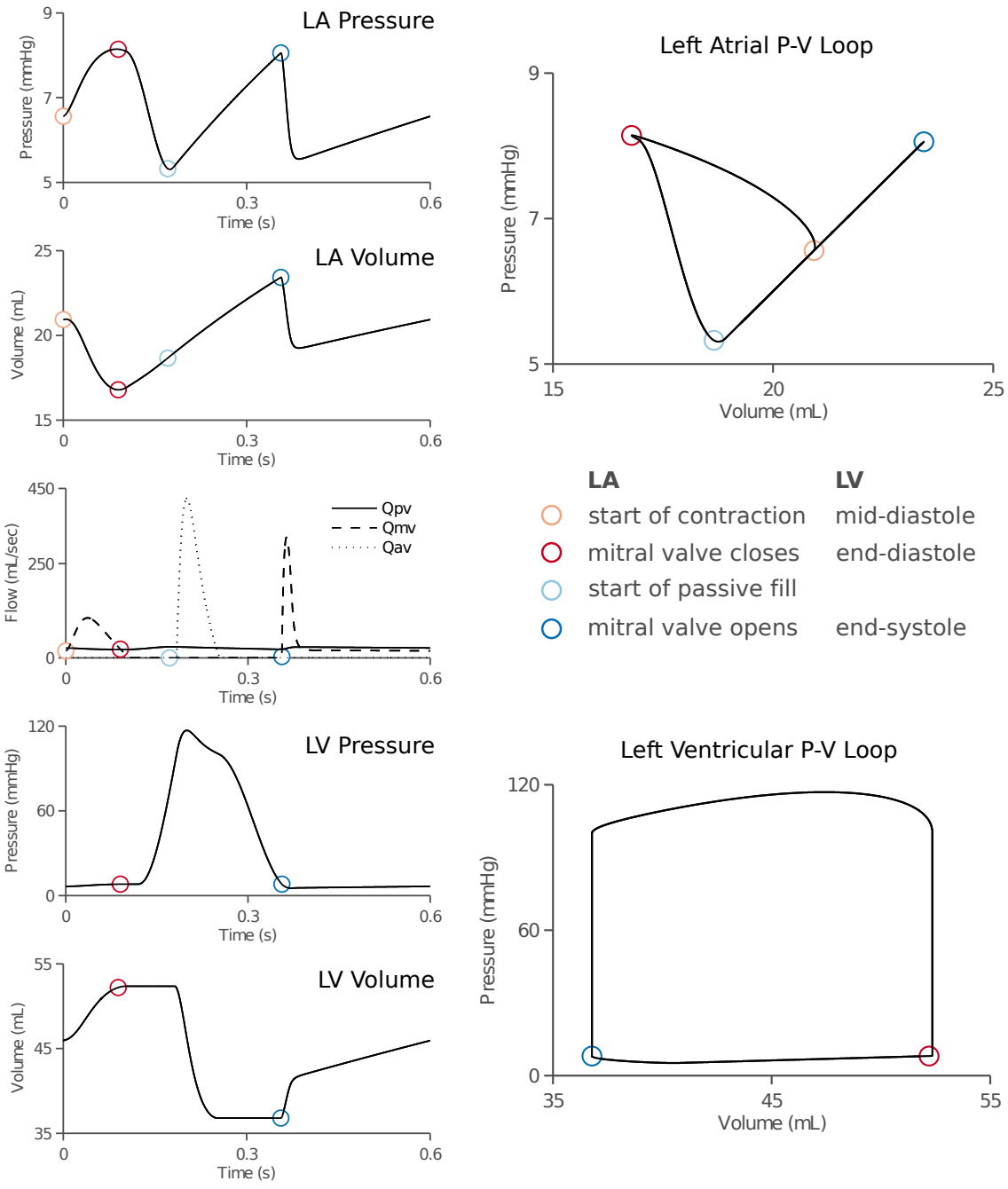

Figure 2.12: Circuit model output. The circuit model generated pressure and volume -vs-time curves for the atrium and ventricle (left), marked with the four key phase points in left heart function. These curves were combined to form atrial and ventricular pressure-volume loops.

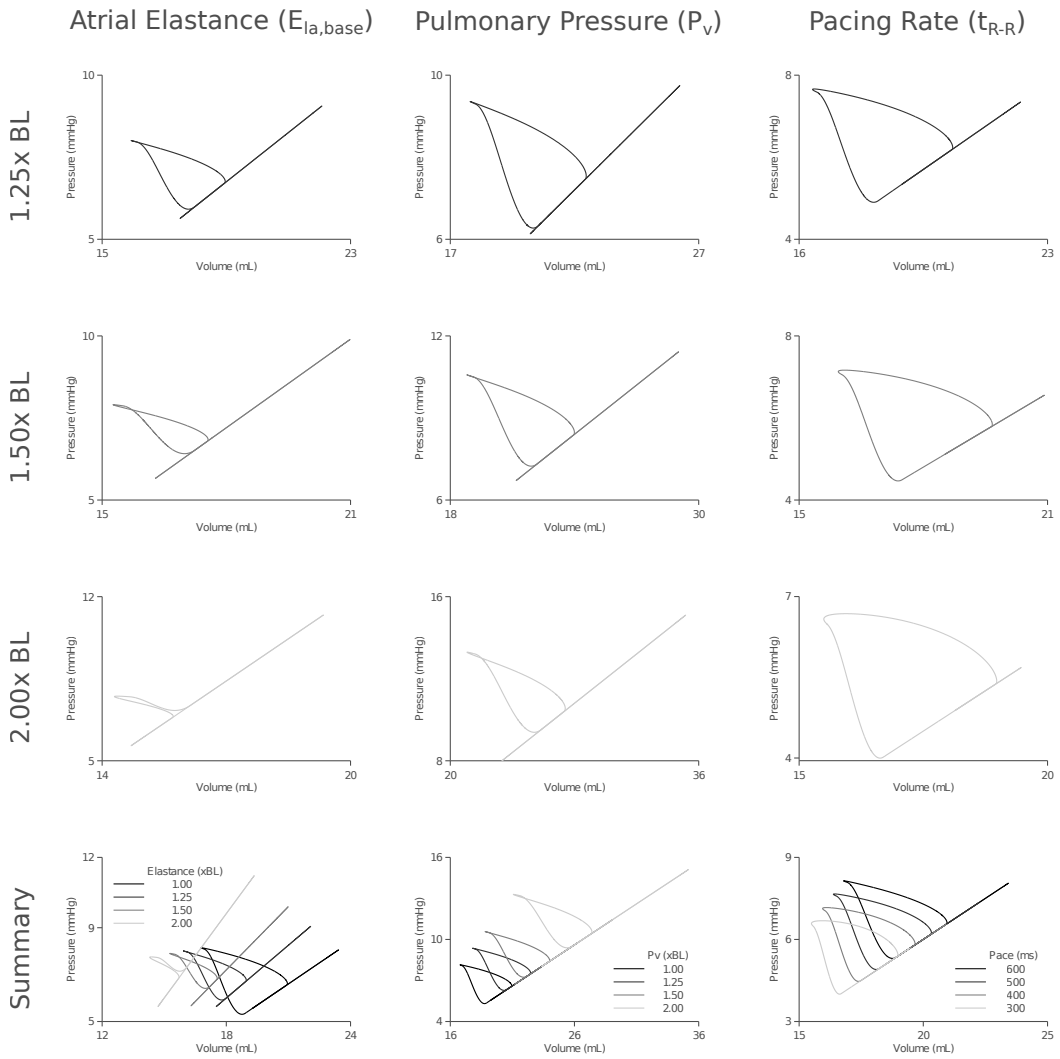

Figure 2.13: Simulated atrial P-V loops were most sensitive to changes in elastance, especially atrial baseline elastance. Higher atrial elastances (stiffer atrium) increased filling pressures and decreased active stroke work. Higher upstream pulmonary venous pressures and faster heart rates both increased stroke work, but only higher upstream loading increased atrial pressures and volumes.

the same influence as pulmonary vein resistance and followed the same patterns of output sensitivity (Fig. 2.14).

2.6 Discussion

We measured left atrial pressure-volume loops in forty six subjects using intravenous catheters. Atrial P-V loops revealed passive filling and emptying along a single exponential curve and an active loop with large variations in shape and size. We calibrated conduction volumes to cine CMR with strong correlation ($R^2 = 0.80$) and controlled atrial pressure variations using breath holds and low-pass data filtering. Individual subjects had unique P-V loop shapes and patterns influenced by left heart hemodynamics. A circuit flow model simulated atrial and ventricular P-V loops and demonstrated that elastance, especially atrial passive elastance, was the largest factor influencing P-V loop shape.

Previous studies of the atrial P-V relationship identified similar patterns in loops seen in the current work. All studies that recorded P-V loops measured energy spent during atrial contraction (stroke work) and fit the passive atrial filling curves to an exponential type function. Hoit and colleagues measured atrial P-V loops in open-chest canine models and found very low stroke work (Hoit et al., 1997), sometimes less than zero (Hoit et al., 1998). It seems as though canine P-V loops have depressed atrial contraction which impedes storke work, possibly due to anesthetization (Gare et al., 2001). Although active function was depressed, Hoit also measured chamber stiffness $k_c = 0.5 \pm 0.1\,\mathrm{mL}^{-1}$ and corrected to tissue stiffness $k_t = 3.4 \pm 0.6$, both in range with our clinical results. In these studies, volume were estimated using sonomicrometry, which may underestimate true volume.

Other groups used 2-D echocardiography to obtain human pressure-area loops, the 2-D analog of atrial P-V loops. Stefanadis and colleagues observed a stroke work of $7.7 \pm 1.8\,\mathrm{mmHg \cdot cm^2}$ in healthy adults (Stefanadis et al., 1998a). If we assume a spherical atrium of 50 mL (a rough approximation), stroke work in healthy adults averaged 3.1 mJ, or about

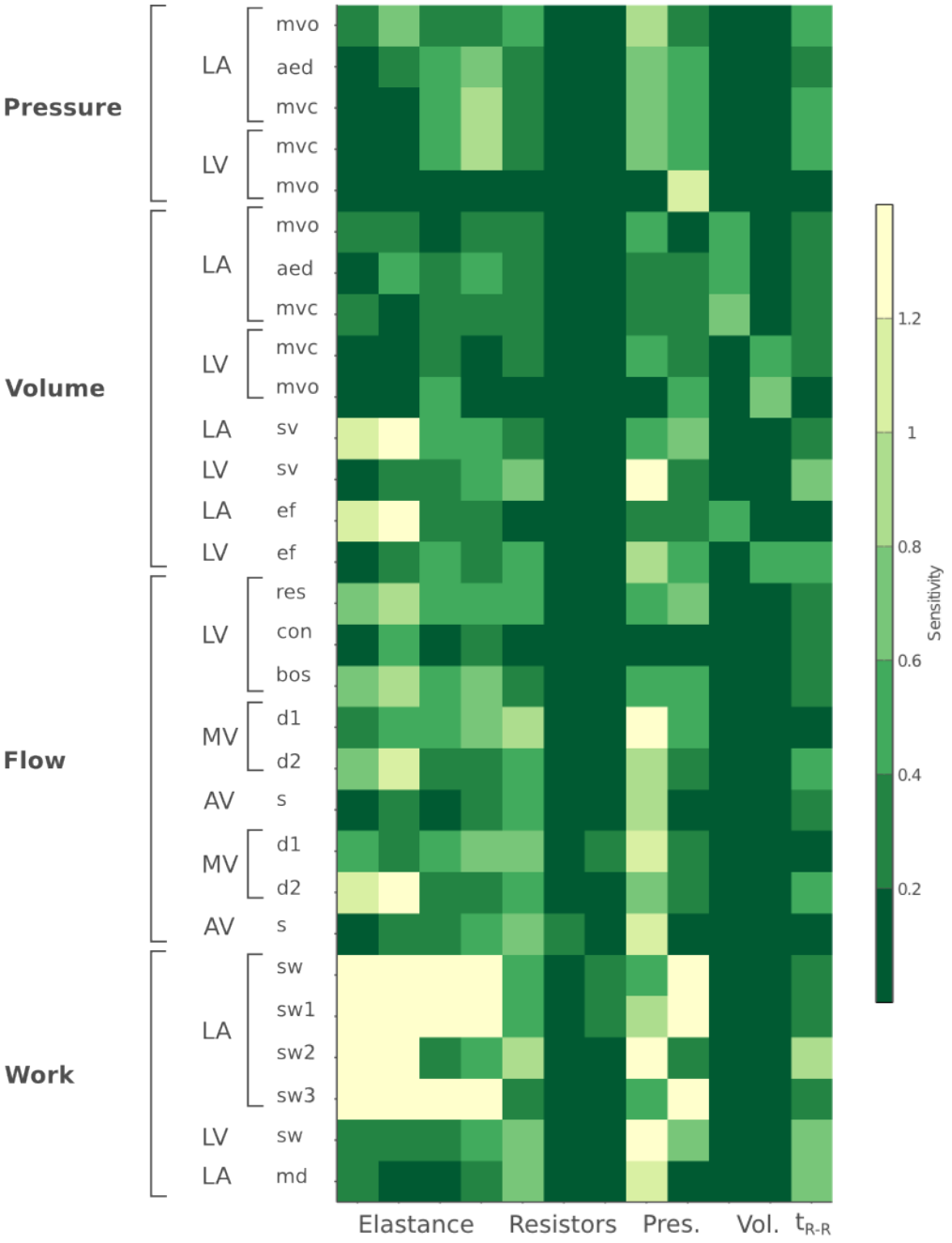

Figure 2.14: Sensitivity analysis of circuit model. Output metrics are on the vertical axis and input parameters are on the horizontal axis. Sensitivity was measured as a normalized slope (change in output / change in input), where lighter/yellow color represents a highly sensitive input-output pair and a darker/green color represents a low sensitivity pair. Outputs include pressures and volumes, changes in each, peak and average flows, as well as stroke work in the atrium and ventricle.

36% of the average we measured in subects with AF (8.8±5.7 mJ). Although the cited study reported healthy stroke work at -1σ compared to our measured distribution, the deviation is expected when comparing healthy adults to subjects with diagnosed atrial fibrillation (who relied more heavily on atrial contraction to fill the ventricle). Stefanadis also reported a passive stiffness of $k = 0.72\,\mathrm{cm}^{-2}$ in AF subjects after fitting an exponential function to passive filling (Stefanadis et al., 1998c). If we use the same 50 mL spherical conversion, this equates to a tissue stiffness of $k_t = 11.8$, within 2σ of our average tissue stiffness (7.6±2.6).

Although nomenclature differed, methods to extract global mechanics from a P-V loop were quite similar between groups. All studies identified a characteristic active loop (the "A loop") that quantified stroke work. They also measured the area formed when passive emptying deviated from the passive filling curve (the "V loop"). This negative area represented energy added to the atrium, though its source and explanation are less clear. In combination, the two loops formed a bow-tie pattern that was especially clear in canine hearts (Hoit et al., 1998; Pagel et al., 2003). Hoit and colleages reported roughly an equal ratio between stroke work and area of the V-loop. This feature seemed to be more prominent in canine models, as cited human studies saw a marked decrease in V-loop area compared to stroke work (4:1) where the active loop dominated the P-V shape and the V-loop was almost non-existent (Stefanadis et al., 1998c). Interestingly, Stefanadis and colleagues demonstrated that mitral valve stenosis and heart failure can enlarge the V-loop area, though the causal relationship is unclear. In the present study, the average V-loop area was slightly *positive* in contrast to previous studies (where it was always negative). Our circuit flow model indicated a minimal influence of mitral valve resistance to P-V loop shape, and a more advanced circuit flow model could help explain the observed differences.

The circuit flow model revealed a strong influence of passive atrial and ventricular stiffness on left heart hemodynamics, and the relatively small influence of valve resistance. Patterns in atrial shape, especially during active contraction, were heavily influenced by atrial elastance (as expected). We expanded upon this analysis by checking the sensitivity of atrial stroke

work to the timing of elastance curves. We found the highest sensitivity between atrial stroke work and the relative timing of atrial and ventricular contraction. That is, if atrial contraction were delayed or ventricular contraction accelerated, atrial stroke work would be drastically reduced. We also found that the components of atrial stroke work were most sensitive to the length and relative onset of atrial contraction. Previous clinical studies have shown that patients who developed AF were more likely to show altered P-wave shape and duration compared to age-matched controls (Holmqvist et al., 2009). Changes in atrial contraction pattern could result in altered shape, confirmed by the high sensitivity between the pair. The next chapter will explore this relationship in more detail among the AF cohort.

2.6.1 Limitations of P-V loops

The largest limitation in atrial P-V loop analysis is the accurate measurement of atrial volumes. Larger atria and atria with unusual geometry distort the electrical field and impede conductance measurements. Although we confirmed the position of the P-V catheter using real-time X-ray fluoroscopy, we cannot be sure that all electrodes remained in the atrium during the cardiac cycle. Repeated measurements within subjects (or as part of an animal study) could help to quantify this variation. Calibration to CMR addressed this limitation to an extent.

Pressure signals obtained from the catheter have a known offset which varied between patients, making it difficult to measure absolute pressures. We subtracted the absolute values (V_o, P_o) to measure stiffness and stroke work in an attempt to reduce the impact of this artifact. Future studies could use a fluid-filled catheter or other external pressure measure to calibration the Millar prior to data collection.

The hydraulic circuit simulated a basic canine pressure-volume loop using simple time-varying elastance models. These simple functions were adequate to understand major components of P-V loops, but the more subtle features (non-linear passive filling, V-loop

area) were lost in this analysis. Future models could expand the circuitry to include such elements.

We were excited by the results of the pressure-volume loop method, especially the large differences in shapes among the clinical cohort. We decided to use these shapes and the P-V loop simulator to understand how atrial fibrillation (and related diseases) alter global mechanics, which we address in Chapter 3.

References

A. V. Abbott. Telephone cables - i. *The Electrical World and Engineer*, 40(23):294, 1902.

J. Alexander, K. Sunagawa, N. Chang, and K. Sagawa. Instantaneous pressure-volume relation of the ejecting canine left atrium. *Circulation Research*, 61(2):209–219, Aug. 1987.

T. Arts, T. Delhaas, P. Bovendeerd, X. Verbeek, and F. W. Prinzen. Adaptation to mechanical load determines shape and properties of heart and circulation: the CircAdapt model. *Am J Physiol Heart Circ Physiol*, 288(4):H1943–H1954, Apr. 2005.

M. Gare, D. A. Schwabe, D. A. Hettrick, J. R. Kersten, D. C. Warltier, and P. S. Pagel. Desflurane, sevoflurane, and isoflurane affect left atrial active and passive mechanical properties and impair left atrial-left ventricular coupling in vivo: analysis using pressure-volume relations. *Anesthesiology*, 95(3):689–698, 2001.

W. Grossman, E. Braunwald, T. Mann, L. P. McLaurin, and L. H. Green. Contractile state of the left ventricle in man as evaluated from end-systolic pressure-volume relations. *Circulation*, 56(5):845–852, Nov. 1977.

B. D. Hoit, Y. Shao, M. Gabel, and R. A. Walsh. In vivo assessment of left atrial contractile performance in normal and pathological conditions using a time-varying elastance model. *Circulation*, 89(4):1829–1838, Apr. 1994.

B. D. Hoit, Y. Shao, M. Gabel, C. Pawloski-Dahm, and R. A. Walsh. Left atrial systolic and diastolic function after cessation of pacing in tachycardia-induced heart failure. *Am J Physiol Heart Circ Physiol*, 273(2):H921–927, Aug. 1997.

B. D. Hoit, Y. Shao, and M. Gabel. Left atrial systolic and diastolic function accompanying chronic rapid pacing-induced atrial failure. *Am J Physiol Heart Circ Physiol*, 275(1): H183–189, July 1998.

F. Holmqvist, P. G. Platonov, J. Carlson, W. Zareba, and A. J. Moss. Altered interatrial conduction detected in MADIT II patients bound to develop atrial fibrillation. *Ann Noninvasive Electrocardiol*, 14(3):268–275, July 2009.

H. Jun. Account of a steam-engine indicator. *Quarterly Journal of Science, Literature, and the Arts*, 13(25):9195, 1822.

R. C. P. Kerckhoffs, M. L. Neal, Q. Gu, J. B. Bassingthwaighte, J. H. Omens, and A. D. McCulloch. Coupling of a 3D finite element model of cardiac ventricular mechanics to lumped systems models of the systemic and pulmonic circulation. *Ann Biomed Eng*, 35(1): 1–18, Jan. 2007.

V. K. Lau, K. Sagawa, and H. Suga. Instantaneous pressure-volume relationship of right atrium during isovolumic contraction in canine heart. *American Journal of Physiology - Heart and Circulatory Physiology*, 236(5):H672–H679, May 1979.

O. Lodge. Mr. preece on lightning protection. *Nature*, 47:536, 1893.

J. D. Marsh, L. H. Green, J. Wynne, P. F. Cohn, and W. Grossman. Left ventricular end-systolic pressure-dimension and stress-length relations in normal human subjects. *The American Journal of Cardiology*, 44(7):1311–1317, Dec. 1979.

M. Matsuzaki, M. Tamitani, Y. Toma, H. Ogawa, K. Katayama, Y. Matsuda, and R. Kusukawa. Mechanism of augmented left atrial pump function in myocardial infarction and essential hypertension evaluated by left atrial pressure-dimension relation. *The American Journal of Cardiology*, 67(13):1121–1126, May 1991.

W. L. Maughan, A. A. Shoukas, K. Sagawa, and M. L. Weisfeldt. Instantaneous pressure-volume relationship of the canine right ventricle. *Circ. Res.*, 44(3):309–315, Mar. 1979.

D. P. Miller. The mysterious case of James Watt's "1785 steam indicator": Forgery or folklore in the history of an instrument? *International Journal for the History of Engineering & Technology*, 81(1):129–150, Jan. 2011.

P. J. Nahin. *Oliver Heaviside: The Life, Work, and Times of an Electrical Genius of the Victorian Age*. JHU Press, Oct. 2002.

T. Nivatpumin, S. Katz, and J. Scheuer. Peak left ventricular systolic pressureend-systolic volume ratio: A sensitive detector of left ventricular disease. *The American Journal of Cardiology*, 43(5):969–974, May 1979.

P. Pacher, T. Nagayama, P. Mukhopadhyay, S. Btkai, and D. A. Kass. Measurement of cardiac function using pressurevolume conductance catheter technique in mice and rats. *Nat. Protocols*, 3(9):1422–1434, Aug. 2008.

P. S. Pagel, F. Kehl, M. Gare, D. A. Hettrick, J. R. Kersten, and D. C. Warltier. Mechanical function of the left atrium: new insights based on analysis of pressure-volume relations and doppler echocardiography. *Anesthesiology*, 98(4):975–994, Apr. 2003.

J. E. Porterfield, A. T. G. Kottam, K. Raghavan, D. Escobedo, J. T. Jenkins, E. R. Larson, R. J. Trevio, J. W. Valvano, J. A. Pearce, and M. D. Feldman. Dynamic correction for parallel conductance, GP, and gain factor, , in invasive murine left ventricular volume measurements. *J Appl Physiol*, 107(6):1693–1703, Dec. 2009.

K. Sagawa. The ventricular pressure-volume diagram revisited. *Circulation Research*, 43(5): 677–687, Nov. 1978.

K. Sagawa, R. K. Lie, and J. Schaefer. Translation of otto frank's paper "Die grundform des arteriellen pulses" zeitschrift fr biologie 37: 483-526 (1899). *J. Mol. Cell. Cardiol.*, 22(3): 253–254, Mar. 1990.

C. Stefanadis, J. Dernellis, S. Lambrou, and P. Toutouzas. Left atrial energy in normal subjects, in patients with symptomatic mitral stenosis, and in patients with advanced heart failure. *The American Journal of Cardiology*, 82(10):1220–1223, Nov. 1998a.

C. Stefanadis, J. Dernellis, C. Stratos, E. Tsiamis, C. Tsioufis, K. Toutouzas, C. Vlachopoulos, C. Pitsavos, and P. Toutouzas. Assessment of left atrial PressureArea relation in humans by means of retrograde left atrial catheterization and echocardiographic automatic boundary detection: Effects of dobutamine. *J Am Coll Cardiol*, 31(2):426–436, Feb. 1998b.

C. Stefanadis, J. Dernellis, C. Stratos, E. Tsiamis, C. Vlachopoulos, K. Toutouzas, S. Lambrou, C. Pitsavos, and P. Toutouzas. Effects of balloon mitral valvuloplasty on left atrial function in mitral stenosis as assessed by pressure–area relation. *J Am Coll Cardiol*, 32(1):159–168, July 1998c.

H. Suga, K. Sagawa, and A. A. Shoukas. Load independence of the instantaneous pressure-volume ratio of the canine left ventricle and effects of epinephrine and heart rate on the ratio. *Circulation Research*, 32(3):314–322, Mar. 1973.

C. W. White, R. E. Kerber, H. R. Weiss, and M. L. Marcus. The effects of atrial fibrillation on atrial pressure-volume and flow relationships. *Circulation Research*, 51(2):205–215, Aug. 1982.

Chapter 3

Global function in atrial fibrillation patients

Atrial pressure-volume loops varied substantially between patients. AF typically develops alongside many other cardiac diseases and we wanted to understand the relationship between the prevalence of those diseases and the observed variations in shape. We therefore used the circuit simulator to model expected changes in P-V loops due to common cardiac diseases and generated several hypotheses about resulting changes in shape. We then analyzed clinical P-V loops for similar patterns, sorting loops based on their shape and testing the sorted clusters for common diagnoses. We accumulated twenty three unique clinical factors from patient histories and separately tested their ability to identify similar patterns in loops, building a link between shape and AF comorbidities.

3.1 Background on atrial fibrillation

In the 18^{th} century, clinicians began observing cases of fibrillation, its causes, and its effects. Jean-Baptiste de Senac studied cardiac function throughout his career, describing fibrillation as when "the muscle fibers form oblique ripples" and noted that "the harmony of their movements is disconcerted". The first time de Senac discussed atrial fibrillation (palpitations),

he describes it in the context of mitral valve disease. He writes "Reflux of the blood into the auricles [atria] causes contractions of greater force, necessarily precipitating palpitations. When the obstacles in the heart obstruct the entrance to the ventricles, blood accumulates in the cavities of the auricles and irritates the fibers of their walls. Their contractions become more lively." Amazingly, de Senac had discovered that AF developed alongside mitral valve disease and was the first to formulate the link (McMichael, 1982).

3.1.1 AF comorbidities

Atrial fibrillation rarely exists in a vacuum. An episode of AF elevates heart rate to over 120 beats per minute and sets off a cascade of cardiac remodeling. Over years, AF increases fibrosis in both the atrium and ventricle, and exacerbates dysfunction from other cardiac diseases (De Jong et al., 2011). External factors such as hypertension, congestive heart failure, and mitral regurgitation are all predictors of AF (Fuster et al., 2006). In fact, AF in isolation ("lone" AF) represents less than 5% of all diagnosed cases (Frost, 2007). Any evaluation of pressure-volume function in AF subjects must be evaluated in the context of other disease pathologies developing alongside AF.

Congestive heart failure (CHF) and atrial fibrillation are inherently intertwined phenomena, in part because they share many common risk factors. In a large study of the Framingham population, AF preceded heart failure as often as heart failure preceded AF (Wang et al., 2003). Developing AF following CHF diagnosis results in increased mortality, as did CHF following AF diagnosis. Previous animal studies of pacing-induced heart failure demonstrate that CHF altered atrial conduction, increase atrial fibrosis, and increase the atrium's propensity to fibrillate (Li et al., 1999; Shimano et al., 2008). We hypothesized that each of these effects will have a significant influence on global mechanics in the atrium. Likewise, previous studies where AF was successfully managed (return to sinus rhythm) result in significant improvements in ventricular function (Shinbane et al., 1997).

Diseases that elevate pressures and volumes and "overload" the atrium are linked to AF. Systemic hypertension creates pressure overload in the atrium. Animal studies in sheep and mice reveal left atrial enlargement and increases in atrial fibrosis as a result of elevated pressures (Kistler et al., 2006; Liao et al., 2010), and those higher pressures increase the chance of developing AF (Lau et al., 2010). Mitral valve regurgitation creates volume overload in the atrium, resulting in enlarged atria and increases atrial fibrosis in an animal model (Verheule et al., 2003). Clinically, mitral valve disease is designated within AF as the "valvular-AF" subset. Mitral valve regurgitation leads to severe degeneration of atrial myocytes and increases interstitial fibrosis (Anne et al., 2005; Thiedemann and Ferrans, 1977). Both hypertension and mitral valve disease are independent predictors of AF risk (Benjamin et al., 1994).

Atrial fibrillation immediately disrupts electrical conduction in both the atrium and ventricle, leading to remodeling of ion channels, atrial refractory period, and conduction velocity (Gaspo et al., 1997; Wijffels et al., 1995). Electrical remodeling caused by rapid atrial pacing is significantly different than the effects of heart failure or valve disease (Everett et al., 2006). Clinically, excessively long p-wave duration has been associated with increased risk of AF (Magnani et al., 2011) and changes in p-wave morphology are associated with increased development of AF (Holmqvist et al., 2009).

A series of other disorders, including left ventricular hypertrophy and diabetes mellitus, are also linked to AF (Benjamin et al., 1994). Obstructive sleep apnea increases the risk of AF recurrence following cardioversion (Kanagala et al., 2003). Diabetes and obstructive sleep apnea are both significantly linked to obesity, which may explain some of these correlated effects (Gami et al., 2007). Coronary artery disease has been shown to be an independet risk factor of AF in some studies, but not as strong as volume and pressure overload or heart failure.

Building upon the methods and results of our atrial pressure-volume loops, we sought to link the shape of observed loops with underlying cardaic diseases. Given the wide array of shapes observed in our patient population, we hypothesized that AF comorbidities (heart

failure, mitral valve disease, and hypertension) were altering the global hemodynamics in the atrium. We used the P-V loop circuit simulator to model many of these common diseases, and predict how they alter loop shape. We then analyzed clinical P-V loops by sorting similar shapes and testing the relationship between shape and disease history.

3.2 Methods to simulate P-V dysfunction

Atrial pressure-volume loops were simulated using a hydraulic circuit model described in detail in Chapter 2. Briefly, the cardiac chambers, vessels, and valves were modeled as simple circuit elements (resistors and capacitors). We simulated blood flow into the heart using a constant pulmonary vasculature pressure and simulated cardiac contraction using time-varying elastance curves. Simulated pressure gradients (passive and active) generated flow across valves and pumped blood out of the heart. Pressures, volumes, and flows were measured for a single cardiac cycle in the left heart (atrium and ventricle). We then altered portions of the circuit to mimic various cardiac diseases and observed how the atrial P-V loop changed. Similar to Chapter 2, we performed a sensitivity analysis between simulated disease states and changes in P-V loop shape. To better compare the simulation with clinical loops, we adjusted circuit parameters to match an average human atrium instead of the canine atrium in Chapter 2. This required adjusting baseline and peak elastance values for the atrium and ventricle with minor adjustments in valvular resistances and pressures. We maintained the ratios between pulmonary, mitral, and aortic resistors (100:1:10). Mean pulmonary pressure was set to 20 mmHg and mean arterial pressure was set to 90 mmHg. We chose baseline and peak elastance values to match realistic filling and emptying volumes and pressures in the two chambers.

3.2.1 Disease sensitivity analysis

We selected five cardiovascular disorders that are commonly associated with AF and could be easily implemented in our model: 1) hypertension, 2) congestive heart failure, 3) left ventricular hypertrophy, 4) mitral valve regurgitation, 5) A-V conduction delay. We also included two common factors of AF directly linked to atrial function: 6) AF disease stage, 7) prior ablations. We chose three levels for each disease (mild, moderate, and severe) and modified one or more circuit elements to represent the disease state.

We modeled hypertension as an increase in mean arterial pressure of 20, 50, and 100%, producing pressures of 108, 135, and 180 mmHg (baseline mean arterial pressure was 90 mmHg). These three elevated levels correspond to the clinical classifications: 1) prehypertension, 2) stage I hypertension, 3) stage II hypertension. We modeled congestive heart failure as a decrease in peak ventricular elastance $E_{lv,max}$ that created a drop in LV ejection fraction. We modeled $E_{lv,max}$ at 2.3, 1.5, 1.1 mmHg/mL, all decreased from the baseline value of 3.9 mmHg/mL. These decreases generated reduced ejection fractions of 50, 40, and 30% from a 60% baseline. We modeled left ventricular hypertrophy as an increase in passive LV elastance, assuming that hypertrophy resulted in a slightly stiffer ventricle. We increased $E_{lv,base}$ from 0.13 mmHg/mL to 0.20, 0.23, and 0.27 mmHg/mL, reducing ventricular stroke volume by 5, 10, and 15 mL respectively from a 70 mL baseline.

We modeled mitral valve regurgitation by inserting an additional resistor in the circuit that allowed retrograde flow across the mitral valve during ventricular systole. We lowered the resistance to increase retrograde flow and simulate a more severe case. We chose resistor values of 2, 0.5, and 0.2 mmHg·sec/mL to create mitral valve regurgitant fractions of 12 (mild), 36 (moderate), and 59% (severe). The baseline resistance was infinite (no retrograde flow). Finally, we modeled disruptions in atrial-ventricular coupling (slowed conduction velocity, A-V node disorder) by lengthening the time period when the atrial elastance curve was active. We modeled three levels of increase (5, 10, 15% R-R). Although we had less clinical basis for these values, we suspected that certain patterns in the active phase of loops

were created from disruptions in relative timing of atrial and ventricular contraction and we sought to explore that effect. Because we were interested in loop shape, we normalized each simulated P-V loop to a (0,1) scale, allowing simpler comparisons between simulated and clinical loops.

We modeled AF disease stages as an increase in atrial elastance (both passive and active elastance). We assumed that progression of AF would increase fibrosis and stiffen the atrium, resulting in higher baseline elastance. We modeled the three levels of AF disease progression: 1) paroxysmal, 2) persistent, 3) permanent AF, corresponding to increases in atrial elastance of 20, 50, and 100%. Similarly, we modeled prior ablations as an increase in passive atrial elastance with no increase in active elastance (ablation would remove some contractility from the atrium). We modeled three levels of prior ablations as increases in baseline elastance of 20, 50, and 100%. Although we had no clinical indicator to validate the magnitude of these increases, we felt that changes in atrial elastance were worth evaluating given the results of the sensitivity analysis in the previous chapter and the clinical history of AF patients.

3.3 Methods of P-V loop shape analysis

All studies were approved by the University of Virginia Institutional Review Board (IRB). Forty three subjects ($n = 43$) were recruited from the University of Virginia Health System for a research study with informed consent. We collected pressure and volume data (P-V loops) from each subject prior to an ablation procedure using the methods and calibration techniques described in Chapter 2. All loops in this chapter were analyzed at "baseline" – held expiration and at an intrinsic heart rate. Once acquired, we used the average loop (one loop per patient) and normalized the pressures and volumes to a (0,1) range. We normalized data to eliminate offsets in pressure and volume between patients. Besides aiding subsequent calculations, normalization focused the analysis on P-V loop shape and removed effects from the size of loops or their absolute position in the pressure-volume plane.

3.3.1 Clinical factors

Measure (units)	Mean±S.D. (Range)		
Category	Threshold	Sample (n)	Fraction (%)
Age (yr)	56 ± 14 (23,77)		
Young	< 60	23	53
Old	≥ 60	20	47
Sex (no. of patients)			
Male		29	67
Female		14	33
Height (in)	69 ± 4 (62,77)		
Short	< 70	21	49
Tall	≥ 70	22	51
Weight (kg)	98 ± 30 (49,215)		
Light	< 90	20	47
Heavy	≥ 90	23	53
Body-mass index (kg/m^2)	30 ± 7 (16,47)		
Normal	≤ 25	11	26
Overweight	≤ 30	15	35
Obese Class I	≤ 35	8	19
Obese Class II-III	> 35	9	21

Table 3.1: Table of patient demographics. Thresholds were chosen based on clinical standards. When no clinical standard was available, threshold were selected manually to equally separate data into two groups. Sample represents the number of patients in each group, and Fraction is the percentage of total loops in the grouping.

We compiled a comprehensive clinical history based on available patient records, imaging sets, ECG recordings, and clinical notes. For each patient, we recorded demographic data: age, gender, height, weight, and body-mass index (Table 3.1). We recorded clinical history of AF: type of AF, duration of AF, any prior ablations, and ECG data (Table 3.2). We measured ECG intervals, focusing on P-R interval, P-wave duration, and the P-R delay (P-R interval minus the P-wave duration). We chose these ECG measures based on the sensitivity between P-V loop shape and timing inputs in the loop simulation. We recorded left ventricular

Measure (units)	Mean±S.D. (Range)		
Category	Threshold	Sample (n)	Fraction (%)
	ECG Measurements		
P-wave duration (msec)	109 ± 21 (60,160)		
Short	< 100	14	33
Normal	< 120	15	35
Long	≥ 120	14	33
P-R interval (msec)	171 ± 31 (90,238)		
Short	≤ 160	17	40
Normal	< 180	12	28
Long	≥ 180	14	33
P-R delay (msec)	61 ± 29 (0,148)		
Very Short	< 40	9	21
Short	< 55	11	26
Long	< 80	14	33
Very Long	≥ 80	9	21
	History of AF		
Type of AF (no. of patients)			
Paroxysmal		31	72
Persistent		7	16
None		5	12
Duration of AF (years)			
Less than a year		8	19
One-five years		8	19
Five or more years		22	51
No. of prior ablations			
None		33	77
One or more		10	23

Table 3.2: Table of AF and ECG histories. Thresholds were chosen based on clinical standards. When no clinical standard was available, threshold were selected manually to equally separate data into three groups. Sample represents the number of patients in each group, and Fraction is the percentage of total loops in the grouping.

Measure (units) Category	Sample (n)	Fraction (%)
Left Ventricular Function		
Congestive heart failure (class)		
None	35	81
Class I-IV	8	19
Ejection fraction (%)		
Normal	37	86
Deficient	4	9
N.A.	2	5
Hypertrophy (thickness)		
Normal	34	79
Hypertrophic	7	16
N.A.	2	5
Diastolic dysfunction (grade)		
Normal	16	37
Grade I	4	9
Grade II-III	3	7
N.A.	20	47
Coronary artery disease (no. of patients)		
Absent	38	88
Present	5	12
Other Heart Disease		
Atrial flutter (no. of patients)		
Absent	36	84
Present	7	16

Table 3.3: Table of AF co-morbidities. Thresholds were chosen based on clinical standards. Sample represents the number of patients in each group, and Fraction is the percentage of total loops in the grouping.

function: evidence of congestive heart failure, LV ejection fraction, LV hypertrophy, diastolic dysfunction, and coronary artery disease (Table 3.3). We also recorded other heart disease

Measure (units) Category	Sample (n)	Fraction (%)
Valvular Disease		
Mitral regurgitation (grade)		
None	10	23
Trivial	22	51
Mild	7	16
Moderate	2	5
N.A.	2	5
Aortic regurgitation (no. of patients)		
Absent	40	93
Present	3	7
Other Disease		
Hypertension (no. of patients)		
Normal	24	56
Hypertensive	19	44
No. of Anti-Hypertensive Drugs		
None	24	56
One	13	30
Multiple	6	14
Diabetes mellitus (no. of patients)		
Normal	38	88
Diabetic	5	12
Obstructive sleep apnea (no. of patients)		
Absent	35	81
Present	8	19
Pulmonary disease (no. of patients)		
Absent	39	91
Present	4	9

Table 3.4: Table of valvular, extra-cardiac AF co-morbidities. Thresholds were chosen based on clinical standards. Sample represents the number of patients in each group, and Fraction is the percentage of total loops in the grouping.

(atrial flutter) and valvular disorders: mitral valve regurgitation and aortic valve regurgitation (there were no cases of valve stenosis). Finally, other recorded diseases included hpyertension and number of anti-hypertensive drugs, diabetes, obstructive sleep apnea, and pulmonary disease (Table 3.4).

We grouped clinical factors into two to four categories for shape analysis. For demographic data, we separated subjects into two groups (young vs. old, short vs. tall, etc.) and chose thresholds that equally divided the groups. We separated subjects age at 60 years old, height at 70 inches, weight at 200 lbs, and BMI based on establish standards of obesity. In cases were groups were small (such as BMI Obese Class II and Class III), we combined two groups into one "Class II and higher". We divided ECG timing data into three groups (short, normal, and long) and chose dividing thresholds that equally divided the groups. AF histories were already grouped based on the diagnosis (paroxysmal vs. persistent AF) and the duration of an AF diagnosis for a subject. We had several Wolff-Parkinson-White (WPW) patients and their AF type was grouped as "none". WPW is a non-AF rhythm disorder where an accessory pathway (tissue link between atrium and ventricle) creates pre-excitation contraction in the LV. WPW subjects served as a control, since they tended to be younger, healthier, and lacked any traditional AF comorbidities.

Other cardiac diseases were grouped as either present or absent and stratified based on standard clinical definitions (e.g. mild, moderate, severe). For some factors, patients did not receive cardiac imaging prior to ablation and could not be classified. For hypertension, we suspected that diagnosed hypertension may not result in higher blood pressure, since pressures were heavily dependent on management of the disease. Thus, we included both diagnosed hypertension and the number of anti-hypertensive drugs, assuming more drugs represented worse cases.

3.3.2 Shape analysis

We used a shape analysis tool to compare and group clinical P-V loops based on their pair-wise similarity. Each subject's P-V loop was treated as a closed curve in 2-D space. There are many shape analysis tools for comparing 2-D curves – we selected one in active development with freely distributed MATLAB code (Srivastava et al., 2011). Briefly, the method scored a pair of two closed curves (in our case two loops) based on the geodesic distance between them. In simplified terms, a geodesic distance is the distance each portion of the curve had to travel to change from Loop A to Loop B. Loops that were identical in shape had no distance between them (zero) and loops that were very different had a larger distance (close to one). We tested this method with a set of standard shapes (stars, squares, circles) and confirmed that the imported method successfully scored shapes with similar characteristics. We performed this analysis on each of the 903 pair-wise comparisons of 43 loops to create a "distance matrix". The distance matrix was used to group subjects based on similarities in their loop shapes.

3.3.3 Cluster analysis

We used two methods to measure how P-V loop shape related to clinical history. First we grouped loops based on similarity of shape, then tested groups for similarities in clinical history. Second, we sorted loops based on clinical histories (similar characteristic grouped together), then tested groups for similarities in shape. The two complementary approaches allowed us to measure which clinical factors dictated shape and the strength of their influence.

In the first analysis, we sorted loops into groups called "clusters" based on the similarity score from the distance matrix (similar loops were grouped together). We used a linkage algorithm to build a hierarchical tree of links between the loops based on the maximum distance within each cluster (MATLAB function: *linkage*, method: *complete*). This method generated a tree-like dendrogram of links, with input loops at the base, similar loops linked towards the bottom, dissimilar loops linked towards the top, and all links converging to a

single average loop at the top (average of 43 input loops). We set a threshold level at 0.40 (about halfway up the tree), such that any links below the threshold were considered a cluster.

Once clusters were created, we searched the clinical histories within each cluster to identify the single, most common factor present in the loops. We then tested that cluster as a binary classification test: if the clinical factor was present in a clustered loop, it was labeled a true positive (TP); if the clinical factor was present *outside* the cluster, it was labeled a false negative (FN). Likewise, a loop in the cluster that did not have the factor was a false positive (FP), and a loop outside the cluster that did not have the factor was a true negative (TN). We then measured the sensitivity and specificity of each cluster-factor relationship. Because sample size in some clusters was small, we used a clustering quality test called the Fowlkes-Mallows Index (FM) (Fowlkes and Mallows, 1983), where

$$FM = \sqrt{\frac{TP}{TP + FP} \cdot \frac{TP}{TP + FN}} \tag{3.1}$$

where a higher value represents a better cluster (a perfect cluster has $FM = 1$). We reported the sensitivity, specificity, and FM measure for each cluster.

In the second analysis, we sorted loops based on each of the 23 clinical factors (see clinical tables). We treated each factor as a clustering mechanism, separating the loops based on their classification and computing a group-average loop. For example, the clinical factor of "height" sorted loops into short and tall groups based on the prescribed threshold. We averaged each group to create a "short" P-V loop and a "tall" P-V loop. We then tested the factor for its clustering capabilities. We used two measures of clustering capability: the Davies-Bouldin Index and the Dunn Index. The Davies-Bouldin Index (Davies and Bouldin, 1979) used a ratio of the distance within clusters (clusters with tighter proximity are better) to the distance between clusters (well-separated clusters are better). The index DB was formulated as

$$DB = \frac{1}{n} \sum_{i}^{n} \max_{i \neq j} \left\langle \frac{S_i + S_j}{M_{ij}} \right\rangle \tag{3.2}$$

where n is the number of clusters, S_i and S_j are the dispersion of clusters i and j respectively, and M_{ij} is the distance between clusters i and j. Here, dispersion S is computed as the average distance between each loop in the cluster and the cluster mean. The distance M between clusters was based on the two mean shapes. Dispersion S and inter-cluster distances M were calculated using the same shape analysis tool discussed previously. Smaller DB indices meant better clustering.

The second measure we used was the Dunn Index (J.C., 1974). Similar in approach, the Dunn Index D compared the compactness of clusters (based on the maximum distance between each pair in a cluster) to the separation of clusters (based on the distance between cluster means). Stated formally,

$$D = \min_{1\leq i\leq n} \left\langle \min_{1\leq j\leq n, i\neq j} \left\langle \frac{M_{ij}}{\max_{1\leq k\leq n} R_k} \right\rangle \right\rangle \tag{3.3}$$

where n is the number of clusters, M is the distance between clusters (discussed above), and R_k is the maximum distance within a cluster based on all pair-wise comparisons. Higher Dunn indicies meant better clustering. Using the maximum pair-wise measure of cluster dispersion put a higher weight on cluster compactness in the Dunn measure compared to DB index above. We report a comparison between metrics and a detailed shape analysis of all the high scoring clusters.

3.4 Results of P-V loop shape analysis

The atrial P-V loop simulator successfully converged for each modeled disease (15 total loops). Simulated changes in ejection fraction, stroke work, systemic pressure, and regurgitant fraction were all confirmed to match specified targets (mild, moderate, and severe cases).

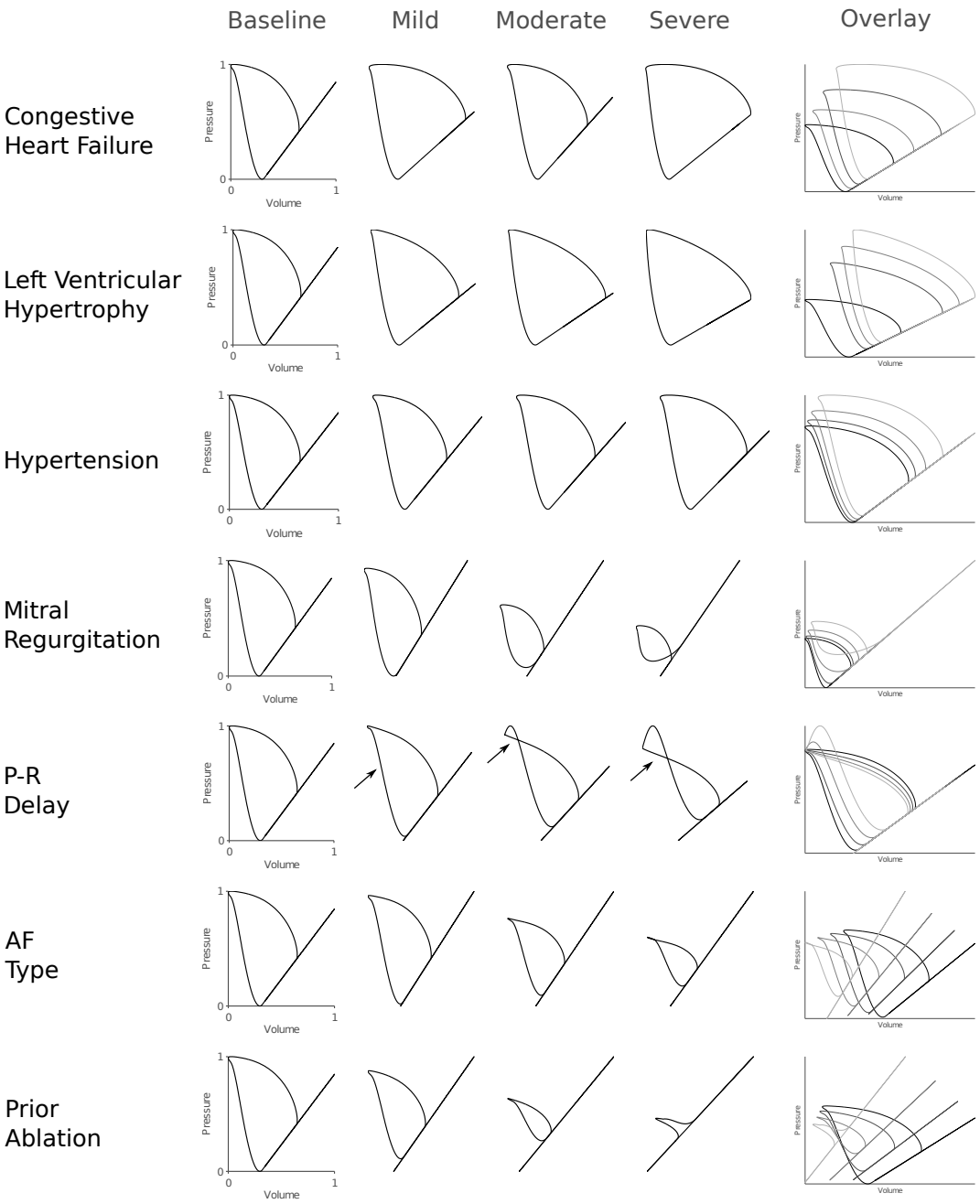

Figure 3.1: Atrial pressure-volume loops of simulated disease states. Three levels of severity (mild, moderate, severe) were simulated for five AF-related diseases and two AF-related factors: 1) Congestive heart failure, 2) left ventricular hypertrophy, 3) systemic hypertension, 4) mitral valve regurgitation, 5) poor conduction, 6) AF type, 7) prior ablation. Each loop was normalized to a (0,1) scale in both pressure and volume. We included an overlay of all levels without normalization.

3.4.1 Simulated P-V loop shapes

Diseases affecting A-V conduction and mitral regurgitation had the largest effect on P-V loop shape based on hydraulic circuit simulations (Fig. 3.1). Changes in A-V conduction pushed the active phases of atrial elastance into ventricular systole, so that the atrium contracted against a closed mitral valve. This resulted in increased pressures in the "relaxation" portion of the atrial P-V loop (the bottom left portion of the loop between minimum volume and minimum pressure, highlighted with an arrow in Fig. 3.1). We noted that at moderate and severe dysfunction, this created an inverted portion of the active loop, with negative stroke work (P-R Delay, Severe case, upper left portion). In contrast, introducing mitral regurgitation extended the passive filling and emptying phases of the atrium. As expected, additional blood volume accumulated during atrial filling which then quickly emptied into the ventricle during early diastole. The passive portion of the curve became much larger compared to the active loop, though the shape of the active loop remained relatively unchanged.

Simulated congestive heart failure and left ventricular hypertrophy (modifications of ventricular elastance) had similar effects to one another – they limited passive filling and emptying and pushed the atrium to rely more on active contraction. Changes in systemic blood pressure (hypertension) did not change the relative shape of atrial P-V loops, except for a slight increase in the active loop compared to the passive curve (only noticeable at severe levels). Changes in ventricular properties (elastance, afterload) made atrial loops more active, while changes in valve resistance and A-V timing made the loops more passive (active loop was relatively smaller in those shapes).

Simulated stiffening of atrial tissue due to progression of AF and prior ablation had similar effects to one another – they increased filling pressures and decreased active work. Simulated ablation had a larger effect because it stiffened the atrium and removed some contractility. As expected, changes in AF factors (AF type, ablation) via changes in atrial elastance exerted strong influence on the shape and size of loops. In general, changes to ventricular elastance (CHF, LVH) made atrial P-V loops more active, while changes in atrial elastance (AF type,

prior ablation) made atrial loops less active. The effects from AF type and ablation were larger than changes due to A-V timing and mitral valve regurgitation.

3.4.2 Clinical P-V loop shapes

Clinical P-V loops were sorted in a heirarchical tree based on similarity of shape (Fig. 3.2). Individual patients loops were displayed at the base of the tree with their links displayed above them. The proximity of the link to the bottom of the tree represented the degree of similarity between the linked shapes. At each linking point, an average loop was calculated from the loops below it. Using a set threshold at 0.40, we identified six ($n = 6$) clusters (colored portions of the tree). The six clusters contained 4, 2, 3, 6, 6, and 19 loops, respectively (3 loops fell outside any cluster). We found 5 clinical factors that stood out in the 5 smaller loop clusters: 1) atrial flutter, 2) persistent AF, 3) congestive HF, 4) WPW syndrome, 5) an AF duration greater than 5 years. These factors were paired to each cluster based on their relative prominence within the grouping. Interestingly, the tree itself revealed some key patterns. Loops identified as atrial flutter had a unique shape that distinguished them from all other groupings, even cases of persistent AF and congestive heart failure. Likewise, dominating factors of persistent AF and congestive heart failure severely distorted loop shapes compared to paroxysmal AF cases. The three larger clusters (WPW syndrome, AF duration $>$ 5yr, Remainder) were more similar to each other than to the flutter, CHF, and persistent AF groups.

We tested each of the five factors using a binary classification test. The dendrogram did the best sorting for WPW syndrome – 4 of the 6 clustered loops had WPW and no WPW cases were outside the cluster (100% sensitivity, 95% specificity, 0.82 FM index). This was followed by congestive heart failure, where 2 of the 2 clustered loops had CHF and one CHF case was outside the cluster, 0.5 FM index). The other groupings were atrial flutter (0.57), persistent AF (0.44), and duration of AF greater than 5 years (0.35). Only WPW syndrome had both a specificity and sensitivity above 50%. This is a surprising result given the location

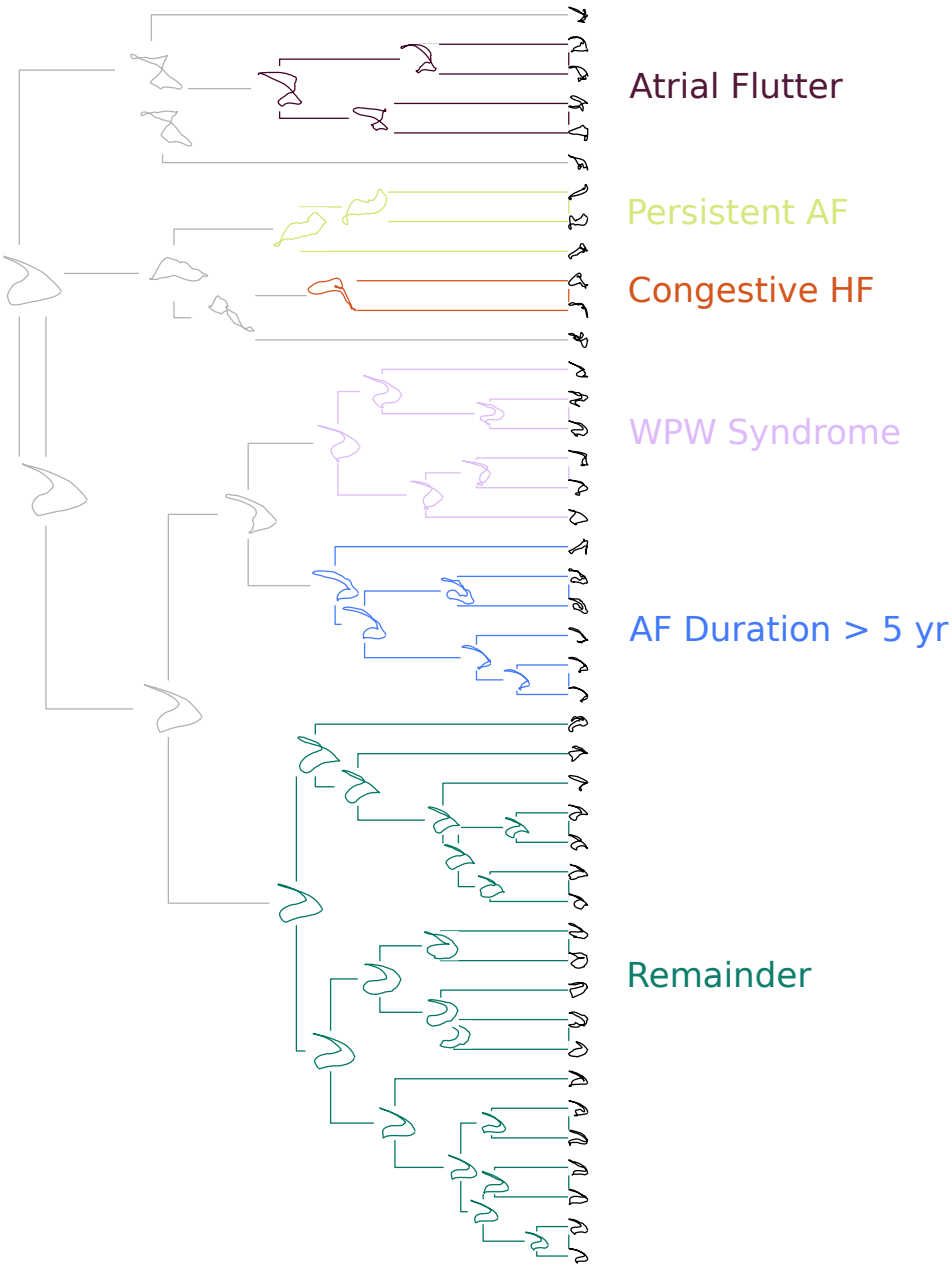

Figure 3.2: Atrial P-V Loop dendrogram. Individual subject loops pictured in black aligned along base of tree, $n = 43$. Dendrogram tree linked loops based on similarity, with more similar loops linked closer to the base. Each link is overlayed with an average of the linked loops. Tree branches meet at the top with a single average loop. A clustering threshold was set at 50% of the tree height and identified six clusters. Each is labeled (colored) with the most common disease pathology within the cluster.

of the WPW cluster within the overall tree, which was not as separated as the atrial flutter cluster. We can conclude that WPW subjects, while otherwise healthy, had P-V loops that were altered in small but highly distinguishing ways.

3.4.3 Factors as clusters

We tested the value of individual clinical factors in identifying groups of similar shapes. The two quality measures (D-B, Dunn Index) had a strong correlation with each other (Fig. 3.3). Based on quality measures (D-B, Dunn index), we found that congestive heart failure, left ventricular hypertrophy, diabetes, prior ablation, and atrial flutter offered the strongest clustering capabilities. In contrast, demographic factors (age, height, weight, gender) and ECG measures (P-wave duration, P-R interval) had minimal clustering capability. The strongest factor (CHF) had almost double the clustering index of the weakest (Age). We selected subset of strong clinical factors and studied their group averages: CHF, LVH, prior ablation, AF type, flutter, and mitral regurgitation.

We calculated the average loops within each group for the six chosen factors (Fig. 3.4). Both CHF and LVH compared well with simulated results (Fig. 3.1) – the diseased loops (Class I+, hypertrophic) had larger active phases and decreased passive emptying compared to the negative controls. The active phases were not as clearly defined in the hypertrophic or CHF Class I+ loops (note wavy lines in the active loop), indicating that individual loops were more variable with less clearly defined passive and active phases. Mitral valve regurgitation showed very minor differences in clinical loops in contrast to the dramatic changes in simulated loops. Moderate to severe MR had no discernible patterns in the average loop, attributable to a smaller sample size and a multitude of comorbidities. Larger sample sizes of more severe MR cases might help elucidate a trend in shape change due to mitral valve disease.

Interestingly, ECG characteristics had little clustering capability, even though our simulation highlighted changes in the active loop due to A-V signal disruption. Hypertension had poor clustering capability, using either diagnosed hypertension or the number of hypertension

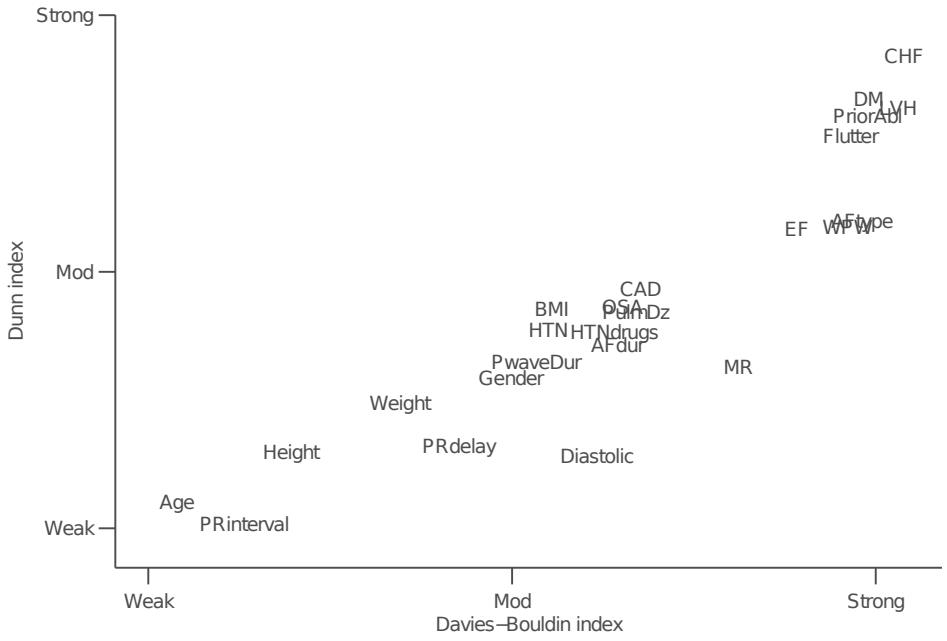

Figure 3.3: Results of factor-based clustering based on two measures of cluster quality - the Davies-Bouldin Index and Dunn Index. Lower D-B indices and higher Dunn indicies represent stronger clusters. There was a strong linear correlation between the two measures. CHF, LVH, diabetes, prior ablation, and flutter all displayed strong clustering capability (upper left portion of graph).

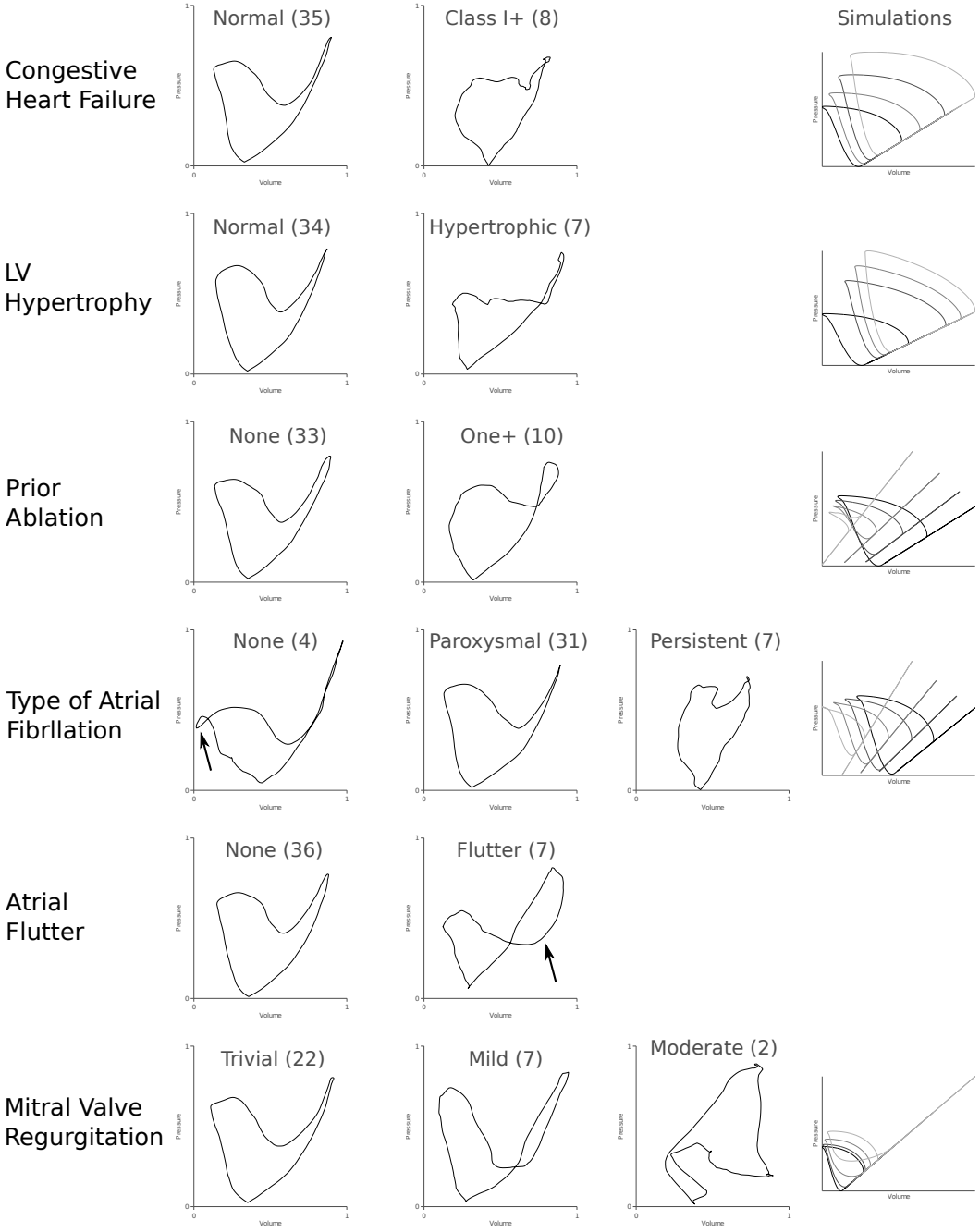

Figure 3.4: Group averages for factors with strong clustering. Six factors were chosen with high clustering capability and their average loops were calculated. Normal or baseline loops are listed in the left most column, followed by disease stages on the right (number of loops in each category listed in parentheses). Simulation results, if available, were added for reference (far right).

drugs. This matched simulated results, which measured only small changes in P-V loop shape due to elevated systemic pressure.

If a patient had any prior ablations, their loops tended to have less passive emptying and a rise in active contraction. We suspect this pattern corresponded to a worsening of symptoms due to AF recurrence, since a similar effect was seen in LVH, CHF, and persistent AF. The type of atrial fibrillation (WPW, Paroxysmal AF, Persistent AF) showed a clear decrease in passive emptying and a relative increase in the size of the active loop as AF progressed. Persistent AF, like moderate MR, was accompanied by a series of comorbidities that disrupted the average shape. Simulation results could not capture the increased reliance on active contraction and tended to overestimate the decrease in active stroke work area. The factors that change during AF and following ablation will be explored in greater detail in later chapters.

Certain factors could not be easily simulated with the hydraulic circuit but displayed strong clustering and had interesting patterns in group averages. Atrial flutter was a significant classifier and created a "bow-tie" pattern while non-flutter loops following a single passive curve. We noted earlier that WPW patients may have had a distinguishing characteristic to accurately group their loops. Using the group average here, we observed a rise in pressure in the later part of the active loop (Fig. 3.4, AF Type - None, arrow).

3.5 P-V shape as a marker of global mechanics

The shape of atrial pressure-volume loops varied significantly between patients with AF, and those differences arose in part from characteristics of AF and its comorbidities. We identified specific patterns in shapes and identified clinical factors that explained some of those differences. We measured the relative influence of each factor on loop shape and studied how loops change with severity of each co-morbidity. Atrial P-V loops offered a clinical window into the progression of AF and the influence of many clinical factors on global mechanics.

We compared the two methods of clustering (shape and factor) for any common threads. There were three common factors: congestive heart failure, type of AF, and atrial flutter. All three had strong clustering capabilities as a single factor and all three arose as distinguishing features in shape-based clustering. We concluded that these three components of the clinical history were the largest clinical contributors to variations in P-V shape.

Congestive heart failure had the most significant influence on atrial P-V loop shape. In a majority of subjects with CHF (5 of 8), the loop was severely distorted with no identifiable passive emptying and elevated pressure during active emptying. We found a common pattern in the active emptying portion of the clinical loops – active pressures and volumes decreased simultaneously and created a more "rounded" loop, instead of the typical pointed pattern. This effect was also visible in the averaged loops (Fig. 3.4, CHF, Class I+). Subjects with CHF had a host of other factors present: half had moderate to severe MR, half had a prior ablation, and 5 of 8 had AF for at least a year. Alone, these factors can change loop shape. In combination, they significantly altered loops away from the average. There were no common patterns within these distortions, and we suspect that CHF clustering removed the "outlier" loops from the primary cluster of normal loops giving it a strong clustering value. A previous study of atrial P-V loops in advanced heart failure patients also observed a rounded active loop in CHF subjects that was not present in control loops (Stefanadis et al., 1998).

The type of atrial fibrillation (paroxysmal, persistent, non-AF) carried a significant influence over atrial shape. We found that non-AF shapes (WPW subjects) were especially tightly clustered. Persistent AF shapes showed more variability within the group, likely due to the increased presence of comorbidities (4 of 7 had diagnosed hypertension). We suspected that the type of AF corresponded to a build-up of fibrosis and increased stiffness. This confirmed the Chapter 2 result that changes in global mechanics were highly sensitive to changes in atrial elastance. Likewise, having a prior ablation was a strong clustering factor – possibly due to a change in $E_{la,max}$ from lost atrial muscle. We found a trend among clinical factors that altered atrial and ventricular elastance (either passive or active) also altered

shape (CHF, LVH, AF type, prior ablation), matching our model's sensitivity to chamber elastances.

With the various types of arrhythmias, Wolff-Parkinson-White patients were especially tightly clustered. Every pair-wise distance within the WPW group was lower (0.35-0.55) than the average pair-wise distance (0.56). Although otherwise healthy (1 case of hypertension, 1 of pulmonary disease), these loops had an altered shape that set them apart from the AF cases. We identified a clear pattern during active recovery (the phase of the active loop between minimum volume and minimum pressure), which tended be "indented" towards a higher pressure in WPW loops. This was present in all 4 loops, so much so in 2 loops that an inverted area formed (visible in the average loop in Fig. 3.4). Interestingly, this matched the pattern of our simulated shortening in P-R delay. It is possible that the LV contracted early than expected through the accessory pathway, creating the same pattern observed *in silico* when we shortened the delay between atrial and ventricular contraction. We searched the literature for any study of atrial P-V loops in WPW subjects, but found only one reference with a single patient (Nagano et al., 1989).

Atrial flutter was also a strong clustering factor, especially in the shape dendrogram. The atrial flutter cluster was clearly separated from all other sub-groups, demonstrating the uniqueness of its shape. The averaged flutter loop had a "bow-tie" pattern while non-flutter loops followed a single passive curve. This bow-tie pattern resembled atrial canine loops observed by other groups (Hoit et al., 1998; Pagel et al., 2003) and had a negative "V-loop" area discussed in Chapter 2. When tested, 7 of 7 (100%) of atrial flutter loops also had a negative V-loop area. From a literature search, most clinical P-V studies of atrial function excluded all patients with atrial flutter, making an external comparison difficult. The origin of this shape and its association with flutter are unknown, but may be influenced by the type of flutter (2 to 1, 3 to 1, 4 to 1). These differences could be tested with a more advanced hydraulic circuit simulator.

Atrial P-V loops revealed changes in global atrial function due to AF and its comorbidities,

confirming our hypothesis. Knowing that function changes in AF patients, we wondered if these changes were spatially homogeneous (same in all regions) or heterogeneous (varied between regions). We addressed this question in the subsequent chapters by measuring global *and* regional function in healthy subjects and AF patients.

References

W. Anne, R. Willems, T. Roskams, P. Sergeant, P. Herijgers, P. Holemans, H. Ector, and H. Heidbuchel. Matrix metalloproteinases and atrial remodeling in patients with mitral valve disease and atrial fibrillation. *Cardiovasc Res*, 67(4):655–666, Sept. 2005.

E. J. Benjamin, D. Levy, S. M. Vaziri, R. B. D'Agostino, A. J. Belanger, and P. A. Wolf. Independent risk factors for atrial fibrillation in a population-based cohort: The framingham heart study. *JAMA*, 271(11):840–844, Mar. 1994.

D. L. Davies and D. W. Bouldin. A cluster separation measure. *IEEE Transactions on Pattern Analysis and Machine Intelligence*, PAMI-1(2):224–227, 1979.

A. M. De Jong, A. H. Maass, S. U. Oberdorf-Maass, D. J. Van Veldhuisen, W. H. Van Gilst, and I. C. Van Gelder. Mechanisms of atrial structural changes caused by stretch occurring before and during early atrial fibrillation. *Cardiovasc Res*, 89(4):754–765, Mar. 2011.

T. H. Everett, E. E. Wilson, S. Verheule, J. M. Guerra, S. Foreman, and J. E. Olgin. Structural atrial remodeling alters the substrate and spatiotemporal organization of atrial fibrillation: a comparison in canine models of structural and electrical atrial remodeling. *Am J Physiol Heart Circ Physiol*, 291(6):H2911–2923, Dec. 2006.

E. B. Fowlkes and C. L. Mallows. A method for comparing two hierarchical clusterings. *Journal of the American Statistical Association*, 78(383):553–569, Sept. 1983.

L. Frost. Lone atrial fibrillation good, bad, or ugly? *Circulation*, 115(24):3040–3041, June 2007.

V. Fuster, L. E. Ryden, D. S. Cannom, H. J. Crijns, A. B. Curtis, K. A. Ellenbogen, J. L. Halperin, J.-Y. Le Heuzey, G. N. Kay, J. E. Lowe, S. B. Olsson, E. N. Prystowsky, J. L. Tamargo, and S. Wann. ACC/AHA/ESC 2006 guidelines for the management of patients with atrial fibrillation: A report of the american college of Cardiology/American

heart association task force on practice guidelines and the european society of cardiology committee for practice guidelines (writing committee to revise the 2001 guidelines for the management of patients with atrial fibrillation): Developed in collaboration with the european heart rhythm association and the heart rhythm society. *Circulation*, 114(7): e257–354, Aug. 2006.

A. S. Gami, D. O. Hodge, R. M. Herges, E. J. Olson, J. Nykodym, T. Kara, and V. K. Somers. Obstructive sleep apnea, obesity, and the risk of incident atrial fibrillation. *J Am Coll Cardiol*, 49(5):565–571, Feb. 2007.

R. Gaspo, R. F. Bosch, M. Talajic, and S. Nattel. Functional mechanisms underlying tachycardia-induced sustained atrial fibrillation in a chronic dog model. *Circulation*, 96 (11):4027–4035, Dec. 1997.

B. D. Hoit, Y. Shao, and M. Gabel. Left atrial systolic and diastolic function accompanying chronic rapid pacing-induced atrial failure. *Am J Physiol Heart Circ Physiol*, 275(1): H183–189, July 1998.

F. Holmqvist, P. G. Platonov, J. Carlson, W. Zareba, and A. J. Moss. Altered interatrial conduction detected in MADIT II patients bound to develop atrial fibrillation. *Ann Noninvasive Electrocardiol*, 14(3):268–275, July 2009.

D. J.C. Well-separated clusters and optimal fuzzy partitions. *Journal of Cybernetics*, 4(1): 95–104, 1974.

R. Kanagala, N. S. Murali, P. A. Friedman, N. M. Ammash, B. J. Gersh, K. V. Ballman, A. S. M. Shamsuzzaman, and V. K. Somers. Obstructive sleep apnea and the recurrence of atrial fibrillation. *Circulation*, 107(20):2589–2594, May 2003.

P. M. Kistler, P. SANDERS, M. Dodic, S. J. Spence, C. S. Samuel, C. Zhao, J. A. Charles, G. A. Edwards, and J. M. Kalman. Atrial electrical and structural abnormalities in an

ovine model of chronic blood pressure elevation after prenatal corticosteroid exposure: implications for development of atrial fibrillation. *Eur Heart J*, 27(24):3045–3056, Dec. 2006.

D. H. Lau, L. Mackenzie, D. J. Kelly, P. J. Psaltis, A. G. Brooks, M. Worthington, A. Rajendram, D. R. Kelly, Y. Zhang, P. Kuklik, A. J. Nelson, C. X. Wong, S. G. Worthley, M. Rao, R. J. Faull, J. Edwards, D. A. Saint, and P. Sanders. Hypertension and atrial fibrillation: Evidence of progressive atrial remodeling with electrostructural correlate in a conscious chronically instrumented ovine model. *Heart Rhythm*, 7(9):1282–1290, Sept. 2010.

D. Li, S. Fareh, T. K. Leung, and S. Nattel. Promotion of atrial fibrillation by heart failure in dogs : Atrial remodeling of a different sort. *Circulation*, 100(1):87–95, July 1999.

C.-h. Liao, H. Akazawa, M. Tamagawa, K. Ito, N. Yasuda, Y. Kudo, R. Yamamoto, Y. Ozasa, M. Fujimoto, P. Wang, H. Nakauchi, H. Nakaya, and I. Komuro. Cardiac mast cells cause atrial fibrillation through PDGF-A-mediated fibrosis in pressure-overloaded mouse hearts. *J Clin Invest*, 120(1):242–253, Jan. 2010.

J. W. Magnani, V. M. Johnson, L. M. Sullivan, E. Z. Gorodeski, R. B. Schnabel, S. A. Lubitz, D. Levy, P. T. Ellinor, and E. J. Benjamin. P wave duration and risk of longitudinal atrial fibrillation in persons 60 years old (from the framingham heart study). *Am. J. Cardiol.*, 107(6):917–921.e1, Mar. 2011.

J. McMichael. History of atrial fibrillation 1628-1819 harvey - de senac - lannec. *Br Heart J*, 48(3):193–197, Sept. 1982.

T. Nagano, M. Arakawa, T. Tanaka, M. Yamaguchi, T. Takaya, T. Noda, H. Miwa, K. Kagawa, and S. Hirakawa. Diastolic compliance of the left atrium in man: a determinant of preload of the left ventricle. *Heart Vessels*, 5(1):25–32, 1989.

P. S. Pagel, F. Kehl, M. Gare, D. A. Hettrick, J. R. Kersten, and D. C. Warltier. Mechanical function of the left atrium: new insights based on analysis of pressure-volume relations and doppler echocardiography. *Anesthesiology*, 98(4):975–994, Apr. 2003.

M. Shimano, Y. Tsuji, Y. Inden, K. Kitamura, T. Uchikawa, S. Harata, S. Nattel, and T. Murohara. Pioglitazone, a peroxisome proliferator-activated receptor-gamma activator, attenuates atrial fibrosis and atrial fibrillation promotion in rabbits with congestive heart failure. *Heart Rhythm*, 5(3):451–459, Mar. 2008.

J. S. Shinbane, M. A. Wood, D. Jensen, K. A. Ellenbogen, A. P. Fitzpatrick, and M. M. Scheinman. Tachycardia-induced cardiomyopathy: A review of animal models and clinical studies. *J Am Coll Cardiol*, 29(4):709–715, Mar. 1997.

A. Srivastava, E. Klassen, S. Joshi, and I. Jermyn. Shape analysis of elastic curves in euclidean spaces. *IEEE Transactions on Pattern Analysis and Machine Intelligence*, 33(7):1415–1428, 2011.

C. Stefanadis, J. Dernellis, S. Lambrou, and P. Toutouzas. Left atrial energy in normal subjects, in patients with symptomatic mitral stenosis, and in patients with advanced heart failure. *The American Journal of Cardiology*, 82(10):1220–1223, Nov. 1998.

K. U. Thiedemann and V. J. Ferrans. Left atrial ultrastructure in mitral valvular disease. *Am J Pathol*, 89(3):575–604, Dec. 1977.

S. Verheule, E. Wilson, T. Everett, S. Shanbhag, C. Golden, and J. Olgin. Alterations in atrial electrophysiology and tissue structure in a canine model of chronic atrial dilatation due to mitral regurgitation. *Circulation*, 107(20):2615–2622, May 2003.

T. J. Wang, M. G. Larson, D. Levy, R. S. Vasan, E. P. Leip, P. A. Wolf, R. B. DAgostino, J. M. Murabito, W. B. Kannel, and E. J. Benjamin. Temporal relations of atrial fibrillation and congestive heart failure and their joint influence on mortality the framingham heart study. *Circulation*, 107(23):2920–2925, June 2003.

M. C. Wijffels, C. J. Kirchhof, R. Dorland, and M. A. Allessie. Atrial fibrillation begets atrial fibrillation : A study in awake chronically instrumented goats. *Circulation*, 92(7): 1954–1968, Oct. 1995.

Chapter 4

Surface fitting to geometric data

Surface fitting is a method to describe relationships in sparse data using parametric functions. For geometric data, surface fitting estimates the boundary of an object based on a sparse sampling of its location. We use surface fitting to assess cardiac function by estimating the location of the heart wall throughout the cardiac cycle, and we apply this technique to measure left atrial wall motion in animals and people. Although the term *surface* refers to a geometric boundary in our work, the techniques advanced here can be applied to many types of multi-dimensional data. In this chapter, we create the mathematical framework of a surface by parameterizing a continuous function. We then generate methods to optimize the surface to a data set by changing its parameters, working to minimize the error between it and the sampled data. This optimization process is commonly referred to as *fitting*, and thus, we refer to the general method as *surface fitting*.

4.1 Background of surface fitting

A surface is simply a multi-dimensional curve, and surface fitting uses many of the same techniques as classical curve fitting. The principle of ordinary least squares (the most basic form of curve fitting) was first developed by Gauss and others in the early 19^{th} century (Gauss, 1857), and expanded by Karl Pearson in the early 20^{th} century (Pearson, 1902a,b). Curve

fitting to geometric objects took hold in the 1960s when two car company employees (Pierre Bézier at Renault and Paul de Casteljau at Citroën) created functions to model automobile shapes in computer-aided design (Bezier, 1971). They adapted Berstein polynomials to create Bézier curves, piece-wise functions that became a cornerstone in computer graphics and vision. These and other functions were quickly adapted to physiologic structures (including the heart) as medical imaging became available. Fitting cardiac shapes and motions arose in the 1970s (Chaitman et al., 1973; Geiser et al., 1980; Strauss et al., 1971) and evolved into more advanced surface fitting techniques alongside 3-D and 4-D imaging capabilities (Duncan and Ayache, 2000).

Bézier curves provided a compact form for smooth deformable surfaces. Young and colleagues (Young et al., 1989) used multiple bézier cubics in a finite element scheme to estimate the epicardial surface of the left ventricle. They then replaced the Bézier curve with the similar cubic Hermite polynomial, and applied it to the ventricular endocardium (Nielsen et al., 1991) and ventricular motion (Young et al., 1992). The same group expanded this work to fit strain data from MR tagging experiments (Young et al., 1995, 1994, 1996) and implanted bead markers (Hashima et al., 1993). The method was later applied to other physiological structures (Bradley et al., 1997; Smith et al., 2000).

Deformable surfaces have found use in all aspects of medical imaging, from segmentation to shape and size estimation, and from 2-D motion to 4-D strain fitting. There are a multitude of ways to define deformable surfaces (Duncan and Ayache, 2000; McInerney and Terzopoulos, 1996; Montagnat et al., 2001), each with advantages specific to an application. We chose to focus on the finite element scheme used by Young and colleagues because of its compact form, simple expansion to multiple dimensions, and proven successes in cardiac applications. This chapter will describe the design of our surface fitting algorithm, along with results for mesh scaling, element density, and speed of convergence. The fitting algorithm will then be used to measure left atrial wall motion in later chapters.

4.2 Principles of surface fitting

We will start with a simple form of fitting to explain some techniques, then expand the method to handle more complex surfaces and multiple dimensions.

4.2.1 A simple example

Imagine a long, thin metal bar. So thin that it can be thought of as a one-dimensional line x. Assume we can measure the temperature of the bar at multiple spots along its length, creating P data points within an interval $x \in [a, b]$. Each data point has a dimensional position x_p and a dimensionless value y_p (the measured temperature). We want to know how the temperature changes across the entire bar based on the points that we measured. A fitting method solves this by creating a function $\hat{y} = f(x)$ that best represents the data using a limited set of parameters. Linear regression, also known as a line of best-fit, is a popular and simple form of this function. It uses two parameters (slope β and axis-intercept α) to create a function

$$\hat{y} = \beta x + \alpha$$

These parameters are chosen via minimization of the summed squared error

$$\sum_{p=1}^{P} (\hat{y}(x_p) - y_p)^2$$

For the thin metal bar, a linear regression would describe temperature as a function of position along the bar.

Although the linear regression function is continuous for any value of x, we are typically interested in fitting over a discrete interval, such as the length of the bar. Given this limit, we can reformulate the function as the sum of two linear functions $f_a(x)$ and $f_b(x)$. Instead of a slope and axis-intercept, the functional parameters are simply points at the interval limits

$y_a = \hat{y}(x_a)$ and $y_b = \hat{y}(x_b)$. These values are scaled by the linear functions

$$f_a(x) = \frac{x-b}{a-b} \qquad f_b(x) = \frac{x-a}{b-a}$$

as

$$\hat{y}(x) = y_a f_a(x) + y_b f_b(x)$$

Instead of formulating the line as a point and a slope, we formulate it as two points connected with a straight line. Although it appears more complicated, this formulation is easily related to the slope-intercept form and contains the same number of free parameters. We use this form because it eases the transition into more complicated problems.

Consider again the metal bar, now heated at its center point c. We expect the temperature to peak in the center and cool towards the ends. The linear function would do a poor job describing this pattern, but two linear functions linked together would fit well. We can create these two linked lines using three points y_a, y_b, y_c, and two pairs of functions describing each connecting line

$$f_a(x) = \frac{x-c}{a-c} \quad f_b(x) = \frac{x-a}{c-a} \quad \text{for} \quad x \in [a, c]$$

and

$$f_c(x) = \frac{x-b}{c-b} \quad f_d(x) = \frac{x-c}{b-c} \quad \text{for} \quad x \in [c, b]$$

The linear fitting function becomes a piece-wise function, where

$$\hat{y}(x) = \begin{cases} y_a f_a(x) + y_c f_b(x) & \text{for} \quad x \in [a, c] \\ y_c f_c(x) + y_b f_d(x) & \text{for} \quad x \in [c, b] \end{cases}$$

We notice that two of the four functions, $f_a(x)$ and $f_c(x)$, share a common form. We can rewrite this pair as one general function $f_0(x) = (x - x_1)/(x_0 - x_1)$. Here x_0 and x_1 are general terms for the bounds of the interval. Similarly, $f_b(x)$ and $f_d(x)$ can be rewritten as

$f_1(x) = (x - x_0)/(x_1 - x_0)$. Now,

$$\hat{y}(x) = y_0 f_0(x) + y_1 f_1(x)$$

where $y_0 = \hat{y}(x_0)$ and $y_1 = \hat{y}(x_1)$. This formulation can be expanded to many intervals, creating a piece-wise function that captures complex, nonlinear patterns with linear functions.

The metal bar example describes the simplest form of a surface, also known as a *mesh*. We parameterize a mesh by dividing it into units, called *elements*, and linking them with common points, called *nodes*. In the metal bar example, the points (x_0, y_0) and (x_1, y_1) are the nodes, and the space between them $x \in [x_0, x_1]$ is the element. The nodal values y_0 and y_1 are the free parameters, and they are chosen to minimize the error between the surface and the data, just like in linear regression. The functions f_0 and f_1 interpret values $\hat{y}$ between nodes, and are commonly referred to as *basis*, *weighting*, *shape*, or *interpolating* functions. The details of surface fitting, including basis functions, mesh design, interpolation, data projection, and optimization, will now be discussed.

4.2.2 Basis functions

Basis functions interpolate values within an element based on values at the bordering nodes. The functions are independent of mesh density and provide a simple framework to create and fit complex surfaces. This inherent flexibility is a core piece of the surface fitting method. In the 1-D bar example in §4.2.1, functions f_0 and f_1 are the basis functions. Because basis functions interpolate values at a relative position in an element, we use an element coordinate ξ to describe this relative location. The ξ coordinate is often referred to as the element domain or local domain, and has no meaning outside the bounds of the element. In contrast, the physical domain x, representing a spot on our metal bar, is often referred to as the global domain or spatial domain.

To give a physical meaning to the element domain, we create a map between ξ and x. For a 1-D linear element, the map is

$$\xi(x) = \frac{x - x_0}{x_1 - x_0} \quad x \in [x_0, x_1] \tag{4.1}$$

and

$$x(\xi) = x_0 + (x_1 - x_0)\xi \quad \xi \in [0, 1] \tag{4.2}$$

We can rewrite the basis functions in terms of element position as $f_0(\xi) = 1 - \xi$ and $f_1(\xi) = \xi$ with $\hat{y}(\xi) = y_0 f_0(\xi) + y_1 f_1(\xi)$. This formulation highlights the idea of basis functions as weighting functions. At $\xi = 0$, $f_0 = 1$ and $f_1 = 0$, weighting the interpolation to only one node, y_0. As ξ increases, the weighting shifts until $f_1 = 1$ at $\xi = 1$. These basis functions are the simplest form of a *Langrangian* basis, one of the most commonly used in surface interpolation. We now realize that the mapping between x and ξ is already formulated as a first degree Langrangian basis, where $x(\xi) = f_0(\xi)x_0 + f_1(\xi)x_1$. We will now explore additional forms of basis functions for the interpolated values $\hat{y}$.

Lagrangian basis functions can be made nonlinear by adding nodes *within* an element. For instance, a third node in an element provides a third degree of freedom and creates a quadratic set of basis functions. Now,

$$\hat{y}(\xi) = y_0 f_0(\xi) + y_1 f_1(\xi) + y_2 f_2(\xi)$$

and $f_i(\xi)$ are the Lagrange polynomials. Just like the linear example, each of the nodal values is optimized against a data set to create a quadratic *curve* of best fit. Any number of nodes can be added to create higher degree functions. The generalized Lagrangian basis functions L_i are polynomials of degree m that rely on $m + 1$ nodes to interpolate an element. They can be summarized as

$$\mathrm{L}_i(\xi) = \prod_{\substack{j=0 \\ j \neq i}}^{m} \frac{\xi - \xi_j}{\xi_i - \xi_j} \tag{4.3}$$

and incorporated into the overall interpolation as

$$\hat{y}(\xi) = \sum_{i=0}^{m} y_i \mathrm{L}_i(\xi) \tag{4.4}$$

The nodal positions are typically set as equally spaced points across the interval of the element, where $\xi_i = i/m$. Internal nodes can be re-positioned, but bordering nodes must be at an element edge to assure continuity with adjoining elements.

Lagrangian basis functions provide continuity at element edges, meaning that values across elements are linked together via common nodes. When multiple Lagrangian elements are linked, their connection does not need to be smooth. A collection of first degree Lagrangian functions linked together can result in a jagged sawtooth pattern while remaining continuous. This is called C^0 continuity, with 0 referring to the order of derivative maintained across element boundaries. Other forms of basis functions provide increasing amounts of continuity, and will now be explored in detail.

Cubic Hermite basis functions are higher-order functions that use a nodal value and nodal derivative to interpolate an element. By sharing a nodal derivative between elements, Hermite basis functions create a smooth surface with C^1 continuity. A separate basis function is attached to each nodal value and each nodal derivative, where the interpolation function for a 1-D element is

$$\hat{y}(\xi) = \mathrm{H}_0^0(\xi)\, y_0 + \mathrm{H}_0^1(\xi) \left.\frac{\partial y}{\partial \xi}\right|_0 + \mathrm{H}_1^0(\xi)\, y_1 + \mathrm{H}_1^1(\xi) \left.\frac{\partial y}{\partial \xi}\right|_1 \tag{4.5}$$

Each basis function attaches to a node i and a derivative order j as H_i^j. The four cubic Hermite basis functions are

$$\begin{aligned} \mathrm{H}_0^0(\xi) &= 2\xi^3 - 3\xi^2 + 1 \quad & \mathrm{H}_0^1(\xi) &= \xi^3 - 2\xi^2 + \xi \\ \mathrm{H}_1^0(\xi) &= -2\xi^3 + 3\xi^2 \quad & \mathrm{H}_1^1(\xi) &= \xi^3 - \xi^2 \end{aligned} \tag{4.6}$$

A single cubic Hermite element has four degrees of freedom, just like a 3^{rd} degree Lagrangian element.

Unlike the Lagrangian basis functions (Eqn. 4.3), the degree of cubic Hermite functions cannot be changed and internal nodes cannot be added. However, the formulation can be extended to quintic Hermite functions (C^2 continuity) and septic Hermite functions (C^3 continuity). Each extension adds one higher order nodal derivative to the interpolation and additional basis functions. We will focus on cubic Hermite elements because C^1 is adequate for our surface fitting. A challenge for all Hermite formulations is linking elements together, since nodal derivatives are domain dependent. This dependence requires scaling nodal derivatives between ξ and x using scaling factors.

4.2.3 Scaling factors

When we link two cubic Hermite elements, they share a common nodal value y and nodal derivative $\partial y/\partial \xi$. Sharing a common nodal derivative ensures C^1 continuity. However, we must be mindful of the differences between the element domain ξ and the spatial domain x. We want a continuous curve in the spatial domain, but still need to interpolate in the element domain. Thus, the nodal derivatives must be scaled between domains, using *scaling factors*.

Consider two elements $e1$ and $e2$ linked by node n. In each element, there is a relationship between the local derivative and the global derivative, defined by the chain rule as

$$\frac{\partial y}{\partial \xi} = \frac{\partial y}{\partial x}\frac{\partial x}{\partial \xi}$$

Because we use a linear mapping between x and ξ in Eqn. 4.2, the partial derivative $\partial x/\partial \xi$ is constant within an element as $\Delta x = (x_1 - x_0)$. Put simply, the scaling factor S is equal to the physical space occupied by the element e along the x dimension, where $S = \Delta x_e$. For neighboring elements, each has a unique scaling factor based on its size, where $S_{e1} = \Delta x_{e1}$ and $S_{e2} = \Delta x_{e2}$. The spatial derivative $\partial y/\partial x$ is a parameter of the node n, while the local

derivative $\partial y/\partial \xi$ is scaled version based on the element it references (n, e).

$$\left.\frac{\partial y}{\partial \xi}\right|_{(n,e)} = \left.\frac{\partial y}{\partial x}\right|_{n} S_e \tag{4.7}$$

When two nodes are joined, the nodal derivative is shared such that

$$\frac{1}{S_{e1}} \left.\frac{\partial y}{\partial \xi}\right|_{(n,e1)} = \frac{1}{S_{e2}} \left.\frac{\partial y}{\partial \xi}\right|_{(n,e2)}$$

The interpolation function for each element e becomes

$$\hat{y}(\xi) = \mathrm{H}_0^0(\xi)\, y_0 + \mathrm{H}_0^1(\xi) \left.\frac{\partial y}{\partial x}\right|_{0} S + \mathrm{H}_1^0(\xi)\, y_1 + \mathrm{H}_1^1(\xi) \left.\frac{\partial y}{\partial x}\right|_{1} S \tag{4.8}$$

Scaling factors maintain continuity when element spacing varies. Variation in element size can arise by design (placing more elements near areas of high variation) or by transformation (elements spaced equally in one domain may not be equal in another domain). If elements are evenly spaced in x, scaling factors can be omitted without loss of optimality or continuity. However, omitting scaling factors would produce inaccurate spatial derivatives, which are used in calculations of curvature, smoothing, and other derivative-based measurements. Thus, scaling factors should always be implemented, even in cases of evenly spaced elements. This is especially important in multi-dimensional problems, where element spacing might be equal within a dimension, but vary between dimensions.

4.2.4 Mesh design

We design a mesh by choosing its size, the density of its elements, the type of basis functions it uses, and the positions of its nodes in physical space. To set the size, we choose an upper and lower bound in x. In our metal bar example, these bounds would be the endpoints of the bar. We then divide that length into elements based on a chosen density. The divisions can be equally or unequally spaced based on expected variations in the data y. Basis functions

are also chosen based on the expected patterns of variation in y. Nodes are assigned at the division point, where each nodal position x_n is fixed in the x dimension.

To keep track of the element and node data, we use some standard bookkeeping techniques. In the 1-D bar example, let us presume we choose E elements with N nodes, so that $N = E+1$. Each node is assigned a global node index $n \in \{1 \dots N\}$. Similarly, each element is assigned an element index $e \in \{1 \dots E\}$. We build a connectivity matrix Δ to translate between local and global numbering schemes so that $n = \Delta(e, i)$, where $i \in \{0, 1\}$ represents the local node index. All of the nodal parameters, including x_n positions, Y_n values and derivatives, and scaling factors, are summarized into a mesh parameter set $\mathbf{u}$.

We can illustrate the mesh design in more detail by returning to the 1-D bar example. Let's say we create 4 elements with 5 nodes and we use cubic Hermite basis functions H_y to interpolate data values and linear Lagrange basis L_x to interpolate position, where

$$\Delta_{ei} = \begin{bmatrix} 1 & 2 \\ 2 & 3 \\ 3 & 4 \\ 4 & 5 \end{bmatrix} \qquad x_n = \begin{bmatrix} 0 \\ L/6 \\ L/2 \\ 5L/6 \\ L \end{bmatrix} \qquad S_e = \begin{bmatrix} L/6 \\ L/3 \\ L/3 \\ L/6 \end{bmatrix} \qquad Y_n = \begin{bmatrix} y_1 & \frac{\partial y}{\partial x}\big|_1 \\ \vdots & \vdots \end{bmatrix}_{N\mathrm{x}2}$$

and

$$\mathbf{u} = \{\Delta_{ei}, x_n, \mathrm{L}_x, S_e, Y_n, \mathrm{H}_y\}$$

The mesh parameter set can be passed into data projection, optimization, or querying routines to add, change, or recall fitted values.

4.2.5 Data projection

Data points must be allocated in a mesh prior to any fitting procedure. Each point must be assigned to an element, then a position within that element. This is denoted mathematically

as

$$(x, y) \xrightarrow{\mathbf{u}} (e, \xi, y) \tag{4.9}$$

We project data based on its position in the x dimension. The data values y are not modified during projection. Each point is assigned to an element based on its location relative to the nodal positions x_n. The element coordinate ξ designates the relative position of the point in its element based on the mesh $\mathbf{u}$ and the mapping in Eqn. 4.1. Since the nodal positions do not change during the fitting process, projection is done once prior to optimization and does not need to be repeated. More advanced projections along alternative dimensions (for instance, at a normal direction to the fitted curve) require repeated projections during fitting. For bookkeeping, each element has a list of points indexed by d as (ξ_d, y_d). We will refer to individual points as $\xi_{(e,d)}$ or just ξ_d if the element has already been specified.

4.2.6 Optimization

We create an error function based on the distance between the mesh surface and the data in the y dimension at every data point in an element

$$f_e(\mathbf{u}) = \sum_{d=1}^{D_e} \left(\hat{y}\left(\mathbf{u}_e, \xi_d\right) - y_d\right)^2 \tag{4.10}$$

then sum those errors across all the elements in a mesh.

$$F(\mathbf{u}) = \sum_{e=1}^{E} \frac{1}{D_e} f_e \tag{4.11}$$

Here D is a counter of data points allocated to each element. We typically normalize the element error f_e to the number of data points in that element D_e, which creates a more balanced optimization.

Although we added some things, the error function in Eqn. 4.10 is the exact same as the linear regression error described in §4.2.1. We optimize our mesh the same way we would

optimize the line in linear regression, by adjusting nodal parameters to minimize the error between the data and the mesh. Thus, we seek to find a minimum of F based on varying parameters in $\mathbf{u}$. Formally, we state this as

$$\mathbf{u}^* = \arg\min F(\mathbf{u}) \tag{4.12}$$

where $\mathbf{u}^*$ is the optimum mesh. We can find this optimum using any number of standard minimization algorithms. I will provide a few simple examples and then review the preferred method in detail.

4.2.7 Linear optimization

In a simple version similar to linear regression, we can use matrix mathematics to relate the nodal values to the interpolated values at every data point, where

$$\hat{y} = f(\mathbf{u}, x)$$
$$\hat{y} = (\mathbf{H}(x) \circ \mathbf{S})\,\mathbf{u}$$
$$\hat{y} = \mathbf{B}(x)\,\mathbf{u}$$

Basis functions and scaling factors are converted into sparse matrices $\mathbf{H}$ and $\mathbf{S}$ with size (number of data points x number of nodal parameters) or (P x Q), arranged to interpolate data in all elements based on all nodal values. The Hadamard product ($\circ$) of the two matrices is a piece-wise multiplication, written as .* in MATLAB notation. The product $\mathbf{B}$ is a global interpolation matrix. The notation is simplified for clarity, we assume a data mapping step, and we assume that $\mathbf{u}$ contains all nodal parameters (values and derivatives) in an (Q x 1) array. We minimize this function against the data points in y to solve for the optimum nodal

parameters

$$\mathbf{u}^* = \arg\min (\mathbf{B}\,\mathbf{u} - y)^2$$
$$\mathbf{u}^* = (\mathbf{B}^{\mathrm{T}}\mathbf{B})^{-1}\mathbf{B}^{\mathrm{T}}y$$

This mesh can be solved in MATLAB using the \ operator, as in $\mathbf{u}^* = \mathbf{B}\backslash y$. Alternative linear solvers, including MATLAB's symmetric LQ method and LSQR method, use iterative techniques to conserve memory. Choice of solver depends on the size of the problem, memory constraints, desired solution tolerances, and required speed of optimization.

The system of linear equations method works well for simple meshes but becomes unmanageable for complex ones, especially those that use multiple dimensions, global smoothing penalties, or nonlinear constraints. Because we want a flexible system capable of solving complex meshes, we have developed an alternative optimization scheme based on Newton's method.

4.2.8 Newton's method

Newton's method in optimization is a 2^{nd} order technique to find function minimums. It is second order because the method uses the first and second derivative of a function. The formulation is analogous to Newton's method of root finding, but in this case we are searching for the zeros of the *gradient* of the function. For instance, take a convex polynomial function $f(x)$ where x is a continuous one-dimensional variable. If we assume $f(x)$ has a global minimum value at x^*, we know that the slope $f'(x^*) = 0$. We find this point by stepping Δx away from an initial condition x^0, then solving and updating the system. This step is repeated multiple times to reach an optimum solution with quadratic convergence. We estimate each step using a Taylor series expansion of $f(x)$ at x^0, ignoring terms beyond the

second derivative

$$f(x) \approx h(x) = f(x^0) + f'(x^0)(x - x^0) + 1/2 f''(x^0)(x - x^0)^2$$

We then solve for the location of the minimum of $h(x)$ by setting its gradient equal to zero and assuming it occurs at point $x^0 + \Delta x$.

$$h'(x^0 + \Delta x) = 0 = f'(x^0) + f''(x^0)(\Delta x)$$
$$\Delta x = -\frac{f'(x^0)}{f''(x^0)}$$

The new point would be updated as $(x^0 + \Delta x) \rightarrow x^0$ and the process repeated. The key point is that the Taylor series approximation is a quadratic function. Thus, if the overall function $f(x)$ is quadratic, $h(x) = f(x)$ exactly and Newton's method will converge in a single step. This is the case for our error function.

When applying Newton's method to a mesh, we are expanding the optimization to multiple dimensions, since each nodal parameter could be varied independently to lower the error. Here, dimensions refer to the degrees of freedom, not the physical dimensions of the mesh. The method formulation is easily extended to multiple dimensions, where

$$f(\mathbf{x}) \approx h(\mathbf{x}) = f(\mathbf{x}^0) + \nabla f(\mathbf{x}^0)^{\mathrm{T}}(\mathbf{x} - \mathbf{x}^0) + 1/2(\mathbf{x} - \mathbf{x}^0)^{\mathrm{T}}\mathbb{H}f(\mathbf{x}^0)(\mathbf{x} - \mathbf{x}^0) \tag{4.13}$$

Here, the gradient ∇ of a function produces a Qx1 vector, where Q is the total degrees of freedom or dimensionality of the optimization. The Hessian matrix $\mathbb{H}$ is the second derivative of the function, with size QxQ. The variable $\mathbf{x}$ is now a Qx1 vector of variables. We apply the same technique of solving for the minimum of the quadratic approximation, then solving

for the position of that minimum.

$$\nabla h(\mathbf{x} + \mathbf{x}^{\Delta}) = \mathbf{0} = \nabla f(\mathbf{x}^0) + \mathbb{H} f(\mathbf{x}^0)(\mathbf{x}^{\Delta}) \tag{4.14}$$

$$\mathbf{x}^{\Delta} = -(\mathbb{H} f(\mathbf{x}^0))^{-1} \nabla f(\mathbf{x}^0) \tag{4.15}$$

Thus, if the Hessian is positive definite (meaning it can be inverted), this equation is easily solved. Like the simpler example, if the function $f(\mathbf{x})$ is quadratic, a Newton optimization will converge in a single step.

A note on dimensionality. The gradient of the error function F is the change in the error with respect to a change in nodal parameters. Each nodal parameter has a gradient, and all must equal zero to reach a true optimum. This generates a multi-dimensional optimization, where each dimension is a different nodal parameter. It is vital to distinguish between the dimension of the optimization (based on the number of nodal parameters) and the physical dimensions of the mesh. These dimensions are entirely different things and should not be confused. When we calculate the gradient of the error function, it generates an array of size Qx1, where Q is the total number of nodal parameters.

To use Newton's method, we will need to calculate the gradient and Hessian of our error function. We set up the gradient as

$$\nabla F = \frac{\partial F}{\partial u_q} \quad q \in \{1, 2, \ldots, Q\}$$

where u_q is a single element from the parameter array in $\mathbf{u}$.

$$\frac{\partial F}{\partial u_q} = \sum_{e=1}^{E} \frac{1}{D_e} \frac{\partial f_e}{\partial u_q}$$
$$\frac{\partial f_e}{\partial u_q} = 2 \sum_{d=1}^{D_e} (\hat{y}(\mathbf{u}_e, \xi_d) - y_d) \frac{\partial \hat{y}(\mathbf{u}_e, \xi_d)}{\partial u_q}$$
$$\frac{\partial \hat{y}(\mathbf{u}_e, \xi_d)}{\partial u_q} = \mathrm{B}_q(\xi_d) S_e$$

Here we assume that B_q is the basis function (and any necessary scaling factor S_e) for nodal parameter u_q and that $\mathrm{B}_q(\xi_d) \neq 0$ for $q \in \Delta_e$ and zero otherwise. Likewise, the Hessian is calculated as

$$\mathbb{H}F = \nabla(\nabla F)$$
$$\mathbb{H}F_{qr} = \frac{\partial^2 F}{\partial u_q \partial u_r}, \quad (q, r) \in \{1, 2, \ldots, Q\}$$

where

$$\frac{\partial^2 F}{\partial u_q \partial u_r} = \sum_{e=1}^{E} \frac{1}{D_e} \frac{\partial^2 f_e}{\partial u_q \partial u_r}$$
$$\frac{\partial^2 f_e}{\partial u_q \partial u_r} = 2 \sum_{d=1}^{D_e} \frac{\partial^2 \hat{y}(\mathbf{u}_e, \xi_d)}{\partial u_q \partial u_r}$$
$$\frac{\partial^2 \hat{y}(\mathbf{u}_e, \xi_d)}{\partial u_q \partial u_r} = \mathrm{B}_q(\xi_d) S_e \mathrm{B}_r(\xi_d) S_e$$

The goal is then to find $\mathbf{u}^*$ such that

$$\nabla F(\mathbf{u}^*) = \mathbf{0}$$

We apply Newton's method as it is described in Eqn. 4.14. We start with an initial mesh $\mathbf{u}^0$ with nodal parameters u_q^0, then modify that mesh to reach a solution. Each iteration changes

the nodal values by $\mathbf{u}^{\Delta}$ and since the error function is quadratic, the method will converge in a single step, regardless of the initial mesh position.

$$\mathbf{u}^{*} = \mathbf{u}^{0} - (\mathbb{H}F(\mathbf{u}^{0}))^{-1}\nabla F(\mathbf{u}^{0}) \tag{4.16}$$

There are some instances when the mesh would not converge in a single step (adaptive mesh, re-projection, node modification). If multiple steps are required, the optimization is repeated with the new mesh reassigned as $\mathbf{u}^{0} + \mathbf{u}^{\Delta} = \mathbf{u}^{1} \rightarrow \mathbf{u}^{0}$. Using a Newton optimization and a quadratic error function will always result in an exact solution.

With very dense meshes, the Hessian inversion requires too much memory. With some basis functions, the true Hessian cannot be calculated. In these cases, a *quasi-Newton* method can be used to solve the optimization. A quasi-Newton method approximates the Hessian matrix while never explicitly calculating it. There are many quasi-Newton techniques, but a popular form is the Broyden-Fletcher-Goldfard-Shanno (BGFS) method. Generally, the BGFS method approximates the Hessian by using the change in gradients between two iteration points. It is considered a generalization of the secant method for root finding. We do not focus on quasi-Newton methods here, but do use them as a reference for the Newton method, confirming our optimized mesh and comparing computation times. In cases where a quasi-Newton method is used, the mesh converges until a stopping criteria is met. We set a stopping tolerance for the gradient of the error function as

$$\|\nabla F(\mathbf{u}^{*})\|_{\infty} < \text{Tolerance} \tag{4.17}$$

This formula is called the infinity norm or uniform norm, which is a fancy way of stating the maximum magnitude of all the elements in the gradient array. Thus, the gradient in every direction has to be less than the tolerance to stop the algorithm. This step is not required for Newton's method.

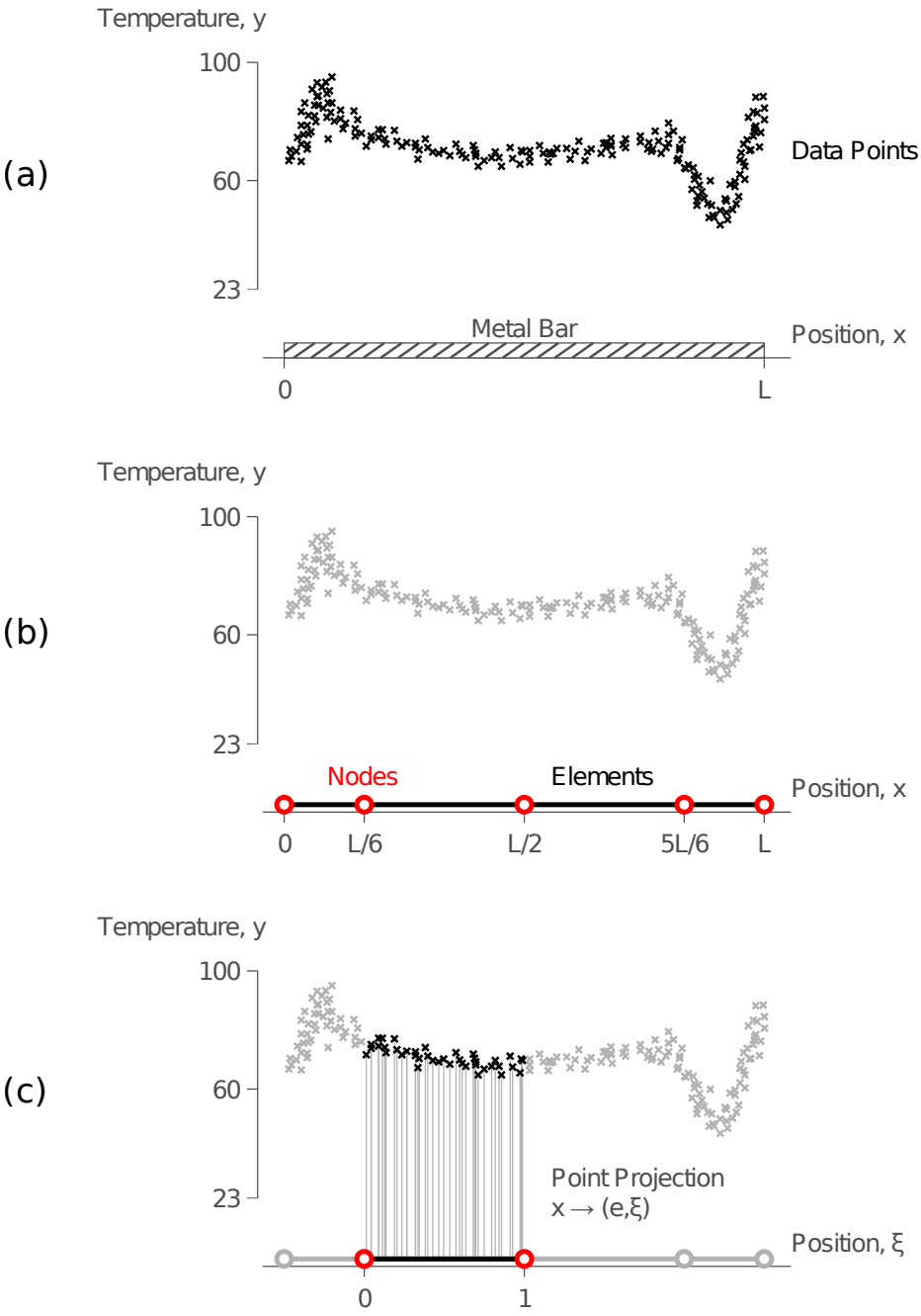

Figure 4.1: A one-dimensional surface to fit the temperature in a metal bar. (a) Temperature data is simulated at random points along a 1-D metal bar. (b) The metal bar is divided into four elements bounded by five shared nodes. (c) Data point position is projected into the element domain, so that each point is assigned to an element e and a relative position ξ within that element.

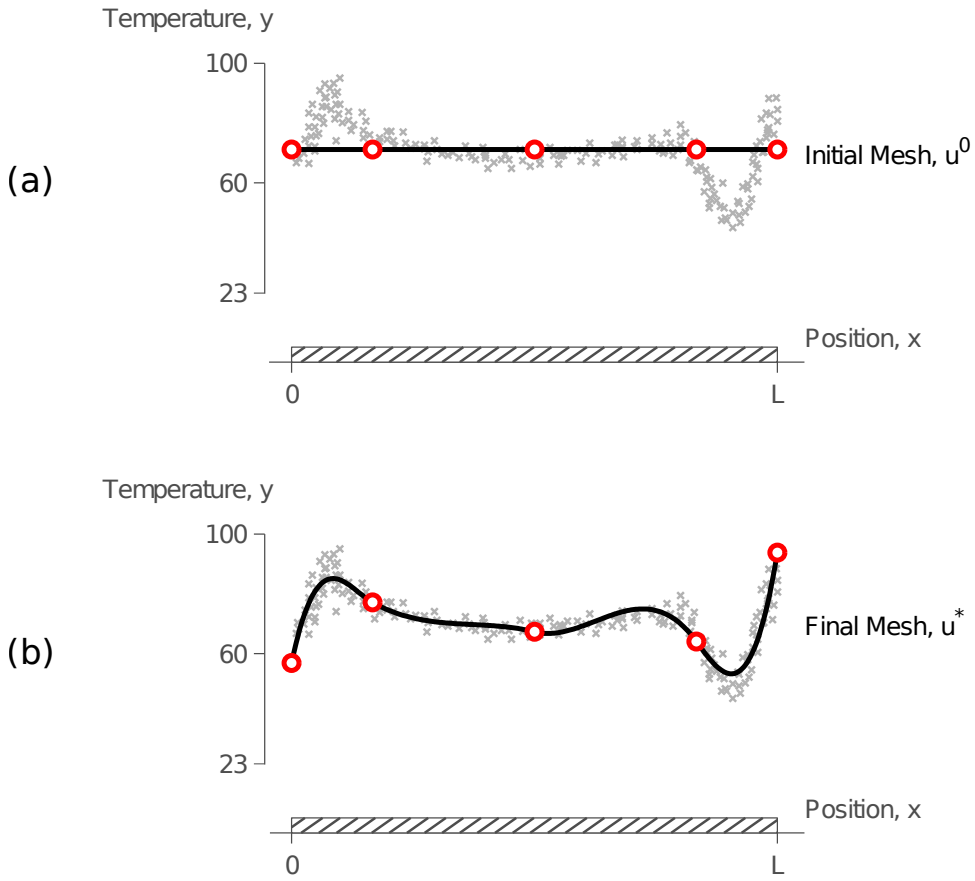

Figure 4.2: A one-dimensional surface fitted to the temperature in a metal bar. (a) An initial mesh is set to the mean of the temperature data, and nodal slopes are set equal to zero. (b) The optimized mesh fits the temperature data will a small amount of error. Scaling factors ensure smooth continuity between elements.

4.2.9 A simple example, solved

For illustration, we simulated the 1-D metal bar problem in §4.2.1 by sampling a polynomial function $p(x)$ and adding random noise to produce a set of (x_p, y_p) points (Fig. 4.1a). The data points were distributed uniformly through the length of the bar $x \in [0, L]$. We created a 1-D mesh following the design in §4.2.4, including unequal node positions and cubic Hermite basis functions with active scaling factors (Fig. 4.1b). Data points were projected from the spatial domain into the element domain (Fig. 4.1c). We set the initial mesh $\mathbf{u}^0$ equal to the average temperature value in the bar (Fig. 4.2a). We then ran an optimization routine that modified nodal parameters (slope and value) to minimize the error between the mesh and the data points. An optimized mesh $\mathbf{u}^*$ in (Fig. 4.2b) followed the patterns in the data with minimal error. Scaling factors ensured a smooth mesh across element boundaries.

4.2.10 Multi-dimensional surfaces

We have thus far only considered a one-dimensional mesh. In 1-D, we have a single spatial dimension x that maps to an element coordinate (e, ξ). A mesh can be extended easily to any number of dimensions. Recall again the bar-temperature problem, but now replace the bar with a metal sheet that has two spatial dimensions x_1 and x_2. We can combine these dimensions into a spatial vector $\mathbf{x}$. Each 2-D element will have four nodes bordering it. Since we have two spatial dimensions, we map onto a two-dimensional element with coordinates ξ_1 and ξ_2 in a vector $\boldsymbol{\xi}$. We will assume that the spatial and element coordinates are aligned, with each dimension mapping independently of the other. We will now extend each part of the method to handle these extra dimensions.

In two dimensions, we have four nodes bordering an element, written as $\mathbf{x}_{()()}$. Each of those four nodes will have two spatial coordinates. The mapping onto the element domain is written as

$$\mathbf{x}(\xi_1, \xi_2) = \mathrm{L}_0(\xi_1)\mathrm{L}_0(\xi_2)\mathbf{x}_{00} + \mathrm{L}_1(\xi_1)\mathrm{L}_0(\xi_2)\mathbf{x}_{10} + \mathrm{L}_0(\xi_1)\mathrm{L}_1(\xi_2)\mathbf{x}_{01} + \mathrm{L}_1(\xi_1)\mathrm{L}_1(\xi_2)\mathbf{x}_{11} \quad (4.18)$$

which can be simplified using Einstein notation as

$$\mathbf{x}(\xi_1, \xi_2) = \mathrm{L}_i(\xi_1)\mathrm{L}_j(\xi_2)\mathbf{x}_{ij} \quad (i,j) \in \{0,1\} \tag{4.19}$$

If we assume the two coordinate systems are always aligned, then the inverse relationship $\boldsymbol{\xi}(x_1, x_2)$ is easily solved as

$$\boldsymbol{\xi} = \frac{\mathbf{x} - \mathbf{x}_{00}}{\mathbf{x}_{11} - \mathbf{x}_{00}} \qquad \xi_1 = \frac{x_1 - x_{00,1}}{x_{11,1} - x_{00,1}} \qquad \xi_2 = \frac{x_2 - x_{00,2}}{x_{11,2} - x_{00,2}} \tag{4.20}$$

If the coordinate systems are not aligned and $x_1 = f(\xi_1, \xi_2)$, the mapping relationship in Eqn. 4.19 still holds but the inverse mapping in Eqn. 4.20 does not. Although a point *can* be mapped from $x \to \xi$, there is no simple relationship or equation. These problems, and those with higher dimensions or nonlinear basis functions, require an alternative projection method. One such method is a searching algorithm, where a n-D grid of points is generated at regularly spaced points through an element. Then, a search algorithm is used to identify the closet grid point to the spatial point of interest, classically known as a nearest neighbor search. We have used a *k-d tree* algorithm, although many similar ones are available. This approach is quite useful for nonlinear mapping in higher dimensions. For applications here, we will always use linear elements aligned to spatial dimensions, thus the inverse mapping relationship in Eqn. 4.20 will hold and no alternative methods are required.

We build an interpolation function for $\hat{y}$ in a similar manner as Eqn. 4.8. We use cubic Hermite functions in two dimensions, commonly called a bicubic Hermite interpolation. In two dimensions, Hermite functions create derivatives in both x_1 and x_2 dimensions, as well as a cross-derivative. So, for each node in a bicubic Hermite function, there are four nodal parameters

$$y_n, \left.\frac{\partial y}{\partial x_1}\right|_n, \left.\frac{\partial y}{\partial x_2}\right|_n, \left.\frac{\partial^2 y}{\partial x_1 \partial x_2}\right|_n$$

and for each element, there are 16 total parameters contributing to the interpolation.

Scaling factors are the exact same in multiple dimensions, assuming that the mapping functions are linear and independent. Each derivative is scaled by the length of the element in the direction of interest, and the cross derivative is scaled by the product of the individual scaling factors. Just like the 1-D case, scaling factors belong to the element (not the node) and will scale nodal derivatives differently depending on which bordering element is interpolated.

The overall interpolation function is

$$\begin{aligned}\hat{y}(\xi_1,\xi_2) = \quad & y_{00}\mathrm{H}_0^0(\xi_1)\mathrm{H}_0^0(\xi_2) + y_{10}\mathrm{H}_1^0(\xi_1)\mathrm{H}_0^0(\xi_2) + y_{01}\mathrm{H}_0^0(\xi_1)\mathrm{H}_1^0(\xi_2) + y_{11}\mathrm{H}_1^0(\xi_1)\mathrm{H}_1^0(\xi_2) + \\ & \left.\frac{\partial y}{\partial x_1}\right|_{00} S_1\mathrm{H}_0^1(\xi_1)\mathrm{H}_0^0(\xi_2) + \left.\frac{\partial y}{\partial x_1}\right|_{10} S_1\mathrm{H}_1^1(\xi_1)\mathrm{H}_0^0(\xi_2) + \\ & \left.\frac{\partial y}{\partial x_1}\right|_{01} S_1\mathrm{H}_0^1(\xi_1)\mathrm{H}_1^0(\xi_2) + \left.\frac{\partial y}{\partial x_1}\right|_{11} S_1\mathrm{H}_1^1(\xi_1)\mathrm{H}_1^0(\xi_2) + \\ & \left.\frac{\partial y}{\partial x_2}\right|_{00} S_2\mathrm{H}_0^0(\xi_1)\mathrm{H}_0^1(\xi_2) + \left.\frac{\partial y}{\partial x_2}\right|_{10} S_2\mathrm{H}_1^0(\xi_1)\mathrm{H}_0^1(\xi_2) + \\ & \left.\frac{\partial y}{\partial x_2}\right|_{01} S_2\mathrm{H}_0^0(\xi_1)\mathrm{H}_1^1(\xi_2) + \left.\frac{\partial y}{\partial x_2}\right|_{11} S_2\mathrm{H}_1^0(\xi_1)\mathrm{H}_1^1(\xi_2) + \\ & \left.\frac{\partial^2 y}{\partial x_1 \partial x_2}\right|_{00} S_1S_2\mathrm{H}_0^1(\xi_1)\mathrm{H}_0^1(\xi_2) + \left.\frac{\partial^2 y}{\partial x_1 \partial x_2}\right|_{10} S_1S_2\mathrm{H}_1^1(\xi_1)\mathrm{H}_0^1(\xi_2) + \\ & \left.\frac{\partial^2 y}{\partial x_1 \partial x_2}\right|_{01} S_1S_2\mathrm{H}_0^1(\xi_1)\mathrm{H}_1^1(\xi_2) + \left.\frac{\partial^2 y}{\partial x_1 \partial x_2}\right|_{11} S_1S_2\mathrm{H}_1^1(\xi_1)\mathrm{H}_1^1(\xi_2)\end{aligned} \tag{4.21}$$

We simplify this formulation using Einstein notation as

$$\begin{aligned}\hat{y}(\xi_1,\xi_2) = \quad & y_{ij}\mathrm{H}_i^0(\xi_1)\mathrm{H}_j^0(\xi_2) + \left.\frac{\partial y}{\partial x_1}\right|_{ij} S_1\mathrm{H}_i^1(\xi_1)\mathrm{H}_j^0(\xi_2) + \\ & \left.\frac{\partial y}{\partial x_2}\right|_{ij} S_2\mathrm{H}_i^0(\xi_1)\mathrm{H}_j^1(\xi_2) + \left.\frac{\partial^2 y}{\partial x_1 \partial x_2}\right|_{ij} S_1S_2\mathrm{H}_i^1(\xi_1)\mathrm{H}_j^1(\xi_2)\end{aligned} \tag{4.22}$$

Looking at Eqn. 4.8 and Eqn. 4.22, we see an emerging pattern. When we add a dimension to an interpolation function, we scale each nodal parameter by a new basis function in that added dimension. The type of basis function used will dictate how the interpolated value changes *in that dimension*. We can combine similar basis functions, as in bicubic, tricubic,

or quadcubic Hermite interpolation, as well as mixed meshes of Hermite and Lagrangian interpolations. There is no dimensional limit in this formulation. Each dimension will add a set of nodes based on the type and degree of basis function used, as well as a new set of scaling factors. As long as the spatial dimensions align with the element dimensions, assumptions about projection and scaling will hold true. The generalized interpolation for a V-dimensional problem can be stated as

$$\hat{y}(\boldsymbol{\xi}) = \sum_{w=1}^{W} \mathbf{u}_{I_w}^{J_w} \prod_{v=1}^{V} \mathrm{B}_{I_w(v)}^{J_w(v)}(\xi_v) S_v^{J_w(v)} \tag{4.23}$$

$$\text{Dimension, } v \in \{1, 2, \ldots, V\}$$

$$\text{Degree of Freedom, } i_v \in \{0, 1, \ldots, \mathrm{DoF}_v\},\ i \in \{i_1, i_2, \ldots, i_v\}$$

$$\text{Order, } j_v \in \{0, 1, \ldots, \mathrm{Order}_v\},\ j \in \{j_1, j_2, \ldots, j_v\}$$

$$(I, J) = \mathrm{Permute}(i, j, w),\ w \in \{1, 2, \ldots, W\}$$

The notation can be burdensome in the generalized model, but we see how a nodal parameter $\mathbf{u}_{I_w}^{J_w}$ is scaled by a product of basis functions and scaling factors in every dimension v. We sum parameters across the degrees of freedom and order for every dimension (W nodal parameters). We assume that scaling factors are attached to every basis function, and basis functions that do not require scaling (Lagrangian functions, nodal values) have scaling factors set to unity.

Scaling factors become more complex when spatial dimensions and element dimensions do not align. They are also complicated when using nonlinear basis functions in a spatial x dimension. For instance, in the 1-D bar problem, if the bar were curved instead of straight, the element dimension would follow the path of the bar through 2+ physical dimensions. The physical length of an element would not equal the difference in bordering node positions. In these cases, scaling factors are generalized by the pathlength of an element edge, regardless of what physical dimensions it occupies. This pathlength calculation is used by (Bradley

et al., 1997), and is stated formally as

$$S_{v,I_w} = \int_{\xi_v=0}^{\xi_v=1} \left\| \frac{\partial \hat{y}(\boldsymbol{\xi})}{\partial \xi_v} \right\| d\xi_v \tag{4.24}$$

The notation (v, I_w) indicates the edge of an element along the v dimension, between nodes indexed by I_w. This integral can be solved discretely using Gaussian quadrature or by querying points along the edge and summing the distance between them.

Mesh design and data projection are the same as the 1-D mesh, with a natural extension of the nodal arrays and matrices to accommodate additional dimensions. Projection uses the mapping techniques of Eqn. 4.20. The error function and optimization techniques are also equivalent. For calculations of the gradient and Hessian, the nodal derivatives are simply the product of the scaled basis functions in each dimension.

$$\frac{\partial \hat{y}(\mathbf{u}_e, \boldsymbol{\xi}_d)}{\partial u_q} = \prod_{v=1}^{V} \mathrm{B}_{q,v}(\xi_{d,v}) S_{e,v}$$

The Hessian matrix is calculated as the second derivative using this formulation. Newton and quasi-Newton convergences and other properties are the same regardless of mesh dimensions.

4.2.11 Smoothing

We sometimes want to maintain a smooth mesh during fitting, even if it produces a less-than-optimum solution. We also want to avoid overfitting when data is sparse. Both of these conditions can be met by using a smoothing penalty as part of the optimization. We measure smoothness as the change of a fitted value $\hat{y}$ with respect to a change in an element dimension ξ. This general method uses a mathematical concept called a Sobolev space. The details of this approach were proposed in (Tikhonov and Arsenin, 1977), constructed in (Terzopoulos, 1986), then applied to surface fitting in (Bradley et al., 1997) and (Hashima et al., 1993), among many. We will focus on the resulting formula, without worrying about its detailed derivation. The formula is a *p^{th}-order weighted Sobolev norm*, where p refers to

the highest order of derivative to be smoothed. We are most concerned with variations in the first and second derivative, and will ignore higher orders. For a one-dimensional problem, a mesh element can be smoothed against both the first and second order derivative ($p = 2$) by minimizing the Sobolev norm

$$\|\hat{y}\|_2^2 = \int_{\Omega_e} w_0(\hat{y})^2 + w_1 \left(\frac{\partial \hat{y}}{\partial \xi}\right)^2 + w_2 \left(\frac{\partial^2 \hat{y}}{\partial \xi^2}\right)^2 d\xi \tag{4.25}$$

The w terms are weighting functions. Since we do not want to weight the fitted value itself we set $w_0 = 0$. The derivatives of the mesh with respect to an element coordinate ξ are simple to calculate given the additive nature of the interpolation function. For instance, to differentiate a 1-D Hermite element, we use Eqn. 4.8 and differentiate each basis function H_i^j with respect to ξ. All nodal parameters act as constants. Since we want to measure smoothness of the entire surface, we use a 12-point Gaussian quadrature to estimate the integration, which is done through the entire element domain Ω_e. We can extend this formulation to a 2-D element as

$$\|\hat{y}\|_2^2 = \int_{\Omega_e} w_1 \left[\left(\frac{\partial \hat{y}}{\partial \xi_1}\right)^2 + \left(\frac{\partial \hat{y}}{\partial \xi_2}\right)^2\right] + w_2 \left[\left(\frac{\partial^2 \hat{y}}{\partial \xi_1^2}\right)^2 + 2\left(\frac{\partial^2 \hat{y}}{\partial \xi_1 \partial \xi_2}\right)^2 + \left(\frac{\partial^2 \hat{y}}{\partial \xi_2^2}\right)^2\right] d\xi_1 d\xi_2$$

and generalize it to V dimensions for an entire mesh $\mathbf{u}$ as

$$\|\mathbf{u}\|_2^2 = \sum_{e=1}^{E} \int_{\Omega_e} \sum_{v=1}^{V} w_1 \left(\frac{\partial \hat{y}}{\partial \xi_v}\right)^2 + w_2 \left(\frac{\partial^2 \hat{y}}{\partial \xi_v^2}\right)^2 + 2w_2 \sum_{\substack{w=1 \\ w \neq v}}^{V} \left(\frac{\partial^2 \hat{y}}{\partial \xi_v \partial \xi_w}\right)^2 d\boldsymbol{\xi} \tag{4.26}$$

Weighting functions are held constant ($w_1 = \alpha$ and $w_2 = \beta$) based on (Hashima et al., 1993) format. (Terzopoulos, 1986) describes α as penalizing "the small deflection energy of a membrane" and β as penalizing "small deflection bending energy of a thin plate". (Hashima et al., 1993) describes α as penalizing "large stretches and rotations" and β as penalizing "changes in curvature".

We treat Sobolev smoothing as a penalty G, and we enforce that penalty by adding it to

the error function F. Since the goal of optimization is finding a minimum, the smoothing penalty shifts the location of the minimum. We summarize this as

$$\mathbf{u}^* = \arg\min F(\mathbf{u}) + \gamma G(\mathbf{u}) \tag{4.27}$$

Here $F + \gamma G$ is called the objective function. We weight the smoothing penalty by a constant γ. Using the same Newton optimization, we need to calculate

$$\nabla F + \gamma \nabla G$$

$$\mathbb{H}F + \gamma \mathbb{H}G$$

where

$$\nabla G = \frac{\partial G}{\partial u_q}$$

and

$$\frac{\partial G}{\partial u_q} = \sum_{e=1}^{E} \int_{\Omega_e} \sum_{v=1}^{V} 2\alpha \left(\frac{\partial \hat{y}}{\partial \xi_v}\right) \frac{\partial}{\partial u_q}\left(\frac{\partial \hat{y}}{\partial \xi_v}\right) + 2\beta \left(\frac{\partial^2 \hat{y}}{\partial \xi_v^2}\right) \frac{\partial}{\partial u_q}\left(\frac{\partial^2 \hat{y}}{\partial \xi_v^2}\right) + \cdots$$
$$4\beta \sum_{\substack{w=1 \\ w \neq v}}^{V} \left(\frac{\partial^2 \hat{y}}{\partial \xi_v \partial \xi_w}\right) \frac{\partial}{\partial u_q}\left(\frac{\partial^2 \hat{y}}{\partial \xi_v \partial \xi_w}\right) d\boldsymbol{\xi}$$

with

$$\frac{\partial}{\partial u_q}\left(\frac{\partial \hat{y}}{\partial \xi_v}\right) = \frac{\partial \mathbf{B}_q}{\partial \xi_v} \qquad \frac{\partial}{\partial u_q}\left(\frac{\partial^2 \hat{y}}{\partial \xi_v \partial \xi_w}\right) = \frac{\partial^2 \mathbf{B}_q}{\partial \xi_v \partial \xi_w}$$

and

$$\frac{\partial \mathbf{B}_q}{\partial \xi_v} = \frac{\partial \mathrm{B}_{q,v}}{\partial \xi_v} S_{e,v} \prod_{\substack{w=1 \\ w \neq v}}^{V} \mathrm{B}_{q,w} S_{e,w}$$

$$\frac{\partial^2 \mathbf{B}_q}{\partial \xi_v \partial \xi_w} = \frac{\partial \mathrm{B}_{q,v}}{\partial \xi_v} S_{e,v} \frac{\partial \mathrm{B}_{q,w}}{\partial \xi_w} S_{e,w} \prod_{\substack{\zeta=1 \\ \zeta \neq v,w}}^{V} \mathrm{B}_{q,\zeta} S_{e,\zeta}$$

For the Hessian,

$$\mathbb{H}_{qr} G = \frac{\partial^2 G}{\partial u_q \partial u_r}$$

$$\frac{\partial^2 G}{\partial u_q \partial u_r} = \sum_{e=1}^{E} \int_{\Omega_e} \sum_{v=1}^{V} 2\alpha \frac{\partial \mathbf{B}_q}{\partial \xi_v} \frac{\partial \mathbf{B}_r}{\partial \xi_v} + 2\beta \frac{\partial^2 \mathbf{B}_q}{\partial \xi_v^2} \frac{\partial^2 \mathbf{B}_r}{\partial \xi_v^2} + 4\beta \sum_{\substack{w=1 \\ w \neq v}}^{V} \frac{\partial^2 \mathbf{B}_q}{\partial \xi_v \partial \xi_w} \frac{\partial^2 \mathbf{B}_r}{\partial \xi_v \partial \xi_w}$$

and the basis function derivatives are equal to those calculated for the gradient array.

4.2.12 Constraints

There are times when we want to constrain the mesh during optimization. In some cases, we sometimes need to link nodes together (set them equal to each other) or constrain edge nodes (set them equal to a constant). We also need to create a feasible space by setting upper and lower bounds of a problem. For instance, in the temperature-bar problem, every nodal value should be greater than zero. In these cases, equality or inequality constraints are included in the optimization. We use a formulation called the *Lagrangian* to include constraints in the optimization process. This should not be confused with Lagrangian basis functions, which have nothing in common with this except the namesake (Joseph-Louis Lagrange). In the Lagrangian, each constraint is given a weight (its Lagrange multiplier) that allows it to exert influence on the optimum. Active constraints have a Lagrange multiplier greater than zero, inactive constraints have ones equal to zero. Inequality constraints can be rewritten as equality constraints, assuming the constraint is *active* only when the mesh is contacting the

constraint. All constraints are rearranged so that $\mathbf{C} = \mathbf{0}$, where $\mathbf{C}$ is a system of constraint equations. Constraints are added into the objective function to create the Lagrangian $\mathcal{L}$, where

$$\mathcal{L}(\mathbf{u}, \gamma, \boldsymbol{\lambda}) = F(\mathbf{u}) + \gamma G(\mathbf{u}) + \lambda_k C_k \tag{4.28}$$

with implied summation over $k \in 1, \ldots, K$ constraints. The Lagrangian is solved using the same Newton method, where

$$\begin{aligned} (\mathbf{u}^*, \boldsymbol{\lambda}^*) &= \arg\min \mathcal{L}(\mathbf{u}, \gamma, \boldsymbol{\lambda}) \\ \nabla\mathcal{L}(\mathbf{u}^*, \gamma, \boldsymbol{\lambda}^*) &= \mathbf{0} \\ \lambda_k^* C_k &= 0 \end{aligned} \tag{4.29}$$

We typically used linear constraints, so that $\lambda_k \nabla C_k$ was an array of summed coefficients, and $\lambda_k \mathbb{H} C_k = \mathbf{0}$.

4.2.13 Types of fitted data

We have used a general term, $\hat{y}$, to represent fitted data values in constructing this mesh optimization framework. Temperature was used in the simple examples, either of a bar (1-D problem) or sheet (2-D problem). However, we can fit any type of data. In many applications of surface fitting, the fitted value is actually *another spatial dimension*. For instance, in a 3-D Cartesian (x, y, z) system, a 2-D mesh could fit $\hat{z}$ as a function of (x, y). Similarly, blood vessels are fitted in a cylindrical coordinate system (r, θ, z), where a 2-D mesh is fit as $\hat{r}(\theta, z)$. Previous work in our lab (Herz et al., 2005, 2010) used a prolate spheroid coordinate system to fit the left ventricle as $\hat{\lambda}(\theta, \phi)$. And more recent work in the left atrium used a spherical coordinate system as $\hat{r}(\theta, \phi)$. Using one of the spatial dimensions as the fitted variable simplifies the mesh design, turning a 3-D surface mesh into a 2-D mesh with the third, fitted dimension. Sequestering one dimension as the fitted variable does not impede adding other dimensions (time), such as $\hat{\lambda}(\theta, \phi, t)$ and $\hat{r}(\theta, \phi, t)$. For our work in the atrium,

we will rely heavily on 2-D and 3-D meshes, applied to 3-D and 4-D problems respectively as $\hat{r}(\theta, \phi)$ and $\hat{r}(\theta, \phi, t)$.

4.2.14 Software

Any algorithm designed to optimize a smoothed, constrained, multi-dimensional mesh requires compatible software. We relied heavily on MATLAB (The Mathworks, Inc., Natick, MA, USA) as the core environment. The form of optimization described in Eqn. 4.28 is referred to as *convex quadratic optimization with linear constraints*. We installed a sequential quadratic solver called SQPlab (Bonnans et al., 2007), designed to solve a series of quadratic programs regardless of convexity within the MATLAB environment. As designed, SQPlab uses MATLAB's built-in quadratic solver QuadProg. In our testing, we found that QuadProg did not converge for certain constrained meshes. We therefore replaced it with the CPLEX solver (IBM iLOG, Sunnyvale, CA, USA), which uses interior point (barrier) methods to solve quadratic programs. It handled linear constraints with ease.

4.3 Results

A basic 1-D mesh was used for the temperature-bar problem earlier in this chapter (Fig. 4.1). We extended these principles to create a time-varying spherical mesh (4-D), which was used to analyze left atrial wall motion in Chapter 5. In these results we focus on the spherical mesh design (density of elements, smoothing, constraints) and optimization techniques. Chapter 5 will explain how point sets were obtained and how left atrial function was measured from an optimized mesh.

4.3.1 Mesh design

We used a time-varying spherical mesh defined as $\hat{r}(\theta, \phi, t)$, where radius was the fitted dimension. The spherical mesh was parameterized into elements in the other three dimensions

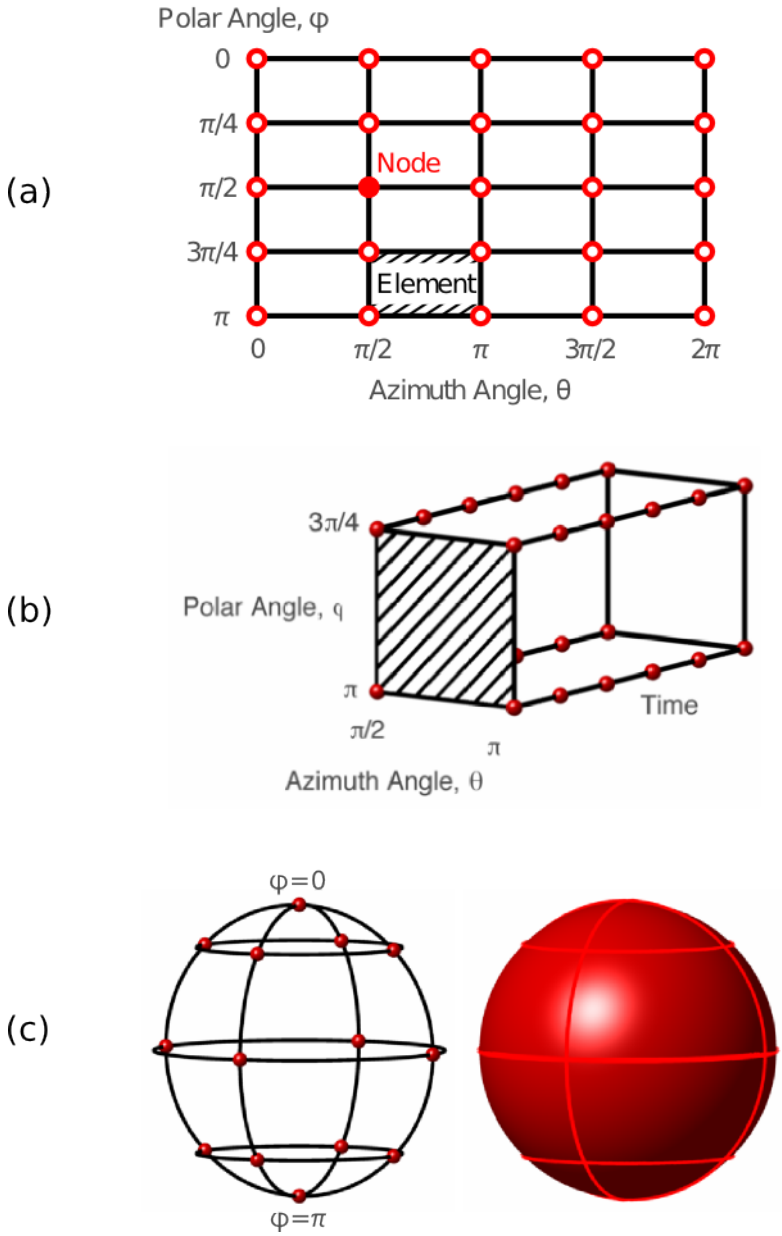

Figure 4.3: The design of a time-varying spherical mesh. (a) The angular dimensions of the sphere are divided into multiple elements, bounded by common nodes. Each spatial dimension is interpolated with a cubic Hermite function, requiring two nodes bounding each element edge. (b) Each element extends through time, populated with multiple temporal nodes based on the degree of Lagrangian interpolation. (c) The mesh is wrapped into a sphere by fusing nodes at $\theta = (0, 2\pi)$ and at $\phi = (0, \pi)$ then interpolated to create a smooth surface.

(θ, ϕ, t). The azimuth angle θ is the position about the horizontal plane where $\theta \in [0, 2\pi)$. It is the equivalent of longitudinal position on a globe. The polar angle ϕ is the position from the north pole (top) of the sphere to the south pole (bottom) where $\phi \in [0, \pi]$. It is the equivalent of latitudinal position on a globe.

We chose cubic Hermite basis functions to interpolate the spatial dimensions (θ, ϕ) and a Lagrangian basis function to interpolate through time t. These choices were based on the expected shape of the left atrium and its expected motion through the cardiac cycle, which are described in more detail in Chapter 5. The spatial domain was divided into multiple elements while the time domain was interpolated with a single higher-degree Lagrangian function (Fig. 4.3a,b). The spatial nodes were "wrapped" to create a sphere, where nodes at $\theta = 0$ and $\theta = 2\pi$ were fused as a single node. Since the mesh converged to a single point at the poles $\phi = (0, \pi)$, we opted to maintain the rectangular gridding in Figure 4.3a and apply constraints rather than fuse nodes. We constrained a pole so that the radii were equal, the change in radius with respect to θ was zero, the change in radius with respect to θ, ϕ (the cross-derivative) was zero, and the change in radius with respect to ϕ was equal to the value at $\theta = \pm\pi$. The spherical form of the mesh and a fully interpolated surface are shown (Fig. 4.3c).

4.3.2 Scaling factors

Scaling factors maintain C^1 continuity in a surface mesh. To confirm this, we built toy meshes for the 1-D bar 2-D atrium problems. We started with continuous meshes that contained equally spaced elements (Fig. 4.4a). A uniform element size resulted in a continuous mesh, regardless of scaling factors. We then shifted the location of some nodes to create a mesh with unequal element sizes. Without scaling factors, these shifted meshes lost their continuity and were no longer smooth (Fig. 4.4b). We computed the scaling factors based on the new element sizes. In a spherical mesh $\hat{r}(\theta, \phi, t)$, scaling factors are set in the angular spatial

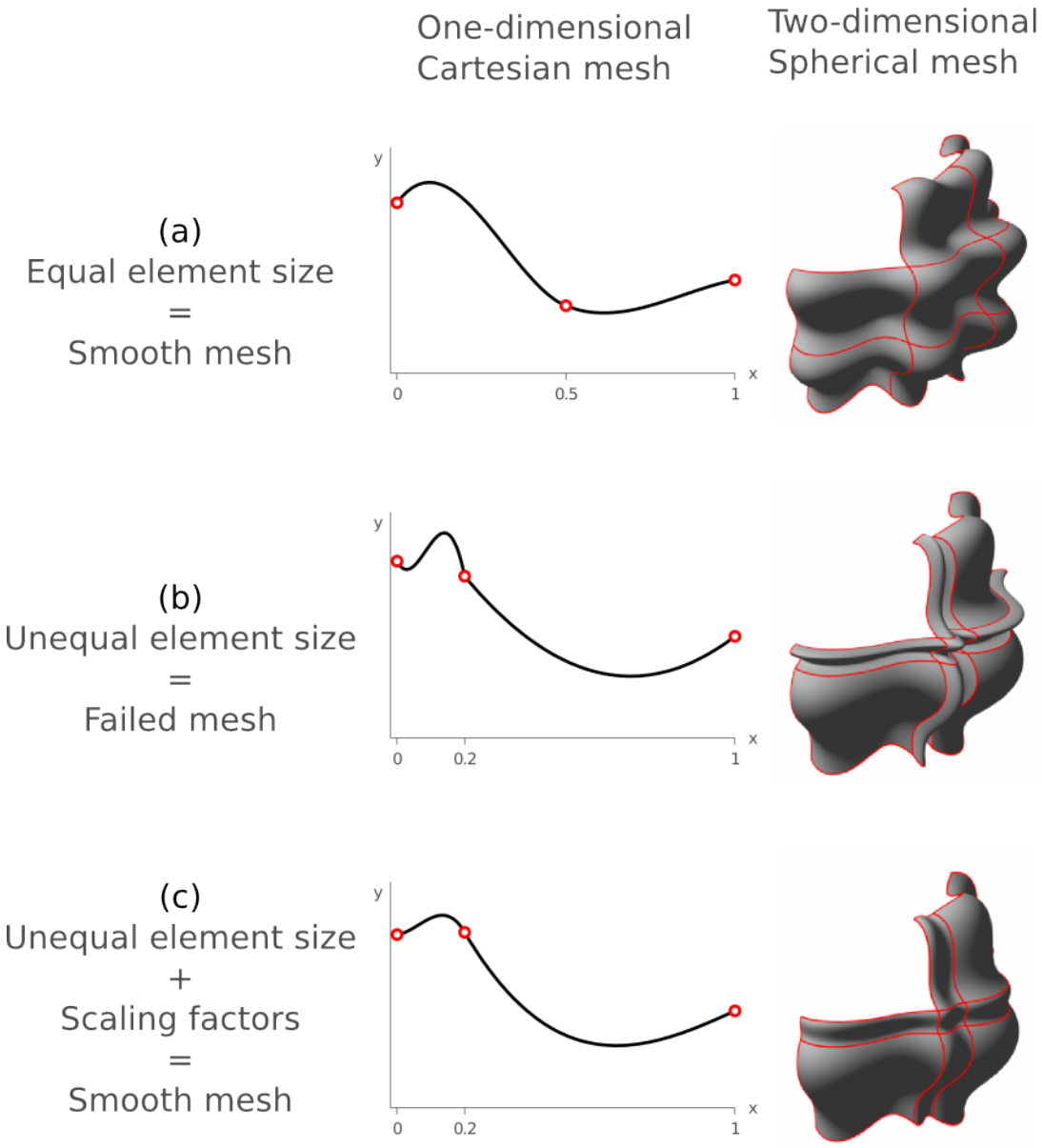

Figure 4.4: Scaling factors maintained mesh smoothness (C^1 continuity) in 1-D and 2-D cubic Hermite surfaces. (a) Equally-spaced elements created a smooth mesh in both 1-D Cartesian and 2-D Spherical systems, since scaling is equal in neighboring elements. (b) Shifting nodal positions generated unequal element sizes, removing mesh continuity. (c) Applying scaling factors restored C^1 continuity in both the 1-D Cartesian and 2-D Spherical meshes. Surfaces are shown in gray to highlight element edges.

Metric	quasi-Newton	Newton's Method	Improvement
CPU Time (s)	117±33	11±3	11x
Iterations (no.)	86±18	1±0	86x
Time per Iter. (ms)	1.4±0.2	10.8±3.4	-8x
Time per Point (ms)	2.29±0.72	0.20±0.02	11x
RMSE (mm)	2.4±0.5	2.3±0.5	0.02x
		with Smoothing	
CPU Time (s)	87±15	38±6	2x
Iterations (no.)	39±4	1±0	39x
Time per Iter. (ms)	2.3±0.2	38.4±5.5	-17x
Time per Point (ms)	1.73±0.54	0.76±0.24	2x
RMSE (mm)	4.1±0.7	4.1±0.7	0.01x

Table 4.1: Newton's Method optimized meshes in fewer iterations than quasi-Newton alternatives, saving substantial computational time. Newton's method converged to the exact solution in a single iteration, regardless of smoothing constraints. Algorithms were tested with $n = 23$ data sets containing an average of 54,500 data points per set. RMSE was measured in the radial (fitted) dimension.

dimensions as S_θ, S_ϕ. Scaling factors restored element smoothness in both the single- and multi-dimenional meshes (Fig. 4.4c).

4.3.3 Solver comparisons

A mesh can be optimized using either Newton or quasi-Newton methods. We built algorithms for each method then compared the two approaches and confirmed their convergence to a single solution. Using left atrial surface data obtained in Chapter 5 (Fig. 4.5a), we generated a spherical mesh and aligned it with the data (Fig. 4.5b), then optimized it using either the Newton or quasi-Newton method (Fig. 4.5c). We applied the two methods to twenty-three ($n = 23$) data sets. The results are summarized in Table 4.1. As expected, the spherical mesh converged in a single iteration using Newton's method. Newton's method reduced total computation time by over 90% compared to quasi-Newton alternatives. The two approaches

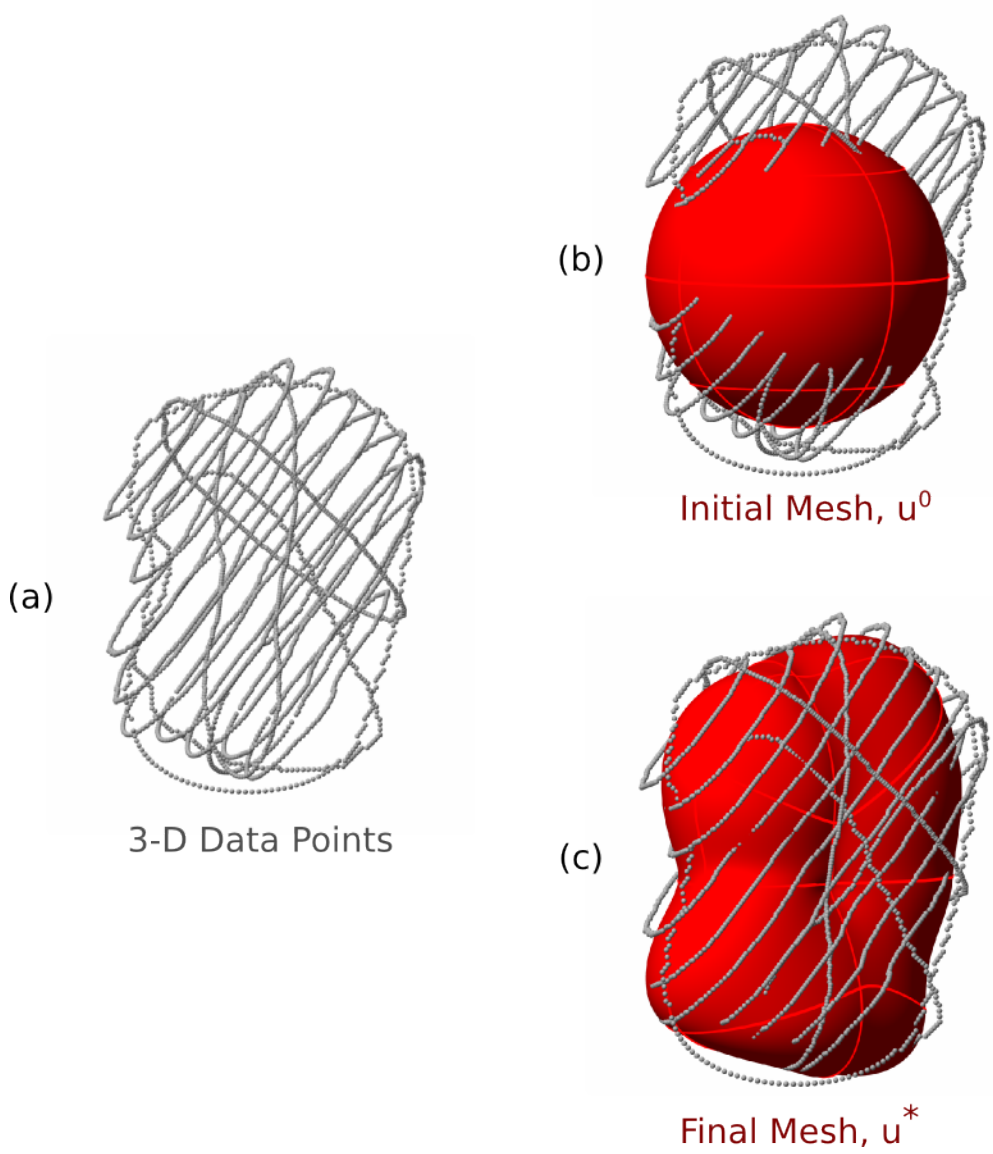

Figure 4.5: Nonlinear solvers were tested by optimizing a spherical mesh to 3-D data of the left atrial surface. (a) The time-varying position of the left atrial wall, obtained from methods detailed in Chapter 5, was used as input data. (b) A spherical mesh was oriented with the point set, parameterized, and set to the average point radius. (c) Newton and quasi-Newton methods found the optimized mesh.

converged to a single solution, but the Newton method was more exact with a slightly lower root-mean-square error (RMSE). We saw similar trends when Sobolev smoothing was included, although improvements were muted. Based on these findings, we chose Newton's method as the best optimization method for left atrial wall motion analysis.

4.3.4 Mesh density

The density of a mesh controls its flexibility during fitting. We can add nodal parameters (degrees of freedom) by increasing element density or raising the degree of a basis function. More degrees of freedom lowers RMSE, but too much flexibility creates over-fitting. We used a series of statistical tests to find the ideal atrium mesh, aiming for low RMSE without over-fitting. We used a combination of tests, including the Akaike information criterion (AIC), the Bayesian information criterion (BIC), and k-fold cross-validation, and applied them to six ($n = 6$) data sets selected randomly from our data pool.

Both the AIC and BIC are statistical tests that compute a sum (the "information criterion") of two competing terms, one representing model error and the other a penalty on complexity. An ideal model seeks the minimum information criterion, balancing low model error and low complexity. The AIC (Akaike, 1974) is defined as

$$\mathrm{AIC} = P \log\left(\frac{\mathrm{RSS}}{P-Q-2}\right) + \frac{2PQ}{P-Q-1} + P(\log 2\pi + 1) \tag{4.30}$$

where RSS is the summed-square error of the fit. Recall that P is the number of data points and Q is the total number of nodal parameters. We reduced Q based on nodal constraints. The BIC (Schwarz, 1978) followed a similar definition with

$$\mathrm{BIC} = P \log\left(\frac{\mathrm{RSS}}{P}\right) + 2Q \log P + P(\log 2\pi + 1) \tag{4.31}$$

These formulations are found in (Hansen and Yu, 2001) and (Claeskens and Hjort, 2008). We tested element density in the angular dimensions (θ, ϕ) by varying $E_\theta = \{4, 6, \ldots, 18\}$

and $E_\phi = \{2, 3, \ldots, 9\}$. We tested the temporal dimension by varying the degree m of the Lagrangian basis function as $m = \{2, 3, \ldots, 10\}$. These ranges were chosen based on expected variation in shape and motion, discussed in Chapter 5. The AIC test failed to identify an optimum surface (it did not have a local minimum). The BIC test found an optimum mesh at $(E_\theta = 8, E_\phi = 6, m = 5)$ based on the average of six data sets tested. To confirm this finding, we used a k-fold cross validation.

K-fold cross validation separated a data set into k subsets. For each, we excluded it and fit a model to the remaining data, then measured fit error against the excluded subset. This process was repeated for each of the k subsets then averaged. This method implicitly penalized over-fitting by measuring the RMSE of unfitted portions of the data. Based on results from the BIC tests, we chose $k = 5$ and tested the same ranges of element densities. We found an optimum mesh at $(E_\theta = 8, E_\phi = 6, m = 4)$, fairly close to the BIC minimum (Fig. 4.6a) but with less temporal nodes. The optimum mesh for individual subjects varied substantially, with some subjects requiring dense meshes (Set 3, $E_\theta = 16, E_\phi = 5, m = 4$) and others requiring more temporal variation (Set 5, $E_\theta = 6, E_\phi = 4, m = 8$, Fig. 4.6b). In addition, the optimum mesh for individual subjects differed between the k-fold and BIC metrics (the BIC minimum tended to select meshes with higher temporal variation). We chose to use k-fold cross-validation over BIC because it was a simpler, more robust method that did not require a penalty factor. We chose a dense mesh that encompassed all individual patient optimums and then relied on Sobolev smoothing to handle any excess variation. The optimum mesh was set to $(E_\theta = 18, E_\phi = 6, m = 8)$.

4.3.5 Mesh smoothing

Since a dense mesh was chosen in the previous section, additional smoothing was required. We applied the same k-fold cross-validation method to find the correct amount of smoothing. Using Eqn. 4.26, we set $\alpha = 10$ and $\beta = 1$. This ratio was shown to provide roughly equal penalties against smoothness based on our early tests (data not shown). To choose the

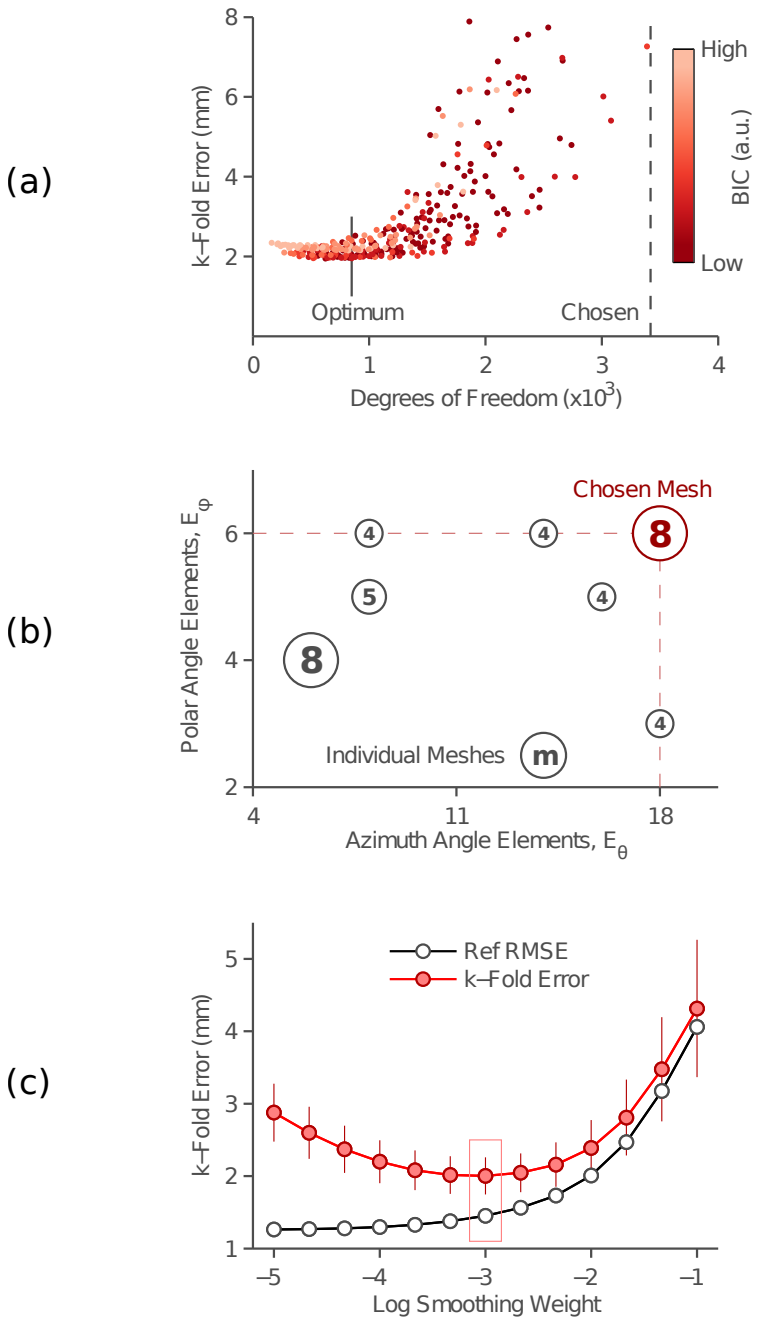

Figure 4.6: The left atrial mesh was chosen to have a high density of elements and high degree of temporal variation, with strong Sobolev smoothing to handle excessive variation. (a) K-fold cross-validation identified an optimum mesh at approximately 900 degrees of freedom. The Bayesian information criterion confirmed this result. (b) Individual data sets had unique optimums. Some sets required more spatial elements and others required higher degree temporal interpolation, m. A mesh was chosen to encompass every individual set optimum. (c) Sobolev smoothing controlled for excess variation in the chosen mesh. K-fold cross-validation confirmed an optimum smoothing at $\gamma = 10^{-3}$. All six data sets had the same optimum smoothing point.

optimum mesh, α and β were scaled equally using the weighting factor γ in Eqn. 4.27. K-fold cross-validation produced a fit error that increased with higher penalties, and a test error (the k-Fold error) that had a minimum at $\gamma = 10^{-3}$. Interestingly, each of the six data sets tested had the same smoothing optimum. We used these results to create the final atrial mesh: $(E_\theta = 18, E_\phi = 6, m = 8, \alpha = 10, \beta = 1, \gamma = 10^{-3})$, and this mesh was used for all subsequent work.

4.4 Discussion

We developed a finite element mesh with multi-dimensional fitting capabilities and non-linear optimization routines. The mesh has been proven to fit both 1-D toy data and 3-D left atrial surface data. We used scaling factors to handle cubic Hermite elements and used Newton's method to speed up optimization. k-Fold cross validation and BIC testing helped us identify an optimum mesh that balanced low RMSE during fitting and low amounts of surface variation. The mathematical framework and methods established in this chapter will be applied to clinical data in later chapters.

4.4.1 Basis functions

There are many other choices for basis functions besides Lagrangian and Hermite forms. A variety of functions are used in computer graphics, finite element modeling, and 3-D computer aided design renderings.

Alternate functions that achieve C^0 include Newton polynomials and Fourier functions. Newton polynomials (unrelated to Newton's method) are similar to Lagrange polynomials, but use a recursive formulation, such that higher degree functions can be written as a lower degree function added to a higher order term. This is helpful to save on computation time if multiple degrees are calculated simulateously, but that rarely happens in surface mesh interpolation. Newton polynomials cannot be scaled by nodal values easily, making it challeng-

ing to incorporate them into multi-dimensional schemes. Similarly, Fourier (trigonometric) interpolation is not incorporated easily into problems with mixtures of basis functions. Fourier functions are better suited for periodic functions with known patterns between elements.

Other basis function sets maintain continuity of the first derivative (C^1), such as Bezier curves, based on the Berstein polynomials. Like Hermite functions, Bezier curves use a nodal value and a nodal slope, but do so by creating additional nodes away from the element path, known as control points, to generate a tangent vector. For our purposes, this was a less compact form of interpolation with no added benefit, and became exceedingly complicated in multi-dimensional problems (Bezier surfaces). Bezier curves are more useful for irregular curves that do not have a unique value y for a given position x.

Bezier curves can be combined in certain ways to generate C^2 continuity, commonly referred to as cubic splines, or more generally, b-splines. The control points are still used, but the relationship between points is constrained to match both the first and second derivatives at nodes, also called knots. B-splines are valuable in pure interpolation problems, where a series of points derived from a continuous function needs to be filled in with a curve. In these cases, b-splines are more useful than Lagrangian polynomials because they avoid the noise of Runge's phenomena. This phenomena does not appear in surface fitting methods, where nodal parameters vary independently to achieve a single optimum without interpolation noise. Although b-splines require only four control points to to create C^2 continuity, the additional constraints on those control points adds unnecessary complexity to the fitting process. We stored more information at each node (nodal values and their derivatives) as an acceptable trade-off for avoiding additional constraints.

A more general form of b-splines is the non-uniform rational b-spline, also known as NURBs. NURBs are quite popular in finite element modeling and computer aided design for rendering and manipulating surfaces. Like Bezier curves, NURBs rely on basis functions and control points, as well as weighting factors of each control point. These functions are typically used when data point density is very high and surface features are sharp, containing edges or

points. Fortunately, physiological structures like the heart and its chambers are smooth and do not require this additional complexity. Continuity of second and third derivatives can be useful for some applications, such as estimating surface curvature, but are unnecessary for fitting physiologic structures and add unnecessary complexity to the model.

4.4.2 Optimization

To optimize a mesh, we defined an error function along a single dimension ($\hat{y}$ generally and $\hat{r}$ for the atrium). This formulation created an ordinary least squares fitting problem. An ordinary least squares formulation simplified the data projection and optimization steps. In contrast, a total least squares fitting problem uses a Euclidean distance error defined along multiple dimensions. The total least squares method is used less often due to differences in scaling between dimensions, but it can be applied to surface meshes fit in 2-D or 3-D. Groups like (Bradley et al., 1997) use this formulation.

Total least squares requires more computation time compared to ordinary least squares. It also requires an iterative projection, since meshes can move in multiple dimensions during each fitting step. For instance, if data were projected along a surface normal, it would have to be projected after each iteration and require multiple steps to converge. Similarly, if the mesh were adaptive (nodal positions changed between iterations) the algorithm would require multiple iterations to converge. These additional steps improve RMSE at the expense of additional CPU time.

Beyond time requirements, total least squares also provides more mesh flexibility, since fitting error is measured in all spatial dimensions. A total least squares mesh is more adaptive to a wider array of geometries, and does not require an application-specific coordinate system. However, when a surface fits a coordinate system well (prolate spheroid in the LV or spheroid in the LA), ordinary least squares fitting excels with lower complexity and faster computation times. Because atrial geometry is roughly spherical, we held to the ordinary least squares method as the simpler of options.

References

H. Akaike. A new look at the statistical model identification. *IEEE Transactions on Automatic Control*, 19(6):716–723, 1974.

P. E. Bezier. Example of an existing system in the motor industry: The unisurf system. *Proc. R. Soc. Lond. A*, 321(1545):207–218, Feb. 1971.

J. J. F. Bonnans, J. C. Gilbert, and C. Lemarchal. *Numerical Optimization*. Springer, Feb. 2007.

C. P. Bradley, A. J. Pullan, and P. J. Hunter. Geometric modeling of the human torso using cubic hermite elements. *Ann Biomed Eng*, 25(1):96–111, Feb. 1997.

B. R. Chaitman, J. D. Bristow, and S. H. Rahimtoola. Left ventricular wall motion assessed by using fixed external reference systems. *Circulation*, 48(5):1043–1054, Nov. 1973.

G. Claeskens and N. L. Hjort. *Model Selection and Model Averaging*. Cambridge University Press, 1 edition, July 2008.

J. Duncan and N. Ayache. Medical image analysis: progress over two decades and the challenges ahead. *IEEE Transactions on Pattern Analysis and Machine Intelligence*, 22(1): 85 –106, Jan. 2000.

C. F. Gauss. *Theory of the Motion of the Heavenly Bodies Moving about the Sun in Conic Sections: A Translation of Gauss's "Theoria Motus." With an Appendix*. Little, Brown and Company, 1857.

E. A. Geiser, S. M. Lupkiewicz, L. G. Christie, M. Ariet, D. A. Conetta, and C. Conti. A framework for three-dimensional time-varying reconstruction of the human left ventricle: Sources of error and estimation of their magnitude. *Computers and Biomedical Research*, 13(3):225–241, June 1980.

M. H. Hansen and B. Yu. Model selection and the principle of minimum description length. *Journal of the American Statistical Association*, 96(454):746–774, June 2001.

A. R. Hashima, A. A. Young, A. D. McCulloch, and L. K. Waldman. Nonhomogeneous analysis of epicardial strain distributions during acute myocardial ischemia in the dog. *Journal of Biomechanics*, 26(1):19–35, Jan. 1993.

S. L. Herz, C. M. Ingrassia, S. Homma, K. D. Costa, and J. W. Holmes. Parameterization of left ventricular wall motion for detection of regional ischemia. *Ann Biomed Eng*, 33(7): 912–919, July 2005.

S. L. Herz, T. Hasegawa, A. N. Makaryus, K. M. Parker, S. Homma, J. Wang, and J. W. Holmes. Quantitative three-dimensional wall motion analysis predicts ischemic region size and location. *Ann Biomed Eng*, 38(4):1367–1376, Apr. 2010.

T. McInerney and D. Terzopoulos. Deformable models in medical image analysis: a survey. *Medical Image Analysis*, 1(2):91–108, June 1996.

J. Montagnat, H. Delingette, and N. Ayache. A review of deformable surfaces: topology, geometry and deformation. *Image and Vision Computing*, 19(14):1023–1040, Dec. 2001.

P. M. Nielsen, I. J. L. Grice, B. H. Smaill, and P. J. Hunter. Mathematical model of geometry and fibrous structure of the heart. *Am J Physiol Heart Circ Physiol*, 260(4):H1365–H1378, Apr. 1991.

K. Pearson. On the systematic fitting of curves to observations and measurements. *Biometrika*, 1(3):265–303, Apr. 1902a.

K. Pearson. On the systematic fitting of curves to observations and measurments: Part II. *Biometrika*, 2(1):1–23, Nov. 1902b.

G. Schwarz. Estimating the dimension of a model. *Ann. Statist.*, 6(2):461–464, Mar. 1978.

D. B. Smith, M. S. Sacks, D. A. Vorp, and M. Thornton. Surface geometric analysis of anatomic structures using biquintic finite element interpolation. *Annals of Biomedical Engineering*, 28(6):598–611, 2000.

H. Strauss, B. L. Zaret, P. J. Hurley, T. Natarajan, and B. Pitt. A scintiphotographic method for measuring left ventricular ejection fraction in man without cardiac catheterization. *The American Journal of Cardiology*, 28(5):575–580, Nov. 1971.

D. Terzopoulos. Regularization of inverse visual problems involving discontinuities. *IEEE Transactions on Pattern Analysis and Machine Intelligence*, PAMI-8(4):413 –424, July 1986.

A. N. Tikhonov and V. I. Arsenin. *Solutions of ill-posed problems*. Winston, 1977.

A. Young, P. Hunter, and B. Smaill. Epicardial surface estimation from coronary angiograms. *Computer Vision, Graphics, and Image Processing*, 47(1):111–127, July 1989.

A. Young, P. Hunter, and B. Smaill. Estimation of epicardial strain using the motions of coronary bifurcations in biplane cineangiography. *IEEE Transactions on Biomedical Engineering*, 39(5):526 –531, May 1992.

A. Young, D. Kraitchman, L. Dougherty, and L. Axel. Tracking and finite element analysis of stripe deformation in magnetic resonance tagging. *IEEE Transactions on Medical Imaging*, 14(3):413 –421, Sept. 1995.

A. A. Young, C. M. Kramer, V. A. Ferrari, L. Axel, and N. Reichek. Three-dimensional left ventricular deformation in hypertrophic cardiomyopathy. *Circulation*, 90(2):854–867, Aug. 1994.

A. A. Young, Z. A. Fayad, and L. Axel. Right ventricular midwall surface motion and deformation using magnetic resonance tagging. *Am J Physiol Heart Circ Physiol*, 271(6): H2677–H2688, Dec. 1996.

Chapter 5

Left atrial wall motion of healthy adults

The left atrium expands and contracts during each cardiac cycle. Atrial tissue moves outward during expansion (away from its center of mass) and inward during contraction (toward its center of mass). We refer to this cyclic motion as *left atrial wall motion*. This motion is generated by changes in atrial pressure and contraction of atrial myocytes. Although atrial pressure acts on every part of the wall, there is no guarantee that every part of the wall will move the same amount. Regional motion is influenced by regional wall stress, local mechanical properties of the tissue, and external structures contacted during expansion. During active contraction, regional motion is also influenced by atrial myocyte pre-stretch. These factors are not spatially homogeneous, so we hypothesized that left atrial wall motion should vary between regions. We refer to this spatial variation as *regional heterogeneity*. Atrial function contributes significantly to cardiac output, and some regions may contribute more than others if heterogeneity exists. Quantifying regional wall motion is therefore fundamental to understanding the atrium's contribution to cardiac function.

5.1 Background of regional left atrial function

Clinicians began to measure atrial wall motion following the commercialization of cardiac ultrasound (echocardiography) (Yoshikawa et al., 1975). Strunk and colleagues discovered a relationship between motion in the aorta and motion in the anterior left atrial wall (the part of the wall that touches the aorta) (Strunk et al., 1976). This correlative motion deteriorated during mitral valve disease (Akgun and Layton, 1977), demonstrating for the first time how a disease could alter regional function in the atrium. Subsequent studies used two-dimensional echocardiography to track the left atrial wall (Gutman et al., 1983), but almost always as a proxy for left atrial volume (see Chapter 3). It was not until the 1990s that scientists noticed regional differences in mammalian left atrial tissue (Hoit and Walsh, 1992). Ten years later, clinicians applied advanced ultrasound (tissue Doppler) to study regional function, comparing atrial motion between regions (Thomas et al., 2003). Studies in the last ten years have used tissue Doppler, speckle tracking, and MRI to analyze regional motion.

Because the atrium has passive and active phases, there is no single measure of regional function nor an agreed-upon standard of measurement. Previous studies measured regional expansion during atrial filling and regional contraction during active emptying. These studies measured strain (Sirbu et al., 2006), strain rate (Thomas et al., 2007), and tissue velocity (Boyd et al., 2008) with tissue Doppler, as well as strain (Henein et al., 2012; Vianna-Pinton et al., 2009) and strain rate (Inaba et al., 2005) with speckle tracking and feature tracking in MRI (Nori et al., 2009). Despite the lack of standards, there is a remarkable consistency in regional analysis. Over ten studies in the past ten years have all found the highest function in the lateral and inferior walls. These studies used multiple 2-D views of the heart to estimate regional function. Although they provide insight, these 2-D approaches are limited by available acoustic windows and ignored out-of-plane motion. We sought a three-dimensional method that could avoid these pitfalls and accurately quantify motion heterogeneity.

Many 3-D techniques for measuring regional mechanics, such as 3-D speckle tracking,

cardiac magnetic resonance (CMR) tagging, and cine displacement encoding stimulated echo (DENSE) CMR, have been successfully used to study regional function in the left ventricle. However, their application is limited in the atrium by its thin walls, which are typically only 2-3 mm thick. Spacing of CMR tags in human subjects is typically greater than 5 mm (Liu et al., 2006; O'Dell et al., 1995), while current implementations of 2-D and 3-D DENSE CMR use image resolutions of 2.8 mm (Spottiswoode et al., 2007; Zhong et al., 2010), neither of which could accurately capture atrial motion. We therefore used an alternative wall motion-based approach to measure 3-D regional function in the atrium. It avoided the resolution limitations of strain-based measurements by collecting a series of higher-resolution 2-D cine CMR images. We used the methods detailed in Chapter 4 to fit a surface to this data and generate a continuous representation of the left atrial endocardium in space and time. We then tracked the surface motion through the cardiac cycle to quantify regional function in healthy adults.

5.2 Methods to acquire and process images

We used cardiac magnetic resonance (CMR) to image the left atrium. These images captured the left atrial blood pool and endocardial wall. We manually traced each image, then fit the tracings to a surface mesh discussed in the previous chapter.

5.2.1 Image acquisition

All studies were approved by the University of Virginia Institutional Review Board (IRB). Ten healthy subjects (n=10) were recruited from the University of Virginia Health System for a research CMR scan with informed consent. All scans were performed on a 1.5-T Magnetom Avanto (Siemens Healthcare, Erlangen, Germany). A steady-state free precession (SSFP) imaging sequence was employed, with a median flip angle of 71 (range 48, 79) degrees, repetition time of 39 (30, 45) ms, and echo time of 1.4 (1.1, 1.6) ms. Electrocardiographic

gating was used in a slice-selective imaging acquisition during held expiration with a 6mm slice thickness. A single slice was acquired in the sagittal and coronal planes, as well as the left vertical long-axis (2 chamber), the parasternal long-axis (3 chamber) and horizontal long-axis (4 chamber) planes relative to the heart. A stack of slices was acquired in the axial plane with no interslice gap. Roughly 15-20 axial images were acquired to ensure adequate coverage of the left atrium. The field of view varied depending on the imaging plane, but was approximately 300x300 mm, and the pixel size was 1.2x1.2 mm, where the RF bandwidth was 930 Hz/pixel. Each imaging sequence was reconstructed into 25 time phases, equally spaced across the cardiac cycle based on the R-R interval.

5.2.2 Image processing

CMR images were manually contoured using ARGUS software (Siemens Healthcare) and the open-source SEGMENT software (Heiberg et al., 2010). We developed a standardized contouring process in an attempt to reduce inter-operator variability. The left atrium was isolated in the viewing window by centering and magnifying the image. Operators were trained to trace the edge between bright blood and dark surrounding tissue, which best represents the left atrial endocardial surface (Fig. 5.1). Areas where this edge was absent, specifically the mitral valve orifice, pulmonary vein ostia, and left atrial appendage orifice, required special instruction. Operators were instructed to exclude the left atrial appendage by drawing the contour from the left atrial tissue separating the left pulmonary veins and the left atrial appendage to the intersection of the left atrial appendage and anterior-superior wall (Fig. 5.1a,b,c). For the mitral valve, operators were instructed to draw contours that crossed the mitral valve annulus into the ventricular cavity along the direction of neighboring atrial endocardium (Fig. 5.1e). Contour points below the mitral valve plane were later removed and replaced with a mitral valve cap (§5.2.3).

Four pulmonary vein and four mitral valve landmarks were identified at each phase in the cardiac cycle. Three of the four pulmonary veins, including right superior, right inferior,

and left inferior, were identified using the stack of axial plane images (Fig. 5.1b,c,d). The left superior pulmonary vein was identified using the coronal imaging plane (Fig. 5.1a). Two mitral valve points (lateral and septal) were identified using the horizontal long-axis (4 chamber) plane (Fig. 5.1f), and two (superior and inferior) were identified using the left vertical long-axis (2 chamber) imaging plane (Fig. 5.1e).

5.2.3 Left atrial coordinate system

Contoured and landmarked images were imported into MATLAB r2012a (The MathWorks, Natick, MA, USA), with each contoured pixel treated as a single data point (Fig. 5.2a). We used the landmarks to create a time-varying coordinate system that accounted for rigid-body motion (Fig. 5.2b). First, pulmonary vein and mitral valve planes were fit to their respective landmarks. The plane center was defined as the centroid of each landmark group. A vector between the plane centers formed the z-axis of the coordinate system. This axis controlled for tilting of the heart during the cardiac cycle. The pulmonary vein plane required at least 3 landmarks, but could accept more, accommodating variable pulmonary vein anatomy; the left and right pulmonary vein centroids were calculated separately and averaged to find the plane center. A vector from the right pulmonary vein centroid to the left pulmonary vein centroid defined the x-axis, controlling for rotation of the heart. The remaining axis (y) was calculated as the vector cross-product. The bisection of the pulmonary vein-mitral valve axis established the origin of the coordinate system (Fig. 5.2b, gray arrows) and controlled for translation of the atrium during the cardiac cycle.

We introduced an artificial mitral valve "cap" to standardize behavior of the fits near the mitral valve orifice (Fig. 5.1c). Mitral valve annulus points were identified at the intersection between the mitral valve plane (Fig. 5.2b) and imaging plane contours. Contour points falling beyond the mitral valve plane were removed and replaced with an artificial point set. To ensure a smooth boundary, the position and direction of the left atrial wall immediately adjacent to the annulus were used in a 1-D cubic Hermite function (see Chapter 4) to generate

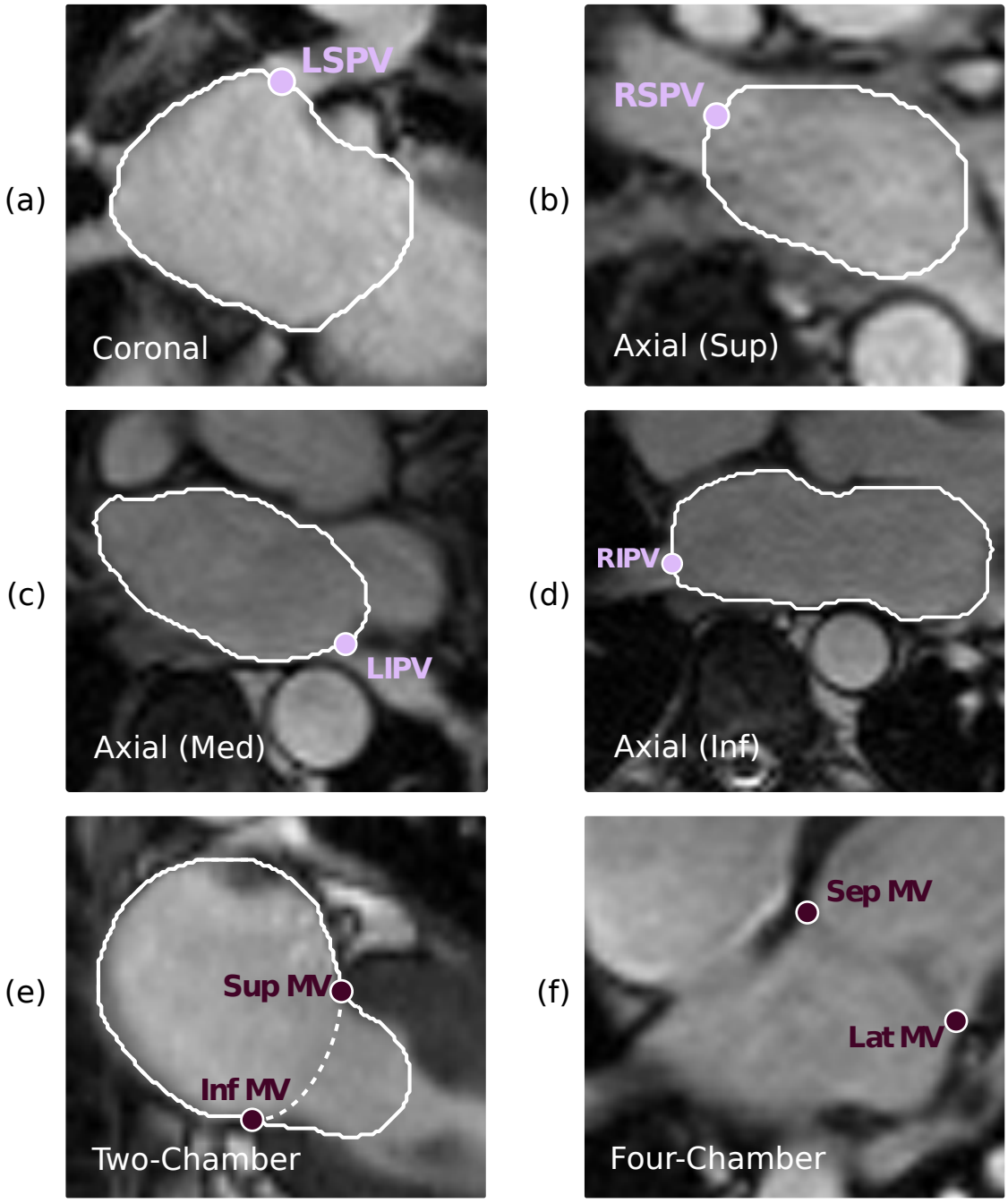

Figure 5.1: SSFP cineMR images were acquired in six cardiac planes, four of which are shown here. (a) Coronal view with left superior pulmonary vein landmark. Contour trace ignores left atrial appendage. (b) Axial view (superior aspect) with right superior pulmonary vein landmark. (c) Axial view (medial aspect) with left inferior pulmonary vein landmark. Contour trace ignores left atrial appendage. (d) Axial view (inferior aspect) with right inferior pulmonary vein landmark. (e) Vertical long-axis (2-chamber) view with superior and inferior mitral valve landmarks. Mitral valve cap (dotted line) corrects tracing below MV (solid line). (f) Horizontal long-axis (4-chamber) view with lateral and septal mitral valve landmarks.

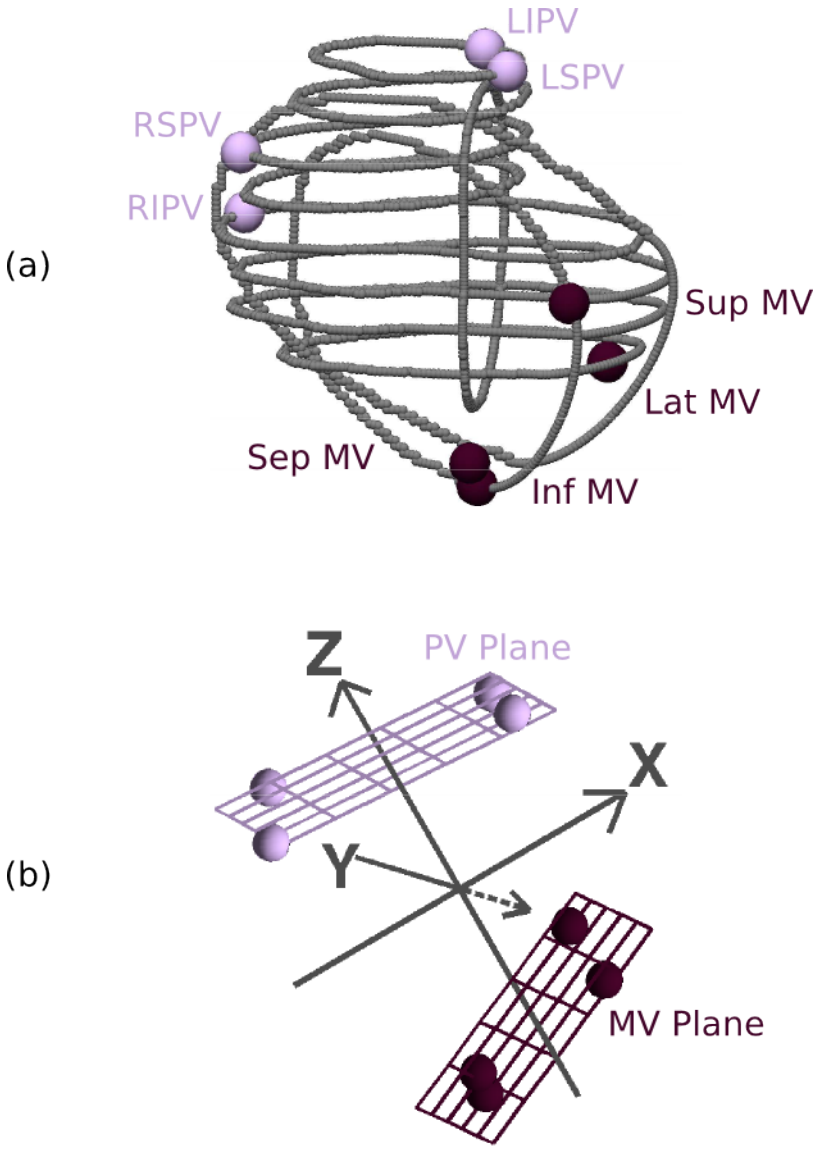

Figure 5.2: A left atrial coordinate system built using pulmonary vein and mitral valve annulus landmarks. (a) Contoured and landmarked pixels from left atrial MR images were imported into MATLAB and combined into a single 3-D data cloud. Four pulmonary vein landmarks and four mitral valve annulus landmarks are labeled accordingly. (b) A 3-D Cartesian coordinate system is defined using landmark planes and centroids.

the cap. The number of artificial points was scaled based on the distance between the annulus points.

5.2.4 Breathing artifacts

We used breath holds to control the position of the diaphragm during imaging. Breathing inconsistently (not fully exhaling) changed the position of the atrium between images. A change in atrial position resulted in a shift of one traced contour relative to other contours in the set. To assess the potential role of breath-hold artifacts, we measured the distance between contours along their line of intersection. Overlapping contours intersected at two points, so each pairing produced two measurements of shift. We expected variations in breath-holds to rigidly translate a contour relative to another, so we calculated the mean of and difference between the two distances, then searched for high-mean, low-difference shifts. Since breath-hold artifacts should shift one contour throughout the cardiac cycle, we averaged these measures through time. This process was repeated for every contour in a data set. The distances were compiled and analyzed for outliers with systematic shifts relative to other contours. These outliers were flagged for removal from the data set.

5.2.5 Contour areas and volumes

Prior to fitting a surface, we calculated the area of traced contours and the volume of contour stacks. These measures were used to quantify variation between operators and to validate the volumes of fitted surfaces. Contour areas were computed for every traced image at every time point in the cardiac cycle. We computed the area by calculating the contour centroid, then summed the areas of triangles formed from neighboring contoured pixels and the centroid (similar to a Delaunay triangulation). Contour area below the mitral valve plane was discarded. We used the stack of axial images to compute a contour volume. We scaled the contour area on each axial slice by its slice thickness, accounting for any gaps between slices. We then summed these slice volumes to estimate the contoured atrial volume.

5.2.6 Operator comparison

Inter-observer agreement in slice contour area and atrial volume was determined in a two-operator comparison using a subset of the CMR data (eight data sets). The operators contoured the eight atria at minimum and maximum atrial volumes (ventricular end diastole and end systole, respectively). We compared individual contours traced by the two operators using a Bland-Altman analysis of contour areas, including all axial and non-axial imaging planes. We also compared the axial stack volumes using a Bland-Altman analysis. We calculated operator error as a percentage of the mean area and mean volume, respectively.

5.3 Image processing results

We recruited ten healthy subjects from the UVa Health System, eight of whom were male. The subjects were 30.6 ± 3.0 years old with an average weight of 72.5 ± 9.9 kilograms. Height was not recorded for all subjects, so body-mass index and body surface area could not be calculated. We reported the results of image acquisition and processing. All results are for $n = 10$ healthy subjects and reported as an average $\pm$ standard deviation unless otherwise noted.

5.3.1 Left atrial coordinate system

We used anatomic landmarks to create a coordinate system that removed bulk chamber motion. To confirm this, we tracked landmark motion through a single cardiac cycle. The centroid of the pulmonary vein plane translated a small amount during the cardiac cycle (0.9 ± 1.5 mm at peak, Fig. 5.3a). The centroid of the mitral valve plane moved much more (13.1 ± 3.0), especially along the PV-MV axis (12.1 ± 2.9 mm; Fig. 5.3b). Motion of the mitral valve annulus landmarks was not uniform; the inferior MV landmark moved the most (15.8 ± 3.5 mm) and the septal MV landmark the least (9.4 ± 3.4 mm), indicating tilting of the mitral valve plane relative to the pulmonary vein centroid (Fig. 5.3c).

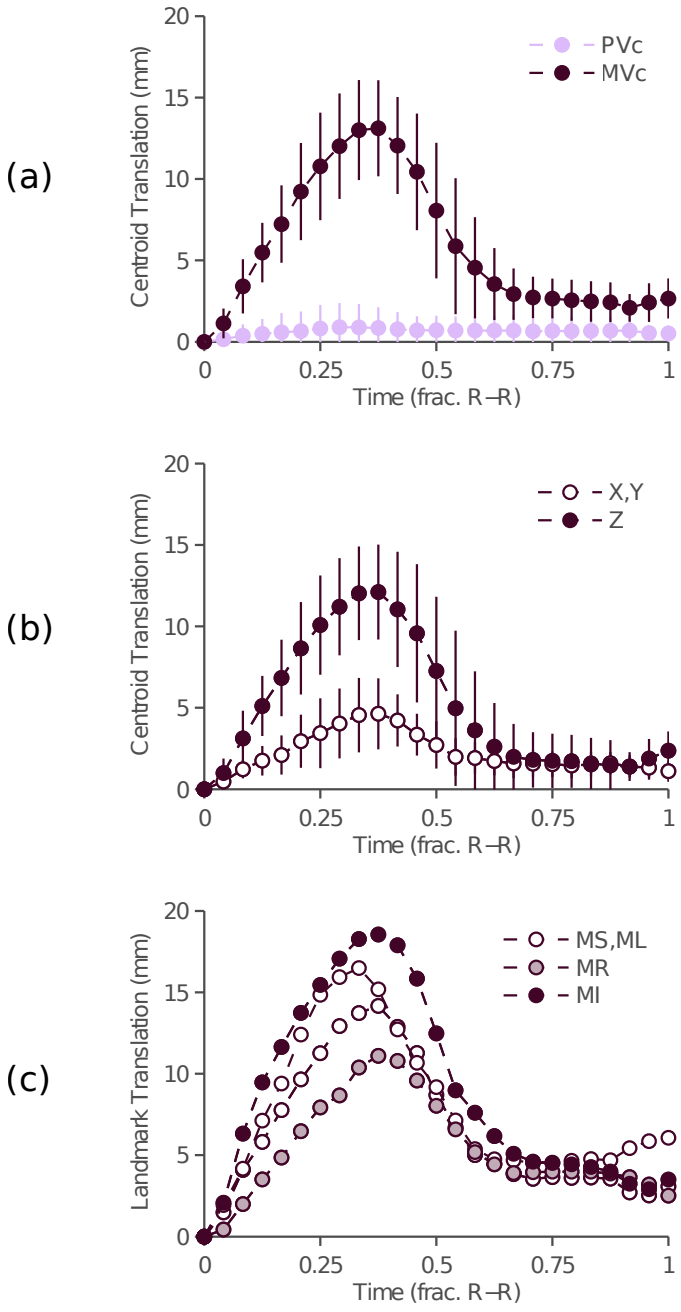

Figure 5.3: MR image landmarks adjust for rigid-body motion in the atrium. (a) The mitral valve plane centroid (MVc) moves the most during the cardiac cycle, while the pulmonary vein plane centroid (PVc) remains relatively stationary. (b) The mitral valve centroid predominately moves along the PV-MV axis (the z-axis of our coordinate system), with a slight tilting effect in the X-Y plane. (c) Individual mitral valve landmarks highlight this tilting. The inferior mitral valve landmark (MI) moves the most during the cardiac cycle, while the septal mitral valve landmark (MR) moves the least.

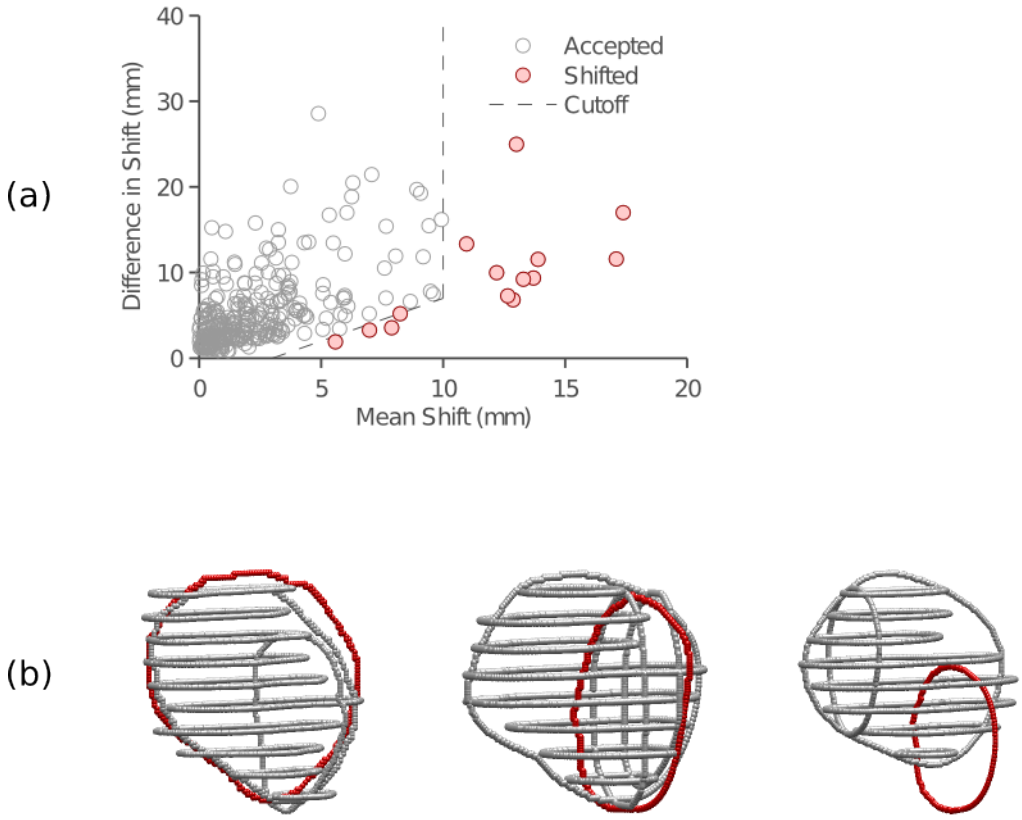

Figure 5.4: Slice misalignment was present in 3% of all contoured images, most likely caused by breath-hold artifacts during acquisition. (a) We identified potential breathing artifacts based on systematic shifts in image contours relative to other contours in the set. Contours that had systematically shifted (a large shift with a low difference between intersection points) were flagged as "shifted". We flagged any shift greater than 10 mm, or any shift greater than 3 mm with a difference less than the mean shift (dotted line). (b) Three data sets with the worst breath-hold artifacts were identified, with the shifted slice highlighted in red. In two data sets, the shifted slice was the coronal plane, while the third was the 2-chamber view.

5.3.2 Breathing artifacts

We tested for the presence of breathing artifacts by measuring 287 intersections of 119 contours. We then plotted the mean of and difference between the two shifts for each contour (Fig. 5.4a). The average "mean shift" was 2.7 ± 3.0 mm or about two image pixels, with an average "difference in shift" of 5.7 ± 4.5 mm between pairs consistent with the expected pattern of intersection differences due to small, random digitizing errors. We identified breath-hold misalignments as any large magnitude shifts greater than 10 mm, as well as smaller, consistent shifts greater than 3 mm (Fig. 5.4a, dotted line). This cutoff isolated 14 of the 287 intersections as having a potentially significant shift. Within the 14 isolated points, there were 3 imaging planes that shifted against multiple other views. Thus, of the 119 slices tested, only three (3%) showed clear evidence of translation against more than one other slice in the same set (Fig. 5.4b). We tested the influence of shifted contours by removing them and refitting the reduced data set (see §5.5.1).

5.3.3 Operator comparison

Operators followed instructions to exclude the left atrial appendage and include the MV plane, tracing into the left ventricle (Fig. 5.5a,b). The artificial MV cap (dotted line) successfully corrected for variable tracing extensions past the MV plane, producing a similar cap even when the two observer tracings were quite different (Fig. 5.5b). We compared the contour areas of each operator in a Bland-Altman plot (Fig. 5.5c). The average difference in area was $1.4\,\mathrm{cm}^2$ (8.6% of mean slice area), with a confidence interval of $\pm 3.4\,\mathrm{cm}^2$. We then compared atrial volumes, based on axial stack volumes, and found a small difference between operators (5.9 mL, with a 95% CI of ± 8.3 mL), which represented 9.0% of the mean volume (Fig. 5.5d). We found a strong concordance between operators based on the concordance correlation coefficient (Lin, 1989), which was greater than 95% for atrial volumes ($p_c = 0.97$) and slice areas ($p_c = 0.96$).

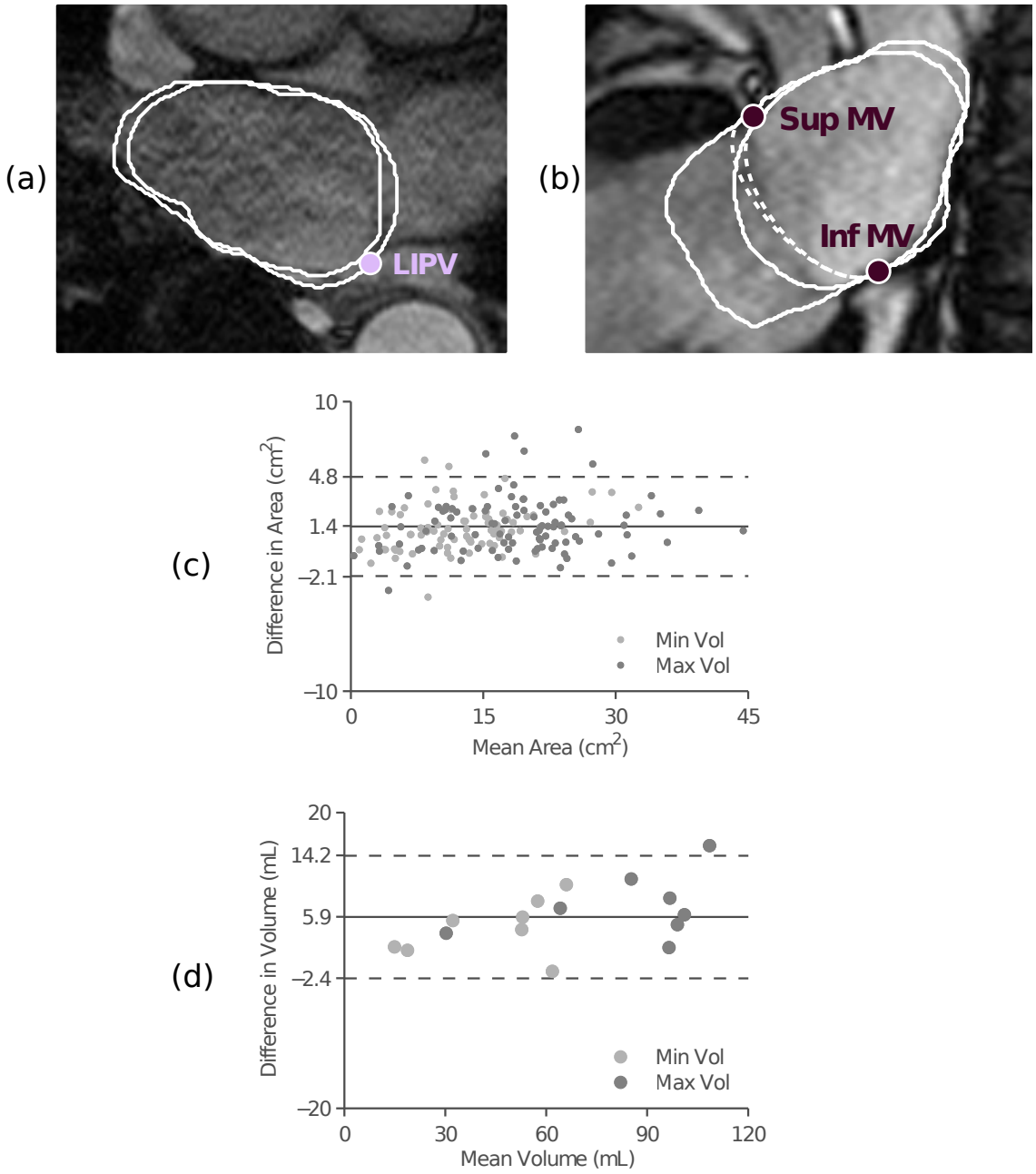

Figure 5.5: Inter-operator variability was the largest source of variation in wall motion measurements, but was minimized using standardized instructions. (a,b) Traces of two operators (solid white lines) follow standards of removing left atrial appendage (a) and tracing through the mitral valve plane (b). The mitral valve cap (dotted lines) successfully standardizes contours below the mitral valve plane. (c) Eight atria were traced by two operators at the minimum and maximum atrial volumes, then compared based on contour area using Bland-Altman analysis. (d) Bland-Altman analysis of atrial volumes, based on summation of axial contour areas. Solid line represents mean difference, and dotted lines represent 95% confidence interval about that mean.

5.4 Methods to fit and quantify a left atrial surface

We fit the traced contours to a spherical surface mesh described in Chapter 4. We transformed the contour points to remove rigid body motion (Fig. 5.6a). We then applied the mitral valve cap to all contours below the MV plane. We repeated these steps for each of the 25 time points in the data set. Because cardiac motion is cyclic, data at the beginning and the end of the cardiac cycle should be close to equivalent. To enforce this, we "padded" the data by replicating the first three time points at the end of the data set and the last three time points at the beginning, creating 31 time points from a 25 time point set.

5.4.1 Mesh creation and optimization

Because the left atrium is roughly spherical, we performed all fitting in spherical coordinates (θ, ϕ, r, t). We represented the endocardium with a finite-element mesh (Fig. 5.6b) where the radius varies as a function of space and time, $\hat{r} = \hat{r}(\theta, \phi, t)$. We used cubic Hermite basis functions to describe the variation of $\hat{r}$ in spatial dimensions (θ, ϕ) and a Lagrangian basis to describe variation through time. Element density and smoothing constraints were set based on the optimized mesh in Chapter 4. We projected all data points radially onto the finite element mesh based on their (θ, ϕ, t) position in spherical space and time (Fig. 5.6c). By projecting through the fitted dimension we ensured a single, constant set of element coordinates (ξ_1, ξ_2, ξ_3) for each data point. The overall interpolation function for an element is

$$\begin{aligned}\hat{r}(\xi_1,\xi_2,\xi_3) = \quad & r_{ijk}\mathrm{H}_i^0(\xi_1)\mathrm{H}_j^0(\xi_2)\mathrm{L}_k(\xi_3) + \left.\frac{\partial r}{\partial \theta}\right|_{ijk} S_\theta \mathrm{H}_i^1(\xi_1)\mathrm{H}_j^0(\xi_2)\mathrm{L}_k(\xi_3) + \\ & \left.\frac{\partial r}{\partial \phi}\right|_{ijk} S_\phi \mathrm{H}_i^0(\xi_1)\mathrm{H}_j^1(\xi_2)\mathrm{L}_k(\xi_3) + \left.\frac{\partial^2 r}{\partial \theta \partial \phi}\right|_{ijk} S_\theta S_\phi \mathrm{H}_i^1(\xi_1)\mathrm{H}_j^1(\xi_2)\mathrm{L}_k(\xi_3)\end{aligned} \tag{5.1}$$

where $i = \{0, 1\}$, $j = \{0, 1\}$, $k = \{0, 1, \ldots, 8\}$, and summation is implied. Scaling factors scale each nodal derivative by the size of the element in the respective direction.

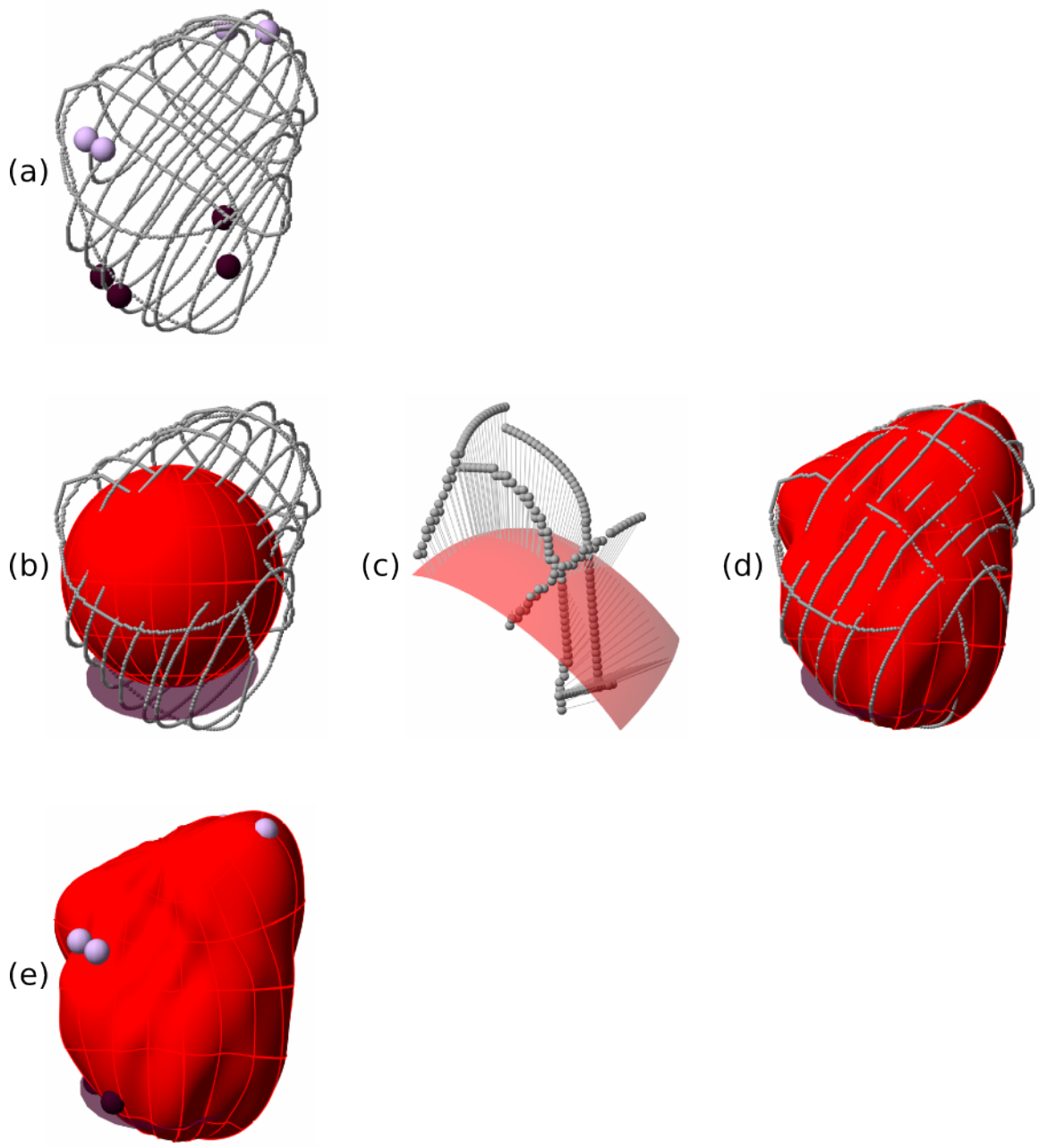

Figure 5.6: Mesh creation, projection, and optimization. (a) An example data set from the atrium of a healthy subject. Pulmonary vein ostia (light pink) and mitral valve annulus (dark maroon) landmarks define a patient-specific time-varying coordinate system. Contour points are shown at a single time point (the maximum volume). (b) A 108-element static spherical mesh (red) is generated in the transformed coordinate system. Elements (red lines) are equally spaced in spherical coordinates (θ, ϕ). (c) Contour points are assigned to an element based on their spherical position and projected along the fitted dimension (radius) onto the surface (gray lines). (d) Mesh parameters are optimized to minimize the error between contour point radii (gray points) and projected mesh radii (red surface). (e) The final mesh is a continuous surface in space and time.

We fit the mesh using Newton's method (Fig. 5.6d,e). Constraints were applied at the poles as described in Chapter 4. The ten data sets had $63,000 \pm 14,000$ points (range 35,000 to 83,000). All MATLAB processing was done on a 2.4 GHz Intel quad-core (i7) processor with 4 GB RAM running Mac OS X 10.7.

5.4.2 Quantifying global and regional left atrial motion

Using the fitted surface, we computed left atrial chamber volume by numerical integration. We divided the surface into a dense collection of triangles. Each triangle was paired with the coordinate origin to create a set of non-overlapping tetrahedrons. Since the coordinate origin is $(0, 0, 0)$, the volume of each tetrahedron reduces to ⅙ of the scalar triple product of its three non-zero vertices. This formula was repeated for every tetrahedron on the surface and the volumes were summed. Phasic changes in atrial volume were calculated from the peaks and valleys of the volume-time curve (Fig. 5.7a). We identified the start of active contraction using the first and second derivatives of the volume-time curve (a peak was not always present at the start of contraction). Fractional changes in volume were computed by normalizing those phasic changes to a reference volume for that subject.

Because the atrium is both passive and active, there is no single measure of atrial function. We identified three key points in the cardiac cycle to separate the passive and active components. At the start of ventricular systole (mitral valve closure), the atrium was at its minimum volume (V_{min}) and began to fill. It reached a maximum volume (V_{max}) as the mitral valve opened. The atrium emptied passively (E-wave) during early ventricular diastole until the LA and LV pressures equalized and the left heart reached diastasis (V_{preA}). The atrium then contracted and actively pumped blood (A-wave) during late ventricular diastole. It reached a minimum volume at the end of contraction (V_{min}) as the cycle repeated. Phasic changes in volume were calculated as the difference between these points, listed in Table 5.1. To calculate fractional measures, we simply normalized those changes in volume to a reference volume. Because we were interested in comparing the active and passive components of flow,

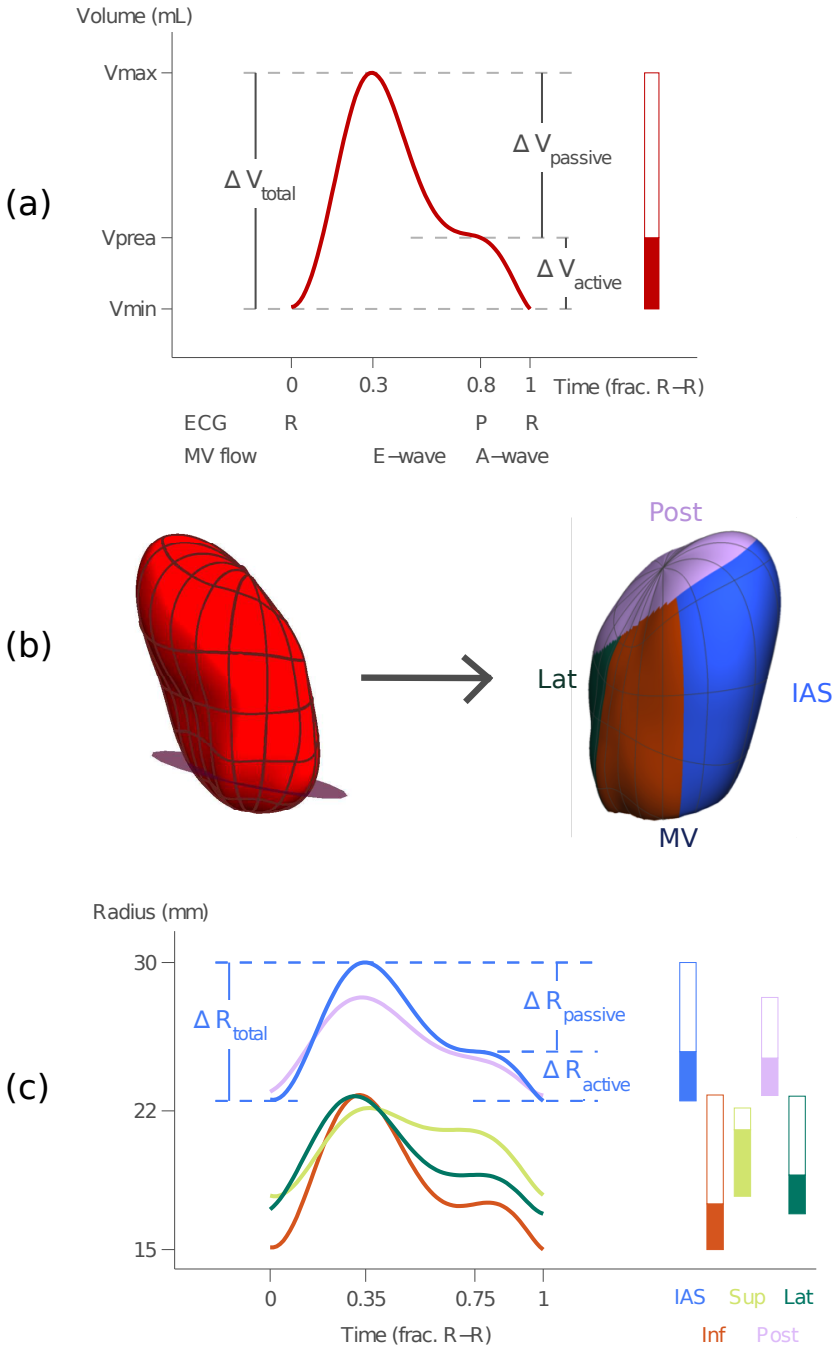

Figure 5.7: Quantification of left atrial motion. (a) Volume is calculated from surface integration at 100 time points through the cardiac cycle. The volume-time curve reveals the maximum and minimum volumes (V_{max} and V_{min}), as well as the start of contraction (V_{preA}). Phasic changes in volume are calculated based on these points, including active emptying as a portion of the total (red bar). (b) The surface is segmented into 6 regions. (c) Regional radius-time curves are calculated similarly to the volume-time curve. Radius-time curves follow a similar pattern of filling and emptying, but with differences in size, motion, and timing of contraction.

Metric	Formula	Abbrev.
Total Emptying Volume	$V_{max} - V_{min}$	ΔV_t
Passive Emptying Volume	$V_{max} - V_{preA}$	ΔV_p
Active Emptying Volume	$V_{preA} - V_{min}$	ΔV_a
Fractional Measures		
Total Emptying Fraction	$\Delta V_t / V_{max}$	EF_t
Passive Emptying Fraction	$\Delta V_p / V_{max}$	EF_p
Active Emptying Fraction	$\Delta V_a / V_{preA}$	EF_a
Passive Emptying as a Fraction of Total	$\Delta V_p / \Delta V_t$	$V_{p\|t}$
Active Emptying as a Fraction of Total	$\Delta V_a / \Delta V_t$	$V_{a\|t}$

Table 5.1: Measures of atrial function, including passive and active components. Measures are based on maximum and minimum volumes identified in the volume-time curve. Phasic changes in volume are reported in milliliters and fractional measures are reported as a true fraction or a percentage (metric x 100%).

we also calculated passive and active emptying as a portion of the total emptying volume (Fig. 5.7a, red bar).

To measure regional motion, we first segmented the fitted surface into six anatomic regions. We used the digitized landmarks (pulmonary veins and mitral valve annulus) to define the posterior wall (the pulmonary valve plane) and mitral valve plane (Fig. 5.2b). Between these two planes, we separated the surface into four midwall regions based on 90-degree rotations about the pulmonary vein-mitral valve (z) axis, offset by 45 degrees from the right-to-left pulmonary vein (x) axis. This defined the inferior wall, intra-atrial septum, superior wall, and lateral wall (Fig. 5.7b). Naming conventions for regions in the atrium were not consistent in the literature, and there is a dearth of standards regarding their definition. The superior wall is also the anterior wall. The lateral wall is sometimes called the free wall. The intra-atrial septum is referred to as the IAS or simply the septal wall. Electrophysiologists refer to the superior aspects of the chamber as the "roof" of the atrium. Others treat the inferior wall as part of the posterior wall. We resolved all naming discrepancies prior to comparing our results with others.

We measured regional function by tracking the average radius of a region through time. To do this, we generated a dense grid of interpolated points (100 per element) in each region, computed the surface area surrounding each point, then averaged the point radii weighted by their surface area. Phasic changes in regional radii were calculated from the peaks and valleys of the radius-time curves (Fig. 5.7c). Similar to the volume-time curve, we used the first and second derivatives of the radius-time curve to identify the start of active contraction. We identified three points (R_{min}, R_{max}, and R_{preA}) and computed the same functional measures used for volume (Table 5.1). To visualize these measures on 2-D maps and estimate their spatial variation, we calculated the metrics for individual grid points prior to averaging.

To create an averaged surface of healthy subjects, we averaged nodal parameters for all the fitted surfaces in the subject group. We then quantified global and regional motion from the averaged surface as described above.

5.5 Healthy left atrial wall motion results

Data sets converged in under 5 minutes to a RMSE of 2.0 ± 0.5 mm (range 1.3 to 3.0 mm). Fitted regional radii varied between 9 and 35 mm with a mean of 23 mm. We observed the largest errors at (θ, ϕ) positions where contours from different imaging planes overlapped but disagreed. This disagreement could have arisen from random errors such as contouring error or beat-to-beat variations in left atrial motion, or due to a shift of one slice relative to others induced by variable diaphragm position during held-expiration image acquisition.

5.5.1 Breathing artifacts

Earlier, we quantified contour shifts potentially caused by variable diaphragm positions (§5.3.2). For each flagged data set, we tested the potential impact of the shift by translating the flagged contour in the imaging plane towards a better match with other contours, reprocessing the adjusted data sets, and comparing the results (maximum volume and total

emptying fraction) to the original results. The corrections removed over 50% of the shift artifact, reducing the mean translation from 15 mm to 6 mm, on average. In two of the three data sets (Fig. 5.4b), maximum volume and total emptying fraction deviated by less than 1%. Regional R_{max} and REF_t deviated by less than 4%. The 3^{rd} data set (Fig. 5.4b, right) had a very large shift that did significantly affect results (3% deviation in EF_t, 11% deviation in REF_t). Because we only found evidence of a shift large enough to influence our analysis in this single imaging plane, and because another study showed that our analysis is not particularly sensitive to omitting data from any one plane (§5.5.4), we decided to drop this single misregistered plane from the final analysis rather than try to"adjust" apparent breath-hold errors on an ad hoc basis.

5.5.2 Quantitative analysis of left atrial volumes

We compared atrial volumes computed by summing axial contours to volumes computed by integrating the fitted 3-D surface. As expected, the two methods generally agreed, and the fitted volumes were smoother in time (Fig. 5.8a). Fitted volumes correlated well with summed axial volumes (Fig. 5.8b, $R^2 = 0.92$). A Bland-Altman analysis (Fig. 5.8c) showed a small positive offset of 8.4 ± 0.3 mL for fitted volumes (mean $\pm$ std. error). The changes in atrial volume during a normal cardiac cycle were divided into three phases: filling (ventricular systole), passive emptying, and active emptying (atrial contraction) (Fig. 5.7a). These three phases were consistently observed in all subject atria, but varied in duration and magnitude. Maximum atrial volumes ranged from 41 to 100 mL, with a mean of 71 ± 18 mL. Total emptying fraction ranged from 46 to 72%, with a mean of $60 \pm 9\%$. Of this total emptying, $32 \pm 9\%$ was active ($V_{a|t}$), ranging from 20 to 49% (see Table 5.2).

5.5.3 Quantitative analysis of regional motion

Average regional radius curves followed similar patterns of filling and emptying (Fig. 5.7c) compared to atrial volume (Fig. 5.7a), and similarly had both passive and active emptying

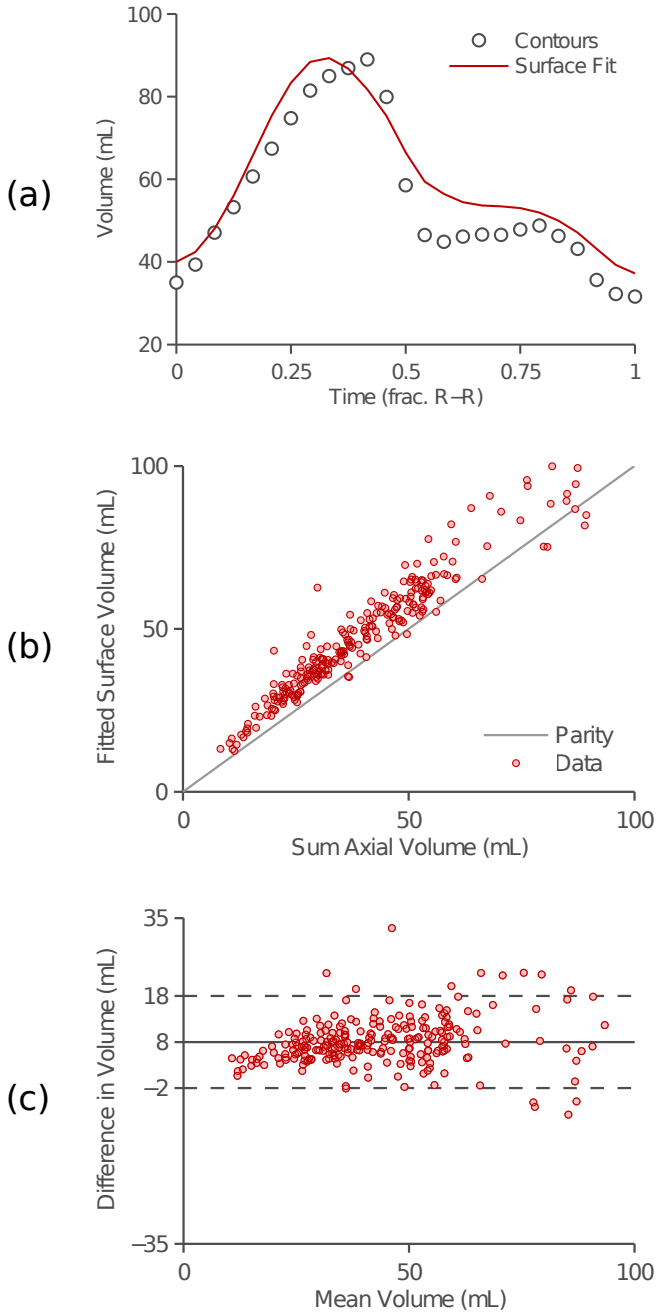

Figure 5.8: Left atrial surface volumes matched volumes calculated from the summation of a stack of axial images. (a) An example subject shows a good match between the surface fit volume and the axial stack volume through the cardiac cycle. (b) Surface volumes correlated with axial stack volumes for the full range of atrial sizes. (c) Surface volumes were slightly larger than axial stack volumes (+8 mL) based on a Bland-Altman analysis.

Metric	Mean ± S.D.	Range
V_{max} (mL)	71 ± 18	$(41, 100)$
V_{min} (mL)	29 ± 11	$(11, 53)$
V_{preA} (mL)	43 ± 15	$(18, 65)$
Changes in Volume		
ΔV_t (mL)	42 ± 11	$(29, 59)$
ΔV_p (mL)	28 ± 7	$(15, 36)$
ΔV_a (mL)	14 ± 6	$(6, 27)$
Fractional Measures		
EF_t (%)	60 ± 9	$(46, 72)$
EF_p (%)	41 ± 9	$(23, 56)$
EF_a (%)	32 ± 9	$(19, 50)$
$V_{p\|t}$ (%)	68 ± 10	$(51, 80)$
$V_{a\|t}$ (%)	32 ± 10	$(20, 49)$

Table 5.2: Global function in ten healthy subjects, including passive and active components. Phasic changes in volume are reported in milliliters and fractional measures are reported as percentages.

phases. The timing and magnitude of emptying varied substantially among regions. We mapped regional data onto a 2-D Hammer projection (Yang et al., 2000) to display the entire left atrial surface (Fig. 5.9a,b). We projected the total radial emptying (ΔR_t), total radial emptying fraction (REF_t), and active emptying as a fraction of the total ($R_{a|t}$) of 10,800 surface points (100 per element) as Hammer maps (Fig. 5.9c,d,e, respectively). The orientation of the Hammer map followed our coordinate system (Fig. 5.2b), where the z-axis extended from the pulmonary vein plane to the mitral valve plane, or from the North to South pole of the map. Total radial emptying was greatest (dark blue) in the inferior wall, and least (light blue) in the superior wall. Although total radial emptying was lower in the superior wall, almost all of the emptying occurred during atrial contraction (Fig. 5.9e). Selected measures of regional motion are summarized in Table 5.3. We performed a repeated-measures 1-way ANOVA for each metric (subject x region), and reported the significance of regional

Regional	*Region* (Mean ± S.D.)					ANOVA
Metric	Posterior	Inferior	Septal	Superior	Lateral	p-value
R_{max} (mm)	30 ± 4	24 ± 3	$\mathbf{31 \pm 2}$	23 ± 3	24 ± 4	< 0.0001
ΔR_t (mm)	6 ± 2	$\mathbf{9 \pm 2}$	8 ± 1	5 ± 1	7 ± 2	< 0.0001
ΔR_a (mm)	2 ± 2	3 ± 1	3 ± 1	$\mathbf{4 \pm 1}$	3 ± 1	< 0.05
			Fractional Measures			
REF_t (%)	19 ± 7	$\mathbf{39 \pm 7}$	25 ± 4	23 ± 6	30 ± 9	< 0.0001
REF_a (%)	8 ± 6	17 ± 8	11 ± 4	$\mathbf{18 \pm 7}$	15 ± 8	< 0.01
$R_{a\|t}$ (%)	35 ± 21	32 ± 13	37 ± 15	$\mathbf{82 \pm 35}$	37 ± 17	< 0.0001

Table 5.3: Regional function in ten healthy subjects, including passive and active components. Phasic changes in radius are reported in millimeters and fractional measures are reported as percentages. A repeated-measures 1-way ANOVA (subject x region) tested the significance of regional differences in motion.

differences in motion. We found significant regional differences in every measure of motion at $p < 0.05$, indicating clear regional heterogeneity in both passive and active components of function.

We analyzed regional motion using both a fixed origin at a constant distance from the pulmonary vein center and a floating origin that moved with the mitral valve (Fig. 5.10). A fixed origin showed the majority of radial emptying and radial emptying fraction occurred around the mitral valve annulus (Fig. 5.10a,b). We expected this based on the motion of atrial landmarks around the mitral valve and pulmonary veins (Fig. 5.3a). Surprisingly, the fixed origin biased $R_{a|t}$ towards the posterior wall, where total motion was the lowest (Fig. 5.10c).

Using local peak detection, we mapped the timing of atrial contraction for each of the 10,800 radial motion points, excluding those where an active contraction peak could not be detected (Fig. 5.11a). To confirm the precision of this dense mapping, we used the average radius of each element to make a coarser map of 108 contraction times (Fig. 5.11b). The dense and coarse maps correlate with one another, confirming the method of peak detection

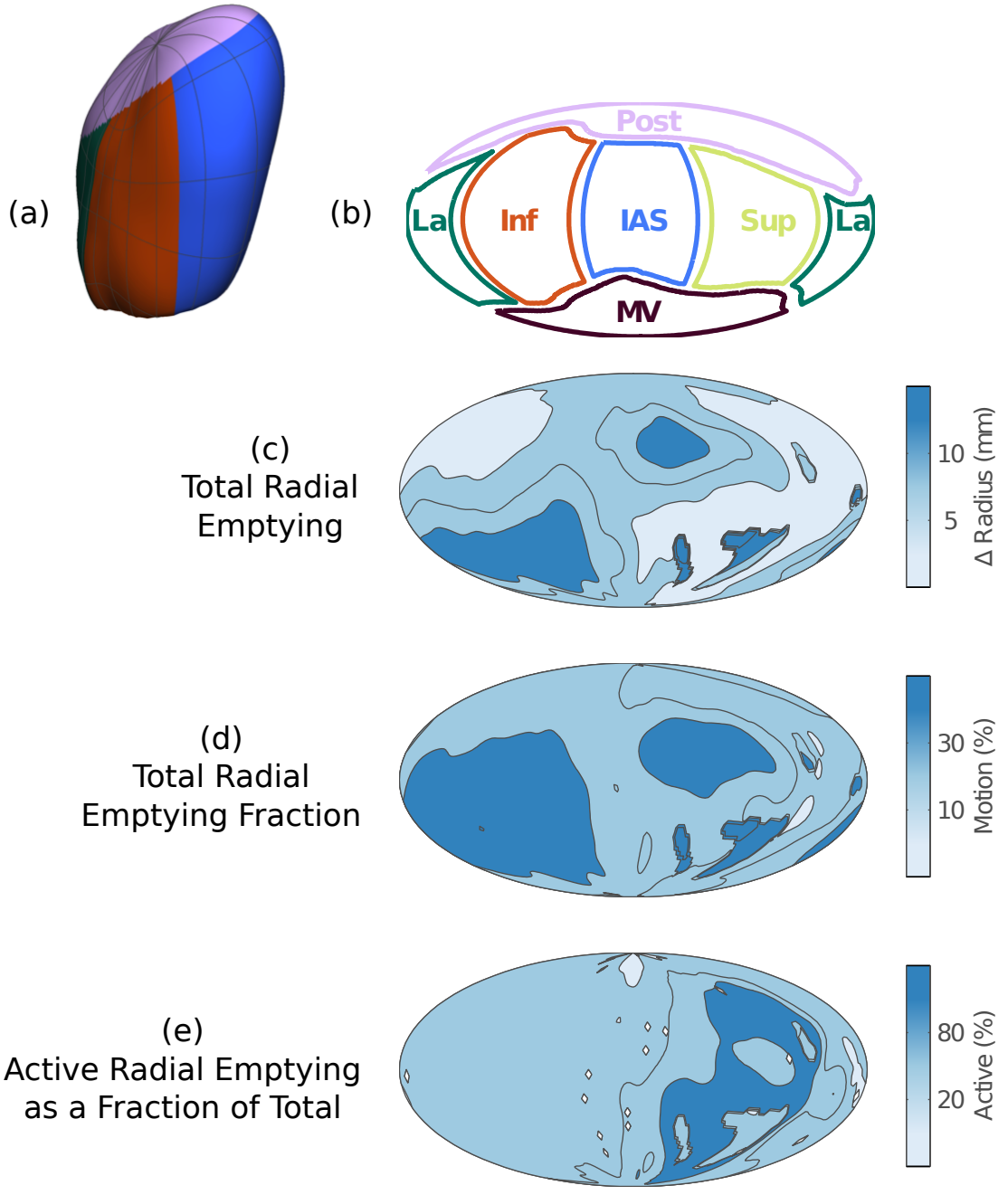

Figure 5.9: Quantification and visualization of regional motion. (a) The left atrial surface was divided into six regions using the left atrial coordinate system. (b) Those regions were projected onto a 2-D map using a Hammer projection. (c) Total radial emptying (ΔR_t) was mapped for 10,800 surface points. Darker blue indicates higher radial motion, which peaked in the annular potion of the inferior and lateral walls. (d) Total radial emptying fraction (REF_t) was mapped in a similar fashion and peaked in the lateral and inferior walls. (e) Active radial emptying as a fraction of total radial motion ($R_{a|t}$) displayed an opposite trend, with peaks in the superior wall and lower values in the inferior wall.

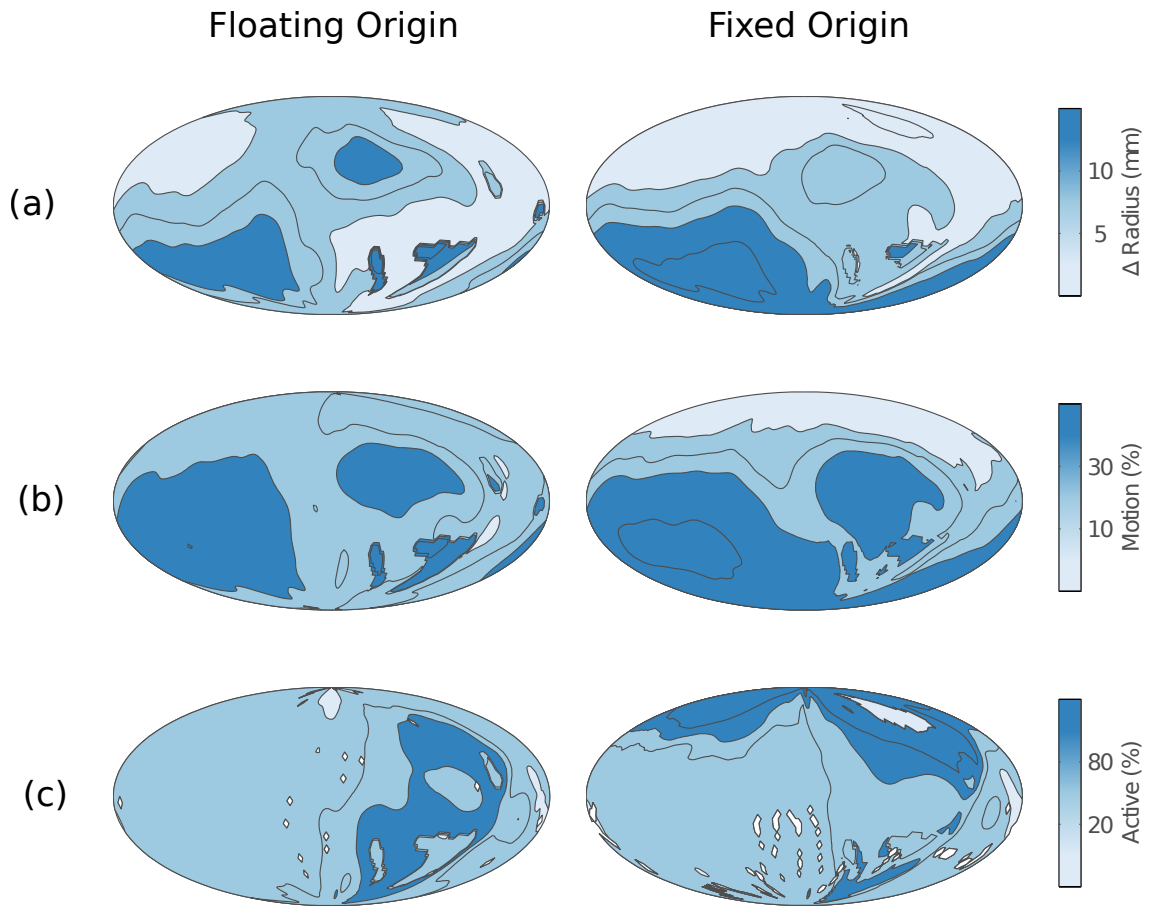

Figure 5.10: The choice of coordinate system origin influenced regional motion maps. We compared a floating origin that moved with the mitral valve to a fixed origin at a set distance from the pulmonary vein plane. (a) Total radial emptying shifted away from the posterior wall and peaked near the mitral valve, as expected based on landmark motion. (b) Total radial emptying fraction followed a similar trend. The fixed origin exaggerated the motion around the mitral valve, but obscured the variation between midwall regions. (c) Active emptying as a fraction of total motion also lost some midwall variation, and instead shifted towards the posterior wall. Total motion around the posterior wall was low in the fixed origin system, so any motion during contraction elevated this ratio.

as an estimate of contraction time, even with finely-sampled points. The patterns of early contraction (orange) appear in the upper superior wall near the right superior pulmonary vein, matching the approximate location of Bachmann's bundle (the preferred pathway of conduction into the LA). Later areas of contraction (purple) include the superior and lateral walls nears the mitral valve, matching the approximate location of the left atrial appendage (known to contract after the LA). We measured timing of contraction in each of the ten subjects, then sorted regional patterns based on their average time of contraction (Fig. 5.11c). A repeated-measures 1-way ANOVA revealed a significant difference between regions ($p < 0.01$). The superior wall tended to contract first, followed closely by the septum. The inferior and posterior walls contracted later, but these patterns were not consistent in all subjects.

5.5.4 Influence of imaging planes

Each imaging plane contributed information to the surface fit, some more than others. We wanted to quantify the value of each imaging plane my measuring its influence on the fitted surface. We quantified the value of each slice by removing it from a data set and refitting the surface. We then measured the deviation in global and regional motion compared to the original, complete data set. Deviations were reported as absolute changes from the original value. Since the axial imaging stack contained a variable number of slices depending on the size of the atrium, we grouped axial images into Inferior, Medial, and Superior groups. The results are summarized in Table 5.4. The coronal and superior axial imaging slices contributed the most to the size of the surface (1.0 mL deviation for both), while the medial axial view was important in measuring motion (1.1 mL deviation in emptying volume). Regional motion matched this ranking with the coronal and medial axial planes contributing the most value to the fit.

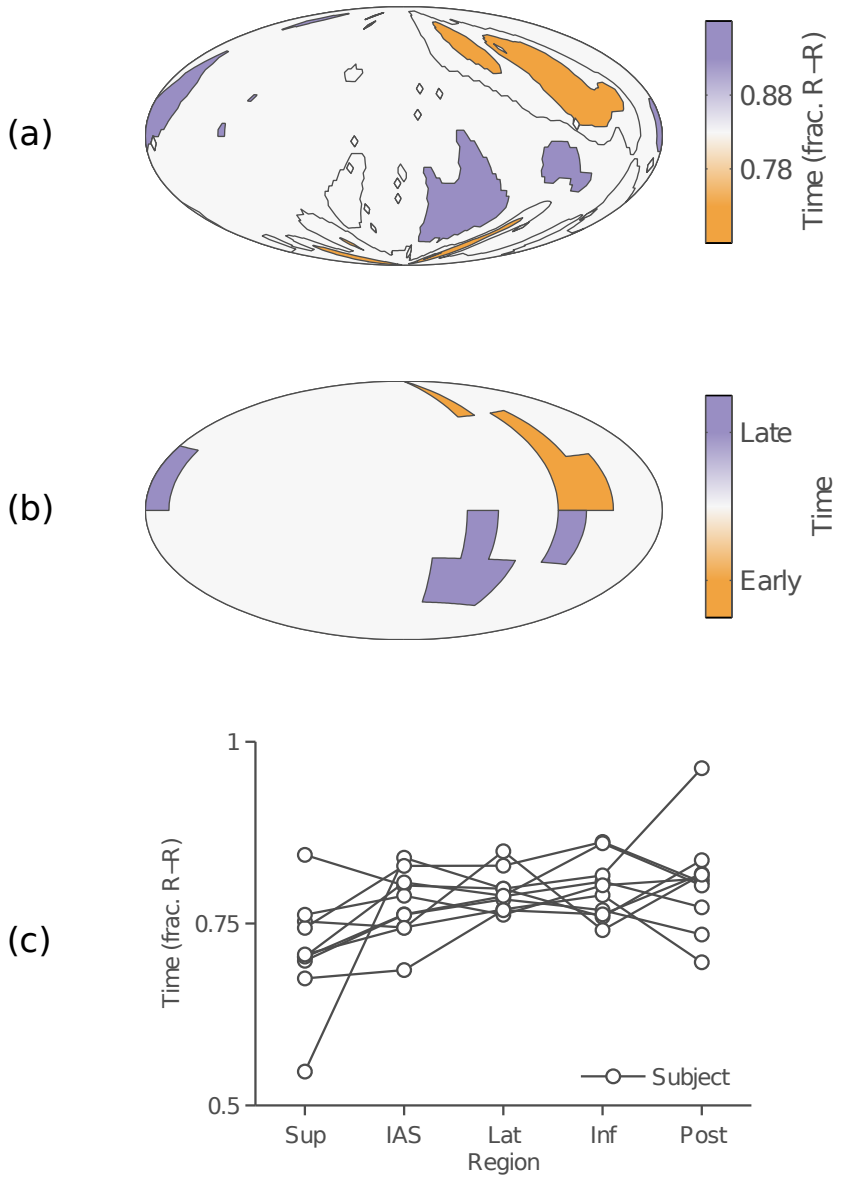

Figure 5.11: Left atrial surface motion captured regional timing of contraction. (a) Timing of contraction was identified in 10,800 radial points using the first and second derivatives of the radius-time curves. Early contraction (orange) starts in the upper septal and superior walls near the right superior pulmonary vein, and ends (purple) in the annular region of the superior wall near the left atrial appendage. (b) Radial motion was averaged for each element, then re-tested with the timing detection algorithm, confirming the results of individual point motion. (c) In healthy subjects, the superior wall generally contracted first and the inferior wall later, although trends were not consistent in all patients.

Imaging Plane	V_{max} (mL)	ΔV_t (mL)	EF_t (%)	ΔR_t (mm)	REF_t (%)
Coronal	$\mathbf{1.0 \pm 0.9}$	0.8 ± 0.8	0.7 ± 0.6	$\mathbf{0.4 \pm 0.5}$	$\mathbf{1.5 \pm 3.0}$
Sagittal	0.5 ± 0.4	0.4 ± 0.4	0.4 ± 0.4	0.1 ± 0.1	0.3 ± 0.4
2-Chamber	0.9 ± 0.9	0.7 ± 0.7	0.6 ± 0.7	0.3 ± 0.3	1.1 ± 1.3
Inferior Axial	0.7 ± 0.7	0.9 ± 1.4	0.6 ± 0.9	0.2 ± 0.5	0.6 ± 1.2
Medial Axial	0.8 ± 0.8	$\mathbf{1.1 \pm 1.5}$	$\mathbf{1.0 \pm 1.8}$	0.4 ± 0.6	1.4 ± 2.3
Superior Axial	1.0 ± 1.0	1.0 ± 1.5	0.9 ± 1.1	0.3 ± 0.5	0.9 ± 1.9

Table 5.4: Imaging plane values was quantified by removing it from a set, then refitting a surface and measuring its deviation. The coronal imaging plane contributed the most to left atrial size and regional motion, while the medial axial stack contributed the most to global changes in volume. The loss of any one plane resulted in small surface deviations (less than 2% in volume and less than 7% in radial motion) indicative of a robust fit.

5.5.5 Operator comparison

Our two-operator comparison in §5.3.3 revealed a small offset between the clinicians. This offset was larger in some imaging slices, especially ones near the pulmonary veins and left atrial appendage. We were curious how these offsets would influence the fitted surface and its motion. We investigated the influence of these outliers by fitting a surface to each operator's traces, then measuring the difference in radius between the two surfaces for eight subjects at maximum and minimum volumes. We averaged these differences into a Hammer map of regional operator variation (Fig. 5.12a). The two surfaces generally agreed (within 2 mm for over 80% of the surface), and deviated the most in the lower superior-lateral wall. We identified the cause of this error by projecting the radial error of one surface set onto the original axial image (Fig. 5.12b. Operator variation was highest in the appendage, which matched the deviations in the original tracings (Fig. 5.12c).

5.6 Discussion

We hypothesized that left atrial wall motion is spatially heterogeneous, that some regions of the atrium move more than others. We used a surface fitting technique in Chapter 4 to

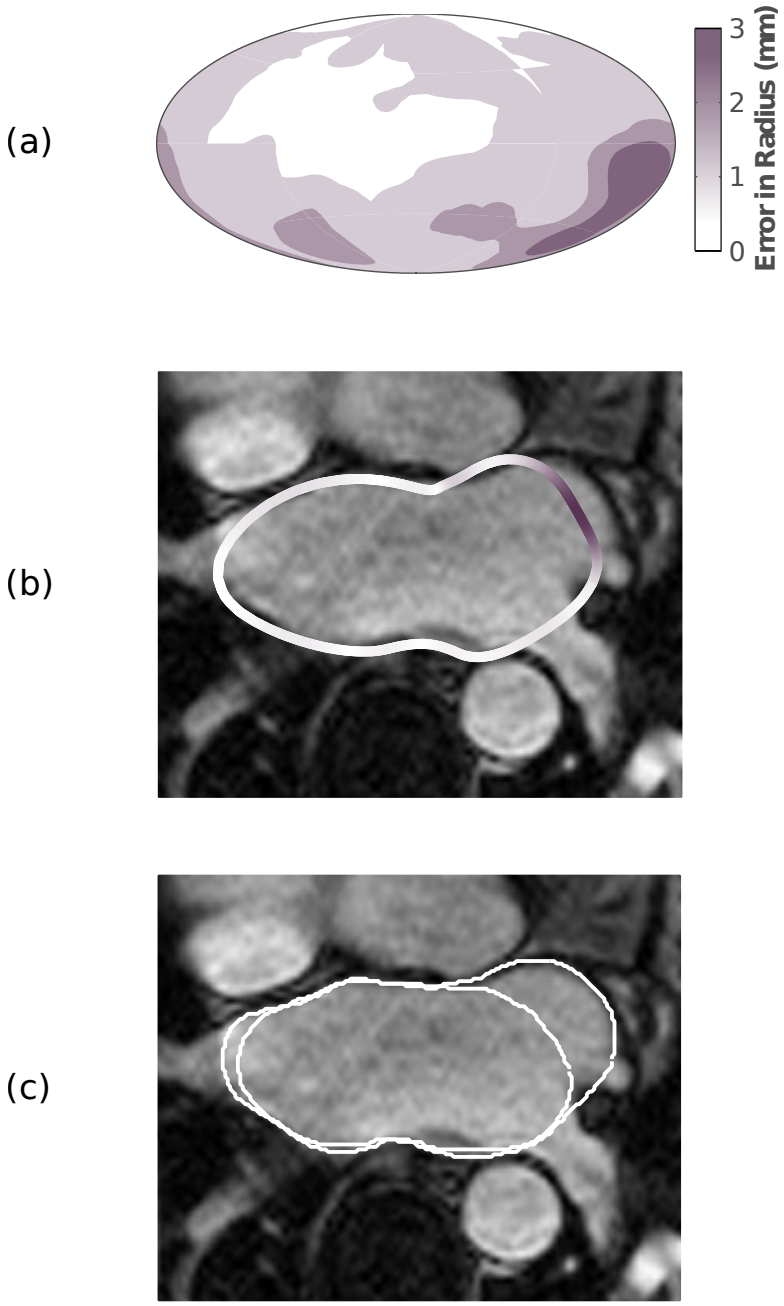

Figure 5.12: Operator variation during tracing resulted in average surface deviations of 1-2 mm. (a) Eight surfaces at minimum and maximum volume were compared, averaged, and projected onto a Hammer map. Darker purple indicates higher deviation between operators. The discrepancy peaked in the lower superior-lateral wall. (b) A single data set was selected that matched the average pattern and its error was back-projected onto an axial image. The surface error peaks (darker purple) in the left atrial appendage. (c) Recalling the two operator tracings from this image confirmed their deviation around the appendage.

measure left atrial wall motion in ten healthy subjects. We contoured the endocardial border from a series of CMR images, then fitted the contours to our surface mesh and quantified motion throughout the cardiac cycle. Fitted surfaces captured heterogeneous patterns of passive and active emptying while maintaining an RMSE of 2.0 ± 0.5 mm, or 9% of the mean fitted radius. Fitting error did not significantly vary with atrial size, regional motion, or active contraction across $n = 10$ data sets, demonstrating a robust fitting method. Radial emptying fraction REF_t and active fraction $R_{a|t}$ significantly varied between regions, confirming our hypothesis that left atrial wall motion is spatially heterogeneous.

5.6.1 Image processing

Manual contouring is typically a considerable source of variation in medical image analysis (Danilouchkine et al., 2005), and we sought to minimize this by standardizing the tracing process. Initial trials revealed that certain regions, including the left atrial appendage, mitral valve annulus, and pulmonary vein ostia, were especially difficult to trace because the operator did not have a clearly identifiable blood-tissue interface. Using standardized instructions and an artificial mitral valve cap, we held operator variation to less than 9% of mean slice area and less than 9% of mean atrial volume. Based on Bland-Altman analysis, we found nine traced images where operator variation exceeded the limits of agreement, and these outliers confirmed our initial suspicions: all nine came from imaging slices that captured the left atrial appendage, pulmonary vein ostia, or the mitral valve. We tested the propogation of these errors by comparing fitted surfaces of each operator, and found that surface radii also differed by 9%. Those same outliers influenced surface radii in the expected locations, increasing variation beyond 10% in the left atrial appendage. Future versions of the tracing procedure will use feedback from orthogonal imaging planes and a database of traced images to help operators handle these ambiguities.

5.6.2 Left atrial coordinate system

We designed a time-varying coordinate system to compensate for known whole heart motion. Although the atrium does move relative to the body during a cardiac cycle, the motion is dominated by the piston-like action of the mitral valve while the pulmonary veins remain relatively stationary (Fig. 5.3a). An important component of this coordinate system is the choice of origin, and whether that origin moves with the filling and emptying atrium (Fig. 5.10). Using a fixed origin emphasized longitudinal spatial heterogeneity (top to bottom in a Hammer map) and masked variations along the midwall (left to right in a Hammer map). Variations between midwall regions were more clearly distinguished using a floating origin. In the averaged volunteer data set, the floating origin lowered the spatial coefficient of variation (spatial standard deviation normalized to mean motion) for radial motion to 0.38 from 0.72 (Fig. 5.10a) and for fractional shortening to 0.36 from 0.64 (Fig. 5.10b); a decrease of 45%. We hypothesize that the smaller coefficient of variation in the floating origin approach will provide greater sensitivity for detecting regional abnormalities in atrial wall motion.

5.6.3 Left atrial volume

Left atrial volume derived from our fitted surface mesh was slightly larger than the traditional CMR volume calculation via the summation of stacked images. Our surface mesh approach incorporated multiple imaging planes beyond the single image stack and utilized data from the entire cardiac cycle to fit a surface. A Bland-Altman analysis (Fig. 5.8c) revealed a positive offset of 8 mL between the fitted surface volumes and the traditional summed axial stack volumes. Jrvinen and colleagues (Jervinen et al., 1994) also reported a small positive offset (1.7 mL) between the true volume and CMR volume of cadaveric LA casts. We suspect that the observed offset is generated in the superior and inferior aspects of the atrium, which have poor definition in an axial stack of images, leading to underestimation, but are clearly defined in the coronal and sagittal views and incorporated into surface fits.

5.6.4 Regional motion

Left atrial surfaces revealed regional heterogeneity of mechanical function, even among healthy subjects. We observed the greatest wall motion in the inferior wall of healthy subjects ($REF_t = 39\%$), of which 68% was passive emptying. In contrast, the superior wall moved the least of the defined walls between the mitral valve and pulmonary veins ($REF_t = 23\%$), but almost all of that motion was active contraction.

We compared our measures of regional motion with regional strain data collected in external studies. If we assume the atrium is roughly spherical, we can relate regional radial motion to regional wall strain. In a local region of atrial tissue with length s and radius r, change in length of the tissue (Δs) will be proportional to the change in radius (Δr), where $s = r\ d\theta$ and $\Delta s = \Delta r\ d\theta$. Normalization eliminates the $d\theta$ term, so that numerical values of wall strain and regional EF should be equal, $\Delta s/s = \Delta r/r$. Strain has been directly measured by several groups using speckle tracking echocardiography and velocity vector imaging, including (Kuppahally et al., 2010; Motoki et al., 2012; Saraiva et al., 2010; Vianna-Pinton et al., 2009). Investigators typically averaged speckle tracking strain data from multiple views into one global measure of function. We compared our results to the average wall strain measured in (n=64) healthy adults (Saraiva et al., 2010). We converted the strain to be zero at maximum atrial volume, matching the normalization we used in regional emptying fraction measurements. Our average REF_t agreed within 8% and had a similar amount of variation (Fig. 5.13a).

Other groups reported regional averages, including a study of (n=84) healthy adults done by Vianna-Pinton and colleagues in (Vianna-Pinton et al., 2009). The investigators used a regional segmentation (5 main regions, 4 mid-wall sections) that was similar to our approach (Fig. 5.9b), with some differences in nomenclature. Regional strains closely agreed with radial emptying fraction, especially in the inferior and lateral walls, which both agreed with less than 10% difference (Fig. 5.13b). Vianna-Pinton and colleagues also used speckle tracking to catalog the relative timing of atrial contraction based on the time to peak strain rate in each

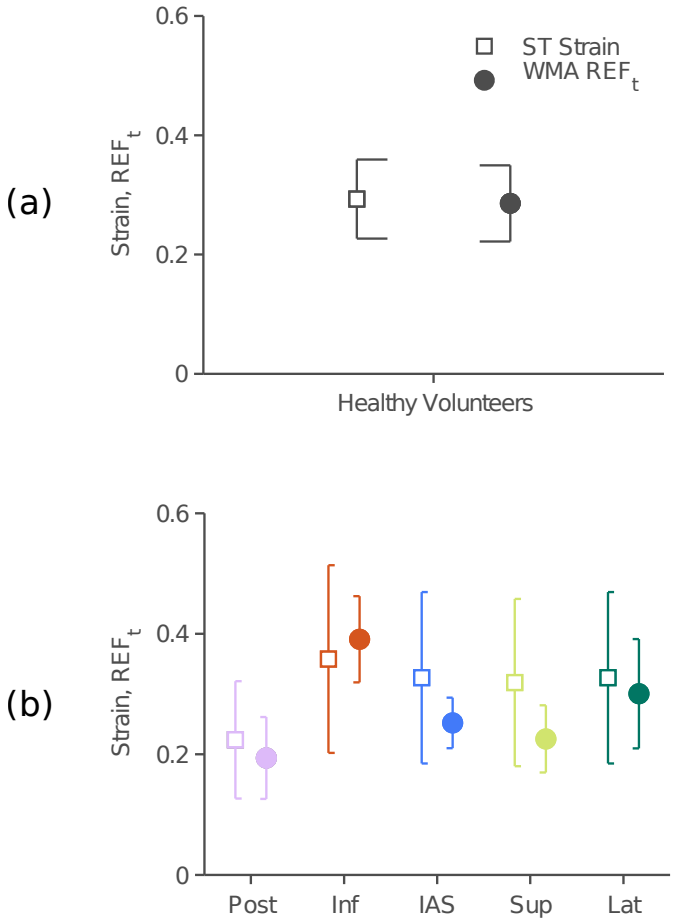

Figure 5.13: Radial emptying fraction (WMA REF_t) compared to speckle-tracking wall strain (ST Strain). Error bars represent mean±SD. (a) We compared the average REF_t of healthy subjects to (Saraiva et al., 2010), averaged over the entire left atrial wall. (b) We compared regional REF_t to (Vianna-Pinton et al., 2009) based on speckle tracking strain measured in 5 separate regions.

region. We compared these results to the average timing of contraction in healthy subjects (Fig. 5.11a) and found very close agreement. Both radial emptying and regional strain rate had early contraction in the septal and posterior walls and later contraction in the superior and lateral walls. The time delay between regional contractions was 3.7% of the R-R interval in our results, compared to 23 msec reported by (Vianna-Pinton et al., 2009). If we assumed a healthy heart rate of 75 beats per minute, this converted to 3% of the R-R interval and agreed with our results.

5.6.5 Limitations of wall motion

Any measure of left atrial function must provide reliable information in a timely manner to have clinical value. In the proposed method, manual contouring represents the largest limitation in both repeatability and analysis time. We showed that operator error can be held to 9% variation in slice contour size, stacked atrial volume, and fitted surface radii. Future contouring will use semi-automated processing and rely on a reference database of traced images to assist operators and further reduce this error. Semi-automated contouring will also lower the required time (currently 6-8 hours) to manually contour 400 images. Future work will explore reducing the number of acquired imaging planes to remove redundant images. Proposed methods of automated contouring, including shape-based approaches described in (Tsai et al., 2003) and propagation of contours through time described in (Jolly, 2006) and (Lynch et al., 2008) also hold promise for dramatically reducing the time required for segmentation of the endocardial surface.

To quantify AF disease severity, we would like to extend left atrial wall motion analysis to include patients with persistent and permanent AF. Current gating of CMR pulse sequences relies on a consistent R-wave to temporally align imaging slices, so all patients must be in sinus rhythm at the time of scan. Advances in CMR sequence design, including real-time cardiac imaging, may circumvent this problem. In addition, patients could be electrically converted back to sinus rhythm immediately prior to the scan, but severe cases of AF have

already failed such therapies. We are unsure of the value in imaging heart wall motion during fibrillation, since true mechanical function would be distorted, but quantifying patterns of motion in a fibrillating atrium would be novel.

We confirmed our hypothesis that left atrial wall motion is spatially heterogeneous in healthy adults. Given this result, we aimed to explore regional function in AF patients before and after catheter ablation.

References

G. Akgun and C. Layton. Aortic root and left atrial wall motion. an echocardiographic study. *Br Heart J*, 39(10):1082–1087, Oct. 1977.

A. C. Boyd, N. B. Schiller, D. L. Ross, and L. Thomas. Segmental atrial contraction in patients restored to sinus rhythm after cardioversion for chronic atrial fibrillation: a colour doppler tissue imaging study. *Eur J Echocardiogr*, 9(1):12–17, Jan. 2008.

M. G. Danilouchkine, J. J. M. Westenberg, A. de Roos, J. H. C. Reiber, and B. P. F. Lelieveldt. Operator induced variability in cardiovascular MR: left ventricular measurements and their reproducibility. *J Cardiovasc Magn Reson*, 7(2):447–457, 2005.

J. Gutman, Y. S. Wang, D. Wahr, and N. B. Schiller. Normal left atrial function determined by 2-dimensional echocardiography. *The American Journal of Cardiology*, 51(2):336–340, Jan. 1983.

E. Heiberg, J. Sjgren, M. Ugander, M. Carlsson, H. Engblom, and H. Arheden. Design and validation of segment - freely available software for cardiovascular image analysis. *BMC Medical Imaging*, 10(1):1, Jan. 2010.

M. Henein, Y. Zhao, M. Y. Henein, and P. Lindqvist. Disturbed left atrial mechanical function in paroxysmal atrial fibrillation: A speckle tracking study. *International Journal of Cardiology*, 155(3):437–441, Mar. 2012.

B. D. Hoit and R. A. Walsh. Regional atrial distensibility. *Am. J. Physiol.*, 262(5 Pt 2): H1356–1360, May 1992.

Y. Inaba, S. Yuda, N. Kobayashi, A. Hashimoto, K. Uno, T. Nakata, K. Tsuchihashi, T. Miura, N. Ura, and K. Shimamoto. Strain rate imaging for noninvasive functional quantification of the left atrium: Comparative studies in controls and patients with atrial fibrillation. *Journal of the American Society of Echocardiography*, 18(7):729–736, July 2005.

V. Jervinen, M. Kupari, P. Hekali, and V.-P. Poutanen. Assessment of left atrial volumes and phasic function using cine magnetic resonance imaging in normal subjects. *The American Journal of Cardiology*, 73(15):1135–1138, June 1994.

M.-P. Jolly. Automatic segmentation of the left ventricle in cardiac MR and CT images. *International Journal of Computer Vision*, 70(2):151–163, Nov. 2006.

S. S. Kuppahally, N. Akoum, N. S. Burgon, T. J. Badger, E. G. Kholmovski, S. Vijayakumar, S. N. Rao, J. Blauer, E. N. Fish, E. V. DiBella, R. S. MacLeod, C. McGann, S. E. Litwin, and N. F. Marrouche. Left atrial strain and strain rate in patients with paroxysmal and persistent atrial fibrillation: Relationship to left atrial structural remodeling detected by delayed-enhancement MRI. *Circ Cardiovasc Imaging*, 3(3):231–239, May 2010.

L. I.-K. Lin. A concordance correlation coefficient to evaluate reproducibility. *Biometrics*, 45 (1):255–268, Mar. 1989.

W. Liu, M. W. Ashford, J. Chen, M. P. Watkins, T. A. Williams, S. A. Wickline, and X. Yu. MR tagging demonstrates quantitative differences in regional ventricular wall motion in mice, rats, and men. *Am J Physiol Heart Circ Physiol*, 291(5):H2515–H2521, Nov. 2006.

M. Lynch, O. Ghita, and P. Whelan. Segmentation of the left ventricle of the heart in 3-d+t MRI data using an optimized nonrigid temporal model. *IEEE Transactions on Medical Imaging*, 27(2):195–203, 2008.

H. Motoki, A. Dahiya, M. Bhargava, O. M. Wazni, W. I. Saliba, T. H. Marwick, and A. L. Klein. Assessment of left atrial mechanics in patients with atrial fibrillation: Comparison between two-dimensional speckle-based strain and velocity vector imaging. *Journal of the American Society of Echocardiography*, 25(4):428–435, Apr. 2012.

D. Nori, G. Raff, V. Gupta, R. Gentry, J. Boura, and D. E. Haines. Cardiac magnetic resonance imaging assessment of regional and global left atrial function before and after

catheter ablation for atrial fibrillation. *J Interv Card Electrophysiol*, 26(2):109–117, Nov. 2009.

W. C. O'Dell, C. C. Moore, W. C. Hunter, E. A. Zerhouni, and E. R. McVeigh. Three-dimensional myocardial deformations: Calculation with displacement field fitting to tagged MR images1. *Radiology*, 195(3):829–835, June 1995.

R. M. Saraiva, S. Demirkol, A. Buakhamsri, N. Greenberg, Z. B. Popovic, J. D. Thomas, and A. L. Klein. Left atrial strain measured by two-dimensional speckle tracking represents a new tool to evaluate left atrial function. *Journal of the American Society of Echocardiography*, 23(2):172–180, Feb. 2010.

C. Sirbu, L. Herbots, J. D'hooge, P. Claus, A. Marciniak, T. Langeland, B. Bijnens, F. Rademakers, and G. Sutherland. Feasibility of strain and strain rate imaging for the assessment of regional left atrial deformation: A study in normal subjects. *European Journal of Echocardiography*, 7(3):199 –208, June 2006.

B. S. Spottiswoode, X. Zhong, A. T. Hess, C. M. Kramer, E. M. Meintjes, B. M. Mayosi, and F. H. Epstein. Tracking myocardial motion from cine DENSE images using spatiotemporal phase unwrapping and temporal fitting. *IEEE Trans Med Imaging*, 26(1):15–30, Jan. 2007.

B. L. Strunk, J. W. Fitzgerald, M. Lipton, R. L. Popp, and W. H. Barry. The posterior aortic wall echocardiogram. its relationship to left atrial volume change. *Circulation*, 54(5): 744–750, Nov. 1976.

L. Thomas, K. Levett, A. Boyd, D. Y. C. Leung, N. B. Schiller, and D. L. Ross. Changes in regional left atrial function with aging: Evaluation by doppler tissue imaging. *Eur J Echocardiogr*, 4(2):92–100, June 2003.

L. Thomas, T. Mckay, K. Byth, and T. H. Marwick. Abnormalities of left atrial function after cardioversion: an atrial strain rate study. *Heart*, 93(1):89 –95, Jan. 2007.

A. Tsai, J. Yezzi, A., W. Wells, C. Tempany, D. Tucker, A. Fan, W. Grimson, and A. Willsky. A shape-based approach to the segmentation of medical imagery using level sets. *IEEE Transactions on Medical Imaging*, 22(2):137–154, 2003.

R. Vianna-Pinton, C. A. Moreno, C. M. Baxter, K. S. Lee, T. S. M. Tsang, and C. P. Appleton. Two-dimensional speckle-tracking echocardiography of the left atrium: feasibility and regional contraction and relaxation differences in normal subjects. *J Am Soc Echocardiogr*, 22(3):299–305, Mar. 2009.

Q. H. Yang, J. P. Snyder, and W. R. Tobler. *Map Projection Transformation: Principles and Applications*. CRC Press, 2000.

J. Yoshikawa, H. Kato, T. Owaki, and K. Tanaka. Study of posterior left atrial wall motion by echocardiography and its clinical application. *Jpn Heart J*, 16(6):683–693, Nov. 1975.

X. Zhong, B. S. Spottiswoode, C. H. Meyer, C. M. Kramer, and F. H. Epstein. Imaging three-dimensional myocardial mechanics using navigator-gated volumetric spiral cine DENSE MRI. *Magn Reson Med*, June 2010.

Chapter 6

Finite element analysis of left atrial mechanics

The finite element method is a numerical technique that simulates the response of a physical system to a set of external stimuli. The system is divided into a *finite* number of small pieces called *elements*. Each element is governed by a simple set of rules that determine its response to the stimuli. Because a system can be divided into many elements, the method can capture complex, non-linear behavior with simple linear elements. The most common form of the finite element method solves static mechanical problems, such as loading of a concrete slab or steel beam. It can also solve physiological problems, including the mechanics of soft biological tissue. We used finite element analysis to simulate left atrial mechanics. Using data from previous chapters, including cine MRI, pressure-volume loops, and fitted surfaces, we constructed a finite element model of the healthy atrium and simulated a complete cardiac cycle. We coupled the model with a time-varying elastance circuit to simulate pulmonary vein and left ventricular blood flow. We then validated the simulation results using *in vivo* data collected in other chapters. The finite element model successfully simulated a full cardiac cycle with accurate representations of global and regional left atrial mechanics. We used this model in later chapters to explore how mechanics change in AF atria and in post-ablation

atria due to scarring.

6.1 Background of cardiac finite element methods

The finite element method finds an approximate solution to *boundary value* problems (Strang and Fix, 1973). Boundary-value problems are well-named as they solve for the interior values of an object given the values at its boundary and the differential equations that govern its interior. A classic form of the boundary-value problem is the stress inside a bending steel beam that has a force applied to one end and a wall attached to the other. The internal stress is found by solving the differential equations to satisfy the prescribed forces on the ends. In cases with complex shapes and multiple boundary conditions, this analytical approach becomes unmanageable. Finite element method offers an alternative approach that approximates the analytical solution but avoids its complexity. FEM was first proposed in the 1950's to find stresses in aeronautical structures (Argyris, 1954; Turner, 1956) and the name was coined by Ray Clough in 1960 (Clough, 2004). FEM was used in the 1970's to solve structural problems in civil engineering, and has since expanded to many areas of science, including physiological modeling. We will focus on modeling the mechanics (stresses, strains, deformations) of biological tissue.

Biological tissue is soft compared to steel and stretches more under normal loading. FEM first gained traction in orthopedic applications (the stiffest biological tissue), as researchers welcomed the method's ability to handle complex shapes (Brekelmans et al., 1972). It quickly expanded to softer tissues, including arterial walls and cardiac muscle (Hunter and Smaill, 1988). In cardiac applications, the left ventricle received the bulk of the attention due to its central role in cardiac function. Finite element methods have been used to study the effects of diseases and therapies, including myocardial infarction (Kerckhoffs et al., 2007a), regional ischemia (Mazhari and McCulloch, 2000), and ventricular dyssynchrony (Usyk and McCulloch, 2003), as well as cardiac resynchronization (Kerckhoffs et al., 2008) and infarct

mechanical support (Fomovsky et al., 2011). The left ventricle is amenable to modeling due to its large size, thick wall, and consistent fiber geometry. Finite element models of other heart chambers are less common, but improved imaging techniques and biological characterization have aided their development in recent years.

The left atrium has rarely been modeled for its mechanical function, partially due to its thin walls and mostly passive state. Instead, most models of the left atrium focused on electrical conduction in the chamber, as scientists tried to simulate rhythm disorders (Courtemanche et al., 1998; Nygren et al., 1998). These models have grown to include both atria, three-dimensional geometry, and fiber orientations (Dossel et al., 2012), but have rarely been adapted for mechanical modeling. A handful of atrial finite element models have arisen in recent years, exploring correlations between wall stress and electrophysiological changes (Hunter et al., 2012) as well as interactions between the atrium and interventional devices (Jernigan et al., 2007). Di Martino and colleagues developed a comprehensive finite element model of the porcine atria based computed tomography imaging (Di Martino et al., 2011a) and used it to study stress distributions during ventricular tachychardia (Di Martino et al., 2011b). They performed biaxial testing on porcine (Bellini and Di Martino, 2012) and human (Bellini et al., 2013) atrial tissue and characterized its mechanical behavior. However, no group has developed a finite element model of the human atrium, nor has any group explored the changes to the atrium during atrial fibrillation. We therefore developed a human left atrial finite element model, including both its passive and active components. We validated this model to available *in vivo* data, then used it to quantify the major factors influencing AF function and measure the effects of ablation scarring in later chapters.

6.2 Principles of the finite element method

The finite element method of solid mechanics relies on the principles of kinematics, equilibrium, constitutive relationships, and energy conservation. Using these principles, the method

simulates how an object deforms under load. The object of interest is sometimes called a *model* or a *geometry* and a load can refer to *forces* or *pressures* or, more generally, *boundary conditions*. We start with the principle of kinematics, which relates deformation and strain in a model.

6.2.1 Kinematics

The atrium starts in a static equilibrium called the *reference*, *unloaded*, *undeformed*, or *initial* state. We will refer to it as the undeformed state. Its nodal positions are the material coordinates $\mathbf{X}$. We will follow the notation of FEBio, the FE software used in this thesis (Maas et al., 2012). When we apply a boundary condition, the atrium displaces in response to the force, creating the *deformed* state with deformed coordinates $\mathbf{x}$. The displacement of each point in the body can be mapped as $\mathbf{u}$ where $\mathbf{x} = \mathbf{X} + \mathbf{u}(\mathbf{X})$. The deformation gradient describes non-rigid-body motion as $\mathbf{F} = \dfrac{\partial \mathbf{x}}{\partial \mathbf{X}}$, where $\mathbf{F}$ is a second order tensor with components $F_{ij} = \dfrac{\partial x_i}{\partial X_j}$. In most finite element models, the deformation is separated into two components: changes in volume (volumetric) and changes in shape (deviatoric). This separation is useful for materials that want to enforce incompressibility by preventing changes in volume. The Jacobian measures a change in element volume as $J = \det \mathbf{F}$ and allows us to separate the deviatoric deformation as $\tilde{\mathbf{F}} = J^{-1/3}\mathbf{F}$. Deviatoric deformation will be important in building an atrial material in §6.5.2. Note that the Jacobian of the deformation gradient is not the same as the Jacobinan of element shapes discussed in §6.3.2.

We calculate strain from the deformation gradient. There are many forms of strain, but we use the right Cauchy-Green deformation tensor $\mathbf{C}$ to calculate the Green-Lagrange strain tensor $\mathbf{E}$ where

$$\begin{aligned} \mathbf{C} &= \mathbf{F}^{\mathrm{T}}\mathbf{F} \\ \mathbf{E} &= \frac{1}{2}(\mathbf{C} - \mathbf{I}) \end{aligned} \tag{6.1}$$

Tensor invariants are useful when designing material strain energy functions. We calculate them for the right Cauchy-Green tensor as

$$
\begin{aligned}
I_1 &= \mathrm{tr}(\mathbf{C}) \\
I_2 &= \frac{1}{2}\left((\mathrm{tr}\,\mathbf{C})^2 - \mathrm{tr}\,\mathbf{C}^2\right) \\
I_3 &= \det \mathbf{C}
\end{aligned}
$$

A deviatoric variation of the deformation tensor $\mathbf{C}$ can also be calculated by substituting $\tilde{\mathbf{F}}$ into Equation 6.1, then computing its invariants.

6.2.2 Equilibrium

Atrial strain increases wall stress and creates a force-balance problem, which can be solved using the conservation of linear momentum. When we apply boundary conditions to an object, the object responds by deforming and building up stress inside of it. When the stress generates a reaction force equal to the boundary condition, the object reaches a static *equilibrium*. Because we are dealing with quasi-static analysis, every step of the model reaches this equilibrium. We can define it formally as

$$
\frac{\partial \sigma_{ij}}{\partial x_j} = \mathbf{0} \tag{6.2}
$$

where $\boldsymbol{\sigma}$ is the Cauchy stress tensor with components σ_{ij}. Cauchy's relationship links the stress in a body to a traction (force) on its surface as

$$
\mathbf{t} = \boldsymbol{\sigma} \cdot \mathbf{n} \tag{6.3}
$$

where $\mathbf{n}$ is the surface normal on which the traction is acting. This is the basic formulation of an object at static equilibrium, based on the stresses inside it and the forces on its surface.

Cauchy stress uses the coordinates of the deformed state; its the stress of a deformed area pointing along a deformed vector. Stresses can be reformulated to reference the undeformed state. These are generally called the *Piola-Kirchhoff* stresses. The second Piola-Kirchhoff stress is helpful in building material strain energy functions and is defined as

$$\mathbf{S} = J\,\mathbf{F}^{-1} \cdot \boldsymbol{\sigma} \cdot \mathbf{F}^{-\mathrm{T}}$$

We use this formulation because it represents stress in the undeformed state and, more importantly, it is the *energy* conjugate of $\mathbf{E}$. The stress $\mathbf{S}$ and strain $\mathbf{E}$ can be combined to find the internal energy in an object. When energy is applied to an object (via boundary conditions), it must be absorbed in the form of stress $\mathbf{S}$ and strain $\mathbf{E}$, since energy is always conserved. An increase in internal energy (δW) is represented as the Frobenius inner product $\mathbf{S} : \delta\mathbf{E}$, which will be quite useful in building *constitutive* relationships.

6.2.3 Constitutive relationships

We can define a general material parameter called the material elasticity tensor $\boldsymbol{\mathcal{C}}$ that relates a change in strain to a change in stress as

$$\boldsymbol{\mathcal{C}} = \frac{\partial \mathbf{S}}{\partial \mathbf{E}} \qquad \mathcal{C}_{ijkl} = \frac{\partial S_{ij}}{\partial E_{kl}}$$

For linear elastic materials, $\boldsymbol{\mathcal{C}}$ is a set of scalar values describing the relationship between stress and strain. Most biological tissues, however, are not linear and become stiffer the more they are stretched. We therefore use an alternative method to describe the relationship between stress and strain using an energy function. Materials described this way are referred to as *hyperelastic* materials.

Instead of an elasticity tensor, hyperelastic materials are defined using a *strain energy density* function. Essentially, strain energy W represents how much the internal energy changes as a function of changes in strain, $W = W(\mathbf{E})$. These changes in strain result in

increased stress, where

$$\mathbf{S} = \frac{\partial W}{\partial \mathbf{E}}$$

A strain energy function can be formulated in terms of the strain tensor $\mathbf{E}$, as well as the deformation tensor $\mathbf{C}$, its invariants (I_1, I_2, I_3), or measures of stretch $(\lambda_1, \lambda_2, \lambda_3)$. Just like earlier, a deviatoric form of each of these terms and the strain energy itself (denoted as $\tilde{W}(\tilde{\mathbf{E}})$) can be formulated by removing the volumetric change.

6.2.4 Energy conservation

Combining the principles of equilibrium, kinematics, and constitutive relationships creates a large set of partial differential equations. If we solved these equations explicitly, we would know the exact amount of stress and strain at every point in the object. This is called the *strong* solution. It works for simple objects like beams and plates, but breaks down quickly for non-regular geometry as the equations become unmanageable. The finite element method offers an alternative approach called the *weak* solution. The weak solution inherently satisfies the principles of equilibrium and Cauchy's relationship by relying entirely on energy conservation. We start with the total potential energy in the system $\mathbf{\Pi}$ and use the calculus of variation where

$$\begin{aligned} \mathbf{\Pi} &= \text{Internal Energy} + \text{External Energy} \\ \delta\mathbf{\Pi} &= \int_V \mathbf{S} \colon \delta\mathbf{E}\, dV \quad + \int_S \mathbf{T}\delta\mathbf{u}^{\mathrm{T}}\, dS \end{aligned} \tag{6.4}$$

At equilibrium, we assume that the variation in energy $\delta\mathbf{\Pi} = 0$. To find this equilibrium, the finite element method searches for the minimum potential energy, which inherently satisfies the other principles. It does this using linearization and discretization. Briefly, the relationship in Eqn. 6.4 is varied by a small "trial" deformation and the change in energy is estimated by taking the directional derivative of $\delta\mathbf{\Pi}$ along the direction of that deformation. This is done for each element (the discretization) and solved using a non-linear solver like

those discussed in Chapter 4. All of these steps occur inside the finite element software (FEBio) and are described in greater detail by Maas and colleagues (Maas et al., 2012).

6.3 Design of a left atrial finite element model

We built a finite element model of the left atrium using endocardial surface data from healthy hearts. Boundary conditions were created from CMR image data and applied to the atrial geometry. Mitral valve motion (an important boundary condition) was prescribed based on motion of annulus landmarks in the CMR data.

6.3.1 Defining a left atrial geometry

We began the FE model by defining the atrial geometry. We used the average left atrial surface from our previous work (Chapters 4 and 5) derived from fits to contoured CMR images of ten ($n = 10$) healthy subjects. We imported the surface into MATLAB as a shell around which we constructed a 3-D geometry. We used a finite element pre-processor called PreView (MRL, University of Utah) to generate an initial "skeleton" mesh (Fig. 6.1a,b). The skeleton was a simple hollow sphere of constant thickness, tessellated into six quadrilaterals with 120° vertices (six curved squares connected across the surface, Fig. 6.1, white lines). Each of the quadrilaterals was divided into a 50 x 50 grid of hexahedral elements with 2 elements through the sphere's thickness (Fig. 6.1c). The skeleton mesh contained 30,000 elements and 45,006 nodes (each element, being a hexahedral, had eight bordering nodes). With two layers of elements in the skeleton, we labeled the outer elements "epicardial" and the inner ones "endocardial". We identified the sides or *faces* of elements that composed the epicardial surface (epicardial faces) and endocardial surface (endocardial faces). Similarly, we separated the three layers of nodes into epicardial, "medial", and endocardial groups. We converted the position of all nodes into spherical coordinates, $(x, y, z) \rightarrow (\theta, \phi, r)$.

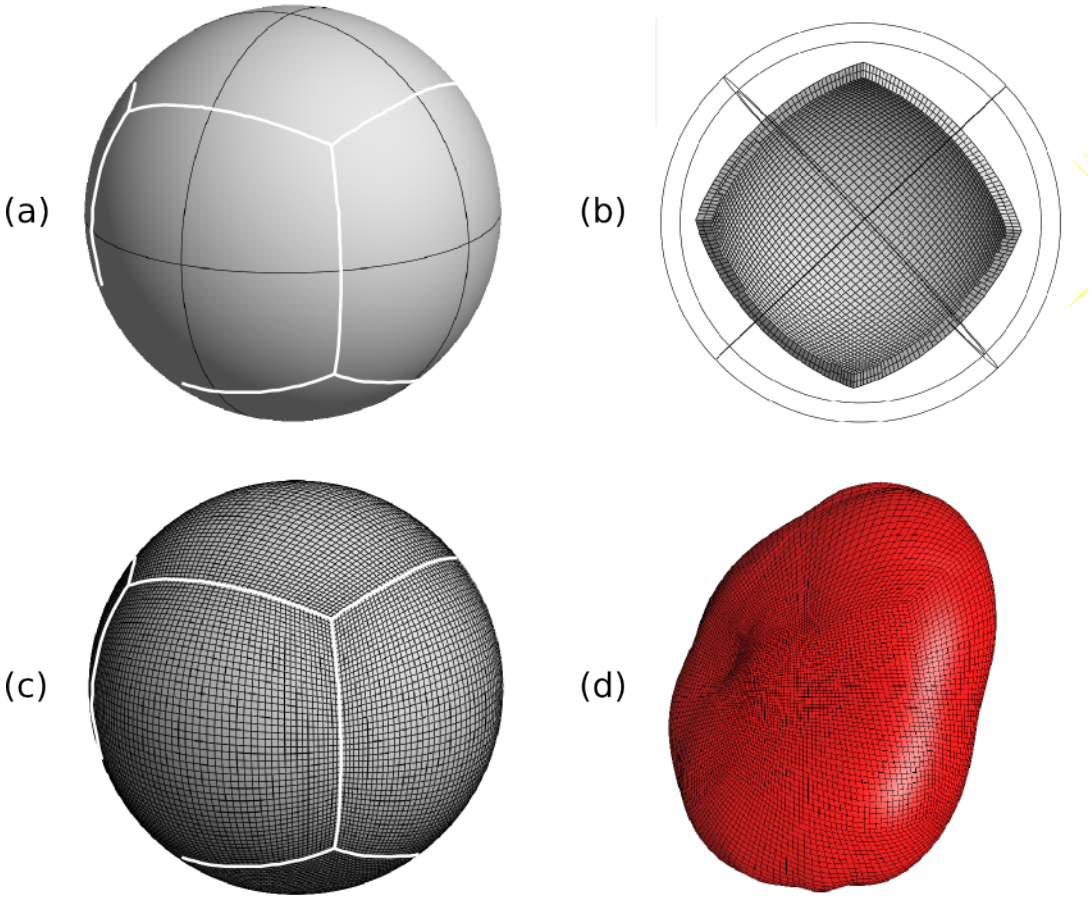

Figure 6.1: Initial mesh design in FEBio. (a) A sphere was generated in PreView with constant radius. (b) The sphere was divided into six quadrilaterals and made hollow at a constant thickness. (c) The mesh was divided into 30,000 elements within 6 symmetric 50x50 grids (white lines). (d) The mesh was projected onto the average atrial surface.

In MATLAB, we projected the endocardial nodes along their radial dimension onto the surface (Fig. 6.1d). (From this point forward, we will use *mesh* to refer to a finite element mesh and *surface* to refer to the fitted geometry from previous chapters.) To project the medial and epicardial nodes, we first calculated the surface normal at each node based on the surface curvature at that point. We used the radius and radial derivatives to calculate the surface tangent vectors along the lines of principle curvature (α, β), where

$$\left(r, \frac{\partial r}{\partial \theta}, \frac{\partial r}{\partial \phi}, \frac{\partial^2 r}{\partial \theta \partial \phi}, \frac{\partial^2 r}{\partial \theta^2}, \frac{\partial^2 r}{\partial \phi^2}\right) \rightarrow \left(\frac{\partial r}{\partial \alpha}, \frac{\partial r}{\partial \beta}\right)$$

then used those vectors to find the surface normal, where

$$\vec{n} = \frac{\partial r}{\partial \alpha} \times \frac{\partial r}{\partial \beta} \tag{6.5}$$

We smoothed each surface normal by calculating its local average in a 3x3 grid of neighboring nodes. We chose to model a constant wall thickness by projecting epicardial nodes 3 mm along the normal vector from the corresponding endocardial point. Medial nodes were placed at the bisection of this segment. The atrial mesh is displayed in Figure 6.2 with the epicardial surface visible in red.

6.3.2 Mesh integrity and refinement

We used tri-linear interpolation for each of the 30,000 hexahedral elements. Recalling the Lagrangian basis functions used in Chapter 4, a set of Lagrangian functions interpolated values in the element interior using values at the nodes. In finite element analysis, these functions are typically called shape functions. Following node projection, we confirmed the integrity of the mesh by calculating each element's Jacobian (the determinant of the Jacobian matrix). The Jacobian is a measure of how far an element's shape deviate from the ideal (for

a hexahedral element, the ideal shape is a cube). We calculated the Jacobian as

$$J = \begin{bmatrix} \frac{\partial x_1}{\partial \xi_1} & \frac{\partial x_1}{\partial \xi_2} & \frac{\partial x_1}{\partial \xi_3} \\ \frac{\partial x_2}{\partial \xi_1} & \frac{\partial x_2}{\partial \xi_2} & \frac{\partial x_2}{\partial \xi_3} \\ \frac{\partial x_3}{\partial \xi_1} & \frac{\partial x_3}{\partial \xi_2} & \frac{\partial x_3}{\partial \xi_3} \end{bmatrix}$$

where each derivative can be reformulated based on the shape functions N_k and nodal positions x_k as

$$\frac{\partial x_i}{\partial \xi_j} = \mathrm{x}_{k,i} \frac{\partial \mathrm{N}_k}{\partial \xi_j}(\xi_1, \xi_2, \xi_3)$$

We calculated the Jacobian at each Gauss point in a 2x2x2 integration scheme. If any Gauss point had a Jacobian less than zero, we locally smoothed the nodes to repair the element's shape.

6.3.3 Pulmonary veins and mitral valve

We imported atrial landmarks from the averaged healthy geometry generated in Chapter 5. These landmarks included the four ostia of the pulmonary veins and four annular points along the mitral valve. We used the landmarks to recreate the pulmonary veins and mitral valve in our model. For the pulmonary veins, we projected each landmark onto the epicardial side of the mesh at the nearest epicardial node. We then created a hollow cylinder 8 mm long, 1.5 mm thick, with a variable diameter based on the average diameter of each pulmonary vein (Lickfett et al., 2005; Wittkampf et al., 2003). The vein thickness and length were estimated from average *in vivo* measurements (Ho et al., 1999), where the length represented the distance from the ostia to the first branch point (Schwartzman et al., 2003). Each cylinder was composed of 200 hexahedral elements arranged in a radial pattern around the tube (10 axial x 20 circumferential x 1 radial). We centered the vein at the epicardial node landmark and oriented it along the local surface normal. Nodes at the vein-atrium interface were

adjusted to create a gapless link between the cylinder and atrial mesh.

We created the mitral valve annulus from the four mitral valve landmarks. First, we approximated the valve as a plane. We then created a ring composed of 80 elements (1 axial x 80 circumferential x 1 radial). We scaled the ring to twice the radius of the atrium, and oriented it in the plane of the mitral valve at its centroid. To recreate the annulus shape, we projected every ring node towards the centroid parallel to the plane. We adjusted the projected nodes so they contacted the epicardial side of the left atrial mesh. Outer ring nodes were set a fixed distance away from the annulus-atrium interface. The process created a thin "ring" of annulus tissue attached to the epicardial side of the atrium.

The three objects (atrium, pulmonary veins, mitral valve annulus) were combined into one environment containing 30,880 elements and 47,086 nodes (Fig. 6.2). We segmented the atrial mesh into six regions using the left atrial coordinate system (posterior, inferior, septal, superior, and lateral walls, and the mitral valve, Chapter 5). The pulmonary vein plane defined the posterior wall while the other four regions comprise the atrial midwall. We defined an annular sub-region in the midwall as nodes within 2 mm of the mitral valve plane. Similarly, we tagged any atrial element that contacted a pulmonary vein as the pulmonary vein region. We extended these regions outward by 5 mm to represent the ostia. Finally, we estimated the pericardial reflection as a 2 mm strip of tissue connecting the right and left superior pulmonary veins. We used these regions in §6.5.2 to define region-based materials.

6.3.4 Boundary conditions

We used boundary conditions to apply forces, pressures, and displacements to the atrium. Boundary conditions are the "values" in the boundary value problem, and FEM uses these values to estimate the stresses and strains inside the atrium. Boundary conditions included nodal forces, nodal displacements, and surface pressures (we did not consider dynamic motion in this method). Boundary conditions were prescribed using a *load curve*, which describes

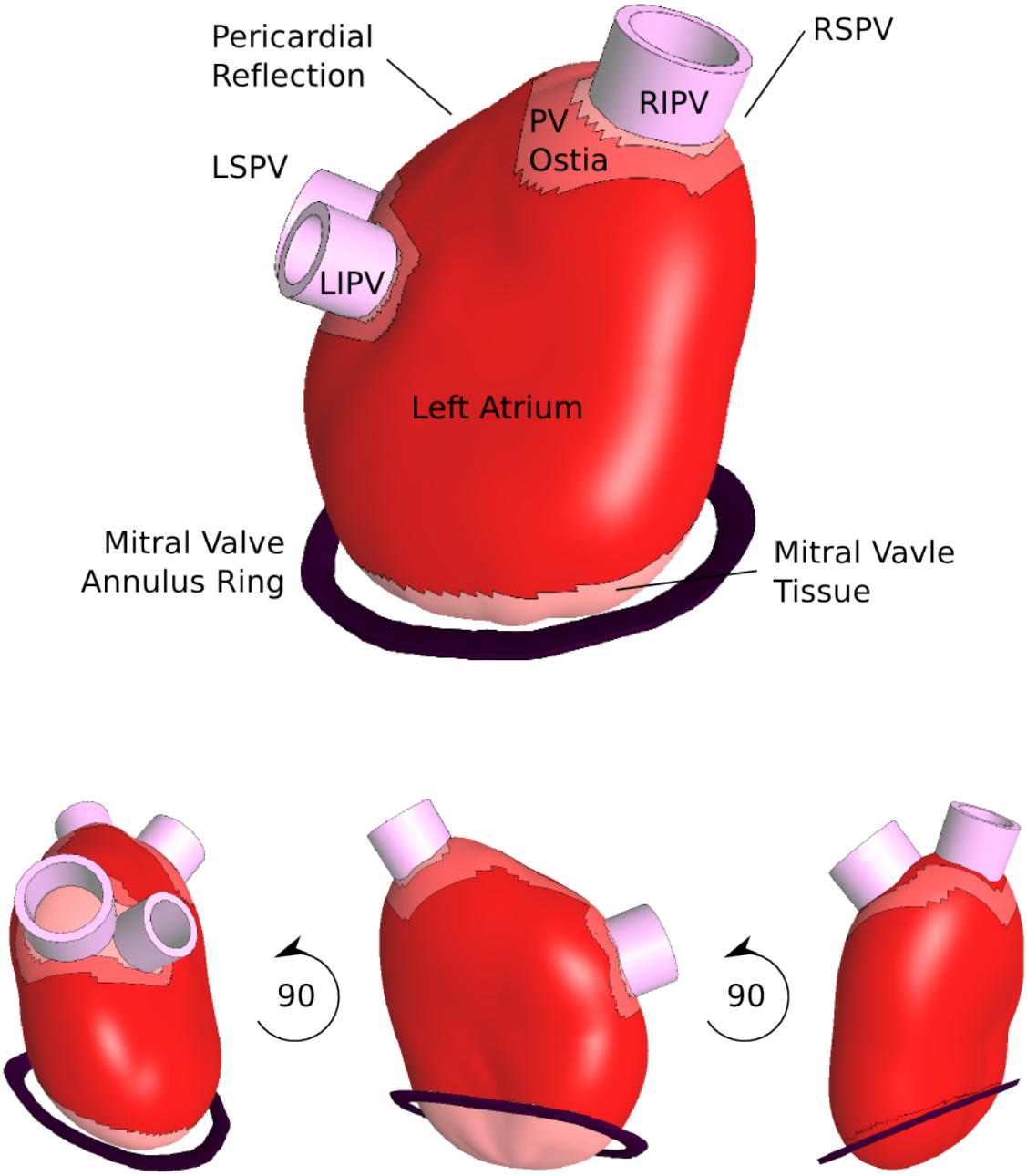

Figure 6.2: The atrial mesh. Materials are labeled accordingly. The gap between the mitral valve and LA body is meaningless since the LA nodes are fixed to the valve. Three views rotated at 90 degrees to capture different portions of the mesh.

the changes in a condition over time. The units of time were arbitrary because we were simulating a quasi-static analysis (no effects of inertial or dynamic motion).

Atrial pressure controls many aspects of chamber mechanics, making it the most important boundary condition. To simulate pressure, we applied a surface force to the endocardial layer of the left atrial mesh. The pressures were set as follower forces, meaning that as the mesh deformed, the direction of the force changed to remain normal to the surface. We used *in vivo* pressure data from clinical studies in Chapters 2 and 3, discussed further in §6.5.1. The pressure-time data were averaged to create a pressure load curve. We set the pressure extrema based on circuit blood flow, discussed in more detail in §6.5.5.

The mitral valve moves like a piston during the cardiac cycle, generating high regional motion in the annular region of the atrium (Chapter 5). The ventricle contributes to this motion by pulling on the valve during atrial filling (ventricular systole), then relaxing during atrial emptying (ventricular diastole). To recreate this motion, we measured the translation of the mitral valve (Chapter 5) and prescribed its displacement to the annulus ring in our model. We simplified valvular motion into planar displacements and treated the annulus ring as a rigid body (moving without deformation). Later, we converted the displacements into a ventricular force to better simulate the action of the ventricle. This step is discussed in more detail in §6.4.2.

The pulmonary veins only move a few millimeters during a normal cardiac cycle. Similar to the mitral valve, we used landmark motion from CMR to guide our choice in boundary conditions. Since they move a small amount *in vivo*, we chose to fix the pulmonary veins in place for all modeling scenarios. We also fixed the nodes of the atrial mesh attached to the pulmonary veins to ensure a gapless attachment. The elements adjacent to the fixed nodes (the ostia) and those along the pericardial reflection were made of a stiffer material to prevent stress concentrations at the edge of the fixed region, discussed in more detail in §6.5.2.

The atrium fills and empties in a confined area, contacting other structures as it moves. An oblate spheroid (the approximate shape of the atrium) would normally become more spherical

when pressurized, but the real left atrium does not because of surrounding structures. We isolated three important structures to include in the finite element model: the aortic root, the right atrium, and the chest wall (Fig. 6.3). The aortic root (the segment immediately distal to the aortic valve) presses against the atrium in the center of the superior wall, forming a concave region in the surface. We identified this region by calculating the principal curvatures (κ_1, κ_2) of the surface at every endocardial node, then isolating the nodes in the superior wall with negative curvatures.

$$\left(\frac{\partial \mathbf{n}}{\partial \alpha}, \frac{\partial \mathbf{n}}{\partial \beta}\right) \rightarrow (\kappa_1, \kappa_2)$$

$$\kappa_1 < 0 \ \wedge \ \kappa_2 < 0 \equiv \kappa_{neg}$$

We applied an inward-facing pressure on every epicardial face that contained a κ_{neg} node. We used the atrial pressure load curve and scaled it to mimic the increased resistance of the aorta as the atrium filled. The inward-facing pressure maintained the concave region, which otherwise would have "popped" into a convex shape absent an external load.

We used a similar method for the right atrium and chest wall. We modeled the right atrium as an inward-facing pressure on the epicardial face of the septal wall. Just the like aortic root, we used the left atrial pressure load curve to model changes in right atrial pressure. Because the right atrium operates at a lower pressure compared to the left, we scaled the load curve to 30% of its original value, based on known right atrial pressures (Guyton et al., 1957) and septal wall motion measured in Chapter 5. We applied a similar external pressure to the posterior wall, where the atrium touches the chest wall. We estimated the chest wall as an external pressure on the epicardial surface of the posterior wall inferior to the pericardial reflection and superior to the midline. We scaled the load curve to allow a small amount of expansion based on regional motion measured in Chapter 5.

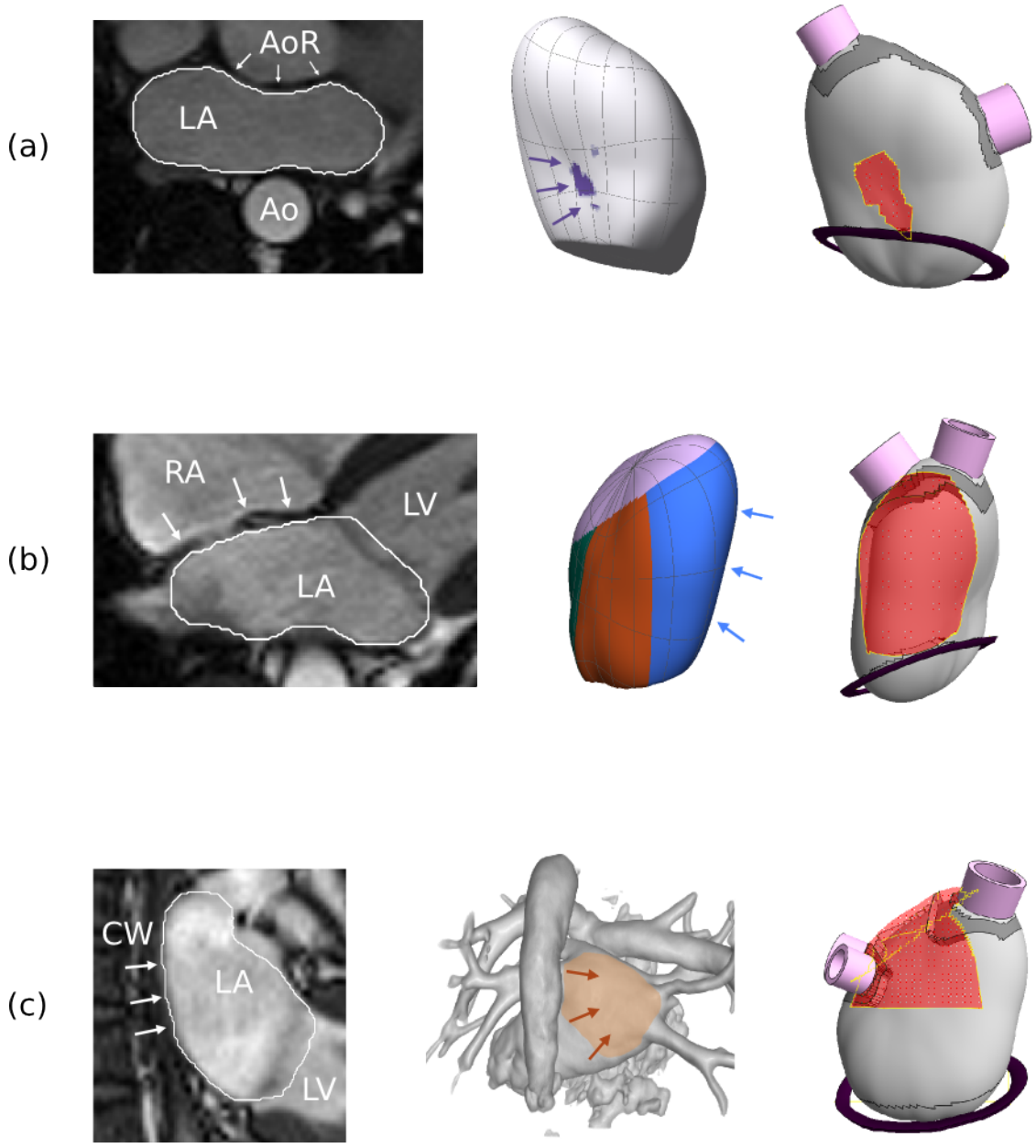

Figure 6.3: Boundary conditions of the model. Regions of interest (aortic root, RA, chest wall) were modeled with an external pressure. (a) Concave region of the aortic root, visible on axial MRI and in surface curvature. (b) Right atrial pressure, visible on 4-chamber MRI and in regional segmentation of surface. (c) Posterior chest wall, visible on 2-chamber MRI and 3-D MRA.

6.4 Methods to precondition a model

We used a series of techniques to pre-condition the finite element model (Fig. 6.4). We estimated the true unloaded geometry using an iterative solver, and corrected for small deviations using nodal force adjustments. We converted mitral valve motion into an estimate of ventricular force, which could then vary in disease models where prescribed motion could not.

6.4.1 Unloaded geometry

The finite element method typically uses a stress-free configuration as the reference state for all stress and strain calculations, yet stress-free states rarely exist inside the body. Most tissues in the body are exposed to forces and pressures that never reach zero. This is especially true in the heart, where each chamber has an internal pressure and multiple attachments to other cardiac structures. When we imaged the heart with CMR, we acquired and fitted a deformed geometry. Although we proposed this surface as our starting shape, cardiac models based on *in vivo* geometries are not starting from a proper reference state. We sought to correct this error by solving for an estimated unloaded geometry given our loaded starting point. There are several techniques to solve "the inverse problem", including (among many) an inverse elastostatics formulation (Govindjee and Mihalic, 1996, 1998), an iterative displacement method (Raghavan et al., 2006), and a pull-back algorithm (Riveros et al., 2013) based on the work of (de Putter et al., 2007). We chose an inverse displacement method most similar to Raghavan and colleagues.

We solved the unloaded atrial geometry through an iterative algorithm. First, we guessed an unloaded shape by scaling the mesh. We scaled the radius of every endocardial node to 80% of its original value (scaling the radius by 0.80 reduces the atrial volume by roughly half). Medial and epicardial node projects were recalculated for the scaled surface with a constant thickness of 3 mm. Since the entire mesh shrank, we had to reestablish the mitral

valve boundary condition. We did so by stretching the annular mesh nodes onto the fixed MV annulus ring using prescribed nodal displacements. The displacements ranged from 0 to 5 mm (average 1.3 ± 0.9 mm). The resulting mesh became the initial unloaded guess that entered the iterative algorithm.

For each iteration, we stretched and loaded the mesh, measured its error, and updated the initial guess. First, we stretched the pulmonary vein nodes to meet the pulmonary vein objects. The veins were held fixed while the atrial mesh was stretched towards them. We used prescribed displacements to ensure proper boundaries for later steps. These displacements ranged from 5.7 to 10.6 mm (mean 7.5 ± 1.3 mm). Once the atrium was stretched, we inflated the mesh to an internal pressure of 5 mmHg, keeping both the annulus and veins fixed. We used 5 mmHg as the minimum atrial pressure during a normal cardiac cycle, based on average atrial pressures in Chapter 3 and external studies (Connolly et al., 1954; Jais et al., 2000; Matsuzaki et al., 1991; Stefanadis et al., 1998). We calculated the difference between the inflated mesh $\mathbf{x}_f$ and the unscaled mesh $\mathbf{x}_i$ as $\epsilon = \mathbf{x}_f - \mathbf{x}_i$, then updated the initial guess by subtracting 70% of the difference $\mathbf{X}_{i+1} = \mathbf{X}_i - 0.7\epsilon$. We recalculated mesh integrity and reduced the subtraction if any elements became "inverted" (had a negative Jacobian). We iterated four times until the solution reached an equilibrium. After iterating, we set the equilibrium mesh as the initial geometry for the full cardiac cycle.

6.4.2 Mitral valve motion

We simulated mitral valve motion by prescribing displacements of the annulus ring. Prescribed displacements worked well in our "baseline" model but may exaggerate motion in a disease case. For instance, if we simulated fibrosis by stiffening the atrium, the mitral valve should move less during atrial filling as a result of a given set of left ventricular forces acting on the annulus. We addressed this discrepancy by solving two FE models in series. First, we simulated the atrial cardiac cycle with prescribed motion at the mitral valve. Since the valve primarily moves along the pulmonary vein-mitral valve axis (the z-axis of our coordinate

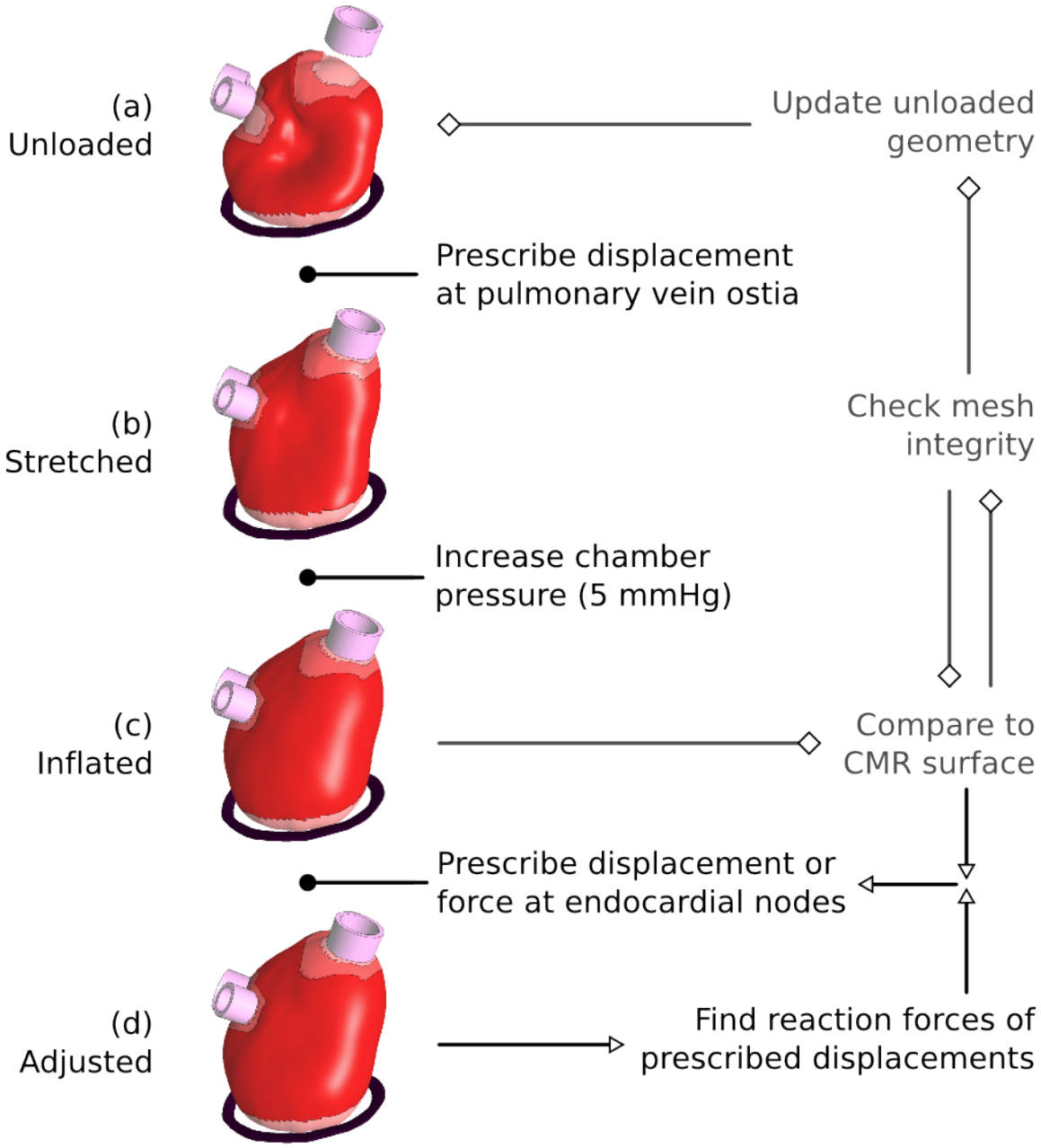

Figure 6.4: Flow chart of FE model preconditioning. (a) Unloaded geometry is estimated iteratively. (b) Geometry is stretched to the PV boundaries, then (c) inflated to 5 mmHg. This surface is compared to the *in vivo* average and adjusted. Three iterations solved the unloaded geometry. (d) Shape adjustments corrected for errors in the unloaded estimate.

system), we prescribed motion along this axis and held other mitral valve displacements fixed. Using the results of this simulation, we calculated the reaction force acting on the valve (the force required to create the prescribed displacement). We did so by relying on Lagrange Multipliers, a fundamental component of constrained finite element analysis.

As part of the linearization step discussed in §6.2, the potential energy of a mesh can be described through a matrix relationship. In a simplified form, we describe this as

$$\Pi = \frac{1}{2}\mathbf{u}^{\mathrm{T}}\mathbf{K}\mathbf{u} + \mathbf{u}^{\mathrm{T}}\mathbf{R}$$

where $\mathbf{K}$ is the global stiffness matrix and $\mathbf{R}$ is a vector of nodal forces. This is the multi-dimensional form of a spring's energy ($\Pi_{int} = \frac{1}{2}kx^2$) balanced with the external energy $\Pi_{ext} = rx$ of the force acting on it. Similar to surface fitting in Chapter 4, Lagrange multipliers enforce a constraint $\mathbf{u} = \mathbf{u}_c$ through a new function called the Lagrangian

$$\mathcal{L}(\mathbf{u}, \boldsymbol{\lambda}) = \frac{1}{2}\mathbf{u}^{\mathrm{T}}\mathbf{K}\mathbf{u} + \mathbf{u}^{\mathrm{T}}\mathbf{R} + \boldsymbol{\lambda}^{\mathrm{T}}(\mathbf{u} - \mathbf{u}_c)$$

When solving for equilibrium using variational calculus $\delta\mathcal{L} = 0$, the derivative of the Lagrangian becomes a matrix equation of

$$\begin{bmatrix} \mathbf{K} & \mathbf{1} \\ \mathbf{1} & \mathbf{0} \end{bmatrix} \begin{bmatrix} \mathbf{u} \\ \boldsymbol{\lambda} \end{bmatrix} = \begin{bmatrix} \mathbf{R} \\ \mathbf{u}_c \end{bmatrix}$$

In the case of the mitral valve, we can simplify the relationship further. The valve is a rigid body, so all nodes move relative to a single center of mass (effectively a single node). Since we assumed motion along a single coordinate axis, all but one of the nodal displacements are fixed at zero. The relationship reduces to motion at a single node in a single direction, where

$$\begin{bmatrix} k & 1 \\ 1 & 0 \end{bmatrix} \begin{bmatrix} u_z \\ \lambda \end{bmatrix} = \begin{bmatrix} f_z \\ u_{z,c} \end{bmatrix}$$

where λ is the force acting on the mitral valve. This simulated force represents the left ventricle, which pulls on the valve during ventricular systole. We then ran a second model that replaced the displacement with the ventricular force, confirming equivalent motion at the valve annulus. We used this simulated force for all subsequent models.

6.4.3 Atrial shape correction

In solving the unloaded geometry in §6.4.1, we estimated an undeformed shape using an iterative solver. Once loaded, this shape approximately matched the known *in vivo* geometry, but not perfectly. Since the iterative solution was approximate and since we knew the exact solution, we applied a small shape correction step to rectify the difference. Similar to the calculation of ventricular force in §6.4.2, we ran two models in series. The first calculated the difference between the two loaded geometries, and applied a prescribed displacement to every free node to correct the difference. We then solved for the nodal reaction forces (the Lagrange multipliers) that generated these displacements, and ran a second model with the nodal forces. We calculated the difference between the corrected model and the *in vivo* geometry, then used the corrected model as the starting point to simulate a cardiac cycle.

6.5 Methods to simulate a cardiac cycle

We relied on pressure-volume loops and literature sources to choose a left atrial material function. We also relied on histological studies to set the preferred atrial fiber direction. Active contraction was added to the material function using an additive active stress term based on the work of Guccione and colleagues. Using a hydraulic circuit, we simulated pulmonary inflow and left ventricular outflow to generate realistic filling and emptying volumes.

6.5.1 Left atrial pressure-volume loops

Pressure-volume (P-V) loops provided useful information as both inputs and outputs of the finite element model. We used features of the averaged P-V loops in WPW subjects and AF patients to guide our choice in material. The pressure-volume curve revealed a non-linear, exponential pattern during atrial filling, indicating increasing tissue stiffness under higher stretch. Since this pattern was evident in both the atrial fibrillation P-V loop and the Wolff-Parkinson-White control loop, we decided that a single material could describe both groups. We chose a material with exponential stress-strain properties, discussed in more detail in §6.5.2. We used the entire pressure-time curve of the WPW control loop to create the loading patterns in §6.3.4. The curve was segmented into four phases: 1) passive filling, 2) passive emptying, 3) active emptying, 4) active filling. Each segment was then scaled by pressure extrema set with the hydraulic circuit in §6.5.5. We used the start of passive filling (minimum pressure following a minimum volume) to denote the start of the simulation. This point corresponded to 12% of the R-R interval, which was used to choose the atrial geometry in §6.3.1, its boundary conditions in §6.3.4, and the total mitral valve translation in §6.4.2.

6.5.2 Left atrial material

We chose a constitutive relationship of the left atrium based on *in vivo* pressure-volume filling curves, biaxial testing of porcine atrial tissue, and previously published strain-energy functions of the left ventricle. There is a dearth material testing on atrial tissue, so we relied heavily on a single group (DiMartino and colleagues) who studied porcine atria (Bellini and Di Martino, 2012; Di Martino et al., 2011a) and cadaveric human tissue (Bellini et al., 2013). To match the available constitutive relationships in FEBio, we used the porcine strain energy function from (Bellini and Di Martino, 2012) as a starting point for our material. In FEBio, we chose a transversely-isotropic uncoupled Mooney-Rivlin material since its form most closely matched the published work. In this relationship, the strain energy function W

was calculated from the invariants of the deviatoric component of $\mathbf{C}$ and fiber stretch λ where

$$W = C_1\left(\tilde{I}_1 - 3\right) + C_2\left(\tilde{I}_2 - 3\right) + F_2\left(\tilde{\lambda}\right) + \frac{K}{2}\left[\ln(J)\right]^2 \tag{6.6}$$

where F_2 represented the energy of the atrial fibers as

$$\frac{\partial F_2}{\partial \tilde{\lambda}} = \begin{cases} 0 & \text{for} \quad \tilde{\lambda} \leq 1 \\ \dfrac{C_3}{\tilde{\lambda}}\left(\exp\left[C_4\left(\tilde{\lambda} - 1\right)\right] - 1\right) & \text{for} \quad 1 < \tilde{\lambda} \leq \tilde{\lambda}_{max} \\ \dfrac{1}{\tilde{\lambda}}\left(C_5 + C_6\tilde{\lambda}\right) & \text{for} \quad \tilde{\lambda}_{max} < \tilde{\lambda} \end{cases} \tag{6.7}$$

We assumed that the atrial fibers would always operated in the exponential range $\tilde{\lambda} \leq \tilde{\lambda}_{max}$ and would not contribute to compression. The free parameters of W included isotropic terms (C_1, C_2), fiber terms (C_3, C_4) and a bulk modulus K that enforced incompressibility. The porcine strain energy function used a microstructure-based function containing an isotropic term (representing the ground matrix) and an anistropic term (representing muscle and collagen fibers). We matched the isotropic components by setting $C_1 = 1.65$ kPa and $C_2 = 0$ kPa, reducing the Mooney-Rivlin material to a Neo-Hookean material. The porcine anisotropic component was a multi-parameter exponential function. We fit our fiber material to this function and found $C_3 = 0.12$ kPa and $C_4 = 10.5$.

We compared the fitted Mooney-Rivlin material to similar ones published for the left ventricle, including (Fomovsky et al., 2011; Humphrey et al., 1990; Kerckhoffs et al., 2008, 2007b). We found that our atrial material appeared stiffer than others when tested under simple spherical inflation (Beatty, 1987). Since there was a discrepancy, and since we had a large set of *in vivo* data, we manually scaled the fiber parameters (C_3, C_4) to match known atrial filling volumes. The final material was set to $C_1 = 1.65$ kPa, $C_2 = 0$ kPa, $C_3 = 0.015$ kPa, and $C_4 = 13.37$. The bulk modulus was set to $K = 500$ kPa, the maximum possible value that did not cause element locking.

The pulmonary vein ostia connected the soft left atrium to the constrained pulmonary veins. To ease the material transition and prevent stress concentrations, we stiffened the ostia by modifying the atrial material linear terms ($C_1 = 16.5\,\text{kPa}$, $C_2 = 1\,\text{kPa}$, $C_3 = 0.150\,\text{kPa}$). We did not scale the exponential portion of the fiber contribution and kept the bulk modulus the same as the atrium. We used the same material for the pericardial refelection, simulating a stiffer region between the veins without prescribing an excessive number of fixed constraints. We set the pulmonary veins and mitral valve as two rigid bodies (meaning their nodes cannot deform) with centers of mass at their respective centroids. Mitral valve displacements and forces were always applied at or about its centroid. We set pulmonary vein elements (atrial elements attached to the pulmonary veins) and mitral valve elements (elements attached to the annulus below the mitral valve plane) as a very stiff Mooney-Rivlin material without fibers ($C_1 = 100\,\text{kPa}$, $C_2 = 10\,\text{kPa}$).

6.5.3 Left atrial fibers

The transversely-isotropic Mooney-Rivlin material relies on a single preferred fiber direction. In mathematical terms, we represented this direction as a unit vector assigned to each element. The vector components in the undeformed coordinate system $\mathbf{A}(\mathbf{X})$ change as the material deforms ($\mathbf{X} \rightarrow \mathbf{x}$), creating a new set of fiber vectors in the deformed coordinate system $\mathbf{a}(\mathbf{x})$. This relationship can be used to calculate fiber stretch λ as

$$\lambda \mathbf{a} = \mathbf{F} \cdot \mathbf{A}$$

$$\lambda^2 = \mathbf{A} \cdot \mathbf{C} \cdot \mathbf{A}$$

where $\mathbf{F}$ and $\mathbf{C}$ are the deformation gradient and Cauchy-Green tensor discussed in §6.2. Fiber stretch is incorporated into the strain energy function in the F_2 component.

We set the fiber direction based on available *ex vivo* tests and *in vivo* estimates. Atrial fibers do not follow an ordered pattern nor do they observe a consistent rotation in the

transmural dimension. Rather than building a continuous map, we relied on regional averages from (Zhao et al., 2012) and (Ho et al., 2002). We used the regions defined with our atrial coordinate system and divided each into two-subregions, then further separated them into an endocardial and epicardial layer (matching the 2 elements in the radial dimension of the mesh). The four midwall regions (lateral, inferior, septal, superior walls) were divided at the midline (the x-y plane of the coordinate system) into an anterior and posterior aspect. The posterior wall was divided at the pulmonary vein midline (the x-z plane) into a superior and inferior aspect. Each aspect was then divided into an endocardial and epicardial layer. The mitral valve was not separated. This division produced twenty sub-regions of the left atrial wall. These twenty sub-regions matched the areas described by histological studies of atrial fibers, which we used to map the average direction in each region.

To simplify the fiber geometry, we set each sub-region to either a "longitudinal" or "circumferential" alignment. In the atrial coordinate system, longitudinal refers to the long-axis direction connecting the mitral valve plane to the pulmonary veins. The circumferential direction is orthogonal, running around the atrial midwall parallel to the mitral valve plane. We assigned each region a single fiber direction based on the literature averages. Using the surface normals calculated earlier, we computed the surface tangent vectors in each direction. These vectors were recomputed each time the unloaded geometry was scaled or modified. The epicardial fibers are displayed in Fig. 6.5a,b against the atrial surface, and both layers of fibers are displayed in Fig. 6.5c,d with the surface removed.

6.5.4 Atrial contraction

We used the material fibers to simulate atrial contraction. FEBio includes a muscle contraction module in each transversely-isotropic material, based on the work of (Guccione and McCulloch, 1993). During contraction, each element's fibers generated an active Cauchy stress $\boldsymbol{\sigma}^a$ which was added to the passive Cauchy stress $\boldsymbol{\sigma}^p$ already present in the strain energy function, such that $\boldsymbol{\sigma} = \boldsymbol{\sigma}^p + \boldsymbol{\sigma}^a$. We calculated the active Cauchy stress using the stress in the fiber T^a

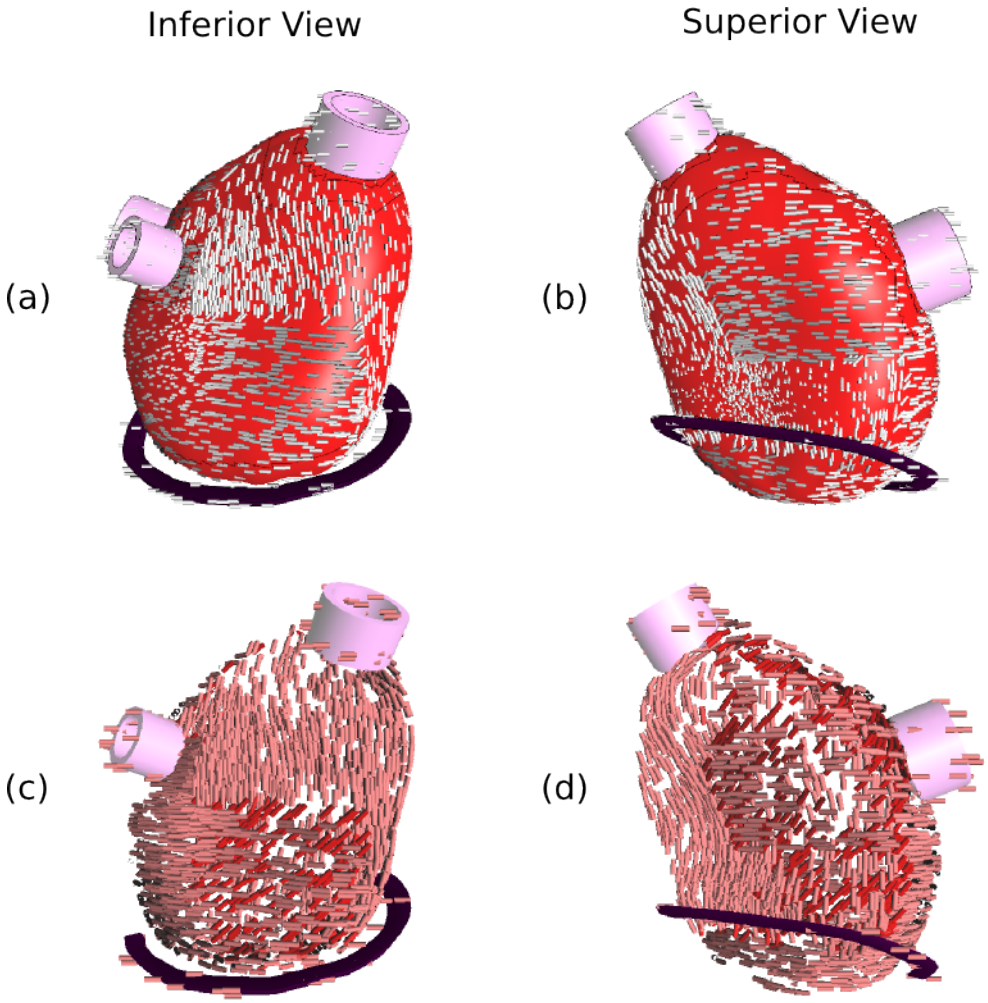

Figure 6.5: Atrial fiber geometry. Inferior and superior views show of atrial fibers in the FE model. (a) Epicardial fibers were longitudinal near the posterior wall and circumferential near the mitral valve. (b) Epicardial fibers on the superior wall. (c) Epicardial and endocardial fibers with high circumferential alignment in the lateral wall. (d) Epicardial and endocardial fibers with high longitudinal alignment in the septal wall.

and the fiber direction $\mathbf{a}$ as $\boldsymbol{\sigma}^a = T^a \mathbf{a} \otimes \mathbf{a}$. Guccione's model relied on a modified Hill-type equation to create a length-dependent fiber stress, where

$$T^a = T_{max} \frac{[\mathrm{Ca}_0]^2}{[\mathrm{Ca}_0]^2 + [\mathrm{ECa}_{50}]^2} C(t) \tag{6.8}$$

Here, T_{max} is the maximum possible stress the fiber can generate. $C(t)$ is an activation curve, equivalent to load curves discussed in §6.3.4. The peak intracellular concentration of Calcium $[\mathrm{Ca}_0]$ is a mathematical way to simulate length-dependent stress. The sensitivity to Calcium $[\mathrm{ECa}_{50}]$ was simulated as

$$[\mathrm{ECa}_{50}] = \frac{[\mathrm{Ca}_0]_{max}}{\left(\exp\left[B\left(l - l_0\right)\right] - 1\right)^{1/2}}$$

where $[\mathrm{Ca}_0]_{max}$ is the maximum peak intracellular Calcium concentration, B is a scaling factor of the force-length relationship, l is the length of the fiber, and l_0 is the reference length where no stress can develop. We used (Guccione and McCulloch, 1993) definitions of constants, setting $B = 4.75\mu\mathrm{m}^{-1}$, $l_0 = 1.58\mu$m, and $[\mathrm{Ca}_0]_{max} = 4.35\mu$M. The length l is calculated as the product of the fiber stretch λ and the reference length $l_{ref} = 2.04\mu$m. We used Guccione's piece-wise definition of the load curve $C(t)$, and set the maximum stress to match expected ejection volumes, where $T_{max} = 10$ kPa.

6.5.5 Hydraulic circuit

During the cardiac cycle, the atrium expands and contracts under varying chamber pressure. The range of this variation is governed by blood flowing into and out of the atrium. We could use the average range of healthy adults to set constant pressure extrema. These fixed values would be adequate in our baseline model, but not in a disease case where we expect pressures and flows to change. To create a more adaptive simulation, we coupled the atrial FE model to a hydraulic circuit of the pulmonary vasculature, mitral valve, and left ventricle (Fig. 6.6). We simulated each phase (filling, empyting, contraction) using an electrical circuit,

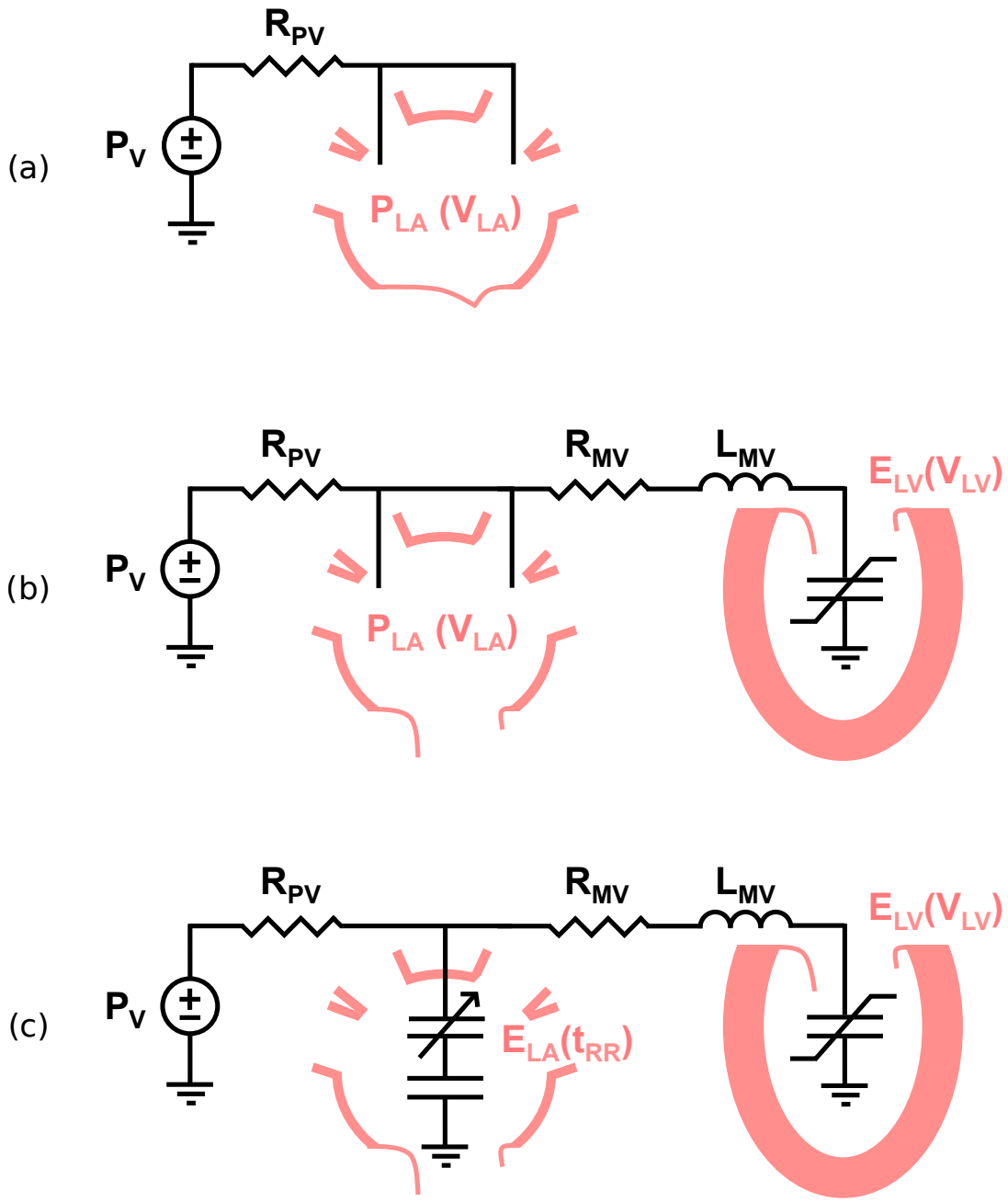

Figure 6.6: Hydraulic circuit model of blood flow. (a) Model during atrial filling, with pulmonary venous pressure P_v and pulmonary vein resistance R_{pv}. Passive atrium represented by P-V curve. b) Circuit during passive emptying, with mitral valve resistor R_{mv} and inductor L_{mv}, and exponential ventricular elastance E_{lv}. (c) Circuit during active emptying, with passive and active atrial elastance based on simulated ESPVR curve.

similar to (Alexander et al., 1987). We modeled the filling phase in Fig. 6.6a by choosing an upstream pressure in the pulmonary vasculature ($P_v = 20\,\text{mmHg}$) and a single resistor linking the vasculature to the atrium $R_{pv} = 0.078\,\frac{\text{mmHg·sec}}{\text{mL}}$. We set these values based on known pulmonary vascular pressure and pulmonary vein blood flow during atrial filling. We estimated atrial stiffness for any given FE model by running a FE simulation, generating a passive pressure-volume curve, then fitting the curve to a three-parameter exponential function where $P_{la}(V_{la}) = A_1 \exp(A_2 V_{la}) + A_3$. In the baseline FE model, we found coefficients of ($A_1 = 3.34\,\text{mmHg}$, $A_2 = 0.024\,\text{mL}^{-1}$, $A_3 = -2.97\,\text{mmHg}$) and used them to approximate atrial filling in the circuit.

At the start of atrial emptying, the mitral valve opens and blood flows into the ventricle. To capture these dynamics, we expanded the circuit in Fig. 6.6b to include resistance across the mitral valve and passive properties of the ventricle. We represented the mitral valve as a resistor and inductor in series with values $R_{mv} = 0.02\,\frac{\text{mmHg·sec}}{\text{mL}}$ and $L_{mv} = 0.0014\,\frac{\text{mmHg·sec}^2}{\text{mL}}$. The inductor captured the intertial force of blood flowing across the valve. Passive filling of the ventricle was modeled as an exponential function where $P_{lv}(V_{lv}) = B_1\left(\exp\left[B_2\left(V_{lv} - V_{lv,o}\right)\right] - 1\right)$. We set the coefficients (B_1, B_2) to achieve 120 mL end diastolic volume at 8 mmHg internal pressure via a 5.5 mmHg increase and 70 mL stroke volume. This resulted in constants of $B_1 = 3.36$ mmHg and $B_2 = 0.011\,\text{mL}^{-1}$ and an unloaded ventricular volume of $V_{lv,o} = 8\,\text{mL}$. Pulmonary vascular resistance was held constant and pulmonary vascular pressure was set to a constant of 10 mmHg during ventricular diastole.

Once the atrial and ventricular pressures equalized (diastasis), we used an active contraction circuit (Fig. 6.6c). The circuit was similar to the passive emptying circuit, but the atrium was simulated using a time-varying elastance curve with passive and active components, where $E_{la}(t) = E_{la,passive} + E_{la,active}(t)$. For a given FE model, we used a constant passive elastance to describe passive properties during contraction based on the passive elastance at the start of contraction and estimated active elastance by finding the end-systolic pressure-volume relationship (ESPVR). We found the atrial ESPVR by running a FE simulation until it

reached *peak active stress*. We then fixed active stress levels in the model and inflated the contracted chamber. We fit the fixed P-V curve to a straight line with slope $E_{la,maxactive}$ and x-intercept $V_{la,o}$. We made an activation curve $E_{la,active}(t)$ using a piece-wise cosine function that peaked at the time of peak active stress and scaled to $E_{la,maxactive}$. We solved for pressure during the active state as $P_{la} = E_{la}\,(V_{la} - V_{la,o})$.

We solved each circuit for pressures, volumes, and flows in each chamber through time. First, we created a set of ordinary differential equations to describe the changes in pressures and flows as a function of time. We then used Euler's method to discretely solve the equation set with $\Delta t \leq 7\,\mu$m. We set the initial conditions of atrial pressure and volume using the finite element model and the initial conditions of the ventricle using references values (50 mL, 2 mmHg). The timing of each phase was measured from the atrial P-V loops. We simulated passive filling for 0.25 seconds (29% R-R), passive emptying for 0.213 (25%) seconds, and active contraction for 0.394 seconds (46%), assuming a heart rate of 70 beats per minute. We did not allow retrograde flow across the mitral valve but did allow reverse flow in the pulmonary veins. We stored the pressure extrema and used them to scale pressure load curves in the FE model. At baseline, the peak pressure at mitral valve opening was $P_{mvo} = 13.1\,$mmHg, the minimum pressure at the end of passive emptying was $P_{epe} = 5.8\,$mmHg, and the maximum pressure during atrial contraction was $P_{sys} = 11.4\,$mmHg.

6.6 Solving the finite element model

All finite element simulations were done in FEBio v1.5 (Musculoskeletal Research Lab, University of Utah, Salt Lake City, Utah) using an implicit quasi-static analysis. We created a load curve for each boundary condition (displacement, force, or pressure) as a function of time (Fig. 6.7). A static analysis rendered time to be an arbitrary unit, since each step ran until it reached equilibrium. We separated the load curves into six steps representing the six phases of the model (three pre-conditioning steps, three parts of the cardiac cycle).

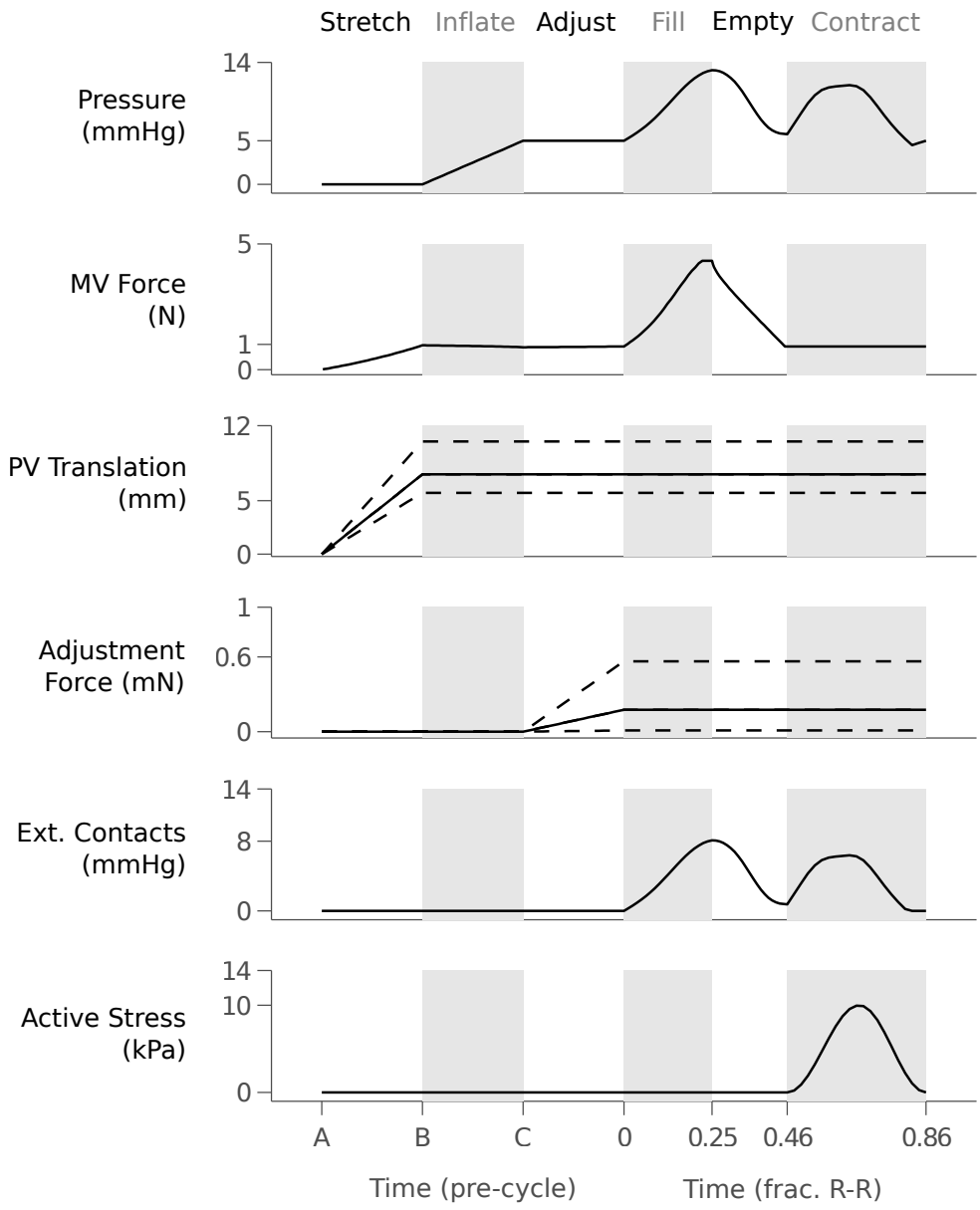

Figure 6.7: Load curves in FE model for six phases. Atrial chamber pressure, force on the mitral valve, motion of the PV boundaries, shape adjustments, boundary condition pressure, and active stress are all shown. Load plots with multiple curves show the range of data between nodes (dotted lines).

Mitral valve force was held constant during atrial contraction. We did not apply external contacts until the start of atrial filling, except in the case of the aortic root, which needed to be present throughout to maintain the concave shape.

6.6.1 FEBio solver

We used a 6-sided, 8-node tri-linear hexahedral solid elements (HEX8 in FEBio) with a 2x2x2 Gaussian integration scheme. We chose a full Newton solving routine and allowed for 100 reformations of the stiffness matrix and 30 attempts at convergence. FEBio achieved convergence when the norm of the displacements fell below a tolerance of $\epsilon_d = 10^{-4}$ and the norm of the energy fell below $\epsilon_e = 10^{-2}$. We used the *pardiso* linear solver that converged in roughly 1-2 minutes for a given static step on the University of Virginia computer cluster (3-GHz Intel Xeon cpu with 8 GB RAM). Each phase ran for 100 time steps, or $\Delta t = 0.01$ on the arbitrary $t \in [0, 1]$ scale. The simulator was adaptive (meaning the time step could automatically adjust given the convergence rates), but limited to $0.005 \geq \Delta t \leq 0.10$.

6.6.2 Global function

Following solver convergence, we exported mesh data into MATLAB for quantitative analysis and PostView (MRL, Univeristy of Utah) for viewing. Exported data included nodal information (position, displacement, reaction force) and element information (stress, strain, deformation) at every converged time step. We computed atrial volume using the endocardial nodes of the mesh and methods discussed in Chapter 5. We discarded the volume below the mitral valve plane and paired volume with the pressure-time input curve to create an atrial P-V loop. The non-linear pattern during atrial filling was fit to a simple exponential function, and energy spent during active emptying was quantified as stroke work. These global measures of mechanics were then compared to *in vivo* averages from Chapter 3. We computed changes in volume, including total, active, and passive filling, along with fractional

measures, including total emptying fraction and active emptying as a fraction of total (see Chapter 5 for details).

6.6.3 Regional function

We analyzed regional function, including regional stress, strain, and motion. For element measures (stress and strain) we computed regional averages weighted by element volume. We calculated the Cauchy stress $\boldsymbol{\sigma}$ and Green-Lagrange strain $\mathbf{E}$ along the wall dimensions (longitudinal, circumferential, shear) and the principal directions. To measure motion, we transformed nodal positions and displacements into spherical coordinates based on our time-varying coordinate system. Essentially, we measured motion in the FE model the same way we measured motion from CMR-fitted surfaces. We computed regional averages of radial motion at every endocardial node weighted by the local surface area. We used PostView to visualize regional data in 3-D and used MATLAB to create 2-D Hammer projections. These projections were then compared to *in vivo* Hammer maps of motion (see Chapter 5).

6.7 Results

The baseline model converged to the specified tolerances and required 30 hours of computation time, including pre-processing, FEM, and post-processing. The output simulated healthy atrial function based on the geometry, motion, and pressures of young adults (mean age 30 years old) with no known cardiovascular disease. We successfully solved for an estimated unloaded geometry, adjusted nodal positions to correct the loaded shape, and converted mitral valve motion into a left ventricular force. We chose an atrial material and fiber geometry that successfully matched global and regional function in both passive and active phases. We simulated blood inflow and outflow using a hydraulic circuit with realistic pulmonary vein and mitral valve flow. The validated model simulated filling, emptying and contraction

(Fig. 6.8) and will be a valuable tool to assess changes during atrial fibrillation and following ablation therapy, both modeled in later chapters.

6.7.1 Unloaded geometry

We estimated the unloaded geometry using an iterative algorithm that converged in 3 iterations. Between each iteration, we compared the inflated geometry to the target geometry (the *in vivo* average) to confirm convergence. We initially guessed an unloaded form as an 80% scaled version of the *in vivo* surface. Once inflated, this initial estimate differed by 5.9 mL or 16% of the *in vivo* average, and had an RMSE of 2.0 mm or roughly 10% of the mean radius. Following the iterative process of adjusting the unloaded geometry described in §6.4.1, the final inflated geometry differed by 0.3 mL in volume (1%) and had an RMSE of 0.8 mm (4%). Based on convergence plots in Figure 6.9, the size of the mesh (volume) converged after one iteration, while the shape of the mesh (RMSE) only converged after three iterations. We tested more iterations (four to six) but found that additional iterations did not improve the RMSE and tended to generate excessive noise in the surface radii. The final unloaded mesh had an average element volume of 0.8 mm^2 (range 0.1 to 3.4 mm^2) and an average Jacobian of 0.10 (range 0.0 to 0.7).

We considered atrial shape an important factor in regional motion, due to local curvatures and its effects on local stress. Because shape was important, *in vivo* geometry was known, and the iterative solver had a 4% error, we corrected the pre-conditioned geometry using small nodal forces. These forces ranged from 10 μN to 6 mN, with a mean of 0.2$\pm$0.4 mN. They successfully corrected the geometry to reach an RMSE of 0.1 mm (0.5% of the mean radius). These forces represented small correction factors for errors in the estimated unloaded geometry, possibly due to regional differences in material properties, fiber orientation, or wall thickness.

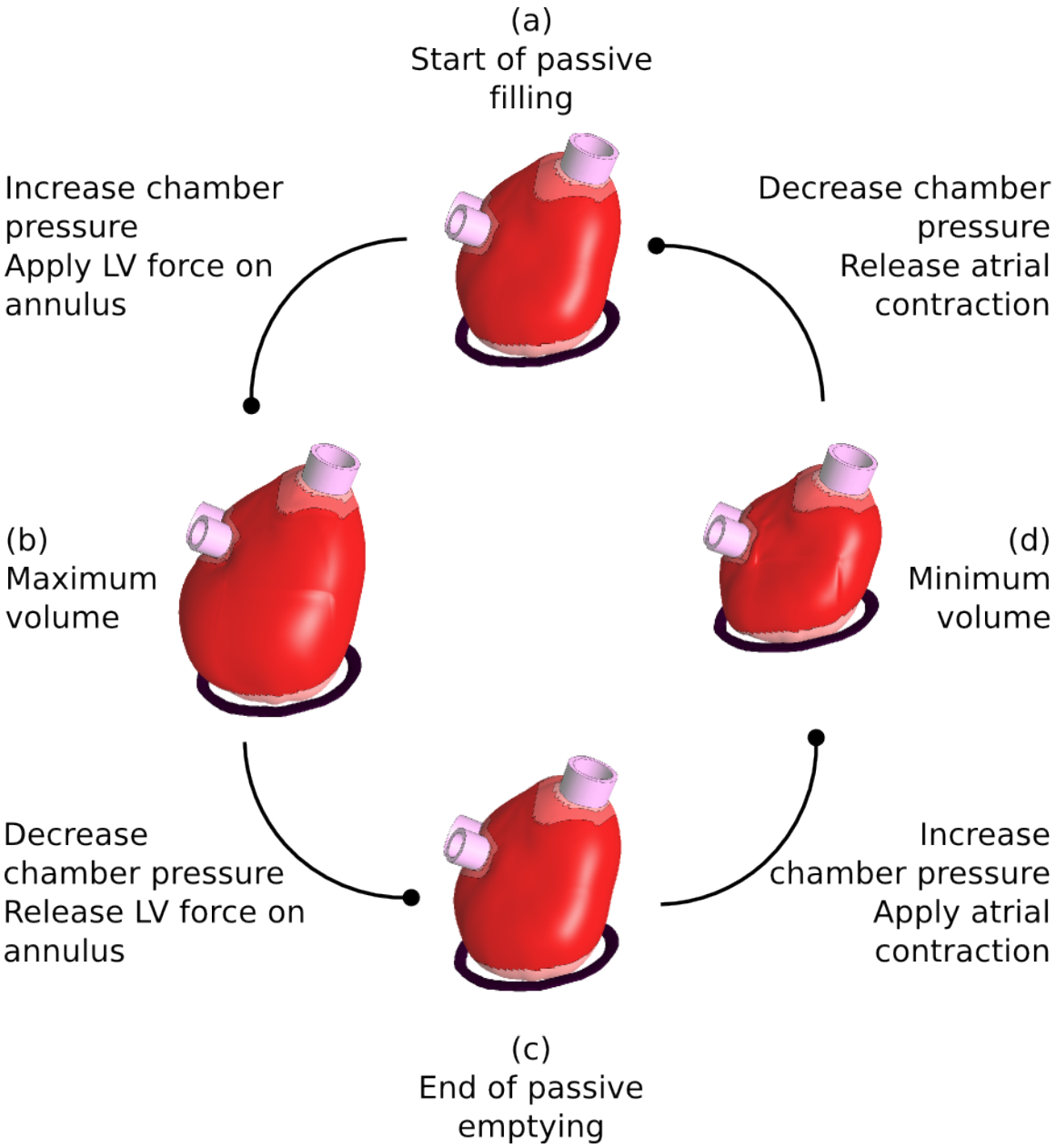

Figure 6.8: Flow chart of cardiac cycle. (a) Atrium starts to passively fill. (b) Atrium reaches its maximum volume. (c) Atrium empties passively. (d) Atrium contracts to minimum volume.

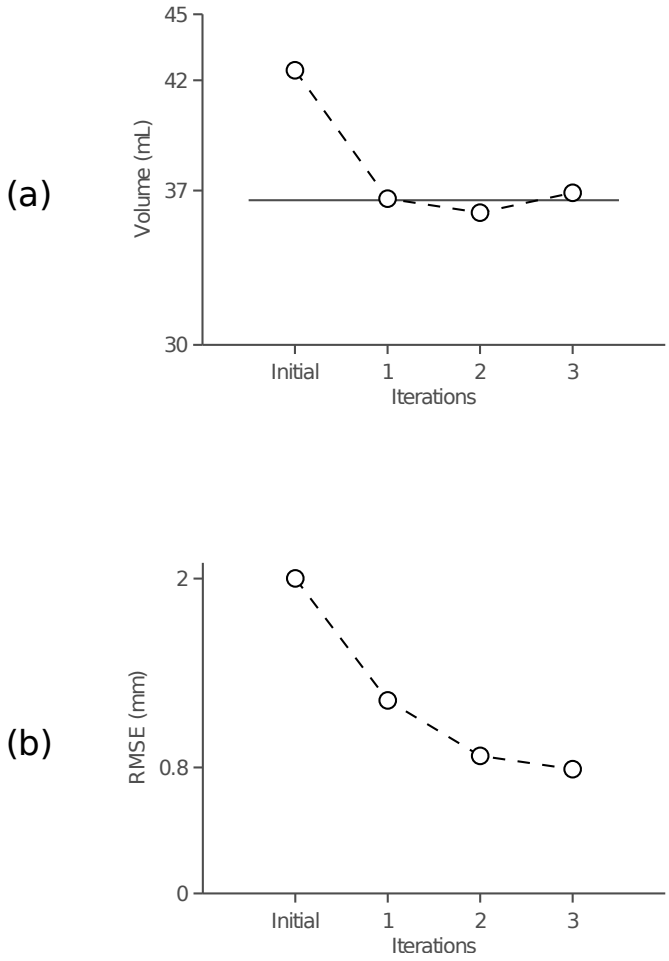

Figure 6.9: Iterative solution of unloaded geometry. (a) Unloaded volume converges to an equilibrium solution in one iteration. (b) Regional RMSE converges to an equilibrium in three iterations.

6.7.2 Mitral valve motion

We prescribed motion of the mitral valve as a rigid body moving about its centroid and chose the amount of translation based on the average *in vivo* motion measured with CMR landmarks. Average translation during filling was prescribed as 10.6 mm, entirely along the pulmonary vein-mitral valve (z) axis. To simplify the simulation, we chose to only model motion along the z-axis, which covered 95% of total *in vivo* translation (11.1 mm). We then converted the prescribed motion into a simulated ventricular force acting on the same centroid. Ventricular force reached 0.9 N at the start of filling and peaked at 4.3 N when the mitral valve opened (maximum atrial volume). In the baseline model, the displacement simulation and force simulation produced the same amount of motion (difference of $< 1\,\mu$m). Motion in the x-y plane was held at zero, with smaller reaction forces present to stabilize the model, peaking at ($F_{mv,x} = 0.2\,\text{N}$, $F_{mv,y} = 0.1\,\text{N}$). Reaction torques (forces resisting mitral valve rotation) were also present, peaking at ($M_{mv,x} = 0.013$, $M_{mv,y} = 0.031$, $M_{mv,z} = 0.001\,\text{N}\cdot\text{m}$). During active contraction the mitral valve moved towards the atrium as it contracted. Instead of prescribing forces and displacements during this phase, we held the ventricular force constant at its basal level ($F_{mv,z} = 0.9\,\text{N}$) and allowed the atrium to pull the valve upward.

6.7.3 Global function

The simulated left atrium filled to a maximum volume of 66 mL, emptied passively to 39 mL in diastasis, and contracted to 27 mL at its minimum. *All* global metrics, including volumes, changes in volume, and fractional measures were within ± 1 S.D. of the *in vivo* average (see Table 6.1), and all but two were within 10% of their *in vivo* counter-parts. Active emptying volume was slightly lower in the FE model, leading to higher errors in measures concerning active motion. We suspected this discrepancy arose from identifying the volume (V_{preA}). In FE simulations, we identified V_{preA} at the end of passive emptying, since it was the end of a simulation phase and an equilibrium point in the hydraulic circuit. In contrast, we identified (V_{preA}) *in vivo* as the peak volume immediately prior to contraction. Despite this discrepancy,

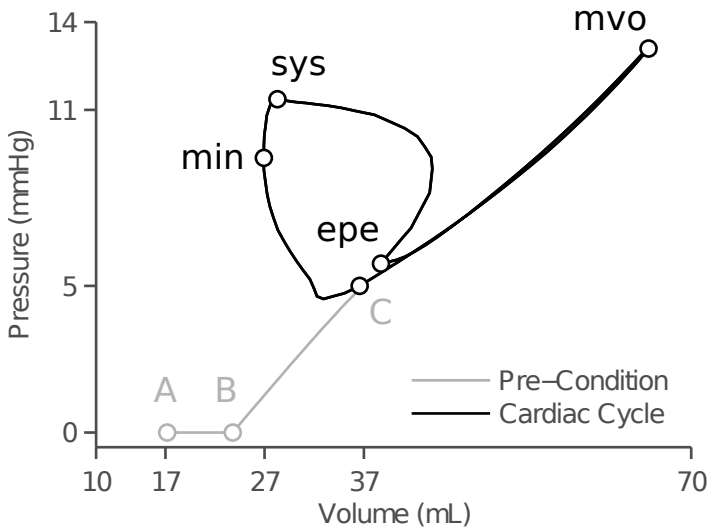

Figure 6.10: Pressure-volume loop of FEBio simulation. Atrium goes through three pre-conditioning steps (A,B,C) described earlier, then completes a full cardiac cycle. The atrium fills until the mitral valve opens (mvo), the empties until pressures equalize (epe). The atrium then contracts to a peak stress (sys) and a minimum volume (mvo) before recovering to a passive state.

we chose to use the end of passive emptying as a marker in our FE models because small pressure rises during diastasis were hard to quantify and difficult to simulate accurately.

The atrial pressure-volume loop matched the shape, size, and patterns observed in clinical WPW P-V loops in Chapter 3 (Fig. 6.11a). We fit the filling curve to a simple exponential function that we used to analyze clinical P-V loops and found a global stiffness coefficient of $k_{chamber} = 0.08\,\mathrm{mL}^{-1}$ and $k_{tissue} = 2.4$, which matched the low-end range of *in vivo* stiffness ($k_{chamber} = 0.11 \pm 0.05\,\mathrm{mL}^{-1}$, $k_{tissue} = 7.6 \pm 2.6$). This was expected since a healthy atrium should be less stiff than clinical P-V curves of atria damaged by AF. Similarly, we integrated the active area of the loop to quantify stroke work and found it to be 66 mmHg·mL (8.8 mJ), in the middle of *in vivo* ranges (average 8.8 ± 5.6 mJ). This was expected given the variety of ways AF and its co-morbidities can increase or decrease stroke work in the atrium.

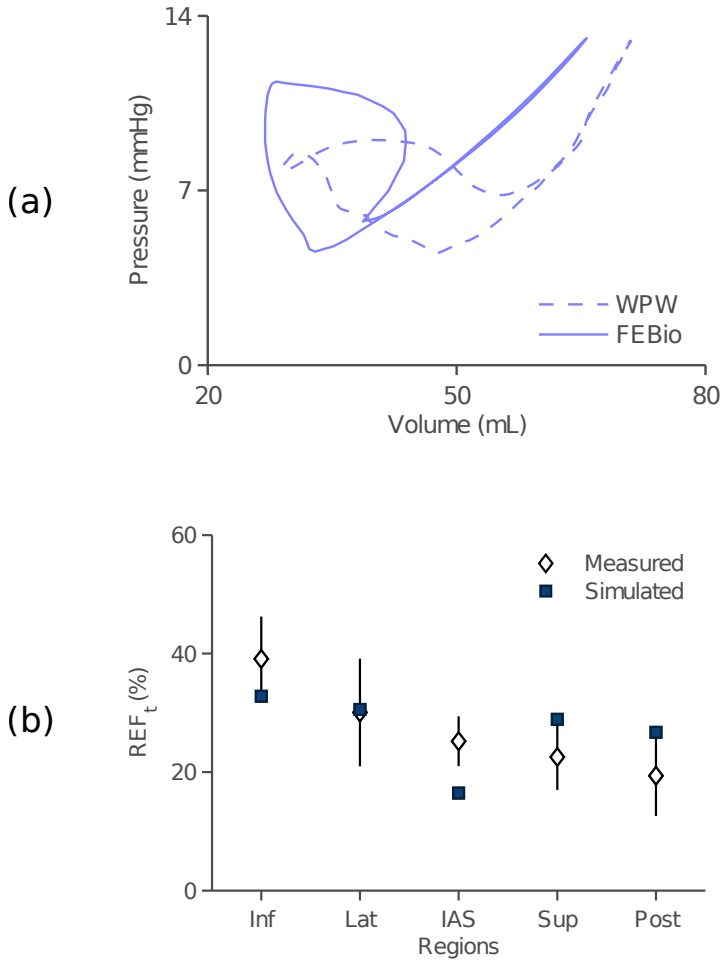

Figure 6.11: Validation of global and regional function with *in vivo* averages. (a) Global P-V loop mechanics of baseline FE model compared to average WPW syndrome P-V loops from Chapter 3. (b) Regional REF_t from baseline FE model compared to averages from wall motion analysis of healthy subjects in Chapter 5. Results agree in 4 of 5 regions within 1 S.D.

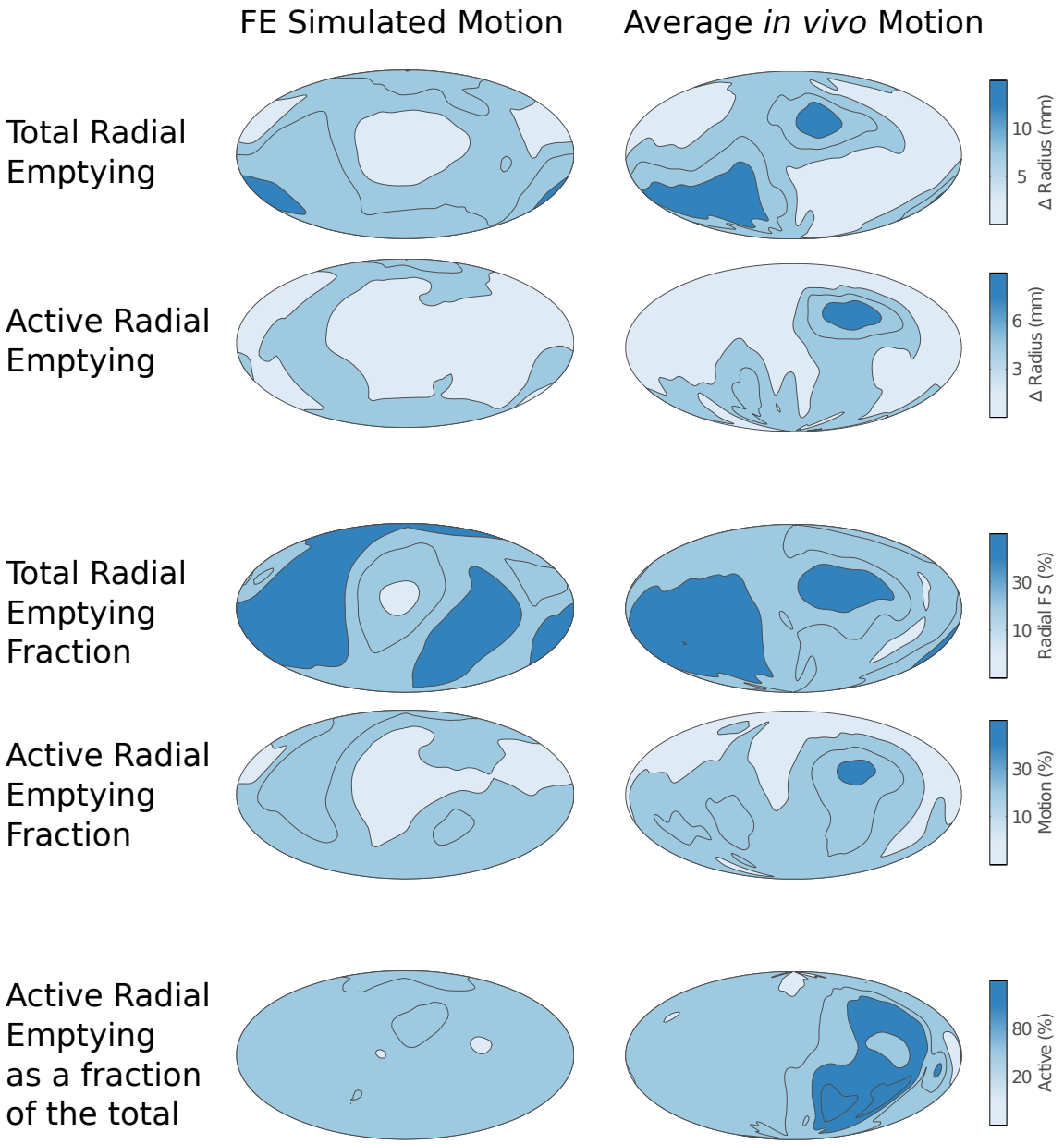

Figure 6.12: Hammer maps of regional motion, including changes in radius and fractional measures. Simulation results are compared to *in vivo* maps of the averaged healthy atrium.

Metric	Finite Element Simulation	*in vivo* Mean±S.D.	Error (%)
V_{max} (mL)	66	71 ± 18	7
V_{min} (mL)	27	29 ± 11	7
V_{preA} (mL)	39	44 ± 12	11
Changes in Volume			
ΔV_t (mL)	39	42 ± 11	7
ΔV_p (mL)	27	27 ± 8	< 1
ΔV_a (mL)	12	15 ± 6	20
Fractional Measures			
EF_t (%)	59	60 ± 9	2
EF_p (%)	41	38 ± 7	8
EF_a (%)	31	34 ± 12	9
$V_{p\|t}$ (%)	69	65 ± 10	6
$V_{a\|t}$ (%)	31	35 ± 10	11

Table 6.1: Table of global function (volumes, changes in volume, fractional measures) from finite element simulation. Results compared to *in vivo* averages from Chapter 5.

6.7.4 Regional function

We observed regional heterogeneities in atrial motion that were similar to variations we saw in the averaged *in vivo* data in Chapter 5 (Fig. 6.12). Among the four atrial midwall regions, total motion range from 16 to 33% (total radial emptying fraction), peaking in the lateral and inferior walls (Table 6.2). This regional distribution matched the pattern of motion seen in healthy adults (Fig. 6.12, total radial emptying fraction REF_t). We compared five measures of regional function from simulated and *in vivo* motion. For the five measures in five different regions, 21 of 25 simulated values ($> 80\%$) agreed with the average *in vivo* results within one standard deviation. REF_t agreed within one standard deviation in four of five left atrial wall regions (Fig. 6.11b). The general patterns of regional motion matched as well, indicating that the finite element simulation successfully captured the regional heterogeneity in atrial

Metric	Source	*Region*				
		Posterior	Inferior	Septal	Superior	Lateral
ΔR_t (mm)	FEM (μ)	7	8	4	7	**8**
	in vivo ($\mu \pm \sigma$)	6 ± 2	$\mathbf{10 \pm 2}$	8 ± 1	6 ± 1	8 ± 2
ΔR_a (mm)	FEM (μ)	**3**	3	2	2	3
	in vivo ($\mu \pm \sigma$)	2 ± 2	3 ± 1	3 ± 1	$\mathbf{4 \pm 2}$	3 ± 2
	Fractional Measures					
REF_t (%)	FEM (μ)	27	**33**	16	29	31
	in vivo ($\mu \pm \sigma$)	19 ± 8	$\mathbf{41 \pm 8}$	27 ± 6	25 ± 7	32 ± 9
REF_a (%)	FEM (μ)	15	**17**	7	12	13
	in vivo ($\mu \pm \sigma$)	7 ± 8	19 ± 8	13 ± 4	$\mathbf{21 \pm 6}$	13 ± 13
$R_{a\|t}$ (%)	FEM (μ)	**45**	40	40	34	33
	in vivo ($\mu \pm \sigma$)	32 ± 25	34 ± 16	46 ± 24	$\mathbf{75 \pm 34}$	40 ± 35

Table 6.2: Simulation results of regional function compared to *in vivo* averages.

function.

We measured stress and strain in each element in the model, focusing on the maximum stresses and strains during the cardiac cycle (at mitral valve opening). We reported stress as the Cauchy stress tensor $\boldsymbol{\sigma}$ and strain as the Green-Lagrange strain tensor $\mathbf{E}$. Components of these tensors in the circumferential and longitudinal directions were computed, as well as the principal directions based on the eigenvalues of the tensor. All strains were referenced to the "true" unloaded geometry. Regional strain was highest in the lateral wall (mean of 128%), especially near the endocardial border (140%, Fig. 6.13). Longitudinal strains were much higher than circumferential or shear strains in both the endocardial and epicardial elements (47% vs. 29% and 2%; 49% vs. 20% and 1%, respectively). Higher longitudinal strains were most likely caused by the mitral valve motion in the longitudinal (z-axis) direction and circumferentially-oriented fibers (the atrium stretched more easily in the cross-fiber direction). Generally, strains were highest in the atrial midwall and lower in the posterior wall as seen in the 2-D strain maps. Circumferential strain was highest in the endocardial aspect of the

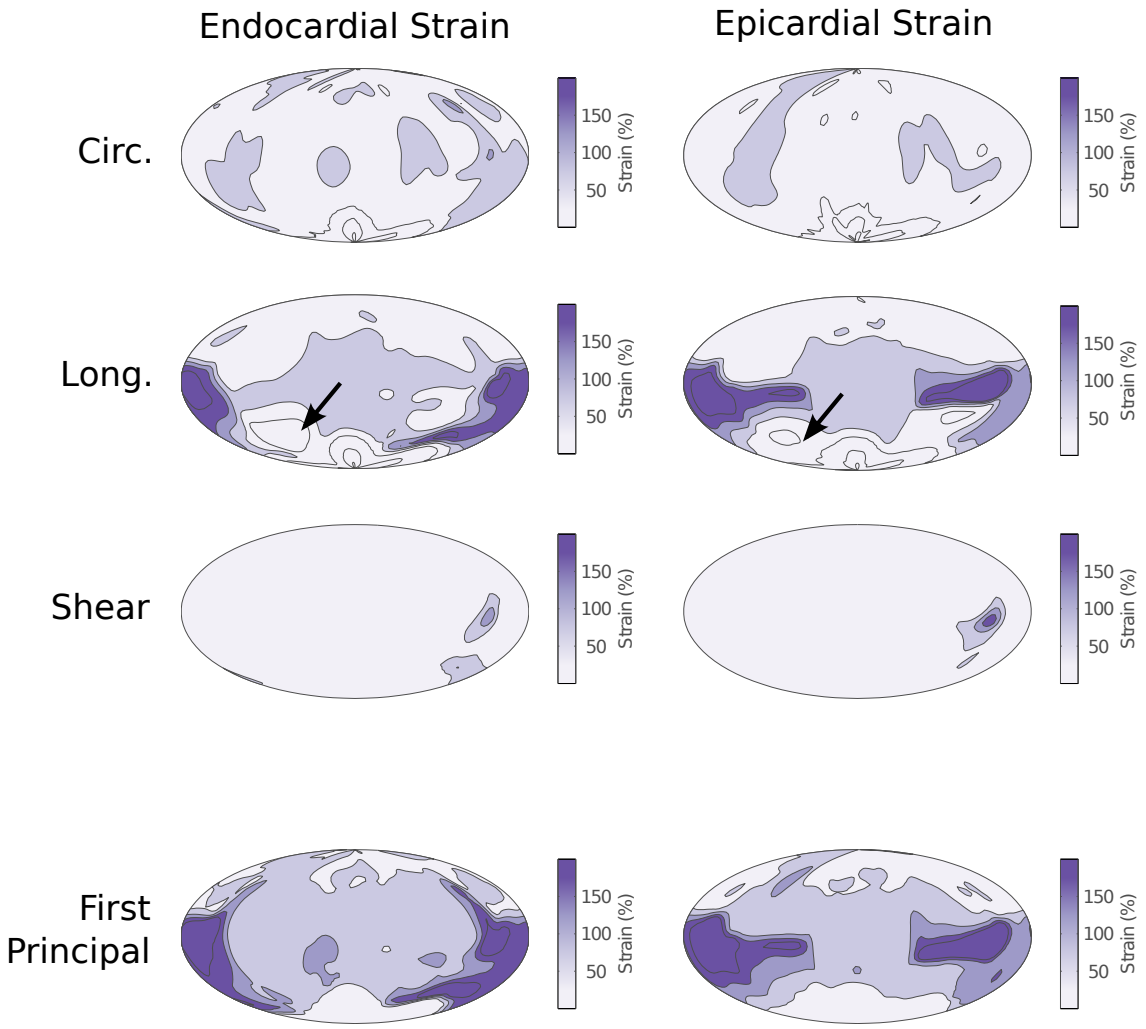

Figure 6.13: Regional strain Hammer maps for the circumferential (circ.), longitudinal (long.), shear, and first principal directions. Maps displayed for both the endocardial and epicardial elements. Arrows highlight low stress in the inferior wall near the mitral valve.

lateral wall (43%) and shear strain was highest in the endocardial aspect of the superior wall (15%). Interestingly, longitudinal strain was close to zero in the annular region of the inferior wall due a confluence of shape, fiber alignment, and regional motion in that area. Strain peaked in the lateral wall immediately inferior to the pulmonary vein, as the tissue stretched between the fixed vein boundary and the prescribed motion of the nearby valve.

Regional stress had a divergent pattern to regional strain and peaked in the septal wall on both the endocardial (29 kPa) and epicardial elements (25 kPa), as depicted on the Hammer projections in Figure 6.14, First Principal Stress. This high stress originated from longitudinal fibers that were highly aligned in the septal wall (peak longitudinal stress of 28 and 24 kPa). These fibers connected the fixed right pulmonary veins to the mitral valve, and their alignment created high stresses as the valve moved. Similar to strain, regional stresses were much higher in the longitudinal direction compared to circumferential or shear directions across the entire atrium (global average of 17 kPa vs. 6 and -0.2 kPa). Average circumferential stress was highest in the endocardial aspect of the lateral wall (12 kPa), while shear stress was highest in the epicardial aspect of the superior wall (2 kPa). The first principal stress showed how dominant longitudinal stress patterns were in the overall stress of the model, contributing more than 90% of the total stress in both the endocardial and epicardial elements.

6.7.5 Hydraulic circuit function

The hydraulic circuit simulated pulmonary vein blood flow during atrial filling and mitral valve flow during atrial emptying (Table 6.3). The circuit simulated a left ventricular stroke volume of 70 mL and an end-diastolic volume of 121 mL, producing an ejection fraction of 58% that matched normal cardiac function. Ventricular pressure rose from 2 mmHg (prescribed) to 8.2 mmHg during ventricular diastole. Mitral valve blood flow was higher during passive emptying compared to active emptying (peaks of 58 vs. 39 cm/s), producing an E-to-A ratio of 1.5, again matching normal cardiac function. As expected, the ventricle filled more during

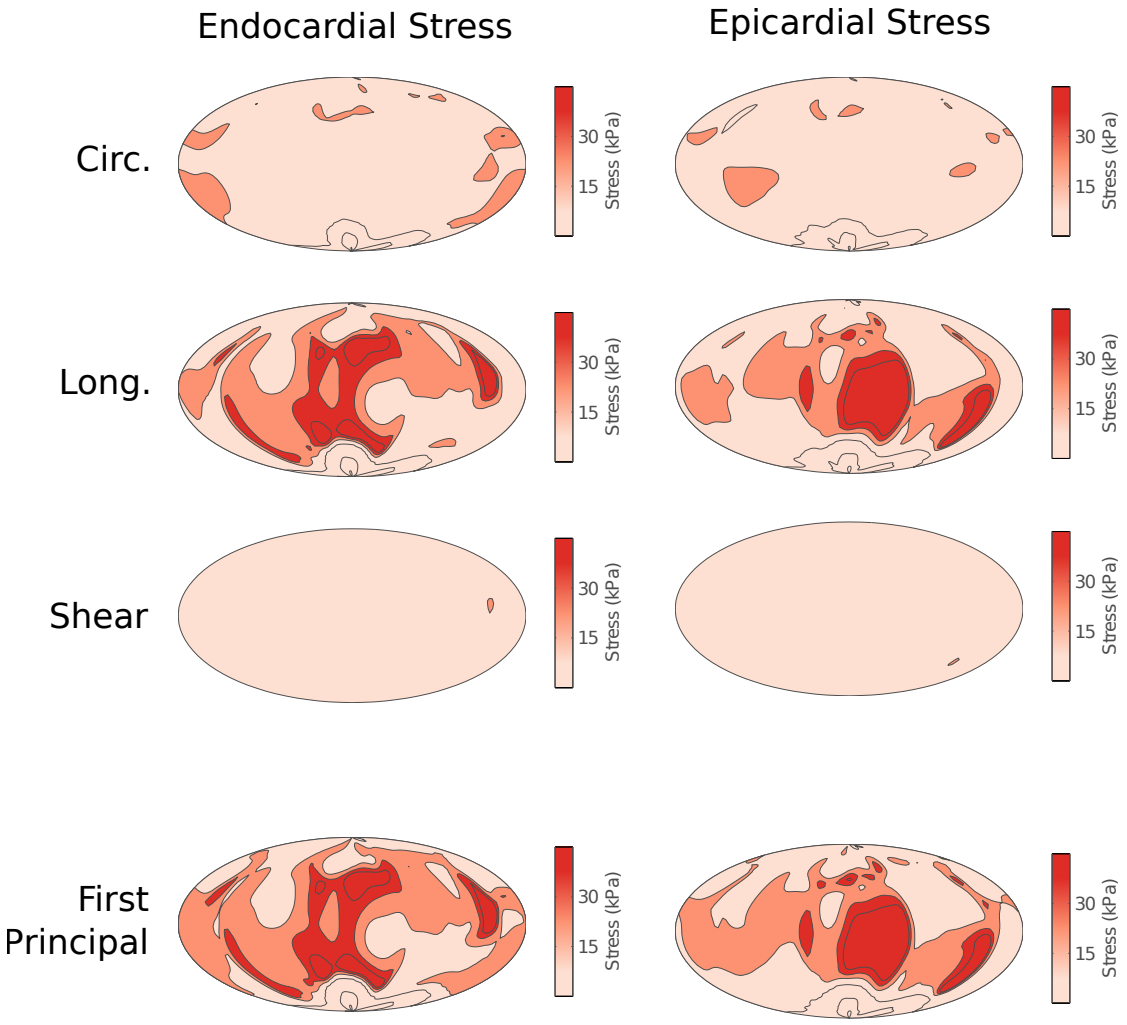

Figure 6.14: Regional stress Hammer maps for the circumferential (circ.), longitudinal (long.), shear, and first principal directions. Maps displayed for both the endocardial and epicardial elements.

Metric	Filling	*Emptying*		
		Passive	Active	Total
		Flow (cm/sec)		
Mean Q_{pv}	37	23	22	22
Peak Q_{pv}	55	32	35	34
Mean Q_{mv}	0	32	12	19
Peak Q_{mv}	0	58	39	58
		Volume (mL)		
ΔV_{la}	29	27	18	42
ΔV_{lv}	n.a.	41	29	70
		Pressure (mmHg)		
ΔP_{la}	8.1	7.7	6.3	8.1
ΔP_{lv}	n.a.	3.1	3.2	6.2

Table 6.3: Results of hydraulic circuit. Circuit simulated pulmonary vein and mitral valve flow (Q_{pv} and Q_{mv}) during atrial filing and emptying (both mean and peak flow). Changes in atrial and ventricular volume were calculated (ΔV_{la} and ΔV_{lv}, respectively), as well as changes in atrial and ventricular pressure (ΔP_{la} and ΔP_{lv}, respectively).

early diastole (passive emptying), collecting 60% of total blood volume during this short time period. The pulmonary veins remained open to flow during all phases of filing and emptying. Pulmonary blood flow during atrial filling (37 cm/sec) and passive emptying (23 cm/sec) matched Doppler studies that measured average flow. Pulmonary vein inflow dropped to near zero during atrial contraction, but did not reach a negative value (no backflow into the veins). Flow reversal was impeded by the constant upstream pressure, which remained higher than atrial pressure even during peak contraction.

6.8 Discussion

We designed a novel atrial finite element model that accurately simulated atrial function within 10% of *in vivo* averages. We used information from cardiac MRI, including surface

fits, anatomic landmarks, and neighboring structures, to generate accurate geometries and boundary conditions. We chose a realistic material and fiber geometry based on referenced studies, then solved for an estimated unloaded geometry using an iterative algorithm. The model simulated regional function that matched *in vivo* data for over 80% of the measured quantities. A hydraulic circuit oriented the FE atrium in a realistic physiological environment that included pulmonary blood flow and ventricular filling. We used the hydraulic circuit to estimate filling and ejection pressures in the atrium, as well as mitral valve flows and ventricular filling volumes indicative of healthy left heart function. We will use this atrial finite element model to study the changes during a disease (AF) and the effects of a procedure (ablation) in later chapters.

6.8.1 Comparisons to other finite element models

Some aspects of the finite element model are impossible to validate with experimental data but can be compared with prior work. Di Martino and colleagues (Di Martino et al., 2011a) published a comprehensive model of the porcine left atrium, including a full cardiac cycle of pressure variation and prescribed mitral valve motion. They estimated an average first principal stress of 11 to 13 kPa, which was low compared to our average of 17 kPa (difference of 35%). This discrepancy stemmed from differences in geometry (the porcine model had a large appendage and did not include atrial fibers) and loading (the porcine model had a maximum pressure of 10 mmHg). A second group built a simpler model that used human atrial geometry (Hunter et al., 2012). They reported a "von Mises" stress of 26 to 52 kPa in the atrial wall when inflated to 20 mmHg. If we do a similar calculation, our model had a effective stress of 8 to 27 kPa, which matches well considering a 2.5x higher filling pressure. Our study matched some of Hunter and colleagues' identified "stress peaks" including ones in the septal wall and near the pulmonary vein ostia. Although choices in materials, loading, and geometry limit the ability to compare models, we found a consistent set of trends between the few atrial FE models that were available.

6.8.2 Global function

The P-V loop in Figure 6.10 showed the changes in atrial size during pre-conditioning, including the stretch to the pulmonary veins and inflation to the minimum operating pressure (points A→B and B→C, respectively). During inflation, the atrium followed a slightly concave path ($d^2P/dV^2 < 0$) to reach the target volume of 37 mL. This portion of the P-V curve arose from the isotropic component of the strain energy function (the Neo-Hookean material), which contributed the majority of strain energy during early inflation from 0 to 5 mmHg. In simple spherical models of inflation, a Neo-Hookean material also followed an initially concave path (Beatty, 1987). Once the model transitioned to atrial filling, the P-V curve took on an exponential shape ($d^2P/dV^2 > 0$) as the atrium expanded. This portion of the loop arose from the exponential strain energy function governing fiber behavior in the model. Although subtle, the balance between components of strain energy (isotropic-dominant at low stretch and fiber-dominant at high stretch) enabled us to simulate a realistic P-V curve that reached target points of pressure and volume while also maintaining a reasonable unloaded geometry. This would not have been possible with a purely exponential strain energy function.

6.8.3 Regional function

Although over 80% of the regional function metrics agreed with *in vivo* data, there were four measures that did not agree. Their discrepancy was rooted in two sources: 1) total motion in the septal wall and 2) active motion in the superior wall. These disagreements were visualized in the Hammer Map comparison (Fig. 5.9, REF_t and $R_{a|t}$ respectively).

The simulation underestimated motion in the septal wall due to the longitudinal fibers, which developed high regional stresses (Fig. 6.14) that limited radial expansion. A more detailed model might include smaller portions of the septal wall, including the fossa ovalis, that would disrupt this alignment and lower stress. In addition, we assumed a constant wall thickness (3 mm), yet it is known that some regions are thicker than others (Ho et al., 2002).

Hunter and colleagues showed that septal wall stress decreased when thickness increased (Hunter et al., 2012).

In the superior wall, the balance between active and passive motion may have been influenced by the external influence of the aortic root beyond the simple pressure boundary condition included in our model. Motion of the aortic root during ventricular systole and its means of attachment to the left atrium both influence superior wall motion. Similar to the septal wall discrepancy, the superior wall is thicker than other regions (Ho et al., 1999) and varying atrial thickness regionally would alter function.

Unlike regional stresses, regional strains can easily be validated due to a plethora of strain-based imaging studies. Many groups have used speckle tracking to estimate atrial strain, and more recent work has parsed these results into a regional analysis (Vianna-Pinton et al., 2009). We used this study to validate simulated longitudinal strain. To compare properly, we estimated a "measured" strain based on a deformed reference at the start of atrial contraction (speckle tracking assumes one image frame as a zero-strain state). We saw reasonable agreement in average strains, both during filling (27% in simulation vs. 25% in speckle-tracking) and active emptying (14% vs. 14%). The agreement was especially strong in the inferior, septal, superior, and posterior walls (average difference of 5% strain). Vianna-Pinton and colleagues measured lower strain in the later wall during filling (30%) compared to our simulated average (60%). We suspected that the highly aligned circumferential fibers in our model exaggerated motion along parts of the lateral wall. A more detailed fiber geometry may correct for this effect.

6.8.4 Limitations

A finite element model is an approximation of the physiological response to loading. All physiological models require assumptions, simplifications, and estimations to offer viable information. Our left atrial model was no exception - we relied heavily on our own clinical data to create accurate geometry and boundary conditions. The global mechanics (pressures and

volumes) were grounded in multiple sources and heavily validated (against both internal and external information), resulting in an accurate portrayal of global function. Regional motion was also quite accurate, with smaller discrepancies due to simplified boundary conditions. Regional stress and strain measures varied more, partially due to the material model and assumed fiber geometry. Improving the material characterization of the atrium should be a high priority, including more biaxial testing experiments on healthy atrial tissue and characterizations of its composition. Improvements in histology and CMR imaging may lead to better representations of fiber geometry.

We made a series of assumptions about the pulmonary veins, including their shape, size, and how they attach to the atrium. Future models could rely on 3-D CMR techniques such as MR angiography to provide a more complete 3-D geometry and accurate vein connection. Veins could be inflated to physiological pressures and allowed to deform (their motion was lost in our fixed boundary assumptions). This would eliminate some of the stress concentrations we saw near the veins. Other boundaries, such as the pericardium and its attachment to the chest wall, could be added if imaged properly. MRA would provide a more detailed atrial shape that included the appendage. This technique could be used in conjunction with cineMR to measure wall motion and landmark translation.

References

J. Alexander, K. Sunagawa, N. Chang, and K. Sagawa. Instantaneous pressure-volume relation of the ejecting canine left atrium. *Circulation Research*, 61(2):209–219, Aug. 1987.

J. Argyris. Energy theorems and structural analysis: A generalized discourse with applications on energy principles of structural analysis including the effects of temperature and non-linear stress-strain relations. *Aircraft Engineering and Aerospace Technology*, 26(11):383394, 1954.

M. F. Beatty. Topics in finite elasticity: Hyperelasticity of rubber, elastomers, and biological TissuesWith examples. *Applied Mechanics Reviews*, 40(12):1699–1734, 1987.

C. Bellini and E. S. Di Martino. A mechanical characterization of the porcine atria at the healthy stage and after ventricular tachypacing. *J Biomech Eng*, 134(2):021008, Feb. 2012.

C. Bellini, E. S. D. Martino, and S. Federico. Mechanical behaviour of the human atria. *Ann Biomed Eng*, 41(7):1478–1490, July 2013.

W. A. Brekelmans, H. W. Poort, and T. J. Slooff. A new method to analyse the mechanical behaviour of skeletal parts. *Acta Orthop Scand*, 43(5):301–317, 1972.

R. W. Clough. Early history of the finite element method from the view point of a pioneer. *International Journal for Numerical Methods in Engineering*, 60(1):283287, 2004.

D. C. Connolly, J. W. Kirklin, and E. H. Wood. The relationship between pulmonary artery wedge pressure and left atrial pressure in man. *Circulation Research*, 2(5):434–440, Sept. 1954.

M. Courtemanche, R. J. Ramirez, and S. Nattel. Ionic mechanisms underlying human atrial action potential properties: insights from a mathematical model. *American Journal of Physiology - Heart and Circulatory Physiology*, 275(1):H301–H321, July 1998.

S. de Putter, B. Wolters, M. Rutten, M. Breeuwer, F. Gerritsen, and F. van de Vosse. Patient-specific initial wall stress in abdominal aortic aneurysms with a backward incremental method. *Journal of Biomechanics*, 40(5):1081–1090, 2007.

E. S. Di Martino, C. Bellini, and D. S. Schwartzman. In vivo porcine left atrial wall stress: Effect of ventricular tachypacing on spatial and temporal stress distribution. *Journal of Biomechanics*, 44(16):2755–2760, Nov. 2011a.

E. S. Di Martino, C. Bellini, and D. S. Schwartzman. In vivo porcine left atrial wall stress: Computational model. *Journal of Biomechanics*, 44(15):2589–2594, Oct. 2011b.

O. Dossel, M. W. Krueger, F. M. Weber, M. Wilhelms, and G. Seemann. Computational modeling of the human atrial anatomy and electrophysiology. *Med Biol Eng Comput*, 50 (8):773–799, Aug. 2012.

G. M. Fomovsky, J. R. Macadangdang, G. Ailawadi, and J. W. Holmes. Model-based design of mechanical therapies for myocardial infarction. *J. of Cardiovasc. Trans. Res.*, 4(1): 82–91, Feb. 2011.

S. Govindjee and P. A. Mihalic. Computational methods for inverse finite elastostatics. *Computer Methods in Applied Mechanics and Engineering*, 136(1-2):47–57, Sept. 1996.

S. Govindjee and P. A. Mihalic. Computational methods for inverse deformations in quasi-incompressible finite elasticity. *Int. J. Numer. Meth. Engng.*, 43(5):821–838, Nov. 1998.

J. M. Guccione and A. D. McCulloch. Mechanics of active contraction in cardiac muscle: Part IConstitutive relations for fiber stress that describe deactivation. *Journal of Biomechanical Engineering*, 115(1):72–81, 1993.

A. C. Guyton, A. W. Lindsey, B. Abernathy, and T. Richardson. Venous return at various right atrial pressures and the normal venous return curve. *Am J Physiol*, 189(3):609–615, June 1957.

S. Y. Ho, D. Sanchez-Quintana, J. A. Cabrera, and R. H. Anderson. Anatomy of the left atrium: implications for radiofrequency ablation of atrial fibrillation. *J. Cardiovasc. Electrophysiol.*, 10(11):1525–1533, Nov. 1999.

S. Y. Ho, R. H. Anderson, and D. Snchez-Quintana. Atrial structure and fibres: morphologic bases of atrial conduction. *Cardiovascular Research*, 54(2):325–336, May 2002.

J. D. Humphrey, R. K. Strumpf, and F. C. P. Yin. Determination of a constitutive relation for passive myocardium: II.Parameter estimation. *Journal of Biomechanical Engineering*, 112(3):340–346, 1990.

P. J. Hunter and B. H. Smaill. The analysis of cardiac function: a continuum approach. *Prog. Biophys. Mol. Biol.*, 52(2):101–164, 1988.

R. J. Hunter, Y. Liu, Y. Lu, W. Wang, and R. J. Schilling. Left atrial wall stress distribution and its relationship to electrophysiologic remodeling in persistent atrial fibrillation. *Circ Arrhythm Electrophysiol*, Jan. 2012.

P. Jais, J. T. Peng, D. C. Shah, S. Garrfgue, M. Hocini, T. Yamane, M. Haissaguerre, S. S. Barold, R. Roudaut, and J. Clementy. Left ventricular diastolic dysfunction in patients with SoCalled lone atrial fibrillation. *Journal of Cardiovascular Electrophysiology*, 11(6): 623–625, June 2000.

S. R. Jernigan, G. D. Buckner, J. W. Eischen, and D. R. Cormier. Finite element modeling of the left atrium to facilitate the design of an endoscopic atrial retractor. *J Biomech Eng*, 129(6):825–837, Dec. 2007.

R. Kerckhoffs, J. Lumens, K. Vernooy, J. Omens, L. Mulligan, T. Delhaas, T. Arts, A. McCulloch, and F. Prinzen. Cardiac resynchronization: Insight from experimental and computational models. *Progress in Biophysics and Molecular Biology*, 97(23):543–561, June 2008.

R. C. P. Kerckhoffs, A. D. McCulloch, J. H. Omens, and L. J. Mulligan. Effect of pacing site and infarct location on regional mechanics and global hemodynamics in a model based study of heart failure. In F. B. Sachse and G. Seemann, editors, *Functional Imaging and Modeling of the Heart*, number 4466 in Lecture Notes in Computer Science, pages 350–360. Springer Berlin Heidelberg, Jan. 2007a.

R. C. P. Kerckhoffs, M. L. Neal, Q. Gu, J. B. Bassingthwaighte, J. H. Omens, and A. D. McCulloch. Coupling of a 3D finite element model of cardiac ventricular mechanics to lumped systems models of the systemic and pulmonic circulation. *Ann Biomed Eng*, 35(1): 1–18, Jan. 2007b.

L. Lickfett, T. Dickfeld, R. Kato, H. Tandri, C. R. Vasamreddy, R. Berger, D. Bluemke, B. Lderitz, H. Halperin, and H. Calkins. Changes of pulmonary vein orifice size and location throughout the cardiac cycle: Dynamic analysis using magnetic resonance cine imaging. *Journal of Cardiovascular Electrophysiology*, 16(6):582588, 2005.

S. A. Maas, B. J. Ellis, G. A. Ateshian, and J. A. Weiss. FEBio: finite elements for biomechanics. *Journal of Biomechanical Engineering*, 134(1):011005, 2012.

M. Matsuzaki, M. Tamitani, Y. Toma, H. Ogawa, K. Katayama, Y. Matsuda, and R. Kusukawa. Mechanism of augmented left atrial pump function in myocardial infarction and essential hypertension evaluated by left atrial pressure-dimension relation. *The American Journal of Cardiology*, 67(13):1121–1126, May 1991.

R. Mazhari and A. D. McCulloch. Integrative models for understanding the structural basis of regional mechanical dysfunction in ischemic myocardium. *Annals of Biomedical Engineering*, 28(8):979–990, Aug. 2000.

A. Nygren, C. Fiset, L. Firek, J. W. Clark, D. S. Lindblad, R. B. Clark, and W. R. Giles. Mathematical model of an adult human atrial cell the role of k+ currents in repolarization. *Circulation Research*, 82(1):63–81, Jan. 1998.

M. L. Raghavan, B. Ma, and M. F. Fillinger. Non-invasive determination of zero-pressure geometry of arterial aneurysms. *Ann Biomed Eng*, 34(9):1414–1419, Sept. 2006.

F. Riveros, S. Chandra, E. A. Finol, T. C. Gasser, and J. F. Rodriguez. A pull-back algorithm to determine the unloaded vascular geometry in anisotropic hyperelastic AAA passive mechanics. *Ann Biomed Eng*, 41(4):694–708, Apr. 2013.

D. Schwartzman, J. Lacomis, and W. G. Wigginton. Characterization of left atrium and distal pulmonary vein morphology using multidimensional computed tomography. *J Am Coll Cardiol*, 41(8):1349–1357, Apr. 2003.

C. Stefanadis, J. Dernellis, C. Stratos, E. Tsiamis, C. Vlachopoulos, K. Toutouzas, S. Lambrou, C. Pitsavos, and P. Toutouzas. Effects of balloon mitral valvuloplasty on left atrial function in mitral stenosis as assessed by pressure–area relation. *J Am Coll Cardiol*, 32(1):159–168, July 1998.

G. Strang and G. J. Fix. *An analysis of the finite element method*, volume 212. Prentice-Hall Englewood Cliffs, 1973.

M. Turner. Stiffness and deflection analysis of complex structures. *Journal of Aero Space Science*, 23:805823, 1956.

T. P. Usyk and A. D. McCulloch. Relationship between regional shortening and asynchronous electrical activation in a three-dimensional model of ventricular electromechanics. *J. Cardiovasc. Electrophysiol.*, 14(10 Suppl):S196–202, Oct. 2003.

R. Vianna-Pinton, C. A. Moreno, C. M. Baxter, K. S. Lee, T. S. M. Tsang, and C. P. Appleton. Two-dimensional speckle-tracking echocardiography of the left atrium: feasibility and regional contraction and relaxation differences in normal subjects. *J Am Soc Echocardiogr*, 22(3):299–305, Mar. 2009.

F. H. M. Wittkampf, E.-J. Vonken, R. Derksen, P. Loh, B. Velthuis, E. F. D. Wever, L. V. A. Boersma, B. J. Rensing, and M.-J. Cramer. Pulmonary vein ostium geometry analysis by magnetic resonance angiography. *Circulation*, 107(1):21–23, Jan. 2003.

J. Zhao, T. D. Butters, H. Zhang, A. J. Pullan, I. J. LeGrice, G. B. Sands, and B. H. Smaill. An image-based model of atrial muscular architecture: Effects of structural anisotropy on electrical activation. *Circ Arrhythm Electrophysiol*, Mar. 2012.

Chapter 7

Changes in regional function due to atrial fibrillation

Atrial fibrillation changes the heart: the atrium dilates and and becomes more spherical, pressures increase, the wall stiffens with fibrosis, and conduction slows. These changes diminish mechanical function over time as episodes of AF increase in frequency and duration. An atrium with AF becomes less efficient at filling the ventricle and expends more energy to move blood. Just like healthy function, these changes vary between regions, affected by local differences in tissue properties and local wall stresses. We used an MR-based wall motion analysis to quantify this loss of function. We found AF hearts to have larger atria, depressed function, and an increased reliance on active contraction to fill the ventricle. These changes were regionally heterogeneous - motion deteriorated the most in high-functioning areas and active emptying increased only in regions that had little active function normally. We used a finite element model to investigate the factors driving these changes, and found that atrial pressure had the single largest influence on function, followed closely by dilation. A three-factor model (pressure, size, fibrosis) explained over 80% of the observed changes in function, but could not explain the increased reliance on active emptying. Of possible changes in the left ventricle, delayed relaxation during early ventricular diastole was the most

likely factor to increase dependence on active emptying. The complete finite element model matched global AF function within 1% of its *in vivo* averages.

7.1 The mechanical implications of atrial fibrillation

Atrial fibrillation is a rhythm disorder that disrupts normal contraction patterns in the heart. Although the nature of AF steers our collective focus towards electrical properties, changes in mechanical function are important indicators and symptoms of AF. The simplest measure of impaired mechanics (elevated atrial volume) is an indicator of future risk of AF (Tsang et al., 2006; Vaziri et al., 1994), a consequence of developing AF (Sanfilippo et al., 1990), and a mechanism to facilitate more episodes of AF (Verheule et al., 2003). Atrial fibrillation and mechanics are intertwined in a complex feedback-driven relationship, and understanding how mechanics change due to AF will improve our understanding of disease pathology and clinical outlook.

Atrial fibrillation decreases global mechanical function (Blume et al., 2011). The major source of this drop is unknown, but complex chamber remodeling offers many candidates. AF episodes double the chamber pressure, lower cardiac output, and increase ventricular heart rate (Clark et al., 1997). Left untreated, AF initiates a series of remodeling pathways that increase interstitial fibrosis (Platonov et al., 2011) and chamber dilation. Beyond simple dilation, left atrial shape also changes due to AF (Gloschat et al., 2011), and has been shown to be an early indicator of AF-recurrence risk following ablation (Bisbal et al., 2013). Conduction remodeling has been well characterized (Nattel, 2002), but delays in conduction also limit mechanical efficiency. These coupled factors reduce mechanical function and impair efficient ventricular filling.

In Chapter 5, we measured the regional heterogeneity of atrial function. In AF patients, we hypothesized a similar heterogeneity in the *changes* to mechanical function. We suspected loss of function would vary between regions because AF and its effects vary between regions.

Multiple types of AF sources (single rotors, multi-rotors, complex fractionated atrial electrograms) demonstrate that some regions will be contracting more frequently than others during each episode (Nattel, 2002). Furthermore, increases in fibrosis have shown a dependence on AF history (Platonov et al., 2011) in some regions and not others. Local wall stress (controlled by regional curvature) will also vary between regions, especially in hearts with non-spherical shapes (Bisbal et al., 2013). We anticipate that a regional analysis of mechanical function will aid our understanding of how much function changes and where it changes the most.

Atrial fibrillation develops alongside other conditions such as hypertension, congestive heart failure, and mitral regurgitation. In fact, AF in isolation ("lone" AF) represents less than 5% of all diagnosed cases (Frost, 2007). Any considerations of mechanical function and its relationship to AF must be evaluated in the context of other disease pathologies developing alongside AF. These other diseases have a strong influence on the atrium's ability to fill the ventricle. Atrial contraction (what we refer to as "active emptying" in previous chapters) contributes approximately 30% of left ventricular stroke volume in healthy adults (20-29 years old) (Boyd et al., 2011). This contribution increases with disease progression. For instance, impaired relaxation in the ventricle caused by ischemia, prior MI, and angina increased atrial contributions from 26 to 38% (Prioli et al., 1998). In the same study, restricted ventricular filling due to dialated cardiomyopathy reduced the contribution from 26 to 18%, as the atrium pumped against larger afterloads during its active phase. Ventricular hypertrophy increased the ratio from 27 to 35% (Kuo et al., 1987), while elevated ventricular pressures decreased it from 42% to 31% (Appleton et al., 1993). Given the link between atrial function and ventricular properties, our analysis of changes to atrial function must consider coupling to the left ventricle.

In this chapter, we used the wall motion analysis developed in Chapters 4 and 5 for healthy subjects and applied it to an AF population. This allowed us to measure both global and *regional* changes in mechanics, revealing which parts of the atrium are mostly affected by AF. We then used the finite element model developed in Chapter 6 to identify the primary

sources of this loss in function. We hypothesized that changes in wall motion in AF patients was caused by changes in atrial pressure and size (changes in wall stress) and not by changes in atrial fibrosis or electrical conduction. Given the complex, multi-faceted pathophysiology of AF, the problem lent itself to a simulation-based experiment. We used the finite element model to test the sensitivity of atrial mechanical function to the major changes observed in AF patients (pressure, size, shape, fibrosis, conduction). Later, we expanded this experiment to include altered ventricular function. The finite element model allowed us to identify the most important sources of AF-related mechanical dysfunction.

7.2 Methods to measure regional function

All studies were approved by the University of Virginia Institutional Review Board (IRB). Thirty one subjects (n=31) with diagnosed atrial fibrillation ("AF patients") were recruited from the University of Virginia Health System for a research CMR scan with informed consent. All scans were performed on a 1.5-T Magnetom Avanto (Siemens Healthcare, Erlangen, Germany). A steady-state free procession (SSFP) imaging sequence was employed, using the same techniques and views discussed in Chapter 5. Each imaging sequence was reconstructed into 25 time phases, equally spaced across the cardiac cycle based on the R-R interval. Patients with abnormal rhythms at the time of the scan were removed from the study (including patients experiencing an episode of AF).

Following techniques described in Chapters 4 and 5, we contoured the left atrial endocardial border and fit it to a continuous surface through space and time. We quantified this surface to measure global and regional function in AF patients. All measures of regional function used the same algorithms from earlier chapters, including methods to detect and quantify contraction. We compared the results of global and regional function to healthy subjects (Chapter 5) using unpaired t-tests and repeated-measures ANOVA.

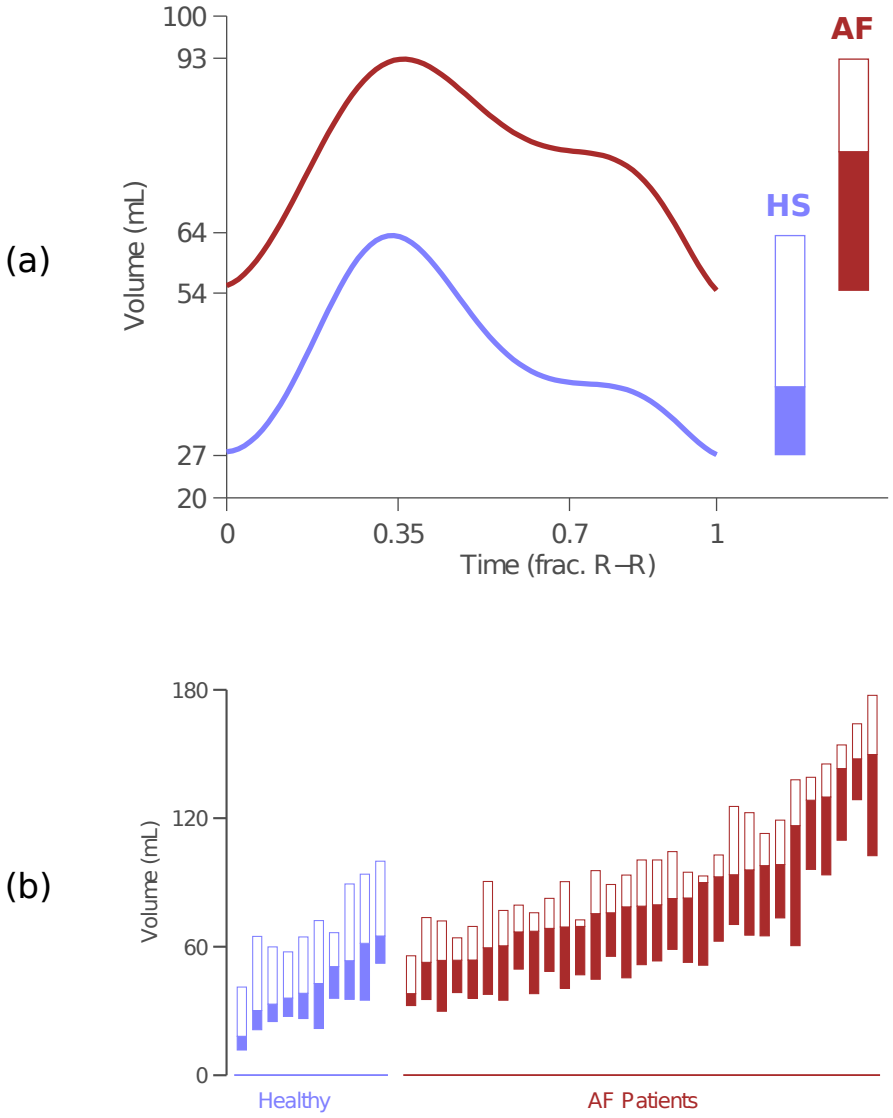

Figure 7.1: AF patients had larger hearts and relied more heavily on atrial contraction to fill the ventricle compared to healthy adults. (a) Averaged atria from healthy subjects (HS) and AF patients (AF) followed similar patterns of filling and emptying, but varied in size and magnitude of volume changes. AF patients relied more on atrial contraction (solid rectangle) as a proportion of total change in volume (outer rectangle). (b) AF atria ranged in size from below 60 mL to greater than 150 mL, while healthy subjects had smaller atria and less variation in the group.

7.3 Results of function in AF patients

Surface fits converged in under 5 minutes to a RMSE of 1.9 ± 0.5 mm (range 1.2 to 3.3 mm). Fitted regional radii varied between 18 and 44 mm with a mean of 29 mm. There was no significant difference in fitting error between AF patients and healthy subjects (ΔRMSE = 0.1 mm, $p = 0.44$). We compared atrial volumes computed by summing axial contours to volumes computed by integrating the fitted 3-D surface and found a difference of 8.5 mL (surfaces were larger), which was almost identical to the offset observed in healthy subjects (8.4 mL). The near identical results between AF patients and healthy subjects from Chapter 5 confirm the robustness of the surface fitting method (Chapter 4) across a heterogeneous population.

7.3.1 Global function in AF patients

AF patients had larger hearts than healthy subjects and relied more heavily on active emptying as a fraction of total emptying (Fig. 7.1). We measured changes in atrial volume through the cardiac cycle and found an average maximum volume V_{max} of 102 ± 31 mL in AF atria, a 31 mL (44 %) increase over the healthy average ($p < 0.01$). An averaged surface (representing all 31 AF patients) had similar patterns of filling and emptying compared to the averaged healthy atrium (Fig. 7.1a). Both curves had passive and active emptying phases with similar durations relative to the R-R interval. Interestingly, AF patients and healthy subjects had almost identical emptying volumes ΔV_t even though the AF atria were much larger. We normalized emptying volume to its maximum to account for differences in size and found that AF atria had depressed function EF_t compared to healthy adults ($p < 10^{-4}$). We did the same for active emptying (including normalization) and found that active function EF_a is almost identical between groups ($p = 0.85$). Thus, AF patients had larger hearts at the onset of contraction but also ejected more volume during active emptying. When we measured

Output (units)	Healthy ($\mu \pm \sigma$)	AF ($\mu \pm \sigma$)	Change	p-value
V_{max} (mL)	71 ± 18	102 ± 31	+31	< 0.01
V_{min} (mL)	29 ± 11	58 ± 25	+29	$< 10^{-3}$
V_{preA} (mL)	43 ± 15	85 ± 30	+43	$< 10^{-4}$
Changes in Volume				
ΔV_t (mL)	42 ± 11	44 ± 12	+2	0.60
ΔV_p (mL)	28 ± 7	17 ± 7	-11	—
ΔV_a (mL)	14 ± 6	27 ± 10	+13	$< 10^{-3}$
Fractional Measures				
EF_t (%)	60 ± 9	44 ± 9	-15	$< 10^{-4}$
EF_p (%)	41 ± 9	17 ± 8	-23	—
EF_a (%)	32 ± 9	32 ± 8	+0	0.85
$V_{p\|t}$ (%)	68 ± 10	39 ± 14	-29	—
$V_{a\|t}$ (%)	32 ± 10	61 ± 14	+29	$< 10^{-6}$

Table 7.1: Global function in 10 healthy subjects and 31 AF patients, including passive and active components. Phasic changes in volume are reported in milliliters and fractional measures are reported as percentages. Significance values are based on unpaired t-tests.

active emptying as a fraction of total emptying $V_{a|t}$ we saw a dramatic increase from 32 to 61% ($p < 10^{-6}$, Fig. 7.1b).

A story began to emerge: AF patients had depressed total emptying fraction but equivalent active emptying fraction compared to controls - as a result, the portion of volume change due to active contraction increased (Table 7.1 and Fig. 7.1b). We tested for correlation among the three measures of function (EF_t, EF_a, and $V_{a|t}$) to see if any two were measuring the same effect among subjects. We used linear regression and found a very low correlation between the measures, with adjusted R^2 values between 0.08 and 0.34. We also tested if the change in $V_{a|t}$ related to overall atrial size (atrial dilation is typically a marker of AF-related dysfunction), but we found minimal correspondence (adj. $R^2 = 0.18$). Although there are multiple indicators of atrial dysfunction (decreased EF_t, increased $V_{a|t}$), the cause of each change may be different. We explored if a simple threshold could delineate dysfunction (Fig.

7.2a) by comparing distributions among groups. For instance, only 58% of AF patients had an EF_t lower than the range in healthy adults (18/31) and less than half (45%) had a maximum volume above the healthy range. In contrast, active emptying as portion of total $V_{a|t}$ better differentiated AF patients, identifying 87% above the normal range. Although there are multiple changes in global mechanics, the portion of emptying during active contraction most clearly separated the AF and healthy hearts.

7.3.2 Regional function in AF patients

AF patients had depressed regional emptying fraction compared to healthy subjects, though the change in function varied between regions. We quantified regional motion using the segmentation and fitting methods described in Chapter 5. The atrial surface was divided into five regions (ignoring the mitral valve), and function was quantified using the regional equivalent of each global measure (substituting radius for volume). We compared global and regional averages for total and active function, and the proportion between them (Fig. 7.2). The three global patterns (decreased EF_t, constant EF_a, and increased $V_{a|t}$ are replicated in regional trends.

In Chapter 5 we noted a heterogeneity in atrial function, where some regions contributed more than others to emptying. Here, we observed a complementary effect - heterogeneity of changes in function (Fig. 7.2b). Regions that had higher REF_t in healthy subjects also had the largest decreases in AF patients. The inferior wall had the largest decrease in REF_t (39 to 25%, $p < 10^{-5}$) and the posterior wall had the smallest decrease (19 to 15%, $p = 0.03$). Active function remained constant globally (EF_a), and there was minimal change on the regional level (a slight, non-significant convergence between regions). We saw a dramatic increase in active emptying as a portion of total emptying $R_{a|t}$ in regions *where it was possible* (e.g. inferior wall 32 to 62%, $p < 10^{-6}$). Regional motion in the superior wall already occurred mostly during the active phase at baseline (82%), it had minimal room to increase that contribution in AF hearts (91%, $p = 0.35$).

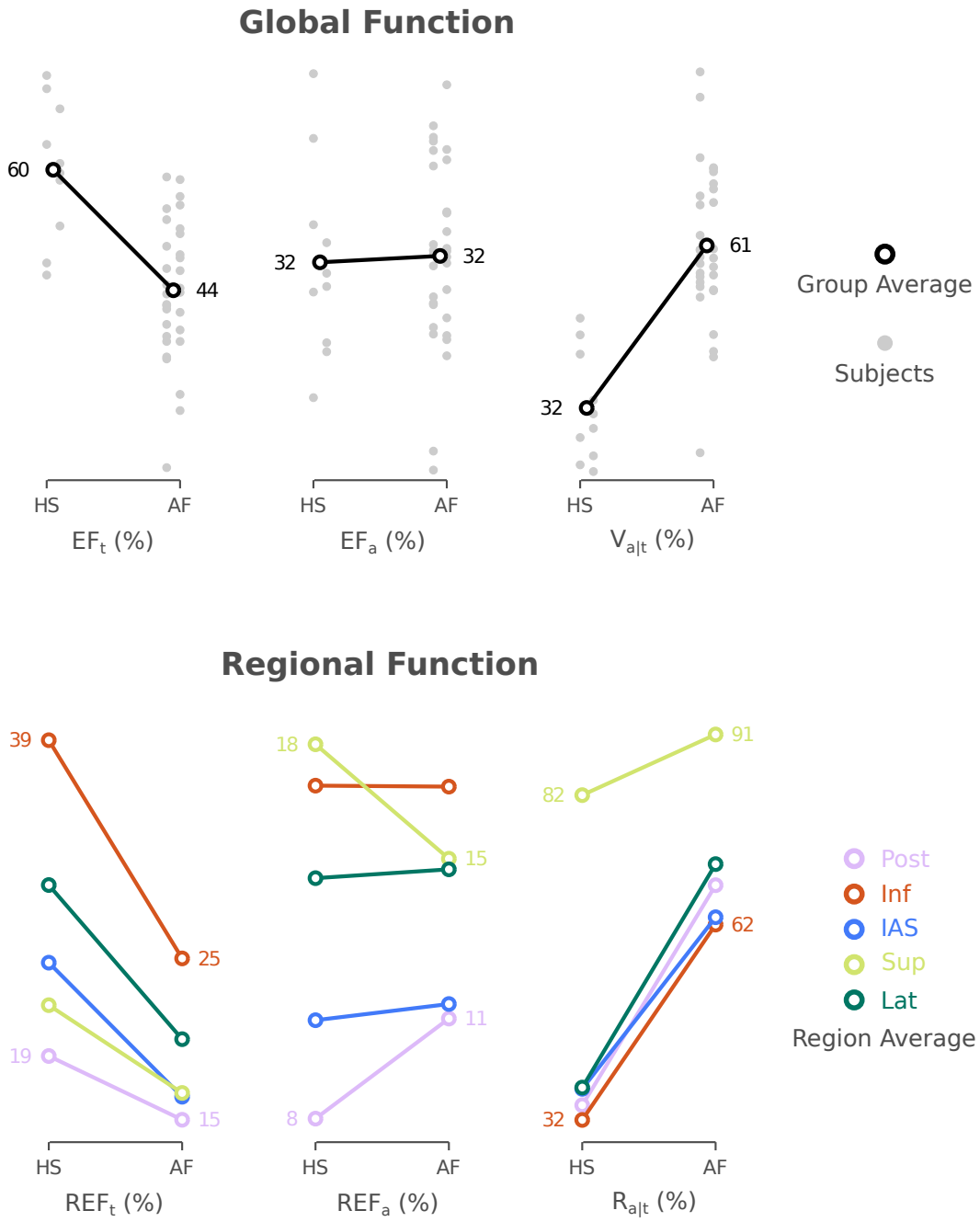

Figure 7.2: AF patients (AF) had decreased atrial function EF_t and increased active emptying as a fraction of total $V_{a|t}$ compared to healthy subjects (HS). AF patients and healthy subjects had similar amounts of active function EF_a. Regional averages (REF_t, REF_a, $R_{a|t}$) matched global changes in mechanics with some regional variation. The inferior wall showed the largest drop in REF_t while the superior wall showed the smallest increase in $R_{a|t}$. Colors indicate region and numbers indicate largest and smallest increase of each measure of function.

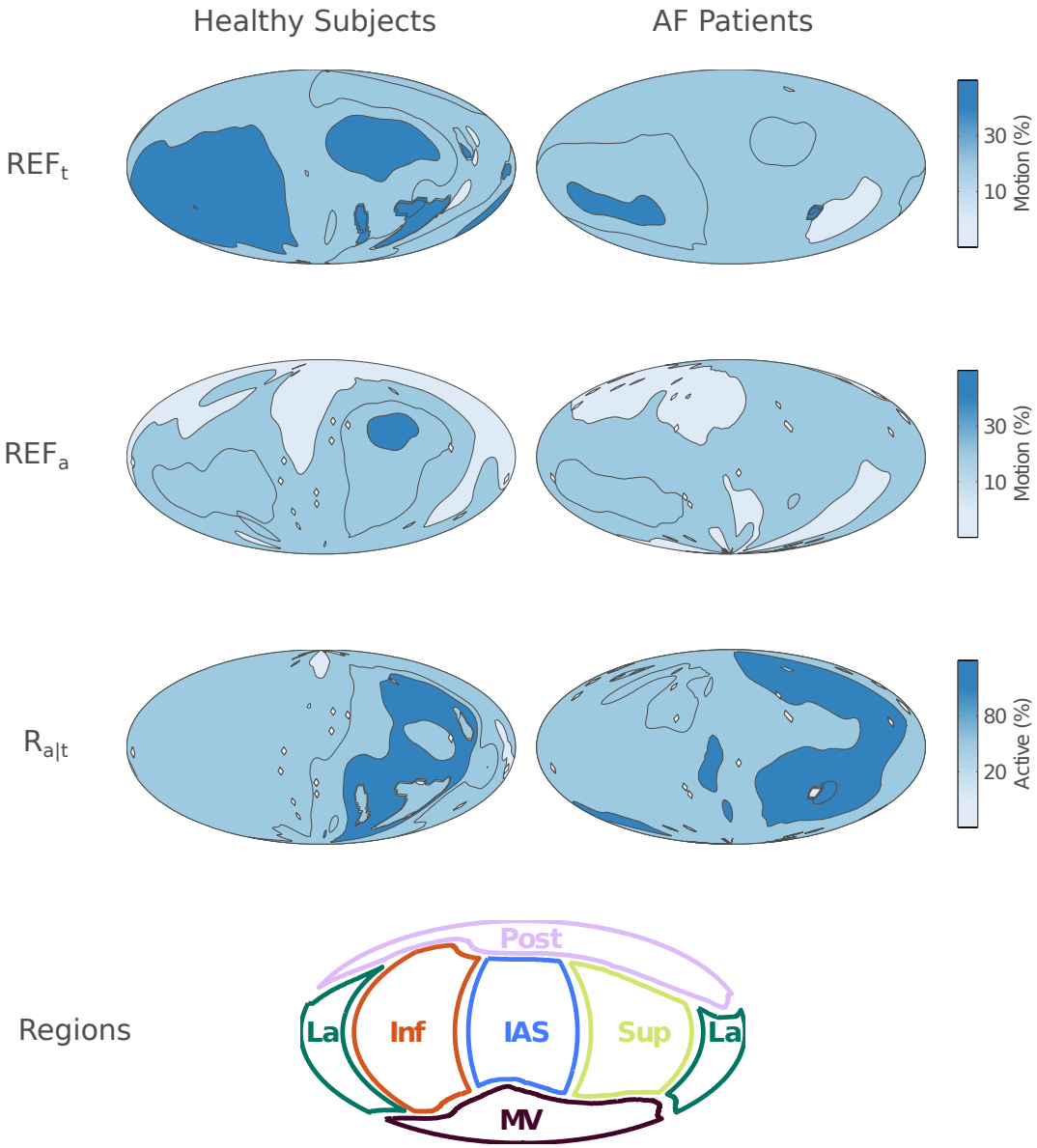

Figure 7.3: Hammer maps revealed patterns of radial motion in healthy subjects and AF patients. (a) Total radial emptying fraction REF_t was highest in the lateral and inferior walls, especially near the mitral valve. AF patients showed depressed function, especially in those regions. (b) Active function REF_a was similar between groups, with slightly less variation in the AF patients. (c) Active radial emptying as a fraction of total emptying $R_{a|t}$ increased in AF patients in most regions except the superior wall, where motion was mostly active even in healthy subjects. (d) Regions were defined using anatomic landmarks and projected in 2-D using a Hammer projection.

We visualized motion for the entire atrial surface using 2-D projections called "Hammer maps" (Fig. 7.3). Hammer maps of REF_t identified peak motion in the inferior and lateral walls near the mitral valve in healthy subjects, which deteriorated the most in AF patients. The homogenization of active function REF_a was also visible, with small decreases in the superior wall and small increases in the nearby posterior wall. The large increases in $R_{a|t}$ are visible on the left side of the map (lateral, inferior, septal walls) while the superior wall remained constantly active.

We measured timing of contraction using regional radius-vs-time curves, but found no difference between AF patients and healthy subjects. The two groups had a remarkable consistency in the spatial patterns of contraction (Fig. 7.4a). Contraction started in the upper superior wall near the pulmonary veins and quickly spread down the septal wall. Contraction ended in the inferior and superior walls near the mitral valve annulus. A more coarse sampling of time curves (Fig. 7.4b) confirmed this result in both groups. Trends were similar in the averaged surface (superior and septal wall early, inferior wall late) but individual subjects had a large amount of variation relative to these differences (Fig. 7.4c). Measuring time of contraction was only useful with averaged surfaces, which revealed minimal differences in contraction times between groups.

Atrial mechanical function decreased in AF patients compared to healthy subjects. We hypothesized that the loss of function arose from changes in atrial physiology; the atrium in an AF patient is larger, stiffer, and operating at higher pressure compared to a control. These factors decreased function, but we had no way of knowing *which* factors decreased it. It was possible that elevated afterload accounted for a majority of functional changes; but it was also possible atrial dilation created most loss in function. Isolating these effects *in vivo*, even in a controlled animal experiment, would be exceedingly difficult. Therefore, we used the finite element model in Chapter 6 to test individual factors associated with AF and measure their individual impact on atrial function.

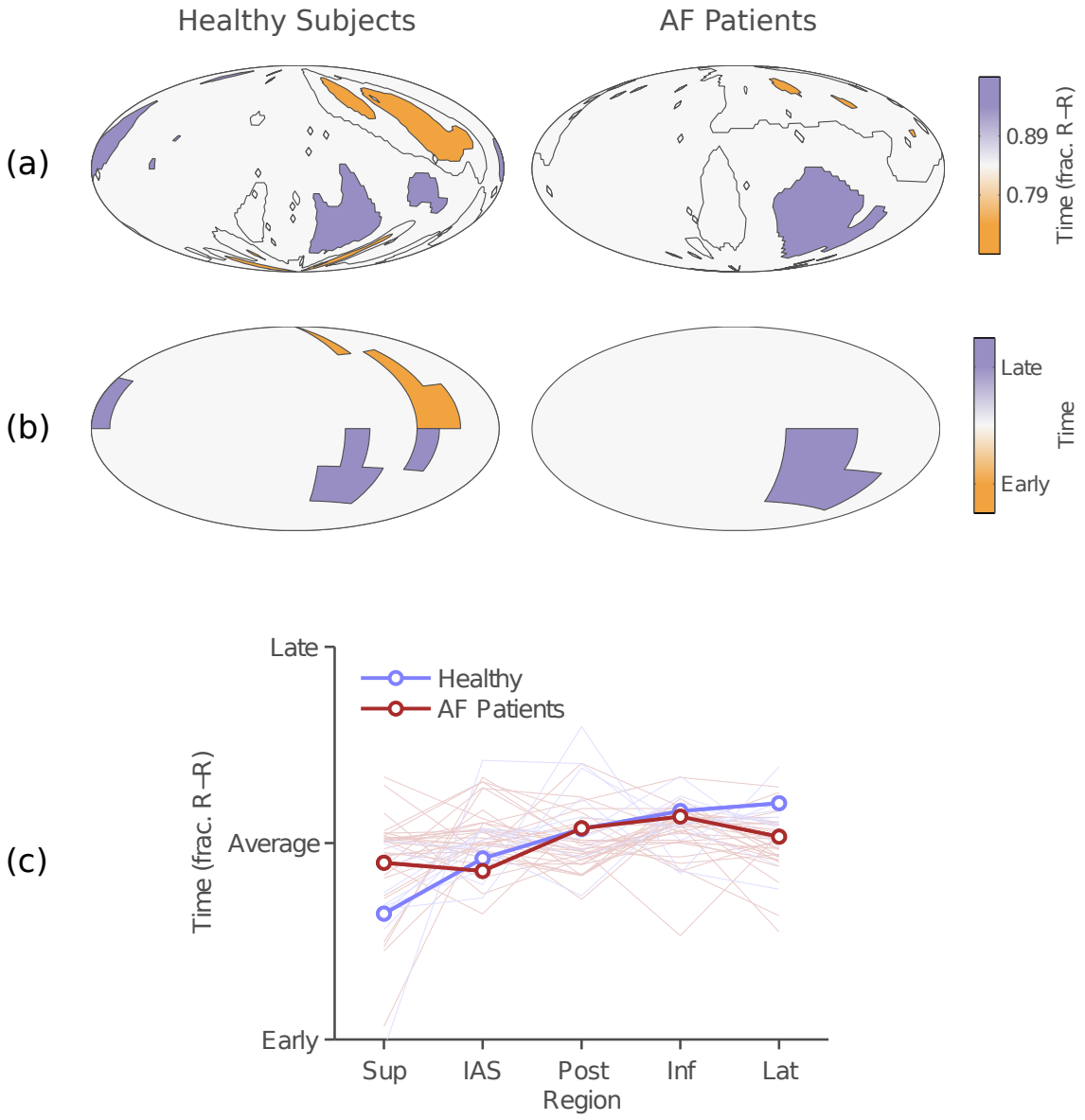

Figure 7.4: AF patients (AF) had similar timing patterns of contraction compared to healthy subjects. (a) The onset of contraction was detected at 10,800 points across the atrial surface using the radius-time curves and their derivatives. Contraction began in the upper superior wall and ended in the superior wall near the mitral valve. Patterns of contraction were identical between groups. (b) A element-based average confirmed the point detection algorithm and patterns of contraction. (c) Averaged surfaces reveal regional trends in timing of contraction (thick lines), but noise within each group (faint lines) overwhelms these differences.

		Level				
Factor (Units)	B_0	1	2	3	4	5
	μ_{HS}	$\mu_{HS,AF}$	μ_{AF}	$+1\sigma_{AF}$	$+2\sigma_{AF}$	$+3\sigma_{AF}$
Size (mL)	37	53	70	94	116	139
Shape (%)*	87	89	89	97	99	100
Pressure (mmHg)	5	7	10	14	18	22
Fibrosis (%)	0	16	25	35	45	55
Conduction ($^{cm}/_{sec}$)	*iso*	90	69	53	36	20

Table 7.2: Design of the FEM parameter sensitivity analysis. Five factors (size, shape, pressure, fibrosis, conduction) were varied to five levels above a healthy baseline B_0. Levels were chosen based on the factor's distribution (μ, σ) in the AF population. *Shape was measured as sphericity with a perfect sphere = 100%, but did not use AF factor's distribution to set levels.

7.4 Methods to simulate AF dysfunction

Patients experience many physiological changes during the progression of AF. We investigated five factors that are central to atrial mechanics and are also known to change in an AF heart: 1) size, 2) shape, 3) pressure, 4) fibrosis, 5) conduction. We incorporated each of these factors into the finite element model discussed in Chapter 6 by manipulating one aspect of the model: the geometry, load curves, or material properties. We then ran each perturbed model for a complete cardiac cycle and observed the changes in mechanical function. By varying each factor independently, we captured its individual influence on the deterioration of function due to AF.

7.4.1 Changes in atrial size

We modeled increases in atrial size by dilating the geometry while maintaining its shape. The endocardial surface was dilated by increasing the radius of every node by a constant factor. For instance, to dilate the atrium to a volume of 70 mL, we scaled nodal radii by 1.24. The pulmonary vein landmarks and mitral valve plane were also adjusted; the

mitral valve plane was scaled along the z-axis and the pulmonary vein landmarks were scaled radially with the surface. Other elements of the geometry were held constant, including mitral plane orientation, pulmonary vein thickness and diameter, and atrial thickness. We used the volumes of the 31 patients in §7.3 to create the levels of atrial dilation. We retrieved surface volumes at 12% of the cardiac cycle to match the point of minimum pressure following minimum volume (see Chapters 2 and 6 for details). In AF hearts, this worked out to an average of 70 ± 25 mL. We used the previously described algorithm to solve for the unloaded geometry. All pre-conditioning steps were used on the dilated geometry, including the iterative solver and the shape adjustment.

7.4.2 Changes in atrial shape

We modeled changes in atrial shape using the averaged AF and averaged healthy atria. AF atria were more spherical than HS atria and we quantified this as a "sphericity" Ψ where

$$\Psi = \frac{\pi^{1/3} (6V)^{2/3}}{A} \tag{7.1}$$

V is the surface volume, and A is the surface area. Since the AF shape was more spherical, we assumed that levels above the AF average (3, 4, 5) would approach a perfect sphere. We used three shapes (HS, AF, sphere) at matched volumes to create the five levels. We averaged the HS and AF atria for Level 1 and used a weighted average between AF and the sphere for Levels 3 and 4 (Level 5 was a perfect sphere). The sphericity calculation for each shape confirmed the pattern. The position of the pulmonary veins was not altered from the baseline model (nodal positions of the veins were held constant while their angles were adjusted to the shape).

7.4.3 Changes in atrial pressure

We modeled increases in atrial pressure by altering the pressure load curve in the baseline model. Recall from Chapter 6 that the atrial surface underwent a series of loading steps in each simulation, starting with pre-conditioning inflation (0 to 5 mmHg) followed by passive filling. We modified this load curve by inserting a step at the end of pre-conditioning which we called "secondary inflation". During secondary inflation, we inflated the atrium from 5 mmHg to the specified starting pressure and began the normal cardiac cycle. In the hydraulic circuit attached to the FEM, we scaled the upstream pulmonary pressure and downstream ventricular pressure by the same amount to maintain reasonable hemodynamics.

We used pressure-volume loops from Chapters 2 and 3 as well as external studies to choose pressure levels. Pressure data for healthy subjects was limited and typically came from catheterizations for chest pain and ablations for non-AF arrhythmias. We found a minimum pressure of 4.3 mmHg in external studies (weighted average from four studies) and a minimum pressure of 10.3 mmHg in our P-V loops (median of $n = 6$ WPW subjects). Since our control sample size was small, we used 5 mmHg as the minimum atrial pressure during a normal cardiac cycle based on the external studies (Connolly et al., 1954; Jais et al., 2000; Matsuzaki et al., 1991; Stefanadis et al., 1998b). For the average AF pressure (Level 2), we found a weighted average of 10.1 ± 3.3 mmHg in six cited works and a median pressure of 12.5 mmHg from Chapter 3 loops (Elvan et al., 2013; Jais et al., 2000; Keren et al., 1987; Probst et al., 1973; Shapiro and Klein, 1968; Stefanadis et al., 1998a). Many external studies used pulmonary catheter wedge pressure as a proxy for atrial pressure, which we assumed to be equivalent (Connolly et al., 1954). Since the cited works were comprehensive (over 100 samples from multiple AF populations), we chose 10 mmHg as the average AF case and used $\sigma_{AF} = 4$ mmHg for variation (Levels 1, 3, 4 were set accordingly).

7.4.4 Atrial fibrosis

We modeled fibrosis by stiffening the material model. We assumed that fibrosis increased collagen content in the atrium and that collagen is stiffer than healthy muscle. The baseline material model (a transversely-isotropic Mooney-Rivlin material, see Chapter 6) used two material coefficients (C_1, C_2) to define isotropic behavior. We isotropically stiffened the material by increasing C_2 (it was set to zero in the baseline model). Increasing this constant made sense given the biphasic behvavior of Mooney-Rivlin material, where C_2 controlled the non-linear stiffening at higher strain states Beatty (1987). We set the maximum stiffness of C_2 to represent an atrium with complete (100%) fibrosis. Although this does not exist *in vivo*, we estimated $C_{2,max}$ based on previous studies of left ventricular infarcts (Fomovsky and Holmes, 2010), ranges of stiffness in P-V loops from Chapter 2, and functional ranges in Table 7.1, as described below.

We used the relationship between material stiffness and collagen content in rat myocardial infarcts (Fomovsky and Holmes, 2010) to estimate the stiffness of a tissue composed entirely of collagen (100% collagen content). This theoretical material was 6-6.5x stiffer than healthy tissue and had 6-6.5x as much strain energy. We assumed our 100% fibrosis atrium would experience a similar increase in strain energy. We calculated the strain energy of our baseline material (0% fibrosis) under spherical inflation at 75% strain (average wall strain, Chapter 6), then scaled the total strain energy by 6.3x. We calculated the increased stiffness to reach this energy and found $C_{2,max} = 4.0$ kPa. This represented the fibrosis material and scaled linearly for fibrosis levels below 100%. We validated this material model by running it through a full cardiac cycle at 100% fibrosis. The resulting P-V loop had a chamber stiffness $k_c = 0.22\,\mathrm{mL}^{-1}$ that was higher than any measured P-V loop stiffness and an emptying volume $\Delta V_t = 17\,\mathrm{mL}$ that was lower than the smallest recorded emptying volume in the AF group.

There was a dearth of studies quantifying the amount of fibrosis in AF populations. We relied on a histological study in post-mortem AF hearts (Platonov et al., 2011) and coupled it with an MR imaging method (delayed enhancement) used to quantify fibrosis in the atrium

(Mahnkopf et al., 2010; Oakes et al., 2009). An average AF heart had $25 \pm 13\%$ collagen based on histology and $21 \pm 6\%$ enhancement based on MRI. Therefore, we chose the average AF heart (Level 2) to have 25% fibrosis. The histological study only found $6 \pm 3\%$ collagen in control atria while delayed-enhancement imaging found only $1.7 \pm 0.3\%$ enhancement in healthy adults, so we assumed the baseline model to have no fibrosis (0%). Delayed enhancement saw variations in collagen content of 6-15% while histology reported variation of 13%. For consistently we chose $\sigma_{AF} = 10\%$ to set the remaining levels.

7.4.5 Changes in atrial conduction

We modeled decreases in conduction velocity by shifting the contraction load curve. Active stress during contraction was generated from a single load curve, described in detail in Chapter 6. We created a unique load curve for each region, then varied the start times based on the relative activation times detected in wall motion analysis (Fig. 7.4). We calculated the total conduction time for a given conduction velocity based on a constant distance traveled (3 cm, roughly the distance from the septum to the appendage). We used the total conduction time to create a delay between the first and last regional activation curve, with each curve (5 in total) spaced equally within the conduction time. The total conduction time was subtracted from the passive emptying time and added to the active contraction time in the hydraulic circuit.

Conduction velocities were typically measured *in vivo* with endocardial mapping catheters or epicardial mapping arrays immediately prior to ablation procedures. Studies of paroxysmal AF conduction found velocities between 60 and 70 cm/sec (Konings et al., 1994; Markides et al., 2003). We used a velocity on the high end of the range (69 cm/sec) to better match the spatial variation we and others observed in mechanical activation (Vianna-Pinton et al., 2009). We set the Level 1 velocity based on the average conduction in WPW studies (89 cm/sec), assuming this fell somewhere between a healthy heart and an AF heart (Hansson et al., 1998). We set more severe levels of conduction delay based on changes in conduction

velocity in more severe cases of AF (Konings et al., 1994), which identified decreases to 54 ± 4 and 38 ± 10 cm/sec in moderate and severe dysfunction. We used these to estimate σ_{AF} as 16 cm/sec and set the other levels accordingly. The five levels of conduction velocity (90, 69, 53, 36, 20 cm/sec) correspond to delay times of (33, 43, 57, 83, 150 msec) or (4, 5, 7, 10, 18 % R-R) based on a 72 beat-per-minute heart rate.

7.4.6 Analysis of parameter variation

We ran a simulation for each level of each factor (25 in total) and compared the results to the baseline model. For each output, we obtained atrial and ventricular hemodynamics, regional wall motion, and regional stress-strain profiles. We analyzed changes in global function (volume, pressure, work) using measures developed in previous chapters. Using the hydraulic circuit, we also analyzed changes in ventricular hemodynamics. For each measure, we reported the change from baseline to the AF average. More generally, we plotted the P-V loop of each factor at 5 levels compared to a baseline P-V loop to observe trends in global function. We fit a linear "trend" line for all five levels and reported the slope as an approximate measure of sensitivity. We plotted the trends of selected output measures than had biphasic or non-linear trends. We focused on the results of the average AF population to understand how each factor might have contributed to the observed changes in §7.3.

Regionally, we compared the trends in function for each factor and compared it to its global average - searching for deviations between regional and global patterns. We also compared regional function at the average AF level (Level 2) with regional results from wall motion analysis. We used both total function REF_t and active function $R_{a|t}$ for these comparisons. Stresses and strains were also analyzed by region, to understand how local effects (curvature, fibers) contributed to changes in function.

		Mean AF (Slope)				
Output (Units)	B_0	Size	Shape	Pressure	Fibrosis	Conduction
V_{max} (mL)	66	108 (+25)	67 (-0)	79 (+8)	59 (-2)	66 (+0)
ΔV_t (mL)	39	55 (+8)	40 (-0)	42 (-2)	29 (-4)	39 (+0)
EF_t (%)	59	51 (-4)	60 (-0)	53 (-6)	49 (-4)	59 (+0)
EF_a (%)	31	32 (-0)	32 (+0)	36 (-3)	21 (-3)	30 (+1)
$V_{a\|t}$ (%)	31	46 (+6)	33 (+1)	51 (+4)	27 (-1)	29 (+2)
Ventricular Function						
LV EDV (mL)	121	136 (+5)	121 (-0)	195 (+24)	115 (-2)	120 (-1)
LV SV (mL)	70	86 (+5)	71 (-0)	55 (-9)	64 (-2)	69 (-1)
LV EF (%)	58	63 (+2)	58 (-0)	28 (-11)	56 (-1)	58 (-0)
Pressure, Work						
P_{mvo} (mmHg)	13	9 (-2)	13 (+0)	19 (+4)	15 (+1)	13 (-0)
P_{sys} (mmHg)	11	14 (+1)	11 (+0)	19 (+4)	10 (-1)	11 (-1)
LV EDP (mmHg)	8	10 (+1)	8 (-0)	23 (+5)	8 (-0)	8 (-0)
Stroke Work (mJ)	9	27 (+7)	10 (+0)	23 (+1)	4 (-2)	6 (-1)

Table 7.3: Outputs of the model experiment. We reported common hemodynamic factors at baseline, and each of the 5 factors. For each result, we present the value at the average AF condition (Level 2), and the trend across all 5 levels. Trend is reported as the slope of a simple linear regression. Abbreviations - V_{max} - maximum volume, ΔV_t - emptying volume, EF_t - total emptying fraction, EF_a - active emptying fraction, $V_{a|t}$ - active emptying as a fraction of total, LV EDV - end-diastolic volume, LV SV - stroke volume, LV EF - ejection fraction, P_{mvo} - atrial pressure at mitral valve opening, P_{sys} - maximum atrial pressure during contraction, LV EDP - end-diastolic pressure

7.5 Results of simulated atrial dysfunction

Each simulation converged to the specified tolerance at 200 time steps in under 48 hours. Models that included additional loading steps (changes in pressure) required additional time to solve. Changes in size and pressure had the largest influence on function (Table 7.3), while changes to atrial shape and electrical conduction had negligible effects. We hypothesized the expected influence of each factor (Fig. 7.5a) and confirmed each change in the factor-specific AF loop (Fig. 7.5b). Each factor had unique trends in P-V loop shape and position at 5 levels compared to a baseline (Fig. 7.6). Linear trend slopes were useful for comparing the relative sensitivity between individual factors and measures of function (Table 7.3). A few factors had biphasic or non-linear trends relative to certain outputs (Fig. 7.7).

7.5.1 Changes in atrial size

Atrial size had the largest influence on function of any single factor. As expected, increasing atrial size shifted the P-V loop rightward in the P-V plane (Fig. 7.5b). With a larger unloaded volume and a fixed amount of time (in the hydraulic circuit) for passive filling, the dilated atria had smaller changes in pressure during filling (Fig. 7.6a, Table 7.3). A lower P_{mvo} decreased the pressure gradient between the atrium and ventricle during passive emptying, resulting in lower passive flow during early ventricular diastole. Active emptying increased as a larger atrium generated equivalent active stress and created higher atrial pressures during contraction, larger active emptying volumes, and higher stroke work. Total emptying volume was higher than baseline, but EF_t decreased due to the larger size of the chamber (Fig. 7.7). Active function EF_a remained relatively steady at higher volumes, and the portion of emptying due to active contraction $V_{a|t}$ steadily increased.

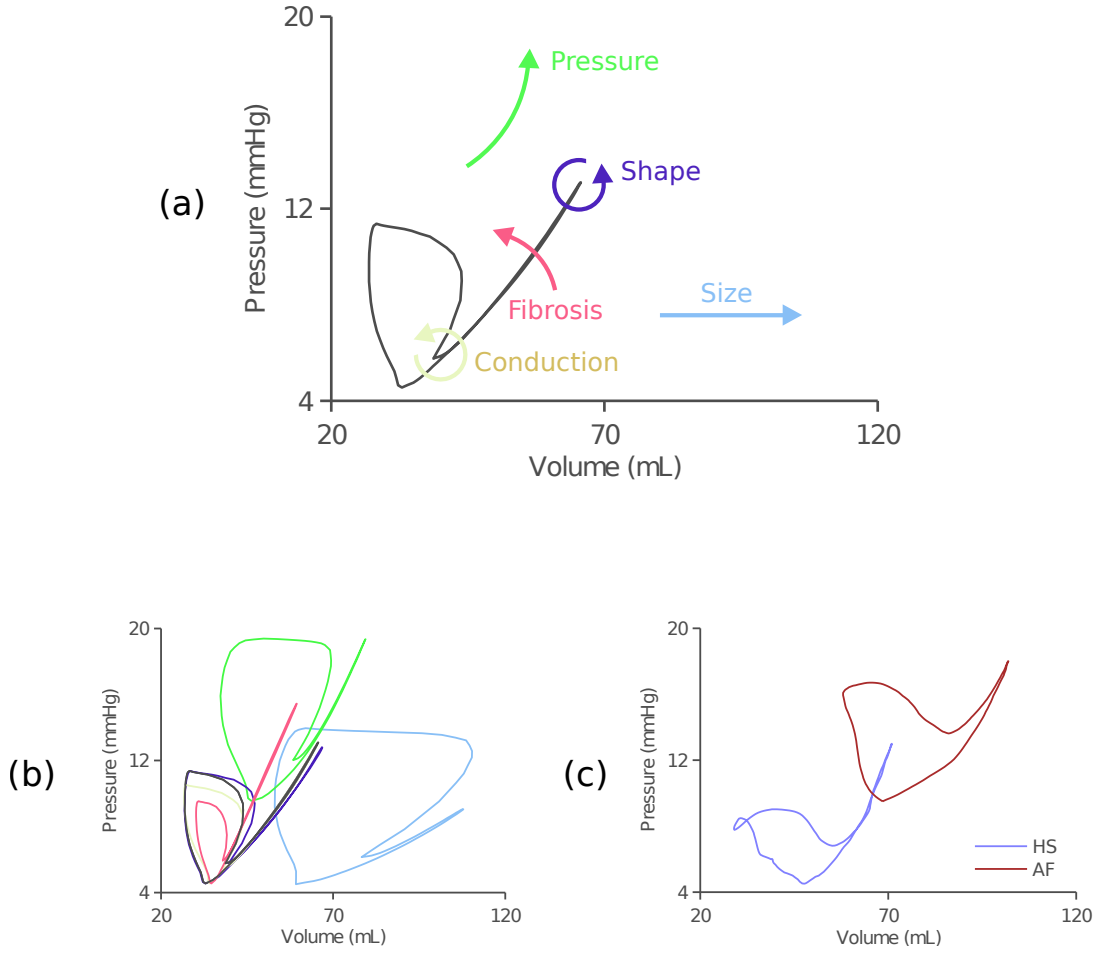

Figure 7.5: The model experiment tested five factors common to AF remodeling. (a) The baseline atrium was modified to a larger size, higher pressure, stiffer material, different shape, or altered conduction - each of which influenced different aspects of loop shape, size, and position. (b) The results of the five-factor study, with each loop representing a factor at the average AF level (Level 2). (c) Average *in vivo* loops from WPW and AF patients.

7.5.2 Changes in atrial shape

Atrial shape had the smallest influence on function of any single factor. Global hemodynamics and active function shifted slightly between levels (Fig. 7.6c), but had no clear trends (Fig. 7.7c-e), Table 7.3). We anticipated that shape would play a larger role in regional function and regional stress-strain behavior.

7.5.3 Changes in atrial pressure

Besides size, atrial pressure had the largest influence on global mechanical function. Increasing atrial pressure shifted the P-V loops upward and rightward on the P-V plane roughly along the passive curve of the material model (Fig. 7.5b). Generally, higher pressures reduced passive filling volume and increased passive filling pressure, as the loop operated on a "steeper" portion of the passive curve. Interestingly, active emptying exhibited a biphasic response to increased loading. Initially, active emptying volume increased, then tapered off at higher pressures (Fig. 7.7d, Levels 4-5). We hypothesized that small changes in pressures increased active stress with higher stretch (similar to a Frank-Starling mechanism). However, once pressures increased further, afterload overwhelmed this effect and decreased EF_a. We explored this result further in our analysis of stress and strain. Total EF_t steadily decreased at all levels (Fig. 7.7c), and accelerated once active emptying decreased. The portion of emptying due to contraction $V_{a|t}$ had a biphasic response, peaking at moderately elevated pressures.

7.5.4 Atrial fibrosis

Atrial fibrosis had a smaller effect on global mechanics compared to size and pressure, but did alter both passive and active function. As expected, fibrosis (stiffening of the material model) created a steeper P-V curve (Fig. 7.5b). Interestingly, fibrosis also made it more difficult to eject blood during active emptying (Fig. 7.6d). Fibrosis increased filling pressures and decreased filling volumes, and generally had a negative impact on total, passive, and

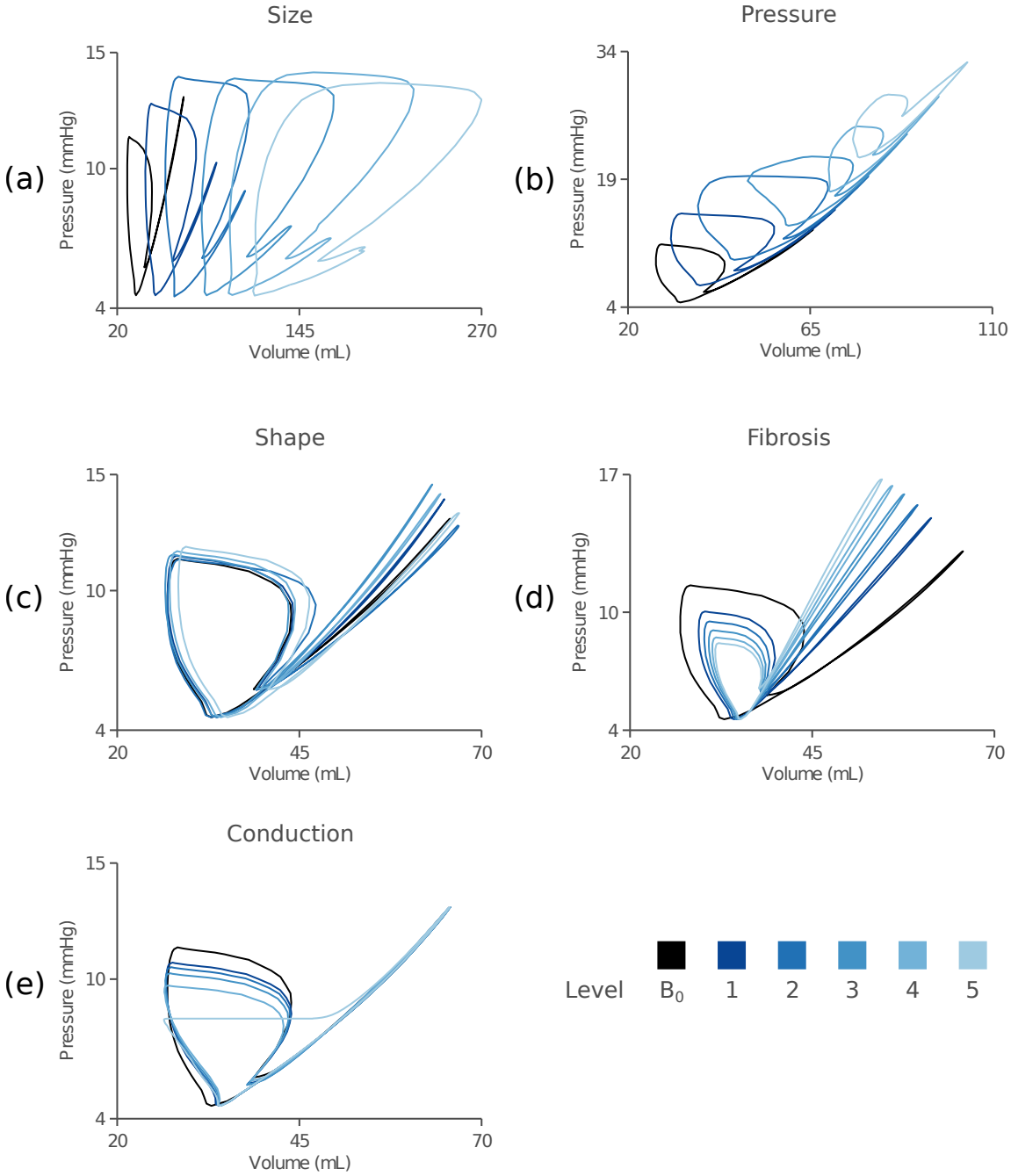

Figure 7.6: Pressure-volume loops for each factor at each level of perturbation. (a) Changes in size created larger atria with lower filling pressures and larger active loops. (b) Changes in pressure shifted the loop up the passive pressure-volume curve and reduced active function. (c) Changes in shape had minimal influence on global function. (d) Adding atrial fibrosis stiffened the passive P-V curve and reduced active function. (e) Slower conduction did not alter passive properties, but did increase active emptying at very slow velocities.

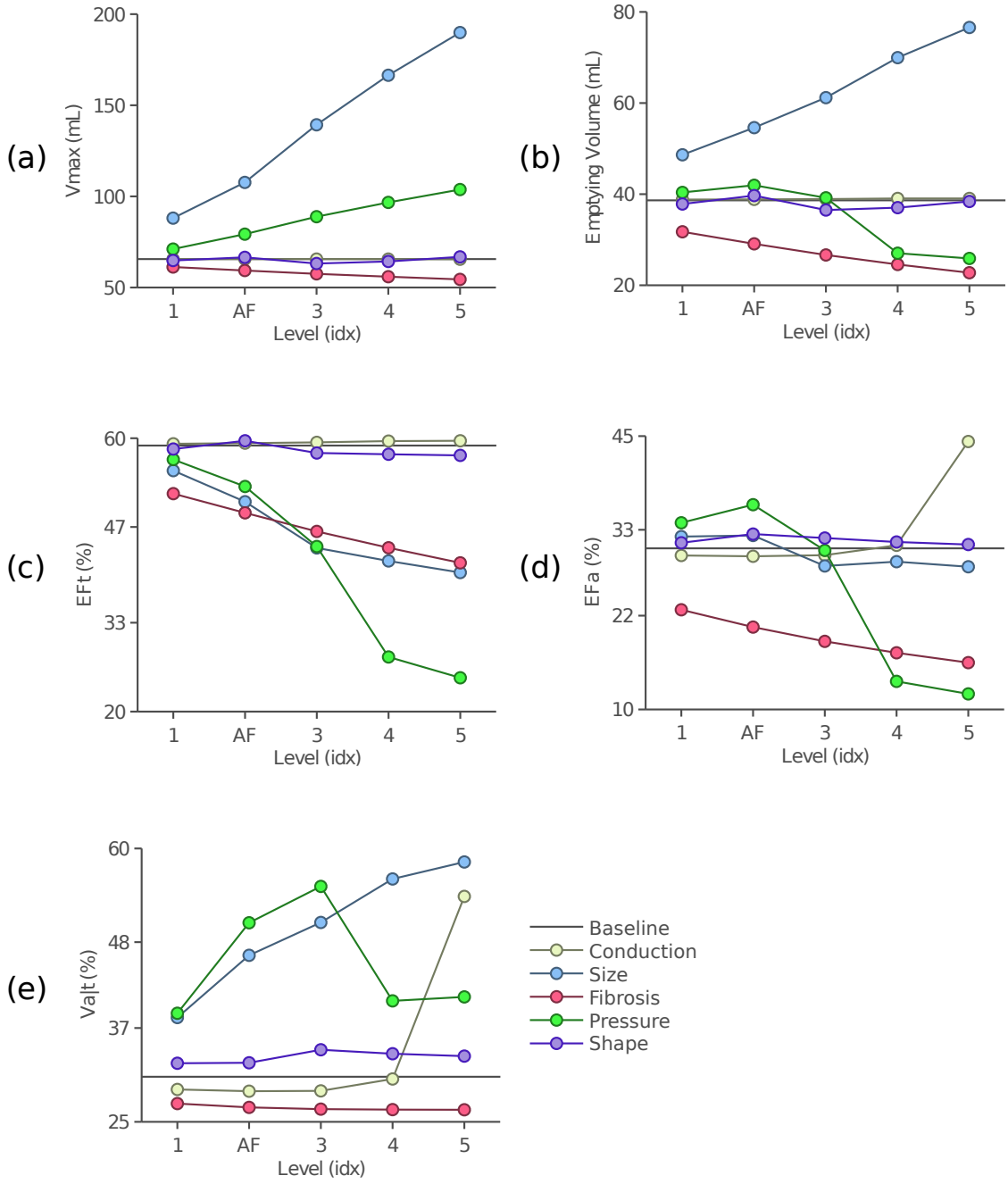

Figure 7.7: Trends in global function for each factor. (a) Changes in maximum volume. (b) Changes in emptying volume ΔV_t. (c) Changes in total emptying fraction EF_t. (d) Changes in active emptying fraction EF_a. (e) Changes in active emptying as a fraction of total $V_{a|t}$.

active function (Fig. 7.7). Most notably, increased fibrosis decreased active emptying as a portion of total $V_{a|t}$, a trend that ran counter to our *in vivo* differences.

7.5.5 Changes in atrial conduction

Slower atrial conduction did not influence passive filling in our model and only modestly influenced active emptying. Slower atrial conduction meant a more distributed active stress curve (some regions would peak before others), which decreased contraction efficiency. This resulted in lower active pressure P_{sys} and lower stroke work, but had a minimal effect on active emptying volume (Fig. 7.6e). Interestingly, small changes in conduction velocity (Levels 1-4) resulted in almost no loss of passive emptying, even though the time allotted for emptying decreased. Since the atrium reached diastasis with the LV prior to contraction (LV), prolonged conduction that "ate into" this time did not alter the prior emptying step. It was only at the slowest level (20 cm/sec) that active emptying began further up the passive P-V curve.

7.5.6 Changes in regional function

Changes in regional function followed trends in global function with a few notable deviations (Fig. 7.8). Total regional REF_t decreased in all regions for size, pressure, and fibrosis factors (Fig. 7.8a), matching global changes (Fig. 7.7). We anticipated that regions with higher REF_t at baseline should have larger losses based on *in vivo* trends (Fig. 7.2). Of all the tested factors at the average AF level (Level 2), atrial fibrosis followed this trend the best – REF_t deteriorated the most in the inferior and lateral walls (highest function at baseline) and had smaller drops in the septal and posterior walls. Although changes in atrial size and pressure also created large drops in function, the magnitude of change from these factors was less correlated with baseline values.

Changes in atrial shape influenced regional function more than global function, especially in regions with low curvature at baseline. As the atrium became more spherical, the "flatter"

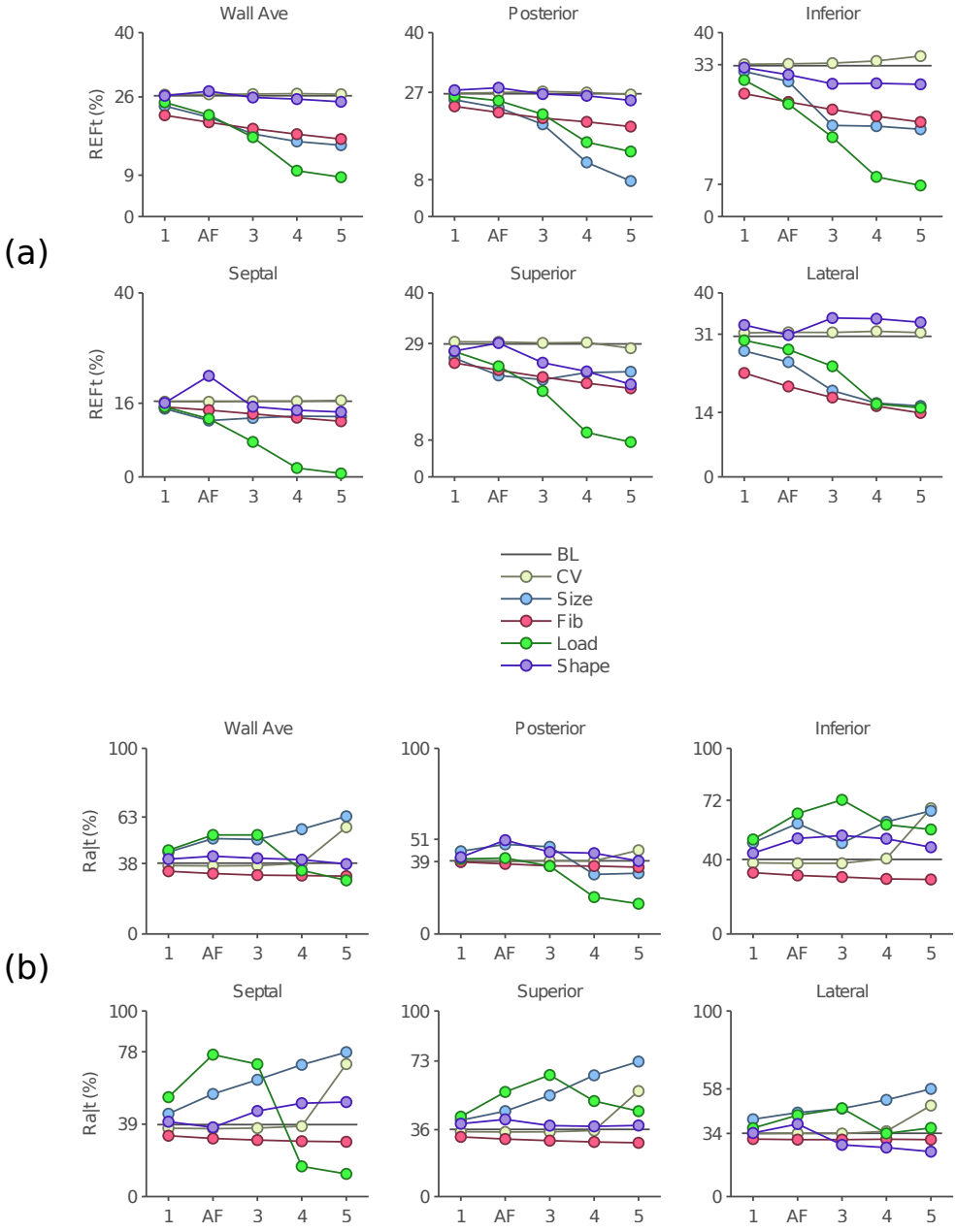

Figure 7.8: Regional motion trends. (a) Total radial emptying fraction REF_t. (b) Active radial emptying as a fraction of total emptying $R_{a|t}$.

regions (superior and inferior walls) had larger drops in REF_t while high curvature regions (lateral wall) showed an *increase* in REF_t. These patterns indicate that local wall curvature had a large influence on regional REF_t, but was swamped in global function by factors of size, pressure, and fibrosis. Atrial shape had a few interesting patterns, including a slight increase in function in the septal wall at Level 2 (average AF shape).

Regional active emptying as a portion of total emptying $R_{a|t}$ generally increased for factors of size and shape and decreased for fibrosis (Fig. 7.8b). Changes in atrial size generated consistent increases in $R_{a|t}$ for all regions except the posterior wall. Changes in atrial pressure also increased reliance on active contraction, but the changes were erratic - large increases at lower levels with steep drop-offs at higher levels and a very large increase in the septal wall compared to other regions. Atrial shape changed how the inferior wall moved, steadily increasing its reliance on contraction as curvature increased. Fibrosis consistently lowered $R_{a|t}$ in all regions, agreeing with its global average.

7.5.7 Changes in regional strain and stress

Peak regional strain increased with changes in atrial pressure and shape and decreased with changes in atrial size and fibrosis, although these trends were not uniform (Fig. 7.9). Circumferential strain (Fig. 7.9b) was more sensitive than longitudinal strain (Fig. 7.9a) to changes in atrial pressure, except in the lateral wall where longitudinal strain increased much more due to loading. The lateral wall had circumferential fibers which created very high longitudinal strains and a high sensitivity to elevated loading. All regions had a clear linear relationship between loading and strain. Highly-aligned longitudinal fibers in the septal wall amplified the effects of loading on circumferential fibers. Generally, aligned fibers in the lateral and septal walls tended to tamper changes in strain in the direction of fibers and amplified changes in strain in the orthogonal direction.

Atrial dilation (increase in size) lowered regional strain for every factor except the septal-circumferential condition, driven by the increase in unloaded length of a larger atrium. Even

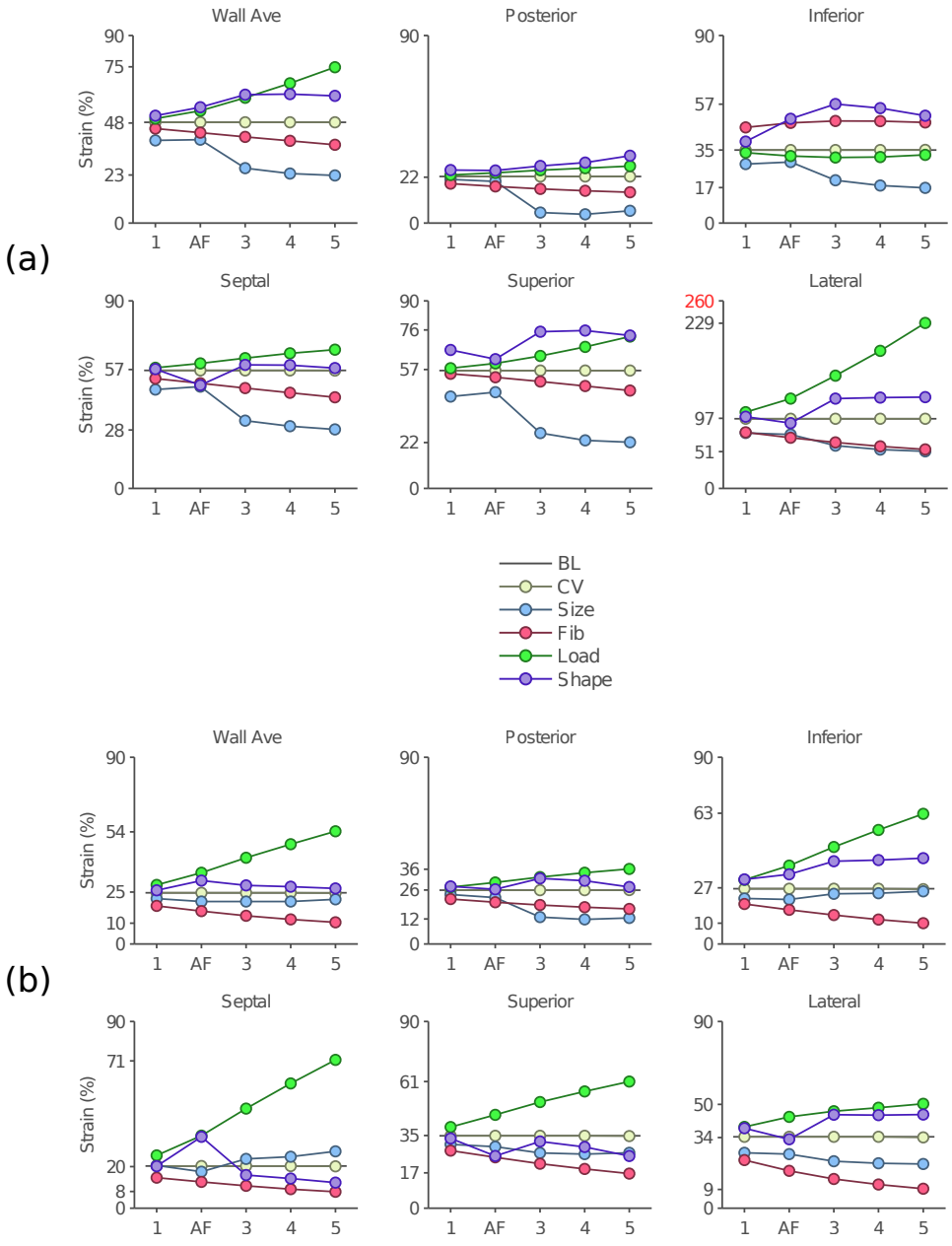

Figure 7.9: Trends in regional strain at mitral valve opening (maximum atrial volume). (a) Longitudinal strain. (b) Circumferential strain.

though larger atria were able to fill more easily, the decrease in pressure coupled with larger unloaded lengths lowered simulated strain. Fibrosis had the same result (lower strain) but for a different reason. Fibrosis limited expansion of the walls during filling, decreasing peak strain values in all regions.

Longitudinal strain in the inferior wall had somewhat anomalous function with trends that ran counter to other regions and directions. Increased loading (pressure) had almost no effect on regional strain, possibly due to the very large effects in the neighboring lateral and septal walls (large stretches in one region might reduce stretch in another). Shape had a disproportionately large influence on regional strain, possibly due to the very low curvature of the inferior wall at baseline. The inferior wall had both circumferential and longitudinal fiber orientations, so these effects could not be attributed to alignment alone.

Atrial pressure had the largest influence on regional stress in all regions and directions. Just like regional strain, regional stresses increased linearly with increases in atrial pressure (levels of dysfunction). The lateral wall (circumferential) and septal wall (longitudinal) had the largest increases, created from the aligned fibers in those regions. In contrast, increases in atrial size decreased regional stresses in all regions and all directions. Although increased size should increase wall stress (Laplace's relationship), this effect was swamped by decreased filling pressure and influence of boundary conditions, which shrank in the dilated models. Fibrosis had a minimal effect on average stress, with small increases in some regions and small decreases in others. In fibrosis, the decreased stress in some regions (septal wall, longitudinal direction) corresponded to a decreased strain in the same region, even though filling pressures increased in fibrotic atria.

We compared changes in regional emptying fraction (decreased REF_t) to changes in regional wall stress. We found that one factor – atrial pressure – displayed a clear link between increased regional wall stress and decreased regional function. That is, regions were wall stress increased the most due to elevated loading (septal, inferior, and lateral walls) also had the largest decreases in regional REF_t. And regions where wall stress increased

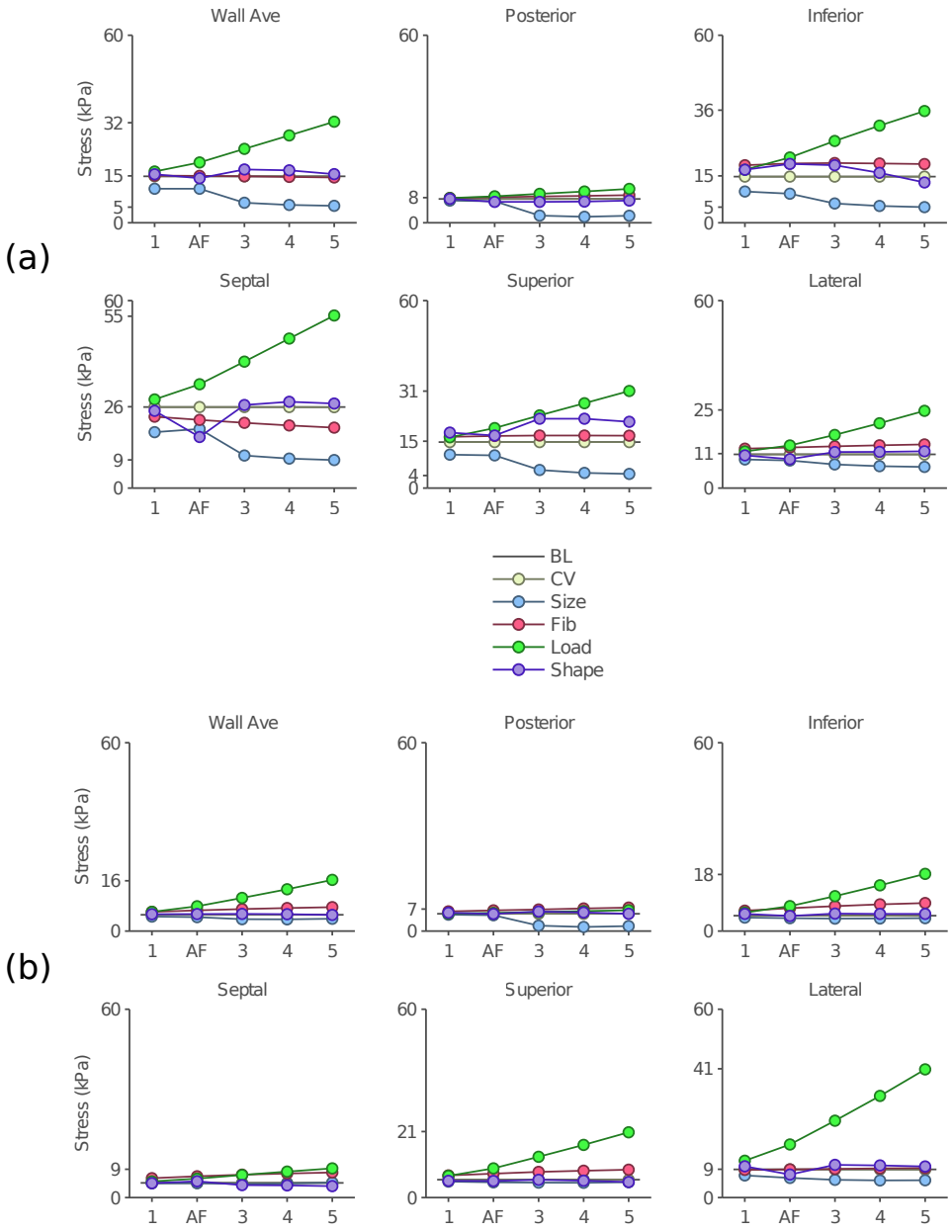

Figure 7.10: Trends in regional stresses at mitral valve opening (maximum atrial volume). (a) Longitudinal stress. (b) Circumferential stress.

by smaller amounts (posterior and superior walls) also had only modest declines in REF_t. This confirmed our hypothesis that changes in regional function due to AF were drive by changes in wall stress. However, this correlative relationship did not hold for other factors (size, fibrosis), where function decreased without increased wall stress.

7.6 Discussion

Atrial fibrillation led to dilation, depressed emptying fraction, and increased reliance on active contraction based on wall motion analysis. We hypothesized that changes in wall motion in AF patients would be spatially heterogeneous. Regional function decreased the most in the inferior and lateral walls (where healthy function was the highest), confirming our hypothesis. The portion of motion attributed to contraction increased in four of five regions (the superior wall was already completely active and could not increase further).

7.6.1 Clinical changes in atrial function

Atrial dilation is both an indicator and symptom of atrial fibrillation (Abhayaratna et al., 2006; Gupta et al., 2012). Our wall motion analysis confirmed dilation in AF patients compared to healthy subjects, and the increase in volume (43.7%) matched the weighted average of 5 previous studies (43.3%) with less than 1% difference (Phang et al., 2004), (Tsang et al., 2001), (Sanfilippo et al., 1990), (Therkelsen et al., 2005) (Thomas et al., 2003). The amount of dilation depends on population sub-groups (paroxysmal vs. persistent AF) and co-morbidities (lone AF vs. valvular-AF). There is no standard for reporting fractional measures like EF_t, but recent studies using 2-D echo and cine MRI calculated an equivalent measure that matched our results almost exactly (48 and 44% vs. 44% EF_t) (Kuppahally et al., 2010; Raman et al., 2005). The same cine MRI study also measured active EF_a that matched our results within one standard deviation ($27 \pm 8\%$ vs. $32 \pm 8\%$ EF_a). No group

analyzed the ratio of active to total function $V_{a|t}$ to the best of our knowledge, although many types of fractional measures have been proposed (Boyd et al., 2011).

Regional function in the atrium is not as well characterized as global function. Various strain-based studies have shown deterioration of motion in AF populations compared to healthy controls, but analysis is typically constrained to the traditional 2-D echo imaging planes (vertical and horizontal long axis, or "two-chamber" and "four-chamber" views). Average strain in the atrium measured via speckle tracking agreed with our average of regional function REF_t within one standard deviation (16 vs. 19 ± 5 %) (Motoki et al., 2012) and regional averages of strain in the septal and lateral walls matched our trend between the regions (Kuppahally et al., 2010). Similar to global function, no previous study has reported active regional motion as a portion of total motion.

7.6.2 Simulated changes in global function

We hypothesized that changes in wall motion in AF patients were caused by changes in atrial pressure and size (related to increased wall stress) and not by changes in fibrosis or electrical conduction. In a five factor FE analysis, we simulated the individual influence of pressure, size, shape, fibrosis, and conduction on global and regional function. We found that size and pressure had the largest influence on function, confirming our hypothesis. Of all the factors tested, only pressure and size recreated portions of the three observed changes in AF function (dilated chamber, decreased EF_t, and increased $V_{a|t}$). No individual factor was able to create the total change in function observed in AF patients.

Many previous studies have tested factors associated with AF, either as causes or symptoms of the disease. We chose the five main factors based on their prevalence in AF literature and their known influence on mechanical function. Previous work has shown that changes in pressure substantially change atrial size (Elvan et al., 2013), and our finite element model demonstrated how maximum volume changes for various levels of pressure. Similarly, multiple studies have shown how function deteriorates due to atrial fibrosis, including correlating

strain with histology (Cameli et al., 2013) and strain with delayed-enhancement imaging (Kuppahally et al., 2010). Our model was able to show that, yes, fibrosis does decrease function, but it is more likely that changes in size and pressure (which accompany fibrosis) are playing a larger role in these studies. In fact, when comparing correlations in (Cameli et al., 2013), the authors found a significant correlation between atrial fibrosis and *left atrial volume* and *pulmonary arterial pressure* - the two factors we identified with high functional sensitivity.

We hypothesized that certain factors related to AF (changes in size, pressure) would recreate the increased reliance on active contraction we observed *in vivo* (61% *in vivo* average). Dilation increased $V_{a|t}$ gradually but the changes never reached observed levels, even at the highest levels of dilation. Atrial pressure had the largest impact on global and regional function, but pressure alone could not explain the increase in $V_{a|t}$. Changes in atrial shape influenced regional function in regions with high or low curvature, but did not influence global function. Atrial conduction velocity had minimal influence on stress, strain, or function, except at extreme values. Extremely slow conduction velocities *could* have influenced $V_{a|t}$ and made active contraction a larger part of emptying but the required velocity would be slower than any observed conduction and thus an unrealistic mechanism. Atrial fibrosis depressed both passive and active emptying, resulting in minimal changes in $V_{a|t}$. No factor tested was able to recreate the observed increase on active contraction $V_{a|t}$, though size and pressure came close.

7.6.3 Minimal model of AF mechanics

We found that no single factor was able to describe the global mechanics observed in AF patients (Fig. 7.5b,c). But could a subset of factors, in combination, capture the majority of functional changes? We explored a "step-wise" approach to answer this question (Fig. 7.11a,b).

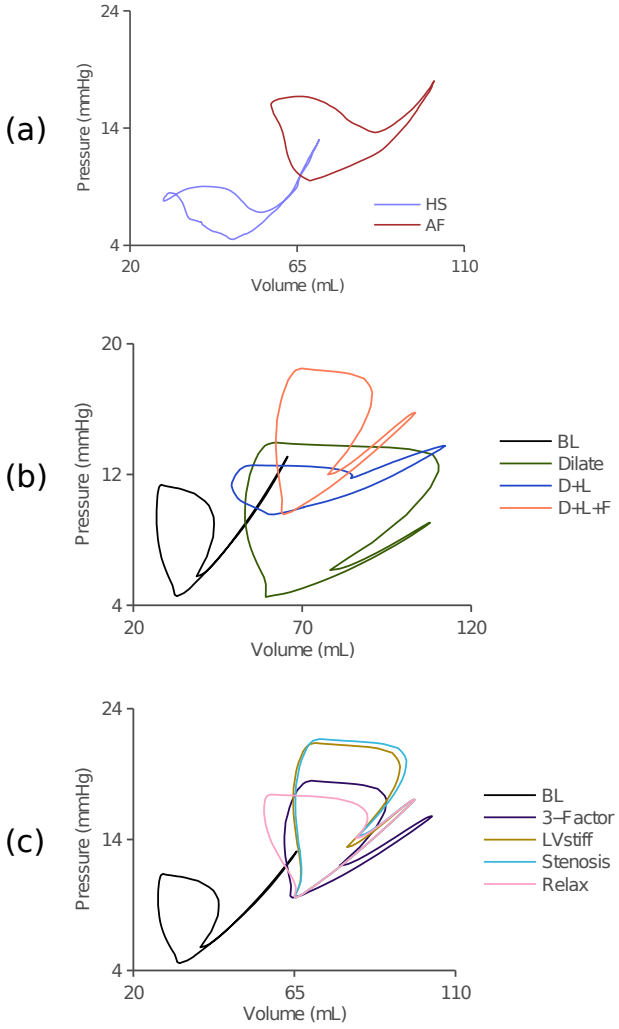

Figure 7.11: The three-factor loop explained a good portion of change in function from healthy baseline to an average AF case. Three ventricular factors 1) LVstiff - increased passive ventricular stiffness, 2) Stenosis - increased mitral valve resistance, 3) Relax - delayed relaxation in the LV during early diastole. Only delayed relaxation correctly simulated the average AF loop.

Increases in atrial size had the largest influence on filling volumes, followed closely by changes in atrial pressure (Table 7.3, trend slopes). Maximum atrial volume increased by 25 mL with each step in atrial size and only increased by 8 mL with each step in pressure. No other factor had a positive influence on atrial dilation. Knowing the average maximum volume in the AF population (102 mL, Table 7.1), we concluded that changes in pressure alone *could not* explain observed dilation, while changes in the unloaded size *could* explain the effect. We concluded that the unloaded geometry must have dilated in AF patients, since no other factor could explain the increase in V_{max}. We assumed this was the first factor in the step-wise model (Fig. 7.11b).

Knowing that atrial pressure is higher in AF patients, we concluded that dilation is not acting alone. Dilation as a single factor decreased maximum pressure - the opposite direction of observed changes. Therefore, we needed a second factor. We tested each factor against peak passive pressure P_{mvo} and found that only fibrosis and increased loading positively influenced this value. We found that fibrosis slightly increased pressure (15 vs. 13 mmHg, +1 trend), but not enough to match *in vivo* averages. The only route to matching measured pressures was explicitly increasing the the operating pressure (19 vs. 13 mmHg, +4 trend). We combined the AF average (Level 2) for these two factors to simulate a "Dilation-Pressure" model. The D-P model found a V_{max}= 112 mL (10% error) and a maximum pressure P_{mvo} of 13.8 (24% error), which was closer to the expected range. However, the change in pressure during filling (ΔP_{fill}) was much lower than expected (3.8 mmHg (> 50% error). AF patients tended to maintain filling pressures compared to controls (both were roughly 8 mmHg in clinical P-V loops). Therefore, we needed a third factor in the step-wise model.

Only one factor consistently increased ΔP_{fill} - fibrosis. This fits well with the clinical pathology of increased fibrosis in AF patients. We created a "Dilation-Pressure-Fibrosis" model and found a better match to the average *in vivo* AF loop. Filling pressures were higher (5.8 mmHg) and maximum volumes were closer to the average AF loop (103 mL). We built a simple algorithm to measure the changes in each of these loops based on key points in the

cycle (P_{mvo}, V_{max}, V_{preA}, P_{sys}, V_{min}). We used the error at these points to quantify the change from healthy to AF and ask - how much of this change can be explained by the isolated factors? The three-factor model explained 84% of the observed differences between healthy and AF function (Fig. 7.11a,b). This calculation was limited to global pressure-volume behavior but it allowed us to identify the *necessary* factors that are contributing to AF-related dysfunction.

7.6.4 Exploration into non-atrial factors

Although the three-factor model explained over 80% of the change in AF loops compared to healthy subjects, it missed some key aspects of function. The drop in total function EF_t was overestimated (40 vs. 44%) and the increase in active function $V_{a|t}$ was underestimated (37 vs. 61%). We tested three non-atrial factors that could address the gap: an increase in left ventricular stiffness, mitral valve stenosis, and delayed LV relaxation. We hypothesized that each of these factors would disrupt passive emptying in the atrium to some extent, and possibly shift $V_{a|t}$ to a higher, more active state. 1) We modeled an increase in LV stiffness by doubling (2x) the exponential coefficient in the passive elastance curve. Thus for a given change in volume during emptying, the ventricle should have higher diastolic pressures. Increased LV stiffness increased LV-end diastolic pressure from 8.2 mmHg to 22.2 mmHg. 2) We modeled mitral valve stenosis by quadrupling (4x) the resistance across the mitral valve in the hydraulic circuit. Increased mitral valve resistance reduced peak mitral valve flow by over 60% and reduced E:A ratio from 1.47 to 0.88. 3) We modeled delayed LV relaxation by adding an active elastance curve to the start of LV diastole that decayed exponentially to zero with a time constant ($\tau = 80$ msec), as previously described by (Hay et al., 2005). In each case, we chose a plausible clinical range that produced significant but reasonable changes in ventricular function. We improved our chance of matching the AF condition by including the true AF shape and non-isochronic conduction, both at average

AF levels. We compared the P-V loops for each of these three ventricular modifications (Fig. 7.11a,c).

All modeled loops (3-factor, LV stiffness, MV stenosis, and LV relaxation) fell within the same general pressure and volume range. Both MV stenosis and LV stiffness created higher pressures during active emptying as the atrium attempted to contract against higher LV pressures or a more resistant valve. LV relaxation did not have the same impact on active emptying, since its effect decayed before passive emptying was finished. The influence of impaired relaxation on early diastolic filling is the key difference for LV relaxation compared to the other tested factors. All other properties of the ventricle (stiffness, pressure, size, valve properties) influence *both* the passive and active emptying phases of the atrium, making it more difficult for them to alter $V_{a|t}$ in a meaningful way. Thus, only impaired LV relaxation affected passive atrial emptying more than active emptying (Fig. 7.12a).

We measured total and active function for the three ventricular factors. We found increased LV stiffness led to an overestimation of total function loss and underestimation of the increase in active contraction ($EF_t = 34\%$, $V_{a|t} = 44\%$). Mitral valve stenosis moved $V_{a|t}$ closer to the clinical average but still underestimated total and active function. ($EF_t = 34\%$, $V_{a|t} = 53\%$). Delayed relaxation in the ventricle was the only factor to accurately match total $EF_t = 43\%$ and active $V_{a|t} = 61\%$ function, matching both within 1% of our measurements from AF patients (Fig. 7.12a). Simulated regional REF_t of the LV relaxation model also fell within one standard deviation of the *in vivo* AF wall motion data in *all five* regions (Fig. 7.12c). This effect has been documented in a prior study, where impaired relaxation in the ventricle (caused by ischemia, prior MI, and angina) increased atrial contributions from 26 to 38% (Prioli et al., 1998). We used the final model as an "AF baseline" alongside the healthy baseline developed in Chapter 6 (Fig. 7.12a,b) to study the effects of ablation procedures in Chapter 8.

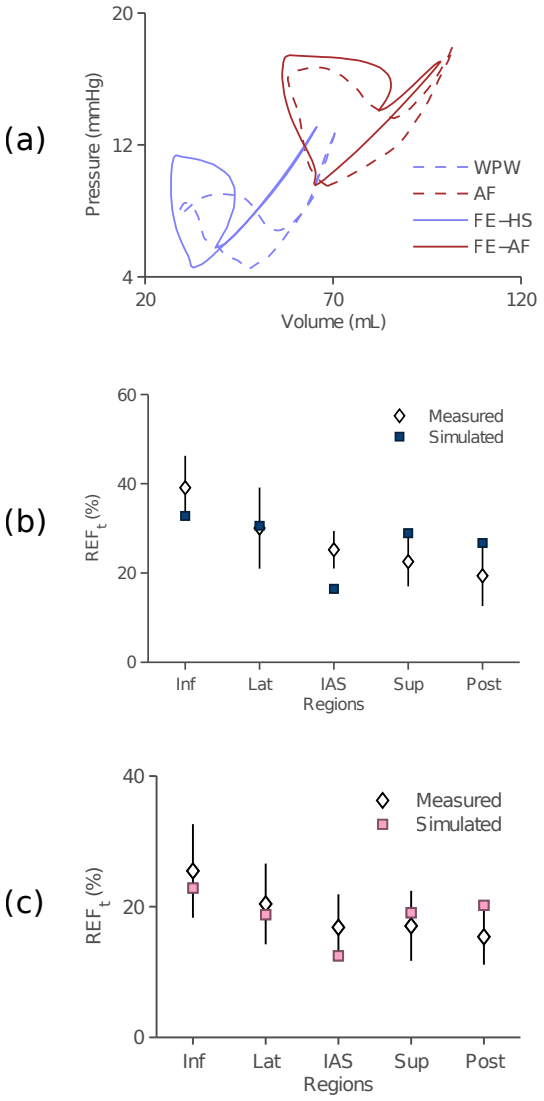

Figure 7.12: Validation of baseline and AF simulations compared to *in vivo* data. (a) Simulated P-V loops showed excellent agreement in size, shape, and hemodynamics compared to healthy (WPW) and AF data. (b) Regional motion agreed in 4 of 5 regions in the HS model compared to wall motion analysis. (c) Regional motion agreed in all five regions in the AF model compared to wall motion data from AF patients (within one standard deviation).

References

W. P. Abhayaratna, J. B. Seward, C. P. Appleton, P. S. Douglas, J. K. Oh, A. J. Tajik, and T. S. M. Tsang. Left atrial size: physiologic determinants and clinical applications. *J. Am. Coll. Cardiol.*, 47(12):2357–2363, June 2006.

C. P. Appleton, J. M. Galloway, M. S. Gonzalez, M. Gaballa, and M. A. Basnight. Estimation of left ventricular filling pressures using two-dimensional and doppler echocardiography in adult patients with cardiac disease: Additional value of analyzing left atrial size, left atrial ejection fraction and the difference in duration of pulmonary venous and mitral flow velocity at atrial contraction. *Journal of the American College of Cardiology*, 22(7): 1972–1982, Dec. 1993.

M. F. Beatty. Topics in finite elasticity: Hyperelasticity of rubber, elastomers, and biological TissuesWith examples. *Applied Mechanics Reviews*, 40(12):1699–1734, 1987.

F. Bisbal, E. Guiu, N. Calvo, D. Marin, A. Berruezo, E. Arbelo, J. Ortiz-Prez, T. M. de Caralt, J. M. Tolosana, R. Borrs, M. Sitges, J. Brugada, and L. Mont. Left atrial sphericity: A new method to assess atrial remodeling. impact on the outcome of atrial fibrillation ablation. *Journal of Cardiovascular Electrophysiology*, page n/an/a, 2013.

G. G. Blume, C. J. Mcleod, M. E. Barnes, J. B. Seward, P. A. Pellikka, P. M. Bastiansen, and T. S. M. Tsang. Left atrial function: physiology, assessment, and clinical implications. *Eur J Echocardiogr*, 12(6):421–430, June 2011.

A. C. Boyd, N. B. Schiller, D. Leung, D. L. Ross, and L. Thomas. Atrial dilation and altered function are mediated by age and diastolic function but not before the eighth decade. *J Am Coll Cardiol Img*, 4(3):234–242, Mar. 2011.

M. Cameli, M. Lisi, F. M. Righini, A. Massoni, B. M. Natali, M. Focardi, D. Tacchini, A. Geyer, V. Curci, C. Di Tommaso, G. Lisi, M. Maccherini, M. Chiavarelli, M. Massetti,

P. Tanganelli, and S. Mondillo. Usefulness of atrial deformation analysis to predict left atrial fibrosis and endocardial thickness in patients undergoing mitral valve operations for severe mitral regurgitation secondary to mitral valve prolapse. *The American Journal of Cardiology*, 111(4):595–601, Feb. 2013.

D. M. Clark, V. J. Plumb, A. E. Epstein, and G. Kay. Hemodynamic effects of an irregular sequence of ventricular cycle lengths during atrial fibrillation. *Journal of the American College of Cardiology*, 30(4):1039–1045, Oct. 1997.

D. C. Connolly, J. W. Kirklin, and E. H. Wood. The relationship between pulmonary artery wedge pressure and left atrial pressure in man. *Circulation Research*, 2(5):434–440, Sept. 1954.

A. Elvan, A. Adiyaman, R. J. Beukema, H. T. Sie, and M. A. Allessie. Electrophysiological effects of acute atrial stretch on persistent atrial fibrillation in patients undergoing open heart surgery. *Heart Rhythm*, 10(3):322–330, Mar. 2013.

G. M. Fomovsky and J. W. Holmes. Evolution of scar structure, mechanics, and ventricular function after myocardial infarction in the rat. *American Journal of Physiology - Heart and Circulatory Physiology*, 298(1):H221–H228, Jan. 2010.

L. Frost. Lone atrial fibrillation good, bad, or ugly? *Circulation*, 115(24):3040–3041, June 2007.

C. Gloschat, J. Cates, B. Walker, and R. S. MacLeod. Statistical shape modeling of the left atrium from MRI of patients with atrial fibrillation. *Journal of Cardiovascular Magnetic Resonance*, 13(Suppl 1):P57, Feb. 2011.

S. Gupta, S. A. Matulevicius, C. R. Ayers, J. D. Berry, P. C. Patel, D. W. Markham, B. D. Levine, K. M. Chin, J. A. d. Lemos, R. M. Peshock, and M. H. Drazner. Left atrial structure and function and clinical outcomes in the general population. *Eur Heart J*, July 2012.

A. Hansson, M. Holm, P. Blomstrm, R. Johansson, C. Lhrs, J. Brandt, and S. B. Olsson. Right atrial free wall conduction velocity and degree of anisotropy in patients with stable sinus rhythm studied during open heart surgery. *Eur Heart J*, 19(2):293–300, Feb. 1998.

I. Hay, J. Rich, P. Ferber, D. Burkhoff, and M. S. Maurer. Role of impaired myocardial relaxation in the production of elevated left ventricular filling pressure. *Am J Physiol Heart Circ Physiol*, 288(3):H1203–H1208, Mar. 2005.

P. Jais, J. T. Peng, D. C. Shah, S. Garrfgue, M. Hocini, T. Yamane, M. Haissaguerre, S. S. Barold, R. Roudaut, and J. Clementy. Left ventricular diastolic dysfunction in patients with SoCalled lone atrial fibrillation. *Journal of Cardiovascular Electrophysiology*, 11(6): 623–625, June 2000.

G. Keren, T. Etzion, J. Sherez, A. A. Zelcer, R. Megidish, H. I. Miller, and S. Laniado. Atrial fibrillation and atrial enlargement in patients with mitral stenosis. *American Heart Journal*, 114(5):1146–1155, Nov. 1987.

K. T. Konings, C. J. Kirchhof, J. R. Smeets, H. J. Wellens, O. C. Penn, and M. A. Allessie. High-density mapping of electrically induced atrial fibrillation in humans. *Circulation*, 89 (4):1665–1680, Apr. 1994.

L. C. Kuo, M. A. Quinones, R. Rokey, M. Sartori, E. G. Abinader, and W. A. Zoghbi. Quantification of atrial contribution to left ventricular filling by pulsed doppler echocardiography and the effect of age in normal and diseased hearts. *The American Journal of Cardiology*, 59(12):1174–1178, May 1987.

S. S. Kuppahally, N. Akoum, N. S. Burgon, T. J. Badger, E. G. Kholmovski, S. Vijayakumar, S. N. Rao, J. Blauer, E. N. Fish, E. V. DiBella, R. S. MacLeod, C. McGann, S. E. Litwin, and N. F. Marrouche. Left atrial strain and strain rate in patients with paroxysmal and persistent atrial fibrillation: Relationship to left atrial structural remodeling detected by delayed-enhancement MRI. *Circ Cardiovasc Imaging*, 3(3):231–239, May 2010.

C. Mahnkopf, T. J. Badger, N. S. Burgon, M. Daccarett, T. S. Haslam, C. T. Badger, C. J. McGann, N. Akoum, E. Kholmovski, R. S. Macleod, and N. F. Marrouche. Evaluation of the left atrial substrate in patients with lone atrial fibrillation using delayed-enhanced MRI: implications for disease progression and response to catheter ablation. *Heart Rhythm*, 7(10):1475–1481, Oct. 2010.

V. Markides, R. J. Schilling, S. Yen Ho, A. W. Chow, D. W. Davies, and N. S. Peters. Characterization of left atrial activation in the intact human heart. *Circulation*, 107(5): 733–739, Feb. 2003.

M. Matsuzaki, M. Tamitani, Y. Toma, H. Ogawa, K. Katayama, Y. Matsuda, and R. Kusukawa. Mechanism of augmented left atrial pump function in myocardial infarction and essential hypertension evaluated by left atrial pressure-dimension relation. *The American Journal of Cardiology*, 67(13):1121–1126, May 1991.

H. Motoki, A. Dahiya, M. Bhargava, O. M. Wazni, W. I. Saliba, T. H. Marwick, and A. L. Klein. Assessment of left atrial mechanics in patients with atrial fibrillation: Comparison between two-dimensional speckle-based strain and velocity vector imaging. *Journal of the American Society of Echocardiography*, 25(4):428–435, Apr. 2012.

S. Nattel. New ideas about atrial fibrillation 50 years on. *Nature*, 415(6868):219–226, Jan. 2002.

R. S. Oakes, T. J. Badger, E. G. Kholmovski, N. Akoum, N. S. Burgon, E. N. Fish, J. J. E. Blauer, S. N. Rao, E. V. R. DiBella, N. M. Segerson, M. Daccarett, J. Windfelder, C. J. McGann, D. Parker, R. S. MacLeod, and N. F. Marrouche. Detection and quantification of left atrial structural remodeling with delayed-enhancement magnetic resonance imaging in patients with atrial fibrillation. *Circulation*, 119(13):1758–1767, Apr. 2009.

R. S. Phang, S. M. Isserman, D. Karia, N. G. Pandian, M. K. Homoud, M. S. Link, N. M. Estes III, and P. J. Wang. Echocardiographic evidence of left atrial abnormality in young

patients with lone paroxysmal atrial fibrillation. *The American Journal of Cardiology*, 94 (4):511–513, Aug. 2004.

P. G. Platonov, L. B. Mitrofanova, V. Orshanskaya, and S. Y. Ho. Structural abnormalities in atrial walls are associated with presence and persistency of atrial fibrillation but not with age. *J Am Coll Cardiol*, 58(21):2225–2232, Nov. 2011.

A. Prioli, P. Marino, L. Lanzoni, and P. Zardini. Increasing degrees of left ventricular filling impairment modulate left atrial function in humans. *The American Journal of Cardiology*, 82(6):756–761, Sept. 1998.

P. Probst, N. Goldschlager, and A. Selzer. Left atrial size and atrial fibrillation in mitral stenosis factors influencing their relationship. *Circulation*, 48(6):1282–1287, Dec. 1973.

S. V. Raman, V. Y. Ng, M. A. Neff, S. Sayar, E. A. Sparks, S. D. Nelson, A. K. Ferketich, and C. F. Wooley. Volumetric cine CMR to quantify atrial structure and function in patients with atrial dysrhythmias. *J Cardiovasc Magn Reson*, 7(3):539–543, 2005.

A. Sanfilippo, V. Abascal, M. Sheehan, L. Oertel, P. Harrigan, R. Hughes, and A. Weyman. Atrial enlargement as a consequence of atrial fibrillation. a prospective echocardiographic study. *Circulation*, 82(3):792 –797, 1990.

W. Shapiro and G. Klein. Alterations in cardiac function immediately following electrical conversion of atrial fibrillation to normal sinus rhythm. *Circulation*, 38(6):1074–1084, Dec. 1968.

C. Stefanadis, J. Dernellis, C. Stratos, E. Tsiamis, C. Tsioufis, K. Toutouzas, C. Vlachopoulos, C. Pitsavos, and P. Toutouzas. Assessment of left atrial PressureArea relation in humans by means of retrograde left atrial catheterization and echocardiographic automatic boundary detection: Effects of dobutamine. *J Am Coll Cardiol*, 31(2):426–436, Feb. 1998a.

C. Stefanadis, J. Dernellis, C. Stratos, E. Tsiamis, C. Vlachopoulos, K. Toutouzas, S. Lambrou, C. Pitsavos, and P. Toutouzas. Effects of balloon mitral valvuloplasty on left atrial function in mitral stenosis as assessed by pressure–area relation. *J Am Coll Cardiol*, 32(1):159–168, July 1998b.

S. K. Therkelsen, B. A. Groenning, J. H. Svendsen, and G. B. Jensen. Atrial and ventricular volume and function in persistent and permanent atrial fibrillation, a magnetic resonance imaging study. *J Cardiovasc Magn Reson*, 7(2):465–473, 2005.

L. Thomas, A. Boyd, S. P. Thomas, N. B. Schiller, and D. L. Ross. Atrial structural remodelling and restoration of atrial contraction after linear ablation for atrial fibrillation. *Eur. Heart J*, 24(21):1942–1951, Nov. 2003.

T. S. Tsang, M. E. Barnes, K. R. Bailey, C. L. Leibson, S. C. Montgomery, Y. Takemoto, P. M. Diamond, M. A. Marra, B. J. Gersh, D. O. Wiebers, G. W. Petty, and J. B. Seward. Left atrial volume: important risk marker of incident atrial fibrillation in 1655 older men and women. *Mayo Clinic Proceedings*, 76(5):467 –475, May 2001.

T. S. Tsang, W. P. Abhayaratna, M. E. Barnes, Y. Miyasaka, B. J. Gersh, K. R. Bailey, S. S. Cha, and J. B. Seward. Prediction of cardiovascular outcomes with left atrial size: Is volume superior to area or diameter? *J Am Coll Cardiol*, 47(5):1018–1023, Mar. 2006.

S. M. Vaziri, M. G. Larson, E. J. Benjamin, and D. Levy. Echocardiographic predictors of nonrheumatic atrial fibrillation. the framingham heart study. *Circulation*, 89(2):724–730, Feb. 1994.

S. Verheule, E. Wilson, T. Everett, S. Shanbhag, C. Golden, and J. Olgin. Alterations in atrial electrophysiology and tissue structure in a canine model of chronic atrial dilatation due to mitral regurgitation. *Circulation*, 107(20):2615–2622, May 2003.

R. Vianna-Pinton, C. A. Moreno, C. M. Baxter, K. S. Lee, T. S. M. Tsang, and C. P. Appleton. Two-dimensional speckle-tracking echocardiography of the left atrium: feasibility and

regional contraction and relaxation differences in normal subjects. *J Am Soc Echocardiogr*, 22(3):299–305, Mar. 2009.

Chapter 8

Changes in atrial function following ablation

Catheter ablation is quickly becoming a primary treatment for atrial fibrillation. An ablation procedure electrically isolates selected regions by burning lines of scar into the atrial wall. If successful, ablation restores sinus rhythm and improves atrial mechanical function. We used our previously developed techniques to quantify the acute and long-term changes in atrial function following ablation. Analysis of P-V loops found increased passive stiffness and decreased contractile work immediately following ablation, most likely caused by temporary edema. Long-term changes, tracked with MR-based wall motion analysis, found a decrease in atrial size and a decreased reliance on active atrial contraction. Changes in regional motion were more sensitive than global measures, with regional differences in the superior and septal wall. Post-ablation changes in most indices represented a return towards healthy levels reported in Chapter 5. We used our finite element model to predict changes in function caused by atrial scarring. We found that higher scar volumes and placement in high-functioning regions both decreased atrial function, especially in the inferior and lateral walls. We also found that the *in vivo* changes in atrial mechanics we observed following ablation were unlikely due to scar. We identified key measures of total and active function, observed how

they changed following ablation, and used the FE model to estimate the effects of scarring.

8.1 History of AF ablation

Surgical treatment of cardiac arrhythmias has been a part of medicine since the 1960s, though its application to AF did not arise until 1982. James Cox, then at Washington University in St. Louis, developed an expertise for surgical intervention of arrhythmias (Cox, 1985) and proposed a method to surgically isolate the atrium (Williams et al., 1980). The group theorized that the electrical abnormality causing AF could be blocked by physically cutting and stitching the atrium together, creating permanent scars that prevent conduction. He wrote following the first human procedure (December 6, 1982):

> The patient has remained in normal sinus rhythm on no antiarrhythmic medications postoperatively, despite the presence of incessant tachycardia confined to the left atrium. She has suffered no adverse hemodynamic sequelae, having returned to her hobby of skydiving.

Cox and colleagues honed this technique into what is known as the "Cox-Maze Procedure" (Cox et al., 1991) and improved upon it through the 1990s (Cox et al., 1995a) (Cox et al., 1995b). The technique, though successful, was technically challenging - it required multiple steps of cutting and suturing the atrium under cardiac bypass. Its complexity precluded any widespread dissemination and the procedure remained clustered in a few research hospitals.

A few years later, researchers in France began using new intravenous catheters to test a less invasive approach. Haïssaguerre and colleagues realized they could mimic the patterns of surgical scar by burning the endocardial surface (Haissaguerre et al., 1994) and expanded the technique to test a variety of scar patterns (Haissaguerre et al., 1996). In a catheter procedure, the clinician could test intraoperatively if regions of tissue had been successfully isolated. They could also test spots of tissue for errant (ectopic) signal formation, which they found in the pulmonary veins (Haissaguerre et al., 1998). This key finding guided subsequent

procedures to isolate the pulmonary veins by adding rings of scar around each, creating the now common ablation technique of "pulmonary vein isolation" (Oral et al., 2002) or PVI.

8.1.1 Current ablation methods

PV isolation grew in popularity (Cappato et al., 2005) to become the most common ablation procedure in the US (Calkins, 2012). It is considered a standard treatment for paroxysmal AF (Wann et al., 2011). As the technique evolved so did its application - PVI was extended to a more heterogeneous patient population, including subjects with persistent or permanent AF. Pulmonary vein isolation was less successful in these cases, driving expansion into a variety of other scar patterns (Brooks et al., 2010). These included a linear "roof line" linking the superior pulmonary veins (Hocini et al., 2005) and an "isthmus line" connecting the left inferior pulmonary vein and the mitral valve (Jais et al., 2004). These additional steps were always added to the standard PVI procedure - creating a "step-wise" PVI model.

Other clinicians addressed the more difficult AF cases by modifying the PVI approach. One group expanded the size of the isolation rings away from the PV ostia into a larger, more encompassing circle and called it a wide-area circumferential ablation or WACA (Pappone et al., 2000). Just like PVI, the inital WACA model was augmented with additional linear ablation patterns connecting the main rings (Oral et al., 2003, 2006), though these steps were not as standardized as the step-wise PVI. There is an ongoing debate as to which procedure produces the best outcomes based on the highest percentage of subjects with no recurrence of AF one year after ablation. Initial studies showed that WACA was clearly superior, especially in a heterogeneous AF population (Oral et al., 2003). This result was later challenged against a segmental-PVI method and found lacking (Hocini et al., 2005), then challenged again and found superior (Lemola et al., 2005b). One randomized trial between the two models found that WACA is better (Arentz et al., 2007) while another found no difference (Karch et al., 2005). A meta-analysis of comparisons between ablation patterns noted a moderate amount of

evidence in support of WACA when coupled with electrical mapping and additional ablation lines targeting residual potentials (Terasawa et al., 2009).

8.1.2 Proposed and experimental ablation methods

More recent studies have moved away from simple isolation towards more complex methods, including targeting areas with complicated electrical signals (Schmitt et al., 2007), sometimes in addition to a WACA model (Oral et al., 2009). Other regions have been targeted, such as portions of the posterior wall (Elayi et al., 2008), the entire posterior wall (Akoum et al., 2010), and the entire septal wall (Segerson et al., 2009), as well as other patterns near the PV ostia, such as radial lines that do not connect (Zhao et al., 2013). More aggressive catheters have been designed to increase scar volume (Pajitnev et al., 2013) and increase transmurality of scar (Gillinov and McCarthy, 2002). General trends demonstrate an expansion of techniques without consideration of preserving mechanical function.

8.1.3 Mechanical function post-ablation

Studies of mechanical function in the post-ablation atrium have been restricted to volume-based analysis. Studies have used CT (Lemola et al., 2005a; Verma et al., 2006), 2-D echocardiography (Thomas et al., 2003), and MRI (Nori et al., 2009; Perea et al., 2008) to measure post-ablation volume and fractional changes in volume. Results were mixed, with some reporting improved function and others reporting no change. As a group, the analysis of post-ablation mechanics suffered from unclear hypotheses. How do we expect total and active function to change following ablation and what changes are signs of improvement? What changes are caused by the ablation itself and what changes reflect true recovery of intrinsic function? The studies were also limited by the global analysis of volume. A few attempted a regional analysis (point-based motion, changes in arc-length) but the analysis remained restricted to 2-D images. There are many studies analyzing strain (using speckle tracking or a variation) as a predictor for AF recurrence, but strain is only measured prior to

ablation and rarely used as a post-ablation tool (Thomas et al., 2007). The only available study observing post-ablation strain restricted the analysis to the left ventricle (Reant et al., 2009).

Given the expansion of ablation procedures and their popularity, we harnessed our capabilities in the measurement and simulation of global and regional mechanical function to measure, analyze, and understand changes in post-ablation function. We hypothesized that ablation scar would temporarily depress atrial function independent of scar location. To test this hypothesis, we used P-V loops to quantify acute changes in function. We also hypothesized that global and regional function will chronically improve following successful ablation despite the presence of ablation scar. We used our MR-based wall motion analysis to measure chronic changes in volume and regional motion. We compared changes in mechanics to previously measured differences between healthy subjects and AF patients. Finally, we hypothesized that ablation scar will chronically depress atrial function dependent on the amount and location of ablation scar. We used our atrial finite element model with added ablation scar to test this hypothesis. We combined simulation-based experiments with clinical results to understand the source of any observed changes in function.

8.2 Methods to measure acute changes following ablation

We measured acute changes in mechanical function following catheter ablation using atrial pressure-volume loops. All studies were approved by the University of Virginia Institutional Review Board (IRB). Fourteen subjects ($n = 14$) were recruited from the University of Virginia Health System for a research study with informed consent. All subjects were scheduled for an interventional ablation procedure prior to recruitment. The ablation procedure followed the current standard of care and was not altered by collection of P-V data. We followed the detailed procedure described in Chapters 2 and 3 for P-V data collection. Briefly, the left

atrium was reached via a trans-septal puncture and the P-V catheter was guided into the left atrium. Real-time cardiac fluoroscopy confirmed the catheter's position. We collected P-V data at intrinsic and paced heart rates (600, 500, 400 msec), all during held expiration. The intrinsic rate data (the "baseline") was calibrated to MR-derived atrial volumes offline and this calibration was applied to all conductance volumes for that patient.

All patients underwent a radiofrequency (RF) ablation procedure, where an RF catheter delivered energy to concentrated areas of tissue, destroying its capacity for electrical conduction. Catheter ablation time, pattern, and power varied between patients, but physicians generally used 25-30 Watts of power and ablated for 20-30 second intervals, tracing around each of the four pulmonary veins (a pulmonary vein "isolation" or PVI procedure). Total ablation time ranged from 30-60 minutes depending on the complexity of PV geometry. Following ablation, the P-V catheter was re-introduced into the left atrium and positioned in the same location as pre-procedure, confirmed with real-time cardiac fluoroscopy. Data were collected at intrinsic and paced heart rates. All data were exported through Millar P-V system and processed exactly as described in Chapter 2. We reported a tissue stiffness k_t and a chamber stroke work SW for each loop. We tested for changes following ablation using a paired t-test, with significance at $p < 0.05$.

8.3 Results of acute changes following ablation

The atrium stiffened and its contraction weakened following RF ablation. In an example patient (Fig. 8.1a), the post-ablation loop followed a stiffer curve during passive filling, while the active loop shrank in area (decrease in stroke work). In this example patient, tissue stiffness k_t increased by 41% and stroke work SW decreased by 72%. We averaged the pre- and post-ablation loops from all $n = 14$ patients into a single loop (Fig. 8.1b). The averaged post-ablation loop had a larger absolute volume, a slightly stiffer pressure-volume curve, and a clear decrease in stroke work. These changes were better visualized by adjusted the absolute

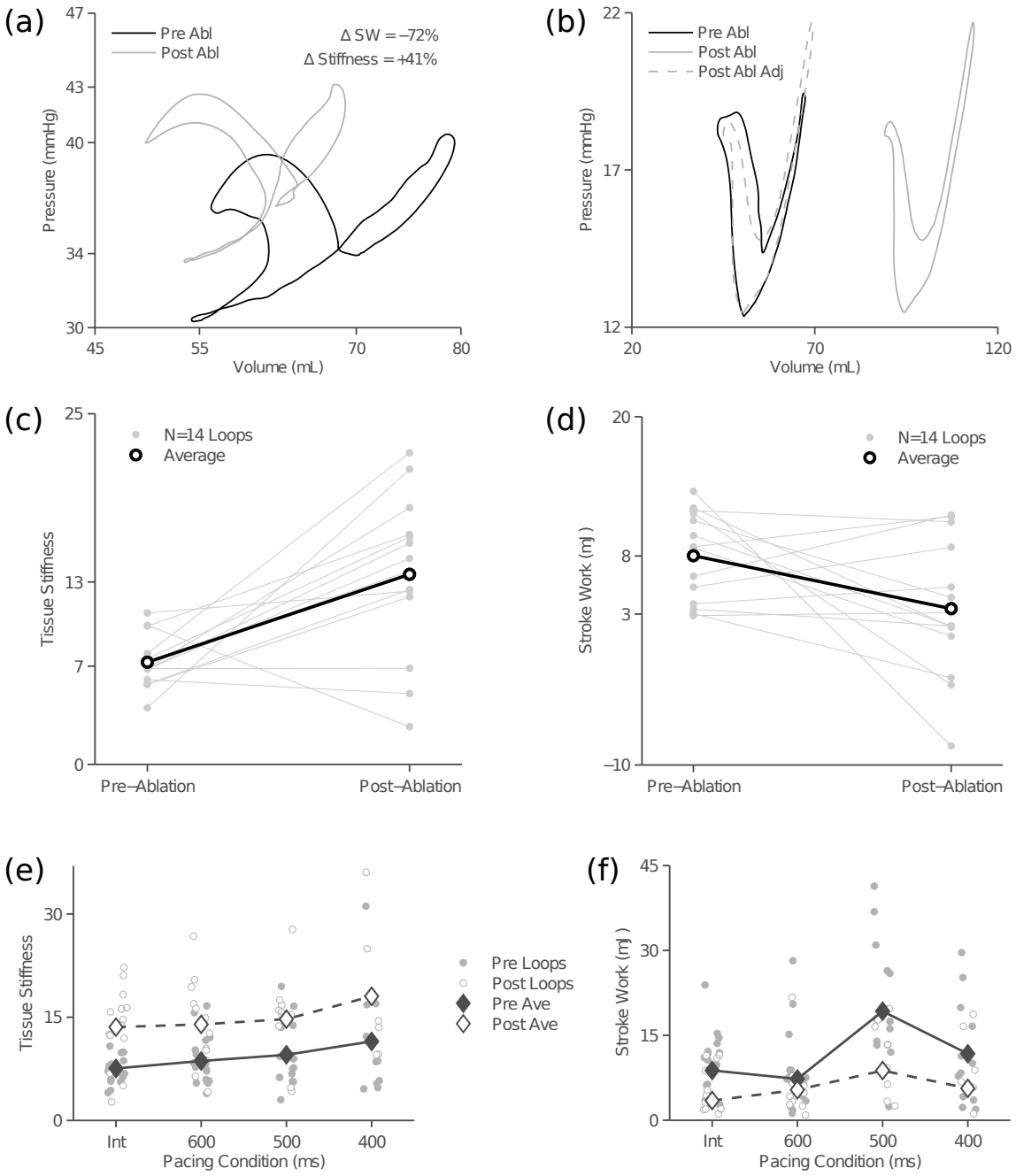

Figure 8.1: Changes in global mechanics following RF ablation. (a) Pressure-volume loops immediately prior to and following an RF ablation for a selected subject. (b) Averaged P-V loops pre- and post-ablation. Shifted curve corrected for volume change. (c) Tissue stiffness increased on average in $n = 14$ tested loops (black line), though changes in individual subjects varied substantially (gray lines). (d) Stroke work decreased on average from pre- to post-ablation (black line), but also varied substantially among subjects (gray lines). (e) Tissue stiffness increased slightly due to higher pacing, and trends vs. pacing rate were quite similar pre- and post-ablation. (f) Stroke work increased with pacing rates, though those increases were muted in post-ablation loops.

size and overlaying the two loops. We quantified the change in tissue stiffness k_t and found an average increase of 86% compared to pre-ablation stiffness (13.5 ± 5.7 vs. 7.3 ± 1.8, $p < 0.01$), mostly driven by an increase in volume. The change in chamber stiffness k_c, which did not account for absolute size, had a smaller non-significant increase (0.13 ± 0.07 vs. 0.12 ± 0.05). We quantified the change in stroke work and found an average decrease of 57% compared to pre-ablation work (3.5 ± 5.9 vs. 8.0 ± 3.8, $p < 0.05$). Twelve of fourteen patients had an increase in stiffness following ablation (Fig. 8.1c, gray lines), whereas only nine of fourteen had a decrease in stroke work (Fig. 8.1d).

We had previously shown that pacing slightly increased stiffness in pre-ablation data, and this trend held in post-ablation loops (Fig. 8.1e). Tissue stiffness increased post-ablation compared to pre-ablation at each pacing rate, and trends with respect to pacing rates were almost identical. We had also shown that stroke work increased with pacing rate as active contraction dominated atrial emptying. Again, this trend held with post-ablation data (Fig. 8.1f). Stroke work was lower in post-ablation loops compared to pre-ablation controls at every pacing rate, and generally increased from 600 to 500 ms, then decreased at 400 ms.

8.4 Longitudinal wall motion study design

Pressure-volume loops measured acute changes in global mechanics but did not capture regional function. Since P-V loops were acquired intraoperatively, they were also unable to measure chronic changes in function. We used MR-based wall motion analysis developed in Chapters 4 and 5 to measure regional function in a longitudinal study following successful RF ablation. We recruited sixty three ($n = 63$) subjects with diagnosed atrial fibrillation ("AF patients") scheduled for an ablation procedure were recruited from the University of Virginia Health System for a research CMR scan with informed consent. A subset of these patients (31 of 63) were analyzed in Chapter 7. Twenty subjects ($n = 20$) completed the full longitudinal study and were included in this analysis.

All scans were performed on a 1.5-T Magnetom Avanto (Siemens Healthcare, Erlangen, Germany). A steady-state free procession (SSFP) imaging sequence was employed, using the same techniques and views discussed in Chapter 5. Patients with abnormal rhythms at the time of the scan were removed from the study (including patients experiencing an episode of AF). Following ablation, patients were excluded for any of the following: 1) had a recurrence of AF, 2) did not return for scheduled follow-up, 3) voluntarily withdrew from the study. The largest reason for removal was a missed follow-up.

We measured global changes in volume and regional changes in wall motion at 6 weeks (6wk) and 6 months (6mth) post-ablation compared to a pre-ablation (pre) baseline. Following techniques described in Chapters 4 and 5, we contoured the left atrial endocardial border and fit it to a continuous surface through space and time. We quantified this surface to measure its volume, radius, and fractional changes in those quantities. We compared post-ablation results of global and regional function to pre-ablation baseline using repeated-measures ANOVA.

8.5 Chronic changes in post-ablation function

All surfaces converged to the specified tolerance in under five minutes with an average RMSE of 1.9 ± 0.4 mm. RMSE did not vary with longitudinal time point (pre, 6wk, 6mth) - there was a maximum difference of 0.08 mm between group means (less than 20% of the pooled standard deviation). The average regional radius was 26 ± 5 mm, similar to previously measured averages for AF patients. We compared atrial volumes computed by summing axial contours to volumes computed by integrating the fitted 3-D surface and found a difference of 10.4 mL (surfaces were larger), which was similar to the offset observed in healthy subjects (8.4 mL) and our initial study of AF patients (8.5 mL). There was less than a 2 mL difference in offset between longitudinal time points (11.1, 11.0, 9.2 mL). These comparisons confirmed a robust fitting method across three longitudinal time points.

Output (units)	Pre-Ablation ($\mu \pm \sigma$)	6-week Post ($\mu \pm \sigma$)	6-month Post ($\mu \pm \sigma$)	ANOVA p-value
V_{max} (mL)	100 ± 27	94 ± 22	91 ± 20	0.08
V_{min} (mL)	56 ± 24	50 ± 18	48 ± 14	0.04
Changes in Volume				
ΔV_t (mL)	44 ± 11	44 ± 9	43 ± 11	0.90
ΔV_a (mL)	28 ± 9	24 ± 11	23 ± 10	0.01
Fractional Measures				
EF_t (%)	46 ± 10	47 ± 7	48 ± 7	0.27
EF_a (%)	35 ± 8	32 ± 8	31 ± 9	0.13
$V_{a\|t}$ (%)	64 ± 14	54 ± 17	52 ± 16	< 0.001

Table 8.1: Changes in global function following ablation. All averages include $n = 20$ patients measured before and after ablation at 6-week and 6-month follow-ups. We reported changes in maximum and minimum atrial volume (V_{max} and V_{min}) as well as total and active emptying volumes (ΔV_t and ΔV_a). We normalized these volumes to correct for size differences, reporting total and active emptying fraction (EF_t and EF_a). We also calculated active emptying as a fraction of total emptying $V_{a|t}$. All statistical tests were based on a repeated-measures ANOVA (time as the factor).

8.5.1 Global changes in function

Following ablation, the atrium decreased slightly in size and decreased its reliance on active contraction (Table 8.1). Atrial volumes were smaller in post-ablation hearts compared to pre-ablation controls, decreasing in minimum V_{min} volume (56 to 48 mL, $p = 0.04$). As expected, the total emptying volume ΔV_t was almost identical between groups (a change less than 10% of the standard deviation). This matched our comparisons between healthy subjects and AF patients in Chapter 7, where the total emptying volume was identical regardless of size. Total emptying fraction EF_t increased slightly but the changes were not significant.

Active emptying ΔV_a decreased slightly following ablation (change of 5 mL, $p = 0.01$) but its fractional equivalent EF_a (active emptying fraction) did not change (EF_a is ΔV_a scaled by the size of the atrium at the start of contraction). The most significant change came in

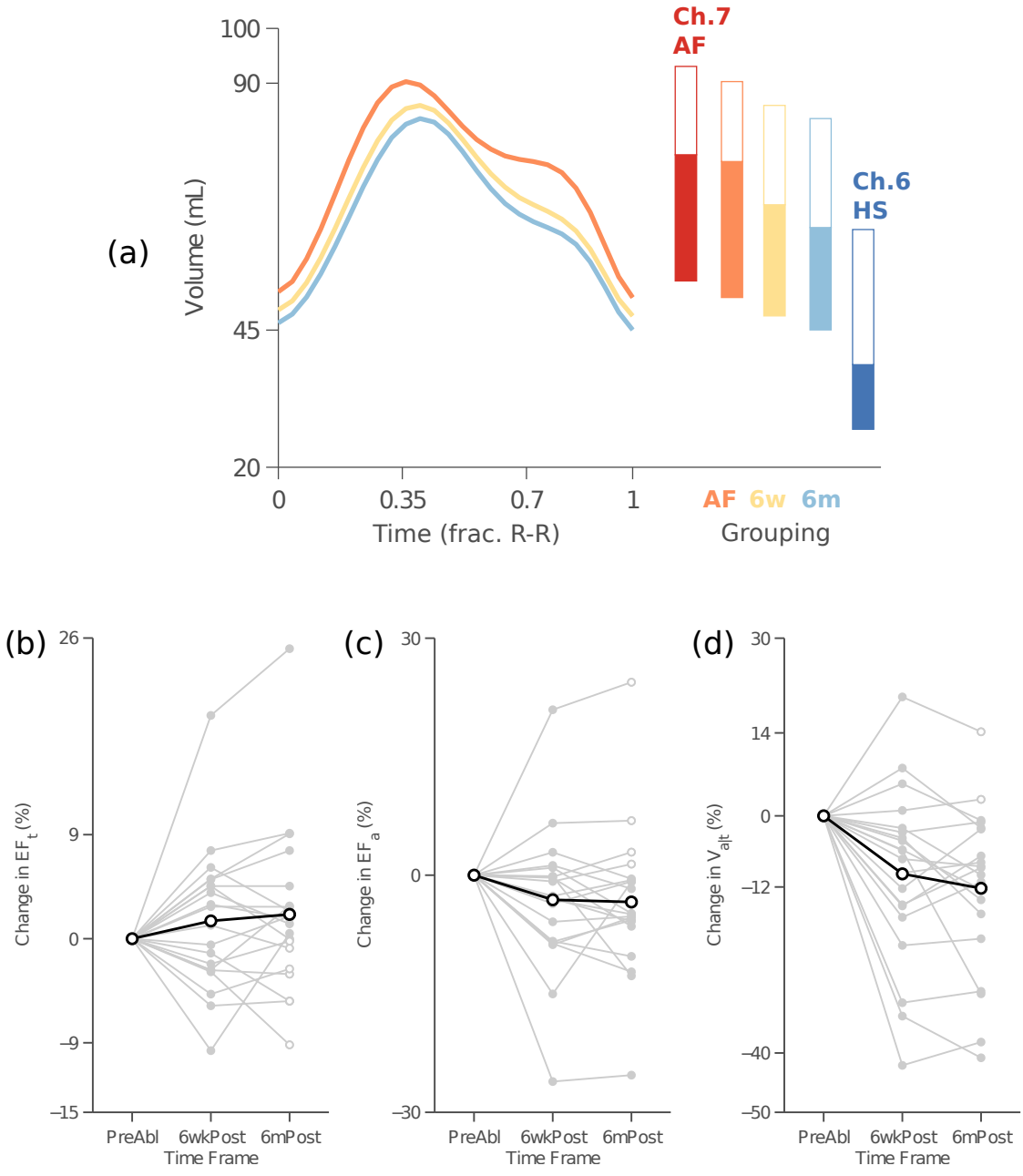

Figure 8.2: Changes in global mechanics following AF-targeted ablation. (a) Averaged pre-ablation (AF) volume-vs-time curve showed a higher volume and larger active emptying volumes compared to 6-week (6w) and 6-month (6m) follow-ups. The bars represent total and active emptying (filled portion). We compared longitudinal results to previous atrial fibrillation (Ch.7 AF) and healthy subject (Ch.6 HS) averages. (b-d) Bump plots for 20 subjects (gray lines) and their average (black line). (b) Changes in EF_t. (c) Changes in EF_a. (d) Changes in $V_{a|t}$.

the ratio of active emptying compared to total emptying $V_{a|t}$ - a decrease of 12% ($p < 0.001$). This change is visible in the volume-vs-time curves (Fig. 8.2a), where post-ablation atria emptied more during the passive phase and less during the active phase. This substantial change matched the most significant result from Chapter 7 - an increase in $V_{a|t}$ in AF patients compared to healthy subjects. The changes in $V_{a|t}$ followed a general trend of post-ablation function: the atrium returned to a healthier state following the removal of AF (Fig. 8.2a, bars). Following ablation, the atrium progressively shrank in size and decreased its reliance on contraction, moving away from the AF average and towards the healthy baseline.

We found two significant changes in global function: 1) a small decrease in atrial volume and 2) a larger decrease in $V_{a|t}$. We tested if the magnitude of these changes correlated with the amount of dysfunction prior to ablation. Atrial dilation is the most classic measure of dysfunction and typically cataloged by the maximum atrial volume. We used that and $V_{a|t}$ prior to ablation to test for correlations. We found a significant relationship between the change in maximum volume following ablation and the maximum volume at baseline (slope $\beta = -0.4$, $p < 10^{-4}$). Larger hearts were severely dilated and thus had more room to "improve" following a successful intervention (Fig. 8.3a). The change in $V_{a|t}$ following ablation correlated with pre-ablation volume ($\beta = 0.2$, $p = 0.004$) but *in the opposite* direction to what we expected. That is, the larger the initial volume (the standard measure of dysfunction), the *smaller* the change in $V_{a|t}$ following ablation (Fig. 8.3b). All significant trends were tested with both the 6-week and 6-month data, as well as just the 6-month data.

Interestingly, there was no significant correlation between the change in $V_{a|t}$ and the initial value of $V_{a|t}$ prior to ablation (Fig. 8.3c). We would expect a significant trend to emerge with a larger sample size since subjects with higher initial $V_{a|t}$ have more opportunity to decrease. Given the two changes in post-ablation atria, we explored the types of changes in each subject, separating them into four quadrants based on change in each of the two measures (Fig. 8.3d). Interestingly, no subject saw an increase in both size and reliance on active contraction. From these patterns, subjects with smaller atria prior to ablation tended

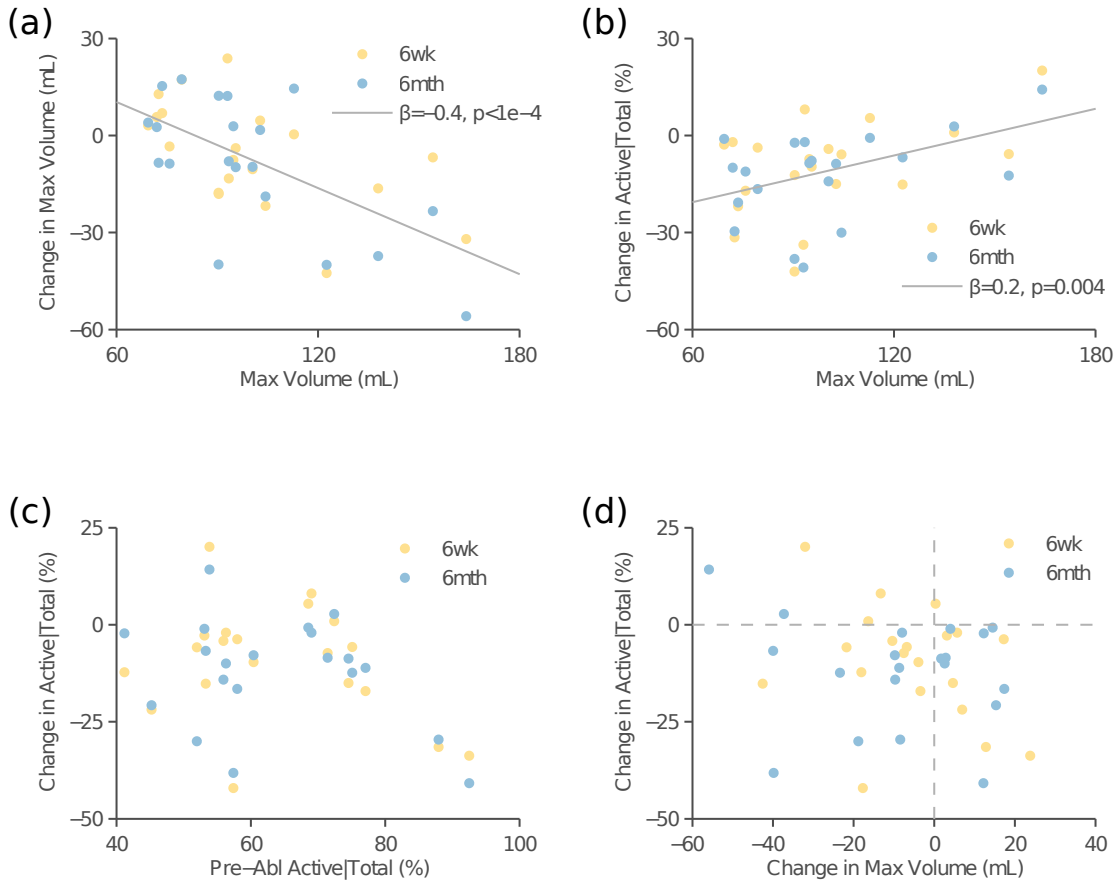

Figure 8.3: Correlative analysis between measures of global function post-ablation. (a) Change in V_{max} post-ablation compared to pre-ablation V_{max}.. Data is presented for two time points (6wk and 6mth) with a linear regression slope β and significance p. (b) Change in $V_{a|t}$ compared to pre-ablation V_{max}. (c) Change in $V_{a|t}$ compared to pre-ablation $V_{a|t}$ (not significant). (d) Change in $V_{a|t}$ compared to change in V_{max}, defined by four quadrants (dashed lines) post-ablation.

Region	Pre-Ablation ($\mu \pm \sigma$)	6-week Post ($\mu \pm \sigma$)	6-month Post ($\mu \pm \sigma$)	ANOVA p-value
Total Radial Emptying Fraction				
Inferior Wall	25 ± 8	25 ± 6	27 ± 6	0.44
Septal Wall	18 ± 6	17 ± 4	17 ± 5	0.63
Superior Wall	19 ± 6	21 ± 4	21 ± 4	0.03
Lateral Wall	22 ± 7	24 ± 5	23 ± 5	0.18
Active Radial Emptying Fraction				
Inferior Wall	18 ± 6	17 ± 5	17 ± 6	0.63
Septal Wall	12 ± 5	10 ± 4	9 ± 4	0.02
Superior Wall	17 ± 5	15 ± 7	15 ± 6	0.31
Lateral Wall	16 ± 4	18 ± 5	18 ± 5	0.17
Active Radial Emptying as a Fraction of Total				
Inferior Wall	64 ± 13	59 ± 15	57 ± 18	0.03
Septal Wall	61 ± 15	56 ± 20	49 ± 20	0.03
Superior Wall	97 ± 25	71 ± 31	71 ± 26	< 0.001
Lateral Wall	73 ± 18	70 ± 16	72 ± 17	0.78

Table 8.2: Changes in regional function following ablation. All averages include $n = 20$ patients measured before and after ablation at 6-week and 6-month follow-ups in four midwall regions. We reported changes in total radial emptying fraction (REF_t), active radial emptying fraction (REF_a), and (EF_t and EF_a). All statistical tests were based on a repeated-measures ANOVA (time as the factor).

to decrease $V_{a|t}$ post-ablation while patients with severely dilated atria had larger changes in volume and little or no change in $V_{a|t}$ post-ablation.

8.5.2 Regional changes in function

Subjects recovered regional function following ablation, especially in the superior wall. Regional function was more sensitive than global function - it captured significant changes in total REF_t and active REF_a function that were not observed in the global counterparts (EF_t and EF_a, respectively). We measured total regional function, active regional function,

and active function as a portion of total function $R_{a|t}$ for four midwall regions (Table 8.2). Regional function generally followed global trends - total function increased, active function decreased, and $R_{a|t}$ decreased. However, there was substantial variation between regions. Only the superior wall had a significant increase in REF_t (increase of 2%, $p = 0.03$) and only the septal wall had a decrease in REF_a (decrease of 3%, $p = 0.02$). These regional changes were masked in the global analysis (no significance). Active radial emptying as a fraction of total $R_{a|t}$ had significant decreases in the inferior ($p = 0.03$), septal ($p = 0.03$), and superior walls ($p < 0.001$). Significant changes in multiple regions matched the global change observed in $V_{a|t}$, which had the largest change of any global measure.

We visualized changes in regional function post-ablation using Hammer projections (Fig. 8.4). We focused on $R_{a|t}$ of all the available measures of function because it showed the most significant regional changes post-ablation. Hammer maps indicated exactly where those changes occurred - in the upper inferior wall near the posterior wall down into the septal wall and in the superior wall along the midline (equator of the Hammer map). The hammer maps also visualized the remarkable spatial consistently of $R_{a|t}$ between time points, with drops in the aforementioned regions and a steady level of function in the others. We also mapped the time at the start of contraction for each of the three averaged surfaces (T_a, right three maps). The delayed contraction in the pre-ablation average surface quickly dissipated in the post-ablation maps, especially in the upper inferior wall and the lower superior wall. Generally, the patterns of contraction (early near the right superior pulmonary vein, late near the appendage) matched the average maps from previous chapters. Although the average maps suggested improvement in conduction, individual patients had too much variation to find any statistical significance.

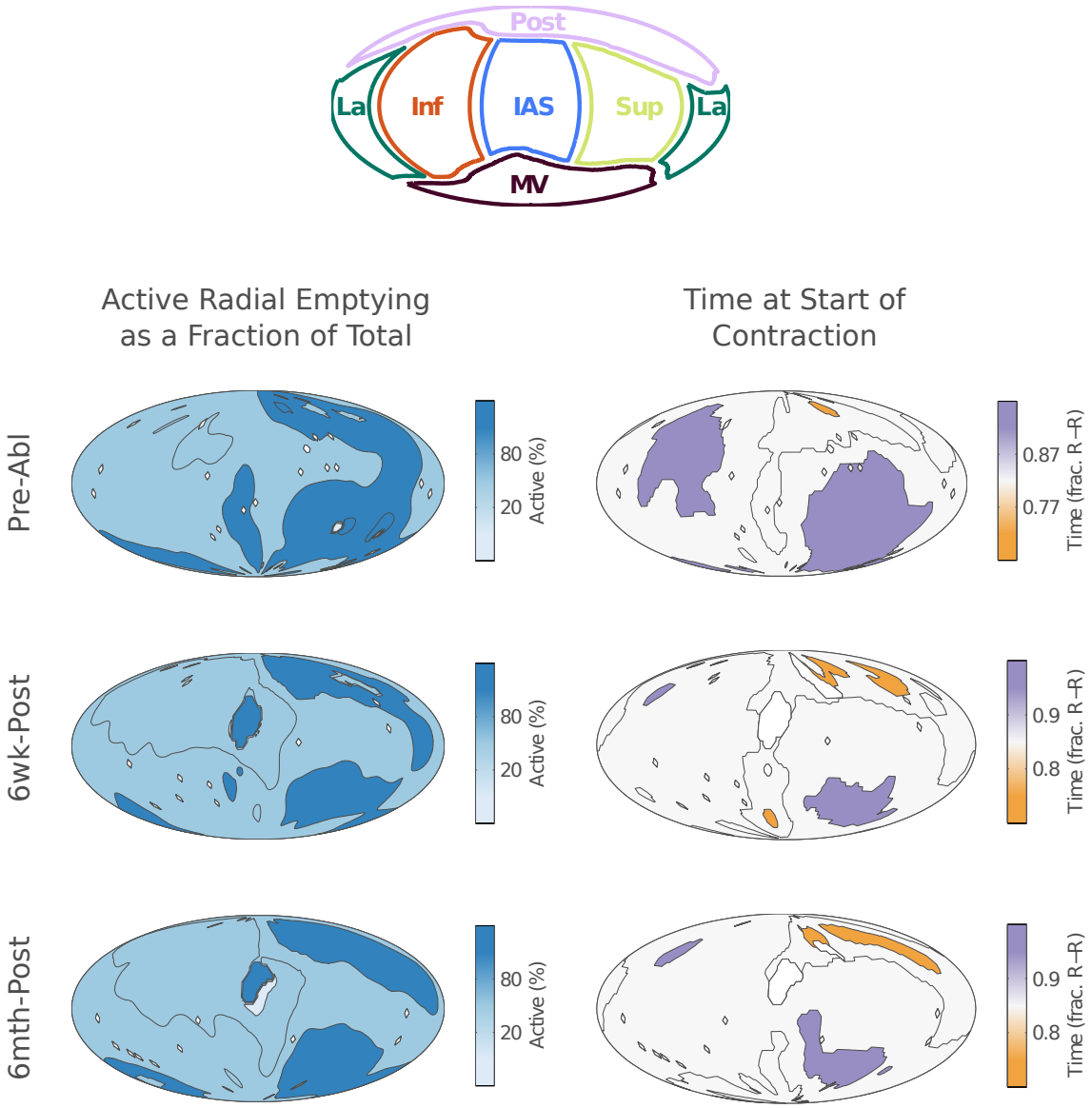

Figure 8.4: Hammer maps for averaged surfaces at each time point (pre-abl, 6wk-post, 6mth-post) representing active radial emptying as a fraction of total $R_{a|t}$ and time of contraction T_a. Hammer maps revealed a decrease in $R_{a|t}$ following ablation, especially in the inferior, septal, and superior walls. Time of contraction also decreased, with less delayed activation in the upper inferior wall and superior wall.

8.6 Methods to simulate mechanical changes due to ablation

Longitudinal analysis of post-ablation function found numerous significant changes in mechanics, but it was not possible to determine the source of those changes. Were all changes due to a recovered sinus rhythm, or could some result from the intervention itself? We explored the effect of adding ablation scar to an atrium using the finite element model described in Chapter 6. We used the approach developed for modeling fibrosis (described in detail in Chapter 7) and applied it to simulate ablation scarring in the atrium. We simulated a set of common scar patterns and sizes in the healthy subject baseline (HS) and the atrial fibrillation patient baseline (AF) models from Chapter 6 and 7, respectively. We measured the changes in global and regional function due to ablation scarring, as well as their effect on regional stresses and strains.

8.6.1 Ablation scar models

We modified the atrial material model (transversely-isotropic Mooney-Rivlin) by isotropically stiffening the material. We used a similar approach to Chapter 7, where we modeled fibrosis by increasing the isotropic coefficient C_2 within the strain energy function to 4.0 kPa. Here, we assumed that ablation scar would be stiffer than interstitial fibrosis, so we doubled this coefficient to $C_2 = 8.0$ kPa. We eliminated all anisotropic material properties (fiber stiffness $C_3 = C_4 = 0$) since RF ablation would obliterate almost all viable muscle in the area. We also removed all active contraction from this material model. We introduced scar by modifying the local material properties prior to simulation and modeled all scars as fully transmural. In summary, the ablation scar material was assumed to be stiff, isotropic, and non-contractile compared to the healthy atrial material.

We used two models of atrial function - the healthy subject baseline described in Chapter 6 and the AF baseline developed at the end of Chapter 7. We wanted an AF baseline that

best represented *in vivo* AF function, so we included all of the five factors tested in Chapter 7 (pressure, size, shape, fibrosis, conduction) at average AF levels, as well as a impaired ventricular relaxation. We used these models in parallel to study two trends: the amount of functional change from a healthy baseline - when there is a lot of function to be lost - and the amount of functional change from an AF baseline, which is closer to the clinical average atrium just prior to an ablation.

8.6.2 Design of parameter study

We modeled two common ablation procedures: a pulmonary vein isolation (PVI) and a wide-area circumferential ablation (WACA). We modeled three versions of each procedure. The PVI procedure was varied based on three common steps, usually done in sequence: 1) a pulmonary vein isolation, 2) a PVI and a "roof line", 3) a PVI, roof line, and "mitral valve isthmus line". This sequence is sometimes referred to as a step-wise ablation, and we modeled these three components as follows. We generated a PVI scar via concentric circles at 150% of the pulmonary vein diameter. This location was roughly at the edge of the pulmonary vein ostia in our model. The pulmonary vein diameters varied from 0.8-1.2 cm, and thus the PVI rings ranged from 1.2-1.8 cm diameter. The roof line was set by the shortest path between the left superior and right superior pulmonary veins, and the isthmus line was set by the shortest path between the left inferior vein and the mitral valve. These ablation patterns have been described in great detail by many groups, including (Haissaguerre et al., 2005; O'Neill et al., 2006).

The WACA procedure was modeled as large concentric circles around the right and left pulmonary veins (the superior and inferior veins were encircled together in this procedure). These circles were positioned at 1 cm away from the edge of vein ostia, creating a large oval shape around each pair of veins as described by (Oral et al., 2003). There was some variation in WACA techniques described in clinical literature; encircling as close as 5 mm away from the ostia (Pappone et al., 2000) or as far as 2 cm (Oral et al., 2006). Because of this variation

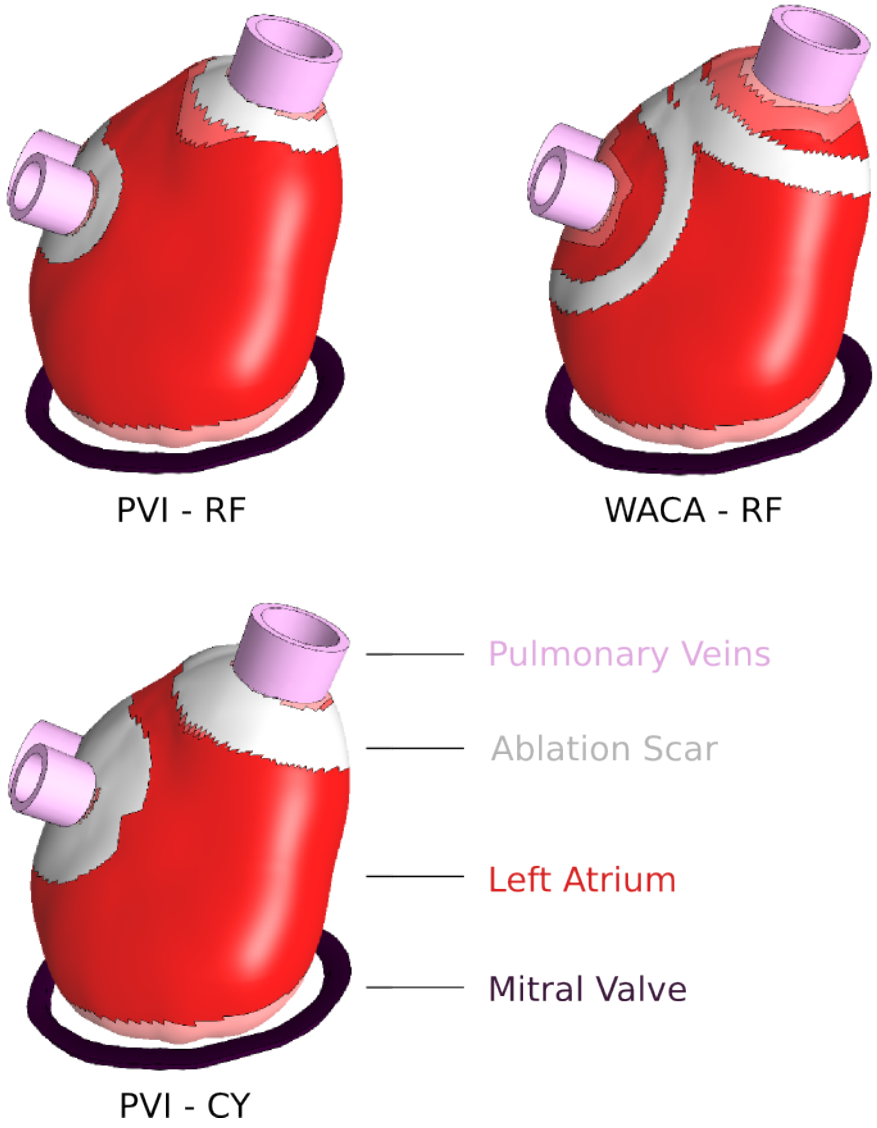

Figure 8.5: Finite element models of ablation scar in a healthy atrium. Two common procedures were modeled - pulmonary vein isolation (PVI) and wide-area circumferential ablation (WACA). Ablation scar was modeled as either a narrow RF scar (4 mm) or a wide CY scar (8 mm), representing radiofrequency and cryo-ablation.

in the procedure, we designed three variations of the WACA model - a "narrow" model (0.5 cm distance), a "normal" model (1.0 cm distance), and a "wide" model (2.0 cm distance). The narrow WACA model was only slightly larger than the PVI scar described previously.

For each pattern we modeled two scar widths: 4 mm and 8 mm. These widths were based on the typical diameter of a radiofrequency (4) and a cryoablation (8) catheter. We abbreviated each as "RF" and "CY" and considered them (roughly) as conservative and aggressive forms of the procedure. The change in material properties was equivalent for the two models, only width varied. In total, the modeling experiment had three factors: 1) finite element model, 2) type of scar pattern, 3) width of scar. This created 2x6x2 factor design with 24 total models. We quantified the scar added to each model as a volume and a percentage of left atrial wall volume. We simulated each model following the steps in Chapter 6 and captured global and regional changes in function.

8.7 Results of simulated mechanical function post-ablation

Simulated ablation scar decreased total and active function in both the healthy and AF atrium. The magnitude of losses correlated with scar volume, reported as a percentage of viable atrial tissue. Generally, the healthy subjects lost more function in scar simulations due to higher "baseline" function. Aggressive procedures such as WACA tended to decrease function more than the conservative PVI, even when scar volumes were equivalent.

8.7.1 Pressure-volume loops

Pressure-volume loops displayed increased passive stiffness and decreased stroke work in ablation simulations. The HS-baseline model had smaller volumes, lower pressures, and more passive emptying compared to the AF-baseline model (Fig. 8.6a). The AF-baseline model had higher stroke work during active emptying (18.9 mJ vs. 8.8 mJ) and a higher tissue stiffness during passive filling (7.6 vs. 5.5). Adding ablation scar decreased stroke work

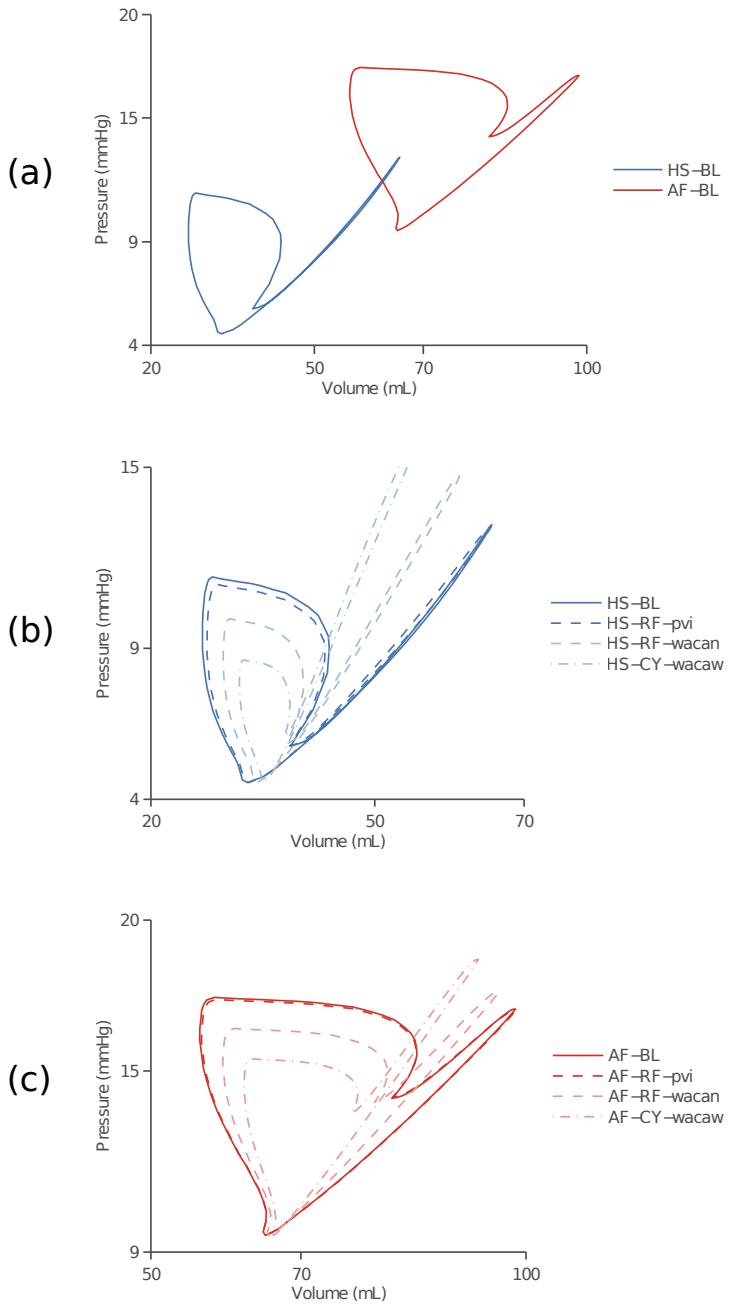

Figure 8.6: Pressure-volume loops of pre- and post-ablation simulations. (a) Baseline (BL) P-V loops for healthy subject (HS) and atrial fibrillation (AF) models. (b) Changes in P-V loops following ablations: Pulmonary-vein isolation (PVI) with radiofrequency catheter (RF), wide-area circumferential ablation (WACA) with RF, wider WACA with cryoablation (CY) catheter. (b) Same ablation patterns applied to AF model.

and increased passive stiffness in both models (Fig. 8.6b-c). We selected three loops that depicted the range of procedures: 1) the simple PVI with an RF catheter, 2) the WACA model with an RF catheter, and 3) a wider WACA model with a cryoabaltion catheter (the most aggressive simulation). A pulmonary vein isolation had a negligible effect on global mechanics while the WACA models had a noticeable impact. The healthy atrium (Fig. 8.6b) was more susceptible to changes in function due to a high-functioning, soft tissue baseline.

8.7.2 Global function

We analyzed the effect of each factor in the modeling experiment (type of baseline, scar pattern, scar width) on changes in EF_t and reliance on active contraction $V_{a|t}$. We measured the effect of each factor by averaging the change of a functional measure from its baseline for each model where that factor was present. For instance, the pulmonary vein isolation was used in four models (HS-RF, HS-CY, AF-RF, AF-CY) and their average change in function represented the effect of PVI. We found that the type of scar pattern (PVI vs. WACA) had the largest influence on function (Fig. 8.7a). EF_t decreased by as little as 2.3 (average of PVI models) and as much as 9.8% (average of wide-WACA), a difference of over 7% between the most conservative and aggressive patterns. Scar pattern had more influence than the type of baseline (3% difference) or scar width (4.4% difference). $V_{a|t}$ was also heavily influenced by scar pattern (Fig. 8.7b), with average decreases ranging from 1.7% to 8.0% between the most conservative and aggressive patterns, a larger range (6.3%) than scar width (3.1%) or baseline type (1.9%). Scar patterns modified both the amount and location of scar in the atrium and, in combination, these changes outweighed other factors in modifying function. A WACA procedure added more scar volume than a PVI and added it in highly functioning regions, increasing its influence on function. Regional analysis in §8.7.3 confirmed this result.

We used the hydraulic circuit (described in Chapter 6) attached to the FE model to analyze changes in two key measures of LV function: stroke volume (Fig. 8.7c) and the fraction of stroke volume added during atrial contraction (Fig. 8.7d). LV stroke volume

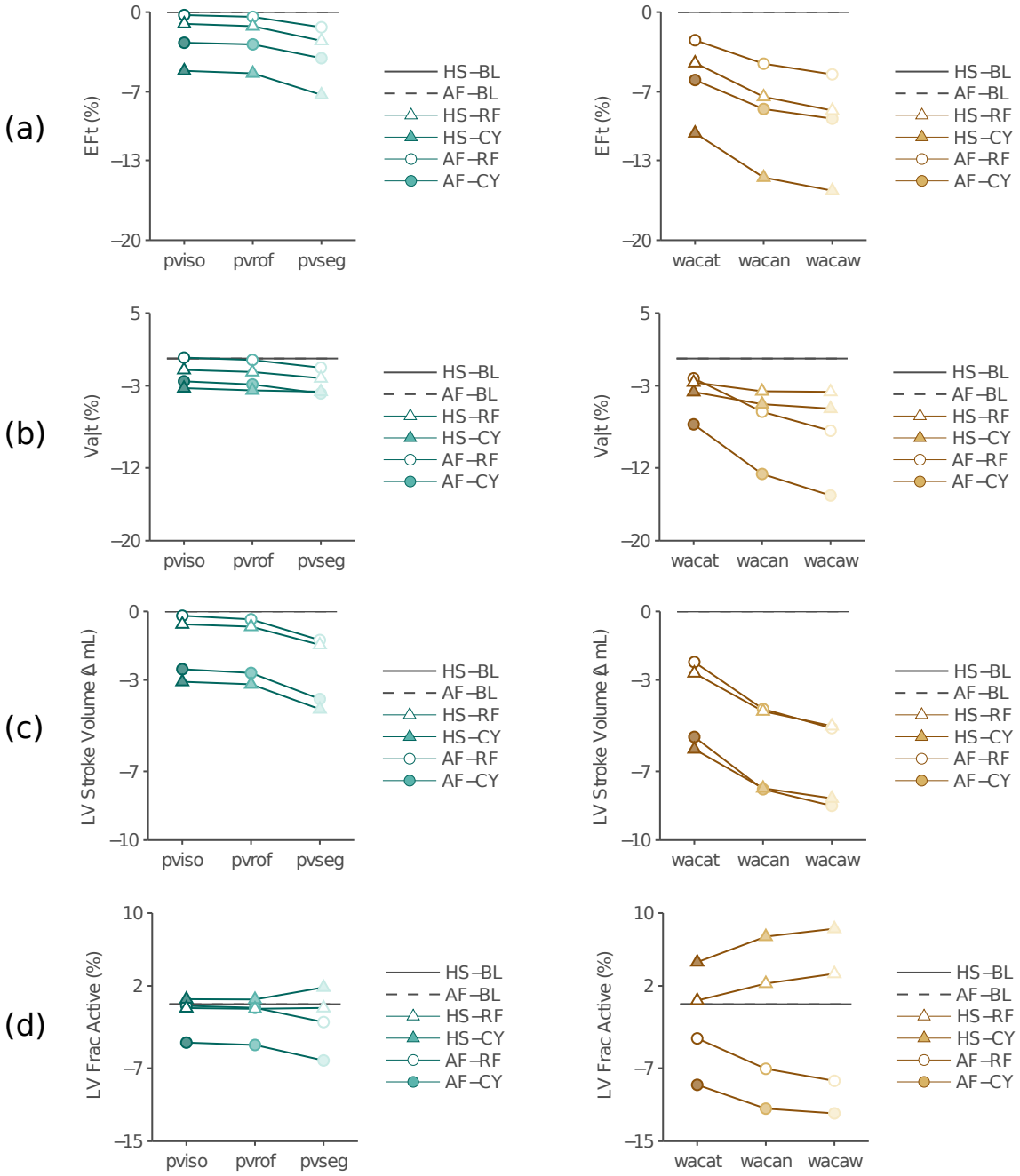

Figure 8.7: Changes in global function in ablation modeling experiment. (a) Changes in EF_t as a function of model type (HS, AF), ablation scar width (RF, CY), and ablation pattern (PVI, WACA). PVI is separated into PV isolation (pviso), PVI+roof line (pvrof), and PVI, roof, and isthmus (pvseg). WACA is separated into thin (wacat), normal (wacan), and wide (wacaw). (b) Changes in active emptying as a fraction of total $V_{a|t}$. (c) Changes in LV stroke volume. (d) Changes in atrial contribution to ventricular stroke volume (atrial active volume as a percentage of LV stroke volume).

decreased for all scar models, influenced by the limited passive filling of the atrium and impaired contraction. Just like atrial function, LV stroke volume was highly influenced by scar patterns, moderately influenced by scar width, and marginally influenced by baseline model. The most aggressive scar models decreased stroke volume by 8-9 mL.

We also analyzed the portion of LV stroke volume attributable to atrial contraction (reported as the LV "fraction active"). Here we found a clear divergence between HS and AF models. In the healthy HS model, LV filling volumes decreased a lot during early diastole (passive atrial emptying and conduit flow) and decreased on slightly during late diastole (atrial contraction). As a fraction of stroke volume, LV filling during atrial contraction *increased*. In contrast, the AF model had larger losses in LV filling volumes during late diastole due to impaired atrial contraction. This result stood in contrast to atrial $V_{a|t}$ which decreased in both the HS and AF models. We believe the difference in LV filling arose from changes in conduit flow (flow from the pulmonary veins through to the ventricle), which decreased following ablation and tended to fill the ventricle more during early diastole. Unlike the measures of atrial function, the baseline model choice (HS vs. AF) was the dominant factor in the measure of fractional LV filling, with smaller influence from choices in scar pattern or scar width.

We analyzed changes in global function (volume and its fractional measures) with respect to the amount of added scar. We included all patterns (PVI, WACA) and widths (RF, CY) in the analysis to create a distribution of $n = 12$ typical scar volumes, ranging from 5 to 41% of atrial tissue. We fit a linear trend line and used the slope as an approximate measure of sensitivity between scar volume and function. Maximum atrial volume V_{max} decreased in all ablation models but the changes were slight. The healthy atrium decreased by 2 mL per 10% of scar added, and the AF model decreased by only 1 mL per 10% of scar. Total emptying fraction EF_t decreased more substantially than volume, with average decreases of 3.0% in HS model and 2.4% in the AF model per 10% of scar. Active function, which was similar in the HS and AF models, decreased by an identical amount (3.1% per 10% of scar). Active

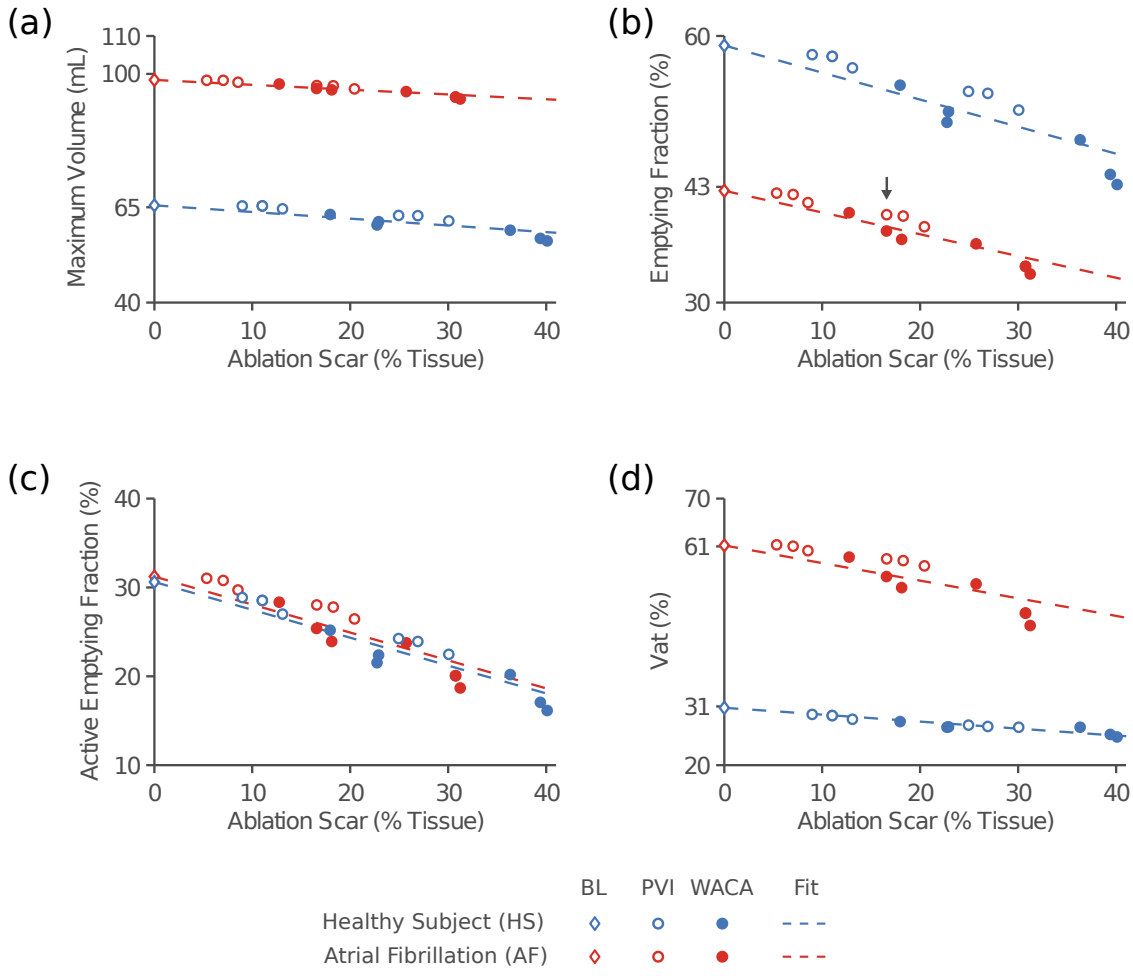

Figure 8.8: Ablation scarring decreased atrial size and global mechanical function based on 12 different procedures. (a) Maximum atrial volumes decreased in both HS and AF models, and changes linearly correlated with amount of scar. (b) EF_t decreased with added scar, with larger absolute changes in the HS model. (c) EF_a decreased at similar rates in the two models. (d) $V_{a|t}$ decreased with added scar, especially in the AF model.

emptying as a fraction of total $V_{a|t}$ decreased by 3.3% in the AF model and only 1.3% in the HS model. Scar affected total function the most in healthy subjects (a lot of function to lose) and affected $V_{a|t}$ the most in AF patients who had an increased reliance on active contraction. Interestingly, EF_a did *not* differ between HS and AF patients but *does* change with ablation scar, making it a potentially valuable indicator of ablation-related damage.

Scar patterns had the largest influence on function, partially due to differences scar volume and partially due to changes in location. We previously showed how function generally decreased with scar volume (Fig. 8.8, linear fit), but individual procedures deviated from this trend. For example, a PVI-CY ablation in the AF model added 16.57% scar, while a WACA-RF ablation in the same model added 16.55% - essentially the identical amount of scar. However, PVI-CY decreased EF_t by 2.7% while WACA-RF decreased it by 4.5% demonstrating the location-dependence of scar and the need to evaluate both global and regional function (Fig. 8.8b, gray arrow).

8.7.3 Regional function

Regional function decreased in scar simulations compared to pre-scar baseline, and the severity of these decreases varied between regions (Fig. 8.9). Regional function generally followed global trends, with decreased total REF_t, active REF_a, and $R_{a|t}$. We restricted the analysis to the AF model for simpler comparisons with *in vivo* results post-ablation. Total REF_t decreased in the inferior (1.6), posterior (2.0), and lateral walls (1.9% per 10% scar volume) at similar rates and less in the superior wall (0.8). The septal wall displayed minimal effect from scarring with a relatively flat trend line (0.4). There was no relationship between rate of function losses in each region (slope) and pre-ablation function in that region (y-intercept). Loss of active function REF_a was more homogeneous in four of five regions (1.4-1.9% per 10% scar), with less sensitivity in the septal wall (0.4%). Active emptying as a fraction of total $R_{a|t}$ had the most substantial regional decreases, ranging from 2.4 to 5.0% per 10% scar. Individual scar patterns deviated from trend lines due to spatial variation of scar. Using

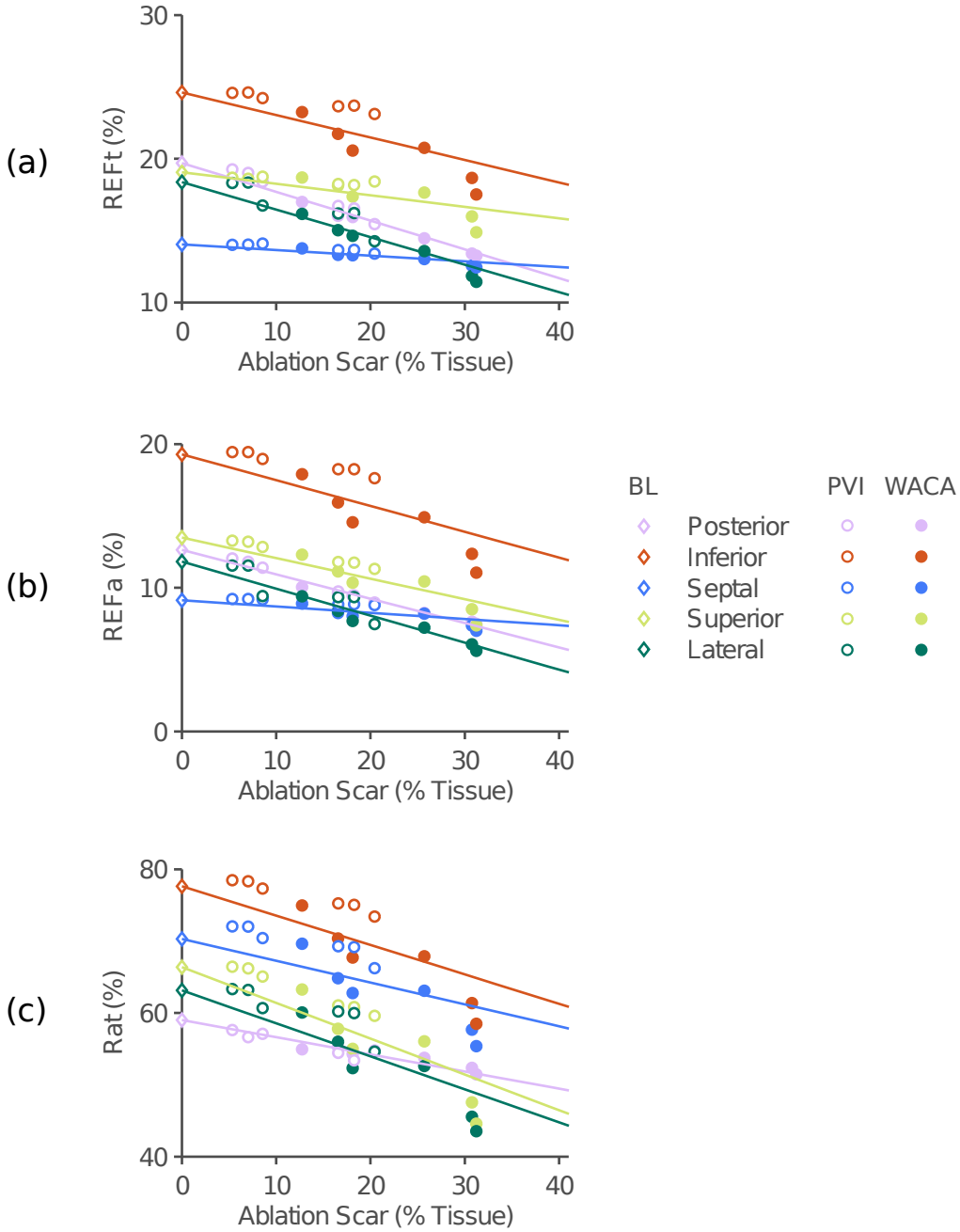

Figure 8.9: Changes in regional atrial function due to ablation scar in 12 scar patterns (only AF model shown). (a) Change in total radial emptying fraction REF_t vs. scar in five regions - posterior, inferior, septal, superior, and lateral walls. Linear trend lines were fit to each region. Open circles are step-wise PVI patterns, closed circles are WACA patterns. (b) Changes in regional active REF_a. (c) Changes in active emptying as a portion of total $R_{a|t}$.

inferior wall REF_t as an example, WACA procedures had a larger-than-expected influence (4 of 6 WACA procedures below trend line, Fig. 8.9a, closed circles) and step-wise PVI procedures had less relative influence (6 of 6 procedures above trend line, open circles). The influence of scar patterns (amount and location) extended from global to regional changes in function.

8.7.4 Regional wall stress

Regional wall stress increased in some regions following simulated ablation, but did not increase in all regions. We averaged wall stress for all left atrial elements and found minimal variation in average stress as a function of scarring (Fig. 8.10a). There was minimal variation in both HS and AF models and in circumferential, longitudinal, and first principal stress. On average, ablation scar did not significantly alter left atrial wall stress. Regional analysis was more revealing - atrial wall stress increased in the posterior, inferior, and lateral walls and decreased in the septal and superior walls (Fig. 8.10b). Changes in regional stress were larger in the longitudinal direction (Fig. 8.10c) while circumferential stress was relatively constant. Individual scar patterns deviated from these trends. Step-wise PVI procedures tended to elevate stress in the posterior wall (dots above trend line, Fig. 8.10b-c, open circles), and the addition of the mitral isthmus line elevated stress in the lateral wall (Fig. 8.10b-c, open circles, 20% scar). Likewise, WACA procedures increased stress in the inferior wall as the wider scar rings encroached on the higher functioning regions (Fig. 8.10c, closed circles, 30% scar). More generally, locations with added scar tended to see higher regional wall stress.

We visualized more detailed changes in regional function and stress using Hammer map projections. We chose two typical ablation procedures (PVI-RF and WACA-RF) and mapped the changes in radial motion REF_t and longitudinal wall stress. To better visualize the *changes* in function, we subtracted the post-ablation Hammer map from the control (pre-baseline) values (Fig. 8.11). Recall that function was highest in the lateral and inferior walls - both PVI and WACA procedures had the largest impact in those regions, especially in the

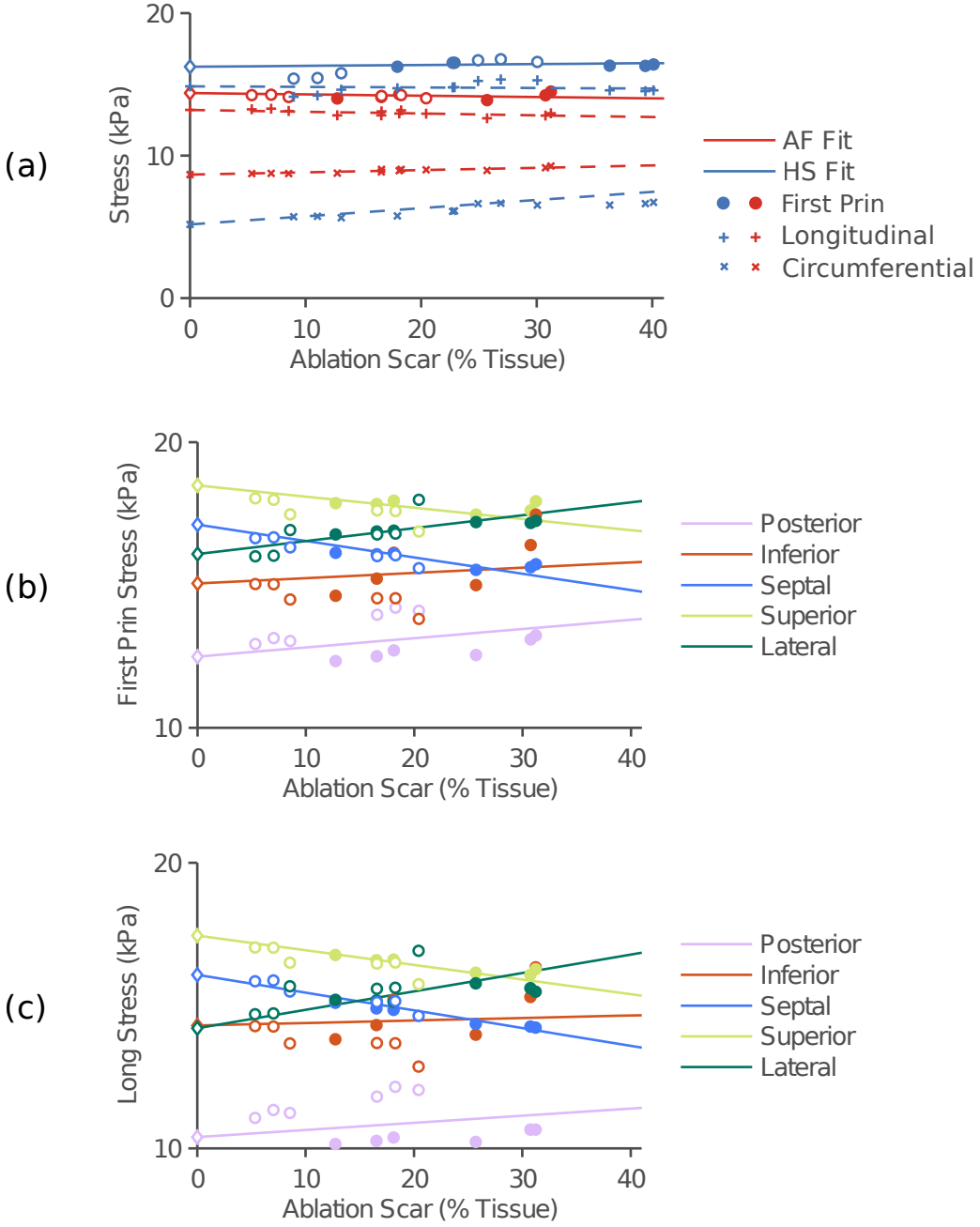

Figure 8.10: Changes in regional wall stress due to ablation scar in 12 scar patterns. (a) Change in average wall stress vs. scar in the circumferential, longitudinal, and first principal directions, for both the HS and AF models. Linear trend lines were fit to each direction. (b) Changes in first principal wall stress in five regions vs. volume of ablation scar (only AF model shown). Open circles are step-wise PVI patterns, closed circles are WACA patterns. (c) Changes in longitudinal wall stress for same five regions.

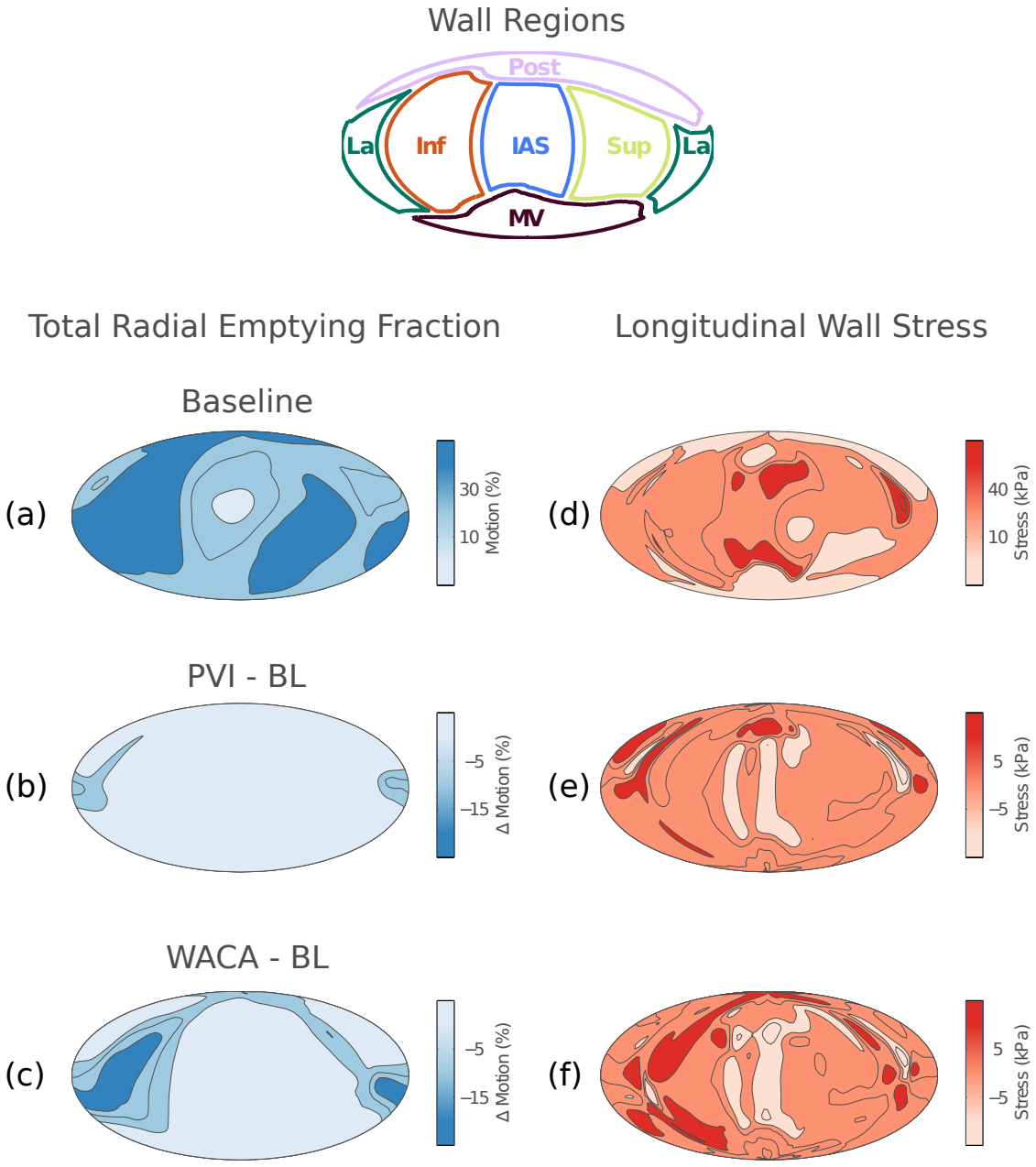

Figure 8.11: Hammer maps of post-ablation regional function and regional wall stress. (a) Baseline radial motion REF_t for atrial wall in HS model. (b) Changes in REF_t following a simulated PVI procedure, with darker colors indicating larger decreases in function. (c) Changes in REF_t following WACA procedure. (d) Longitudinal wall stress in the pre-ablation HS model. (e) Change in stress following PVI simulation, with darker colors indicating larger increases in stress. (f) Changes in stress following WACA procedure. A Hammer map of regions is added for comparisons.

lateral wall below the left inferior pulmonary vein. Longitudinal wall stress increased in the same regions, with the biggest changes in the lower inferior wall. The WACA procedure, which added more scar further away from the PV ostia, saw larger drops in REF_t and larger increases in regional stress. Interestingly, stress in the septal wall (with longitudinally-aligned fibers and high baseline stress) decreased in both the PVI and WACA models.

8.8 Global and regional post-ablation function

Atrial function acutely decreased and chronically improved following ablation therapy for AF. P-V loops revealed decreased stroke work and increased tissue stiffness immediately following ablation, confirming our hypothesis of acute changes in atrial function. These acute depressions were temporary; the longitudinal wall motion study found a recovery of function towards a healthier state (smaller size, less active). The atrium decreased in size and decreased its reliance on active emptying, especially in the superior wall. Simulated FE models of ablation scar demonstrated a strong correlation between scar patterns and changes in total EF_t, active EF_a, and $V_{a|t}$. Changes were driven by variation in scar volume and location (especially in WACA procedures), confirming our hypothesis of location-dependent changes in function. The magnitude of changes in atrial size and function due to scarring were small compared to observed changes in post-ablation function.

8.8.1 Acute changes in function

Radiofrequency ablation locally heats tissue and ruptures cell membranes, destroying atrial myocytes and their conduction pathways. Within 10 minutes of lesion formation, fluid accumulates in and around the ablation site (edema). The amount of local edema varies based on procedure type and subject (Okada et al., 2007), though it quickly spreads to remote regions of tissue (Badger et al., 2011). We anticipated that edema would stiffen the atrial wall and impede its contraction. Atrial P-V loops confirmed this result, with a

near doubling of atrial tissue stiffness and decrease in stroke work. Edema typically resolves within a day following the procedure (Kholmovski et al., 2012) and completely vanishes by one month post-ablation (Okada et al., 2007). If it could be measured at a follow-up, we expected a P-V loop to have only a marginal increase in stiffness from the resolved scar near the pulmonary veins - similar to the increased stiffness in simulated PVI-RF loops in Figure 8.6. The decrease in stroke work would also be muted, impaired only by the ablated regions with lost contraction. Numerous studies have shown that edema fully resolves one month following ablation, so we do not believe that changes in wall motion (discussed in §8.8.2) were caused by edema at either time point in the longitudinal study. Acute changes in atrial mechanics captured by P-V loops were caused from tissue edema, which did not alter chronic function.

There is a dearth of studies observing atrial P-V loops following RF ablation. One group measured atrial P-V loops immediately prior to and following an RF ablation using a similar technique to ours, and found a rightward shift of the loop (larger volumes) but no change in stroke work (Hettrick et al., 2005). Our results had an identical rightward shift in P-V loops to larger volumes (Fig. 8.1b). We suspect that tissue edema interfered with the conductance measurement where a buildup of fluid in and around the atrial wall may have been recorded as part of the blood volume by the catheter. Although not quantified, an example P-V loop pair in (Hettrick et al., 2005) appeared to have a stiffer passive curve similar to our results.

8.8.2 Chronic changes in function

Numerous studies have analyzed atrial function post-ablation, using echocardiography, CT, and MRI. Although the approaches were different, most studies measured change in atrial volume and change in total function EF_t following ablation. All groups found that maximum volume decreased following ablation - the most common and classic indicator of atrial function. However, results with EF_t varied: some groups found that it decreased post-ablation (Lemola et al., 2005a), others found that it increased (Verma et al., 2006), and still others found

no significant change (Nori et al., 2009; Perea et al., 2008). Recall that our results found no significant change in EF_t, though it was trending towards improved function. These muddled results are likely created by variations in patient recruitment (sicker hearts have more function to recover) and the compounding effect of ablation scar lowering EF_t in aggressive procedures. Only one group measured regional function post-ablation using 2-D MR and a fixed centroid method of radial shortening (Nori et al., 2009). Recovery of regional function (similar to REF_t) was highly variable (some regions improved, others worsened), though their choice of landmarks and regions made it difficult to compare their results to ours. Although regional function showed more sensitivity to changes post-ablation (Table 8.2), capturing these changes accurately depends on the robustness of the method. Our Hammer maps of changes in function revealed small pockets of improvement, which may not be detected on 2-D analysis.

8.8.3 Understanding post-ablation function

We used the atrial finite element model to simulate changes in function caused by ablation scar. Earlier, we had posed a question - are portions of observed changes in atrial function due to scarring or are all improvements a functional response to restored sinus rhythm? Using the ablation model, we confirmed that scarring played a minimal role in observed changes in function. We simulated the PVI-RF pattern that added roughly 5-9% ablation scar, depending on the model. We assumed that a typical PVI ablation added no more than 10% ablation scar. Based on the observed trends, 10% scarring would decrease V_{max} by only 1 mL and actually increase in V_{min}, whereas *in vivo* changes saw an average decrease of 8 mL in V_{min} and 9 mL in V_{max} (only V_{min} was significant). Total function (EF_t) was expected to decrease due to ablation scar (-2.4%), but showed a non-significant increase of 2% in the fitted surface data. Likewise, the portion of emptying during active contraction $V_{a|t}$ was expected to decrease by 3.3% based on ablation simulations - much smaller than the actual decrease of 12%. Although scarring may have muted some of the changes or slightly exaggerated others,

we conclude that the majority of recovered function reflects improvements from restored rhythm.

Regionally we saw significant changes in the superior wall (2% increase in REF_t and 26% decrease in $R_{a|t}$), neither of which could be explained by ablation scar. We also saw decreases in $R_{a|t}$ in the inferior and septal walls (7% and 12% respectively), neither of which could be explained by added scar. Although regional trends did show a decrease in simulated $R_{a|t}$ in the inferior wall, the PVI scar pattern only grazed the inferior wall and the resulting changes in function deviated above the downward trend. Regional results confirmed the global function comparison - recovery of function following ablation was not significantly influenced by scar.

If all the changes due to scarring are small, is there any measure of function that captured its effect? We saw that fractional measures of active function EF_a were identical between the healthy subjects and AF patients. AF hearts tended to increase in size and proportionally increase the active empyting volume, keeping the ratio EF_a constant. This was true for the regional equivalent REF_a as well, which had *no* significant changes between HS and AF groups. Thus we would expect only minimal changes post-ablation. Globally, we did see a small but non-significant decrease in EF_a of 4%. From the ablation simulations, we saw a clear linear decrease in EF_a with added ablation scar, with almost identical trends between the HS and AF model. This raises the possibility that the small drop in EF_a was due to added scar. We can test this idea looking at regional active function REF_a. There *was* a significant decrease of REF_a in the septal wall (3% loss), possibly created, in part, by scarring during trans-septal punctures. Unfortunately, we did not include septal scarring in the ablation models, but it could be added in future work. REF_a in the posterior wall (the exact location where most scarring was added during PVI procedures) also significantly decreased (we removed an outlier atrium with abnormally large V_{max}). Although the scarring had a minimal impact on global function, changes in regional motion highlighted the capabilities and sensitivity of a regional wall motion analysis.

We searched for studies specifically measuring changes in active function EF_a and found one (Wylie et al., 2008). The group used CMR to quantify changes in atrial volume and found a significant decrease of 4% in EF_a - an exact match to our result. Their study had a larger sample size (33), implying that our result may become significant with increased patient recruitment. Wylie and colleagues took the analysis one step further and measured atrial scarring post-ablation using DE-MRI. They correlated post-ablation EF_a to amount of scar, and found a *highly significant correlation* between amount of added scar and loss of active function. Thus, the measure of active function EF_a and its regional equivalents could be a useful measure of ablation-related loss of function.

References

N. Akoum, M. Daccarett, C. Mcgann, N. Segerson, G. Vergara, S. Kuppahally, T. Badger, N. Burgon, T. Haslam, E. Kholmovski, R. Macleod, and N. Marrouche. Atrial fibrosis helps select the appropriate patient and strategy in catheter ablation of atrial fibrillation: A DE-MRI guided approach. *Journal of Cardiovascular Electrophysiology*, pages no–no, Aug. 2010.

T. Arentz, R. Weber, G. Burkle, C. Herrera, T. Blum, J. Stockinger, J. Minners, F. J. Neumann, and D. Kalusche. Small or large isolation areas around the pulmonary veins for the treatment of atrial fibrillation? results from a prospective randomized study. *Circulation*, 115(24):3057–3063, June 2007.

T. Badger, G. Vergara, A. Harrison, S. Vijayakumar, E. G. Kholmovski, C. J. McGann, R. S. MacLeod, and N. F. Marrouche. Real-time MRI evaluation of acute left atrial injury progression during radiofrequency ablation of atrial fibrillation. *Journal of the American College of Cardiology*, 57(14):E893, 2011.

A. G. Brooks, M. K. Stiles, J. Laborderie, D. H. Lau, P. Kuklik, N. J. Shipp, L.-F. Hsu, and P. Sanders. Outcomes of long-standing persistent atrial fibrillation ablation: A systematic review. *Heart Rhythm*, 7(6):835–846, June 2010.

H. Calkins. Catheter ablation to maintain sinus rhythm. *Circulation*, 125(11):1439–1445, Mar. 2012.

R. Cappato, H. Calkins, S.-A. Chen, W. Davies, Y. Iesaka, J. Kalman, Y.-H. Kim, G. Klein, D. Packer, and A. Skanes. Worldwide survey on the methods, efficacy, and safety of catheter ablation for human atrial fibrillation. *Circulation*, 111(9):1100 –1105, Mar. 2005.

J. L. Cox. The status of surgery for cardiac arrhythmias. *Circulation*, 71(3):413–417, Mar. 1985.

J. L. Cox, R. B. Schuessler, J. D'Agostino, H J, C. M. Stone, B. C. Chang, M. E. Cain, P. B. Corr, and J. P. Boineau. The surgical treatment of atrial fibrillation. III. development of a definitive surgical procedure. *J. Thorac. Cardiovasc. Surg.*, 101(4):569–583, Apr. 1991.

J. L. Cox, R. D. Jaquiss, R. B. Schuessler, and J. P. Boineau. Modification of the maze procedure for atrial flutter and atrial fibrillation: II. surgical technique of the maze III procedure. *The Journal of Thoracic and Cardiovascular Surgery*, 110(2):485–495, Aug. 1995a.

J. L. Cox, R. D. B. Jaquiss, R. B. Schuessler, and J. P. Boineau. Modification of the MAZE procedure for atrial flutter and atrial fibrillation: II. surgical technique of the maze III procedure. *J Thorac Cardiovasc Surg*, 110(2):485–495, Aug. 1995b.

C. S. Elayi, A. Verma, L. Di Biase, C. K. Ching, D. Patel, C. Barrett, D. Martin, B. Rong, T. S. Fahmy, Y. Khaykin, R. Hongo, S. Hao, G. Pelargonio, A. Dello Russo, M. Casella, P. Santarelli, D. Potenza, R. Fanelli, R. Massaro, M. Arruda, R. A. Schweikert, and A. Natale. Ablation for longstanding permanent atrial fibrillation: Results from a randomized study comparing three different strategies. *Heart Rhythm*, 5(12):1658–1664, Dec. 2008.

A. Gillinov and P. M. McCarthy. Atricure bipolar radiofrequency clamp for intraoperative ablation of atrial fibrillation. *The Annals of Thoracic Surgery*, 74(6):2165–2168, Dec. 2002.

M. Haissaguerre, L. Gencel, B. Fischer, P. Le Motayer, F. Poquet, F. I. Marcus, and J. Clementy. Successful catheter ablation of atrial fibrillation. *Journal of Cardiovascular Electrophysiology*, 5(12):10451052, 1994.

M. Haissaguerre, P. Jais, D. C. Shah, L. Gencel, V. Pradeau, S. Garrigues, S. Chouairi, M. Hocini, P. Le Motayer, R. Roudaut, and J. Clementy. Right and left atrial radiofrequency catheter therapy of paroxysmal atrial fibrillation. *Journal of Cardiovascular Electrophysiology*, 7(12):11321144, 1996.

M. Haissaguerre, P. Jais, D. C. Shah, A. Takahashi, M. Hocini, G. Quiniou, S. Garrigue, A. Le Mouroux, P. Le Metayer, and J. Clementy. Spontaneous initiation of atrial fibrillation by ectopic beats originating in the pulmonary veins. *N Engl J Med*, 339(10):659–666, Sept. 1998.

M. Haissaguerre, M. Hocini, P. Sanders, F. Sacher, M. Rotter, Y. Takahashi, T. Rostock, L.-F. Hsu, P. Bordachar, S. Reuter, R. Roudaut, J. Clementy, and P. Jais. Catheter ablation of long-lasting persistent atrial fibrillation: Clinical outcome and mechanisms of subsequent arrhythmias. *Journal of Cardiovascular Electrophysiology*, 16(11):11381147, 2005.

D. A. Hettrick, D. Schwartzman, H. Tse, and P. S. Pagel. Mechanical basis of atrial fibrillation. In D. S. MD and r. A. Z. MD, editors, *Innovative Management of Atrial Fibrillation*, pages 29–49. Blackwell Publishing, 2005.

M. Hocini, P. Jas, P. Sanders, Y. Takahashi, M. Rotter, T. Rostock, L.-F. Hsu, F. Sacher, S. Reuter, J. Clmenty, and M. Hassaguerre. Techniques, evaluation, and consequences of linear block at the left atrial roof in paroxysmal atrial fibrillation: a prospective randomized study. *Circulation*, 112(24):3688–3696, Dec. 2005.

P. Jais, M. Hocini, L.-F. Hsu, P. Sanders, C. Scavee, R. Weerasooriya, L. Macle, F. Raybaud, S. Garrigue, D. C. Shah, P. Le Metayer, J. Clmenty, and M. Hassaguerre. Technique and results of linear ablation at the mitral isthmus. *Circulation*, 110(19):2996–3002, Nov. 2004.

M. R. Karch, B. Zrenner, I. Deisenhofer, J. Schreieck, G. Ndrepepa, J. Dong, K. Lamprecht, P. Barthel, E. Luciani, A. Schmig, and C. Schmitt. Freedom from atrial tachyarrhythmias after catheter ablation of atrial fibrillation a randomized comparison between 2 current ablation strategies. *Circulation*, 111(22):2875–2880, June 2005.

E. Kholmovski, S. Vijayakumar, C. McGann, and N. F. Marrouche. Comparison between immediately and next day post RF ablation MRI in patients with atrial fibrillation. *J Cardiovasc Magn Reson*, 14(Suppl 1):P200, Feb. 2012.

K. Lemola, B. Desjardins, M. Sneider, I. Case, A. Chugh, E. Good, J. Han, K. Tamirisa, A. Tsemo, S. Reich, D. Tschopp, P. Igic, D. Elmouchi, F. Bogun, F. Pelosi Jr, E. Kazerooni, F. Morady, and H. Oral. Effect of left atrial circumferential ablation for atrial fibrillation on left atrial transport function. *Heart Rhythm*, 2(9):923–928, Sept. 2005a.

K. Lemola, H. Oral, A. Chugh, B. Hall, P. Cheung, J. Han, K. Tamirisa, E. Good, F. Bogun, J. F. Pelosi, and F. Morady. Pulmonary vein isolation as an end point for left atrial circumferential ablation of atrial fibrillation. *J Am Coll Cardiol*, 46(6):1060–1066, Sept. 2005b.

D. Nori, G. Raff, V. Gupta, R. Gentry, J. Boura, and D. E. Haines. Cardiac magnetic resonance imaging assessment of regional and global left atrial function before and after catheter ablation for atrial fibrillation. *J Interv Card Electrophysiol*, 26(2):109–117, Nov. 2009.

T. Okada, T. Yamada, Y. Murakami, N. Yoshida, Y. Ninomiya, T. Shimizu, J. Toyama, Y. Yoshida, T. Ito, N. Tsuboi, T. Kondo, Y. Inden, M. Hirai, and T. Murohara. Prevalence and severity of left atrial edema detected by electron beam tomography early after pulmonary vein ablation. *J Am Coll Cardiol*, 49(13):1436–1442, Apr. 2007.

M. D. O'Neill, P. Jais, Y. Takahashi, A. Jonsson, F. Sacher, M. Hocini, P. Sanders, T. Rostock, M. Rotter, A. Pernat, J. Clementy, and M. Haissaguerre. The stepwise ablation approach for chronic atrial fibrillationEvidence for a cumulative effect. *J Interv Card Electrophysiol*, 16(3):153–167, Sept. 2006.

H. Oral, B. P. Knight, H. Tada, M. zaydn, A. Chugh, S. Hassan, C. Scharf, S. W. K. Lai, R. Greenstein, F. Pelosi, S. A. Strickberger, and F. Morady. Pulmonary vein isolation for paroxysmal and persistent atrial fibrillation. *Circulation*, 105(9):1077–1081, Mar. 2002.

H. Oral, C. Scharf, A. Chugh, B. Hall, P. Cheung, E. Good, S. Veerareddy, F. Pelosi, and F. Morady. Catheter ablation for paroxysmal atrial fibrillation. *Circulation*, 108(19):2355 –2360, Nov. 2003.

H. Oral, C. Pappone, A. Chugh, E. Good, F. Bogun, F. Pelosi, E. R. Bates, M. H. Lehmann, G. Vicedomini, G. Augello, E. Agricola, S. Sala, V. Santinelli, and F. Morady. Circumferential pulmonary-vein ablation for chronic atrial fibrillation. *New England Journal of Medicine*, 354(9):934–941, 2006.

H. Oral, A. Chugh, K. Yoshida, J. F. Sarrazin, M. Kuhne, T. Crawford, N. Chalfoun, D. Wells, W. Boonyapisit, S. Veerareddy, S. Billakanty, W. S. Wong, E. Good, K. Jongnarangsin, J. F. Pelosi, F. Bogun, and F. Morady. A randomized assessment of the incremental role of ablation of complex fractionated atrial electrograms after antral pulmonary vein isolation for long-lasting persistent atrial fibrillation. *J Am Coll Cardiol*, 53(9):782–789, Mar. 2009.

D. Pajitnev, Z. Szalay, M. Kuniss, T. Neumann, S. Zaltsberg, H. Greiss, S. Lehinant, C. Hamm, T. Walther, H. Pitschner, and M. Schnburg. Hybrid ablation of long standing persistent atrial fibrillation utilizing minimally invasive surgical and endocardial catheter approach: A safety and feasibility study. *The Thoracic and Cardiovascular Surgeon*, 61(S 01), Jan. 2013.

C. Pappone, S. Rosanio, G. Oreto, M. Tocchi, F. Gugliotta, G. Vicedomini, A. Salvati, C. Dicandia, P. Mazzone, V. Santinelli, S. Gulletta, and S. Chierchia. Circumferential radiofrequency ablation of pulmonary vein ostia : A new anatomic approach for curing atrial fibrillation. *Circulation*, 102(21):2619–2628, Nov. 2000.

R. J. Perea, D. Tamborero, L. Mont, T. M. DeCaralt, J. T. Ortiz, A. Berruezo, M. Matiello, M. Sitges, B. Vidal, M. Sanchez, and J. Brugada. Left atrial contractility is preserved after successful circumferential pulmonary vein ablation in patients with atrial fibrillation. *J Cardiovasc Electrophysiol*, 19(4):374–379, Apr. 2008.

P. Reant, S. Lafitte, H. Bougteb, F. Sacher, A. Mignot, H. Douard, P. Blanc, M. Hocini, J. Clementy, M. Haissaguerre, R. Roudaut, and P. Jais. Effect of catheter ablation for isolated paroxysmal atrial fibrillation on longitudinal and circumferential left ventricular systolic function. *The American Journal of Cardiology*, 103(2):232–237, Jan. 2009.

C. Schmitt, H. Estner, B. Hecher, A. Luik, C. Kolb, M. Karch, G. Ndrepepa, B. Zrenner, G. Hessling, and I. Deisenhofer. Radiofrequency ablation of complex fractionated atrial electrograms (CFAE): preferential sites of acute termination and regularization in paroxysmal and persistent atrial fibrillation. *Journal of Cardiovascular Electrophysiology*, 18(10): 1039–1046, Oct. 2007.

N. M. Segerson, M. Daccarett, T. J. Badger, A. Shabaan, N. Akoum, E. N. Fish, S. Rao, N. S. Burgon, Y. Adjei-Poku, E. Kholmovski, S. Vijayakumar, E. V. R. Dibella, R. S. Macleod, and N. F. Marrouche. Magnetic resonance imaging-confirmed ablative debulking of the left atrial posterior wall and septum for treatment of persistent atrial fibrillation: Rationale and initial experience. *J. Cardiovasc. Electrophysiol*, Oct. 2009.

T. Terasawa, E. M. Balk, M. Chung, A. C. Garlitski, A. A. Alsheikh-Ali, J. Lau, and S. Ip. Systematic review: Comparative effectiveness of radiofrequency catheter ablation for atrial fibrillation. *Annals of Internal Medicine*, 151(3):191 –202, 2009.

L. Thomas, A. Boyd, S. P. Thomas, N. B. Schiller, and D. L. Ross. Atrial structural remodelling and restoration of atrial contraction after linear ablation for atrial fibrillation. *Eur. Heart J*, 24(21):1942–1951, Nov. 2003.

L. Thomas, T. Mckay, K. Byth, and T. H. Marwick. Abnormalities of left atrial function after cardioversion: an atrial strain rate study. *Heart*, 93(1):89 –95, Jan. 2007.

A. Verma, F. Kilicaslan, J. R. Adams, S. Hao, S. Beheiry, S. Minor, V. Ozduran, S. Claude Elayi, D. O. Martin, R. A. Schweikert, W. Saliba, J. D. Thomas, M. Garcia, A. Klein, and A. Natale. Extensive ablation during pulmonary vein antrum isolation

has no adverse impact on left atrial function: an echocardiography and cine computed tomography analysis. *J. Cardiovasc. Electrophysiol*, 17(7):741–746, July 2006.

L. S. Wann, A. B. Curtis, C. T. January, K. A. Ellenbogen, J. E. Lowe, N. M. Estes, R. L. Page, M. D. Ezekowitz, D. J. Slotwiner, W. M. Jackman, W. G. Stevenson, C. M. Tracy, and A. K. Jacobs. 2011 ACCF/AHA/HRS focused update on the management of patients with atrial fibrillation (updating the 2006 guideline): A report of the american college of cardiology Foundation/American heart association task force on practice guidelines. *Circulation*, 123(1):104–123, Jan. 2011.

J. M. Williams, R. M. Ungerleider, G. K. Lofland, and J. L. Cox. Left atrial isolation: new technique for the treatment of supraventricular arrhythmias. *J. Thorac. Cardiovasc. Surg.*, 80(3):373–380, Sept. 1980.

J. V. Wylie, D. C. Peters, V. Essebag, W. J. Manning, M. E. Josephson, and T. H. Hauser. Left atrial function and scar after catheter ablation of atrial fibrillation. *Heart Rhythm*, 5 (5):656–662, May 2008.

X. Zhao, J. Zhang, J. Hu, D. Liao, Y. Zhu, X. Mei, J. Sheng, F. Yuan, Y. Gui, W. Lu, L. Dai, X. Guo, Y. Xu, Y. Zhang, B. He, and Z. Liu. Pulmonary antrum radial-linear ablation for paroxysmal atrial fibrillation: Interim analysis of a multicenter trial. *Circ Arrhythm Electrophysiol*, Feb. 2013.

Chapter 9

Future directions

Atrial fibrillation is a growing epidemic in the developed world and current methods of evaluating AF patients and therapies are limited. In this thesis, we developed a novel set of tools to measure and simulate global and regional atrial function, both in healthy and diseased hearts. We hypothesized that left atrial function is regionally heterogeneous and changes in atrial function (due to AF and ablation) are regional phenomena that need to be evaluated in the context of regional contributions to heart function. Through nine chapters, we proved that left atrial wall motion is indeed spatially heterogeneous, as are the changes due to AF and ablation. Evidence from AF patients before an after therapy confirmed our hypothesis and demonstrated that regional function should be considered when evaluated AF and its therapies. We captured the magnitude of change in global and regional function due to AF and the potential sources of this change. We measured how function changes following ablation and simulated the effects of scarring. In combination, these discoveries have advanced our understanding of regional atrial function and how it changes due to disease and therapy. The tools developed in this thesis have many avenues of future application.

9.1 Wall motion staging

Current classification of AF is based on the frequency and duration of episodes. We could improve this classification based on global and regional atrial function using our wall motion analysis. Groups studying atrial fibrosis using DE-MRI have already shown that increases in fibrosis are not perfectly correlated with standard AF classifications. Some paroxysmal AF patients may have a severe amount of dysfunction while other persistent AF patients may have retained function. By using a wall motion-based technique, we would be able to classify AF by the amount of dysfunction it has created in the heart. A clinician could use this information to make a more informed decision about treatments.

For instance, a younger patient with paroxysmal AF but clear signs of lost function may be recommended an immediate pulmonary vein isolation, avoiding years of AADs and additional loss of function. Likewise, an older patient with some retained function may be recommended for an ablation (with the procedure chose to avoid that area). If a patient had severe dysfunction in all regions, there may be multiple sources of AF present and AADs might be chosen over an ablation. We already see some signs of functional staging, where treatment decisions are made based on type of AF and the amount of atrial dilation (size). Since we now know that atrial function is regionally heterogeneous, quantifying regional changes will be more sensitive that global measures, possibly improving this classification.

9.2 Wall motion outcomes

An AF therapy is chosen based on the goal of returning a patient to sinus rhythm. We have shown that recovery of sinus rhythm in paroxysmal AF patients resulted in significant functional improvements. However, there was a large variation among patients – some improved substantially while others improved marginally. We saw how function improved in different ways in some patients – some atria shrank in size while others returned to a more passive state. These changes represented the combination of multiple atrial and ventricular

factors changing following ablation. Future work with finite element models and larger patient groups could elucidate these differences. We suspect that some patients may easily return to a passive state (less active contraction) as pressures and volumes decrease to normal levels. Others with more advanced levels of AF-related dysfunction may see a change in size by maintain depressed motion due to fibrosis or altered shape. The discovery of impaired LV relaxation as a source of atrial dysfunction could also be explored in greater detail – quantified via tissue Doppler in post-ablation patients and see if it too changes following ablation. Understanding how we *expect* atrial function to change will allow to monitor patients following intervention and understand how function recovers in a patient-specific way.

Wall motion analysis is a novel tool to measure atrial function that overcomes the limitations of traditional strain-based measurements (speckle tracking, DENSE). We should anticipate that strain-based technologies will evolve with improved resolution and 3-D capabilities. Future studies should compare a DENSE-based analysis of atrial strain to regional atrial wall motion. Based on the finite element model, we expect that the two measures will be correlated (high motion regions have the highest strain), but not perfectly (external structures impair motion). A voxel-based DENSE analysis could capture even smaller regions of atrial function and better quantify the effects of ablation scar, especially smaller scar patterns near the pulmonary veins.

9.3 Regional effects of atrial scarring

In the finite element model of ablation scar, we showed how global and regional function can change due to scarring. Future work could validate these simulations using an *in vivo* animal model. Briefly, an standard scar pattern could be tested in multiple regions in an animal atrium. Global and regional atrial function could be measured pre- and post- ablation to observe changes in function from a healthy baseline entirely due to scar. This simplifies the

confounding factors of any clinical study (an ablation procedure in a human adds scar and removes AF). We suspect that scarring will decrease regional function in the area where scar is added. This experiment is easily possible and would be a nice validation of the finite element simulations. Some limitations would controlling the amount of scar in each ablation – ideally the experiment varies two factors (size and location) independently. Also, the animal must tolerate anesthesia during MRI and procedure measurements, and the choice of anesthisia must not impair atrial function. Previous studies of volatile gases have show that isoflurane has a noticeable effect on atrial function. The same animal procedure could also be used to validate measures of scar deposition, such as DE-MRI on a regional level.

9.4 Treatment planning with FEA

The finite element model of ablation was a powerful simulation tool - we could build any atrial geometry and test it against any scar pattern. In the future, a clinical and scientist could evaluate function in an AF patient using MRI or another imaging modality. Then, they could incorporate the patient-specific geometry into a finite element model and plan a treatment. For instance, if a clinician was considering two or three different ablation scar patterns, and each had the same change of successful recovery of sinus rhythm, the simulation could help guide which scar pattern preserved mechanical function. Likewise, the clinician and patient could use the finite element model and wall motion analysis to evaluate the trade-off between restoring normal rhythm and ablating portions of the heart wall. This type of planning would be vital as the number of ablation patterns has expanded rapidly in recent years.